國立臺灣大學理學院地質科學研究所

碩士論文

Department of Geosciences

College of Science

National Taiwan University

Master Thesis

金門地區減薄大陸地殼中持續的高度變質作用

Sustained High-grade Metamorphism of Thinned Continental Crust in Kinmen Island

黃琮瀚

Tsung-Han Huang

指導教授：羅清華 博士

Advisor: Ching-Hua Lo, Ph.D.

中華民國 111 年 8 月

August, 2022

doi:10.6342/NTU202202659

國立臺灣大學碩士學位論文
口試委員會審定書
MASTER'S THESIS ACCEPTANCE CERTIFICATE
NATIONAL TAIWAN UNIVERSITY

（論文中文題目）(Chinese title of Master's thesis)

金門地區減薄大陸地殼中持續的高度變質作用

（論文英文題目）(English title of Master's thesis)

Sustained High-grade Metamorphism of Thinned Continental Crust in Kinmen Island

本論文係黃琮瀚(姓名)R09224107（學號）在國立臺灣大學地質科學研究所(系/所/學位學程)完成之碩士學位論文，於民國 111 年 7 月 28 日承下列考試委員審查通過及口試及格，特此證明。

The undersigned, appointed by the Department / Institute of Geosciences on 28 (date) 07 (month) 2022 (year) have examined a Master's thesis entitled above presented by Tsung-Han Huang (name) R09224107 (student ID) candidate and hereby certify that it is worthy of acceptance.

口試委員 Oral examination committee:

（指導教授 Advisor）

系主任/所長 Director:

doi:10.6342/NTU202202659

Contents

Master's Thesis Acceptance Certificate I
Contents II
誌謝 V
中文摘要 VII
Abstract IX
Figure Contents XII
Table Contents XV
1 Introduction 1
2 Geological Background 3
3 Materials and Methods 9
3.1 Field Observation 9
3.2 Oriented Thin Sections 11
3.3 Petrographic and Microstructural Analysis 13
3.4 Scanning Electron Microscope 14
3.4.1 BSE Image 14
3.4.2 SEM-EDS 16
3.4.3 EPMA 17
3.5 Mineral Chemistry 18
3.5.1 Mineral Formulae Recalculation 19
3.5.2 Ti-in-biotite Geothermometer 24
3.5.3 Al-in-hornblende Geobarometer 25
3.5.4 Biotite-Muscovite Geobarometer 26
3.6 Whole-rock Geochemistry 27
4 Results and Interpretation 28
4.1 Field Work 28
4.1.1 Reconstructed Lithological Evolution 28
4.1.2 Reconstructed Structural Evolution 31
4.2 Petrography and Microstructural Analysis 50
4.2.1 Sillimanite Mica Schist 50
4.2.2 Biotite gneiss 57
4.2.3 Amphibolite 59
4.2.4 Tonalitic gneiss 61
4.2.5 Summary 63
4.3 Mineral Chemistry 64
4.3.1 18LYA01 Sillimanite Mica Schist 65

doi:10.6342/NTU202202659

4.3.2 181117A01 Sillimanite Mica Schist 77
4.3.3 18LYB03 Biotite Gneiss 80
4.3.4 18TP01 Amphibolite 94
4.3.5 18TP04 Amphibolite 99
4.3.6 18TP04 Tonalitic Gneiss 102
4.3.7 Ti-in-biotite Geothermometer 112
4.3.8 Al-in-hornblende Geobarometer 117
4.3.9 Biotite-Muscovite Geobarometer 121
5 Discussion 124
5.1 P-T Evolution during Crustal Deformation of Kinmen Island 124
5.1.1 Estimated P-T Conditions for each Deformation Event 124
5.1.2 Reconstructed P-T path and Elevated Geotherm in Kinmen Island 130
5.2 Heat Source for the Sustained High-grade Metamorphism in Shallow Crust 132
5.3 Thermochronological Constraints on Reconstructed Structural Evolution 135
5.3.1 Timing for Deformation Events 135
5.3.2 Estimated Cooling Rates and their Tectonic Implication 137
5.3.3 Comparison to Pingtan-Dongshan Metamorphic Belt 140
5.4 Tectonic Setting for Sustained High-temperature in Shallow Crust 144
5.5 Tectonic and Crustal Evolution of Kinmen Island 147
6 Conclusion 151
7 Reference 153
8 Appendices 170
8.1 Procedures for Making Oriented Thin Sections 170
8.1.1 Reorientation 170
8.1.2 Sectioning 172
8.1.3 Impregnation 173
8.1.4 Polishing 176
8.1.5 Mounting 178
8.1.6 Final Sectioning and Polishing 179
8.2 Analytical Results of Major and Trace elements 181
8.3 Field Structural Measurement Data 182
8.4 BSE images with Marked Positions of EPMA Analyses 186
8.4.1 18LYA01 Sillimanite Mica Schist 186
8.4.2 181117A01 Sillimanite Mica Schist 188

doi:10.6342/NTU202202659

8.4.3 18LYB03 Biotite Gneiss 189
8.4.4 18TP01 Amphibolite 191
8.4.5 18TP04 Amphibolite and Tonalitic gneiss 193
8.5 Analytical Results of Mineral Chemistry 196
8.5.1 18LYA01 Sillimanite Mica Schist 196
8.5.2 181117A01 Sillimanite Mica Schist 202
8.5.3 18LYB03 Biotite Gneiss 204
8.5.4 18TP01 Amphibolite 216
8.5.5 18TP04 Amphibolite and Tonalitic Gneiss 219

doi:10.6342/NTU202202659

誌謝

首先碩士的兩年生涯感謝指導教授羅清華老師在學術研究上給予我很大的空間，讓我學習如何制定一份適合碩士班的學術議題、能夠接觸各種不同的研究方法、以及參與國內外的研討會，並且在我提出任何的想法或可能性時，老師都是大力支持並且在我有疑問的時候提供非常實質性的建議，也很謝謝老師每次上台報告前以及時不時日常的鼓勵，總是能讓我更有自信的去發表研究成果以及給自己更多的動力繼續往前進，真的是很幸運能夠在碩士班遇到羅老師，也讓自己有機會踏進變質岩岩石學的領域，完成從高中以來的心願。另外感謝宜瑄學姊在行政事務上的協助，從野外考察、化學分析、參加研討會到口試的準備，因為學姊的幫忙才能讓我很順利且專心地做研究，並且也主動給了我許多建議跟鼓勵，真的是很謝謝學姊。

感謝臼杵直博士指導我變質岩岩石學的分析方法，包含電子微探的分析、礦物化學式的計算、地質溫壓計以及 Perple_X 軟體的使用，也很感謝每一次學術上的討論，您的細心跟謹慎總是能讓我把投稿的摘要、海報跟圖表修改得更加完善，也感謝您在 EPMA 薄片製作上以及全岩地球化學分析上的幫忙。另外謝謝中央研究院地球科學所 EPMA 實驗室的成員，包含飯塚義之博士、王宇翔學長、Masako Usuki 小姐，感謝你們教導我樣品製備、電子顯微鏡的操作以及數據分析。此外，感謝中央研究院地球科學所的彭君能博士使用他的研究經費協助分析本研究岩石樣品的全岩地球化學。

最重要的是感謝師範大學地球科學系的葉孟宛教授(Mary)，從高三下帶我一路到碩士班畢業，從地質樣本的採樣、野外的紀錄、構造的判識與量測、定向薄片製作、顯微構造分析、構造演化史的重建、SEM-BSE 影像的拍攝以及 EDS 的分析、Gplate 軟體的應用、應變分析、礦物的分離與純化、岩石三維 X 射線電腦斷層掃描的開發到如何構想與撰寫研究計畫書、如何找尋適合的研究方法、如何檢視與詮釋數據背後的地質意義、以及將研究成果寫成文章投稿至 SCI 的國際

doi:10.6342/NTU202202659

期刊，真的是非常感謝 Mary 每一件事情都是手把手地教我從基本做起，而讓現在的自己具備非常多的能力。也很謝謝老師陪我一起去金門出了五次的野外才奠定下今天豐碩的研究成果，也謝謝老師給了我很大的自由去使用所有的儀器設備，除了讓我能夠學習到很多機械技術層面的知識外，也能在預定的時間內完成樣本處理。另外也很感謝 Mary 在研究上給了我很多發揮的空間，可以讓我接觸到不只構造地質學的領域，還包含全岩的地球化學、礦物化學到定年學，甚至去挑戰臺灣目前比較少人在接觸的研究方法等，真的是很謝謝老師的用心栽培讓我能夠不斷的嘗試跟探索，能夠在求學生涯遇到 Mary 真的是這輩子最幸運的一件事情之一，我也永遠都不會忘記，謝謝 Mary。待在師大地科系的期間也很謝謝百誼、孟澔、亞芸、詠恬、炳權、葉恩肇老師、東翰、賴昱銘老師、李通藝老師，讓我能夠使用師大的儀器、資源與空間並且在遇到問題的時候都能順利且有效率的解決，我也才能如期畢業。

謝謝四位口試委員，羅清華教授、李通藝教授、葉孟宛教授以及白杵直博士對於論文上不足的地方給予建議以及指正，讓學生能夠將論文修改得更加完善並且在未來要發表的文章上能夠有更好的呈現以及更多的發揮空間。謝謝清淵、浚羽、映存陪我在金門到處看地質才開啟了我的地質學術生涯。謝謝美妃老師在申請科技部大專計畫時的協助、火成岩成因與定年學上的討論與研究指導、以及讓我有機會擔任兩次地球物質實習的助教，精進自己的學識以及培養課程規劃與設計的能力。謝謝國家科學及技術委員會的計畫經費支持才能夠完成這些研究成果，其計畫編號為 110-2116-M-002-029。最後謝謝我的家人讓我能夠專心地在學業上讀到碩士班畢業，尤其是我媽，辛苦妳了。謝謝每一位給過我鼓勵、建議、支持、幫助的人，謝謝你們。

doi:10.6342/NTU202202659

中文摘要

中國東南部的大陸地殼分佈著大面積白堊紀時期的火成岩體以及張裂盆地，這些地質事件的形成被前人研究認為是在古太平洋板塊隱沒後撤的期間所發生的，而古太平洋板塊長時間的後撤讓中國東南部的大陸地殼從原先的主動大陸邊緣轉變為被動大陸邊緣，這樣地體構造轉換的過程就被位於此大陸邊緣上金門地區的基盤岩給記錄下來，因此金門地區的基盤岩就成為探討大陸地殼減薄過程中地殼內部變質溫壓演化的適合地點。前人研究根據金門地區花崗岩基盤構造變形的伸張應變特徵，提出此處的大陸地殼在花崗岩基盤侵入以後是在減薄的狀態，並在減薄的過程啟動這些複雜且高溫的變形事件，但由於缺乏決斷性的溫壓證據，因此本研究將從變質岩岩石學的觀點來探討大陸地殼減薄過程中地殼內部溫壓演化的歷史。

金門島基盤岩的核心由花崗岩體組成，並在花崗岩體的周圍零星分布不同的變質岩體，包含英雲閃長岩質的片麻岩、角閃岩、黑雲母片麻岩與矽線石雲母片岩。根據構造演化重建、岩象學以及變質岩岩石學的分析，雖然這些複雜的岩性源自於不同的母岩，但是它們都是在類似巴坎式溫壓變質作用 (Buchan-type metamorphism) 的溫壓特徵下一起經歷地殼的變形。在這些基盤岩從深部 (28.3-30.4 公里) 出露到近地表 (<6.9 公里) 的過程中共伴隨了六期的變形事件，並且溫壓演化的路徑是一個減壓、退變質的特徵。在基盤的花崗岩體侵入地殼以後，第一期的變形事件為公里規模的片麻岩隆穹，形成的溫度在 644-725 °C 且最大的壓力為 7.9 kbar。第二期變形事件是地殼在重力垮塌的過程中所產生近水平的 S 型構造岩，其溫度環境與 D_1 相同但是位於更低的壓力環境。隨著地殼持續的減薄以及岩體逐漸地上抬，片麻岩隆穹的東西兩側開始發育北北東-南南西走向

doi:10.6342/NTU202202659

的剪切褶皺帶 (D_3)，其形成溫度為 658-704 °C 且最大壓力為 5.5 kbar。隨後地殼的持續張裂以及基盤上抬至中部至上部地殼時發育了東北東-西南西走向具有左移特徵的伸張剪切帶 (D_4)，其形成溫度為 534-682 °C 且最大壓力為 4.6 kbar。由於基盤岩持續的上抬至地殼淺部壓力至少小於 1.9 kar 的地方，地殼開始轉變為脆性變形並且伴隨偉晶岩脈 (D_5) 以及基性岩脈群 (D_6) 的侵入。

從以上重建出的溫壓演化路徑顯示起初在 D_1 以前至 D_3 的期間，地殼經歷了減壓但是溫度範圍維持高溫的演化路徑，從最高的變質溫度 725 °C 與最大的變質壓力 7.9 kbar，減壓成 704 °C 與 5.5 kbar，隨後在 D_{3end} 到 D_6 的期間地殼還是在逐漸減壓的環境但是具有大規模的溫度下降，從在 D_{3end} 時最高變質溫度 682 °C 與最大變質壓力 4.6 kbar，到在 D_5 以前的最低變質溫度 534 °C 與最低的變質壓力為 1.9 kbar，最後在 D_5 與 D_6 期間溫度是低於 534 °C、壓力是小於 1.9 kbar。將重建出的地溫梯度曲線與一般大陸地殼的地溫梯度比較，若是在一般大陸地殼內部要達到這些最高的變質溫度，其地殼深度必須要在 41.8 至 51.9 公里處，這樣的深度明顯遠高於金門地區的基盤岩侵入深度以及後續的變質深度，因此金門地區在過去白堊紀時期具有較高的地溫梯度，在相對地殼的淺處就已經達到上部角閃岩相至粒變岩相的溫度區間。如此長時間的高度變質作用，加上伸張的應變特徵以及同時期的雙模式岩漿活動，並無法在擠壓且地殼增厚的造山帶中形成，相反的必須在大陸地殼持續伸張減薄的過程才有辦法形成這樣相對低壓但是持續高溫的地殼環境。

關鍵字:金門島、伸張應變、高度變質作用、地殼減薄、地質溫壓計

doi:10.6342/NTU202202659

Abstract

The continental crust of southeast China is featured by widespread Cretaceous magmatic complexes and extensional basins, which are attributed to the continual rollback of the subducted Paleo-Pacific plate. This long-lasting slab rollback transformed the original active continental margin into a passive one. Such a tectonic transition was recorded in the crystalline basement of Kinmen Island, along the SE Asia continental margin, making Kinmen Island a great candidate for exploring the metamorphic evolution of the continental crust during crustal thinning processes. Previous studies have reconstructed the structural evolution of the granitoid basements in Kinmen Island and proposed a continual crustal thinning setting, yet without conclusive evidence provided, which has been solved in the present study.

The crystalline basement of Kinmen Island comprises a granite core, surrounded by tonalitic gneiss, amphibolite, biotite gneiss and sillimanite mica schist. Based on a combination of structural, petrographic, and metamorphic petrology analyses, and despite these complex lithologies originating from different protoliths, it is revealed that the granite core along with the surrounding metamorphic rocks were all deformed at similar P-T conditions characteristic of Buchan-type metamorphism. A decompressional and regressive P-T path is revealed accompanying the identified six deformation events as the deep-seated crystalline basements exhumed from 28.3-30.4

doi:10.6342/NTU202202659

km (pre-D_1) to <6.9 km (D_5-D_6). A kilometer-scale gneiss dome (D_1) formed after the intrusion of the granitoid basements at 644-725 °C/<7.9 kbar. A similar temperature range was maintained with pressure decreasing during the gravitational collapse of the continental crust with a generation of subhorizontal S-tectonite (D_2). Further exhumation of the crystalline basements due to continual crustal thinning formed a NNE-SSW striking shear fold belt (D_3) along the east and west limbs of the gneiss dome at 658-704 °C/<5.5 kbar. With further crustal extension and exhumation into the middle to upper crust, an ENE-WSW striking sinistral transtensional shear zone was developed throughout the basement at 534-682 °C/<4.6 kbar. Due to the continual exhumation into shallow levels (<1.9 kbar), the continental crust was further deformed by brittle fracturing along with intrusion of pegmatitic dykes (D_5) and mafic dyke swarm (D_6). The reconstructed P-T trajectory shows nearly sustained high temperatures along a decompressional path from 725 °C/<7.9 kbar (pre-D_1 to D_2) to 704 °C/<5.5 kbar (D_3), followed by continual decompression but a rapid temperature drops from 682 °C/<4.6 kbar (D_{3end}), 534 °C/1.9 kbar (pre-D_5) to <300 °C/<1.9 kbar (D_5 to D_6). Compared with a normal continental geotherm, the corresponding depths to reach such peak metamorphic temperatures should be around 41.8-51.9 km, which is much deeper than the pressure conditions of Kinmen Island. It is therefore suggested that the continental crust of Kinmen Island had an elevated geotherm, which reached upper amphibolite to

doi:10.6342/NTU202202659

granulite facies conditions at shallower crustal levels. Such a sustained high-grade metamorphism since the emplacement of granitoids to D_4 during crustal decompression along with the extensional strain pattern and contemporaneous bimodal magmatism cannot be produced at a contractional setting. Instead, a prolonged thinned crust under extension is preferred.

Keywords: Kinmen Island, extensional strain, high-grade metamorphism, crustal thinning, geothermobarometer

doi:10.6342/NTU202202659

Figure Contents

Figure 1. Simplified tectonic and geological map of southeast Asia from Huang and Yeh (2020).. 6
Figure 2. Simplified geological map of Kinmen Island showing the distribution of Mesozoic basement rocks and the sample locations...7
Figure 3. Oriented sample mark showing the orientation of the marked reference surface...................10
Figure 4. Field equipment used to conduct field measurement and sample collection...........................10
Figure 5. Procedures for making oriented thin sections with the equipment used in each step.............12
Figure 6. SEM-BSE image from sample 18LYA01...15
Figure 7. BSE image with marked analyzed spots for EDS analysis. 17
Figure 8. Complex lithologies in Kinmen Island..30
Figure 9. Compiled field structural measurement data from three basement rocks in Kinmen Island. ..32
Figure 10. The 20-meter digital terrain model map overlaid by the geological map showing outcrop photos with measured S_1 gneissic foliation and L_1 mineral lineation to demonstrate D_1 gneiss dome.. 36
Figure 11. Outcrop photos and sketches showing D_2 domain within different lithologies....................38
Figure 12. Topographic map overlaid by the geological map showing measured D_3 structures. 41
Figure 13. Outcrop photos and sketches showing D_3 structures within Kingueishan Schist at TGF location with a schematic diagram illustrating the structural relationships between D_1, D_2 and D_3. 41
Figure 14. Outcrop photos and sketches showing D_{3b} shear zones within Taiwushan Granite and Chenggong Tonalite.. 42
Figure 15. Topographic map overlaid by the geological map showing measured D_4 structures. 45
Figure 16. Outcrop photos, sketches, measured structures, and a schematic diagram to show interpreted structural relationships (D_1-D_4) within Kingueishan Schist at JMS location.. 45
Figure 17. Outcrop photos and sketches showing interpreted D_4 structures within different lithologies. Figure E and F are from Huang and Yeh (2020).. 46
Figure 18. Outcrop photos and sketches showing interpreted D_4 structures and lithological relationships between amphibolite, leucogranite and the granitoids. Figure A is from Huang and Yeh (2020). 46
Figure 19. Outcrop photos and sketches showing interpreted post-D_4 structures within Chenggong Tonalite at JMS location.. 47
Figure 20. Outcrop photos and sketches showing the crosscutting relationships between D_5 Tienpu Granite, pegmatite and granitoid basements (Taiwushan Granite and Chenggong Tonalite). Figure B, C, D are revised from Huang and Yeh (2020).. 48
Figure 21. Outcrop photos and sketches showing the crosscutting relationships between D_6 mafic dyke and the crystalline basements. Figure D is revised from Huang and Yeh (2020)..........................49
Figure 22. Microphotographs showing microstructures and petrographic relationship of D_2, D_3, D_4 in 181117A01 sillimanite mica schist.. 51
Figure 23. Microphotographs showing microstructures and petrographic relationship of D_3 and D_4 in

doi:10.6342/NTU202202659

181117A01 sillimanite mica schist.. 52
Figure 24. Microphotographs showing microstructures and petrographic relationship of D_2 and D_3 in 18LYA01 sillimanite mica schist.......... 55
Figure 25. Microphotographs showing microstructural relationship of D_3 in 20LYB11 sillimanite mica schist. 56
Figure 26. Microphotographs showing microstructures and petrographic relationship of D_2 in 18LYB03 biotite gneiss.. 58
Figure 27. Microphotographs showing microstructures and petrographic relationship of D_{3b} in amphibolite (sample 18TP01, 18TP04).. 60
Figure 28. Microphotographs showing microstructures and petrographic relationship of D_{3b} in tonalitic gneiss (sample 18TP04).. 62
Figure 29. Relationship between metamorphic mineral growth and deformation events. 63
Figure 30. Feldspar composition and SEM-BSE image showing mineral relationship of feldspar in sample 18LYA01. 66
Figure 31. Plots of chemical composition of biotite from sillimanite mica schist (sample 18LYA01)... 68
Figure 32. Plot of Al^{VI} vs. $Si+Fe^{2+}+Mg$ based on 22 oxygens of muscovite of sample 18LYA01.. 70
Figure 33. Microphotographs of sillimanite mica schist (sample 18LYA01) showing complex inclusion patterns within garnet porphyroblasts under plane-polarized light. The thin section is a vertical plane parallel to L_{3b} mineral lineation defined by fibrolite. 74
Figure 34. Three garnet grains (Grt1, Grt2, Grt3) in sillimanite mica schist (sample 18LYA01) with EPMA chemical mapping and line profile analysis. 75
Figure 35. Garnet compositional profiles and variation of (FeO+MgO) with (CaO+MnO) in garnets from different metamorphic grades (Nandi, 1967), and the garnets are from sillimanite mica schist (sample 18LYA01). 76
Figure 36. Plots of chemical composition of biotite from sillimanite mica schist (sample 181117A01). 78
Figure 37. Plot of Al^{VI} vs. $Si+Fe^{2+}+Mg$ based on 22 oxygens of muscovite in sample 181117A01. 80
Figure 38. Thin section photos under cross-polarized light with green and yellow arrows marking the position of line profile analysis for feldspars and garnets respectively. 84
Figure 39. Line profile analysis of feldspar chemical compositions in the boudin and host rock of the biotite gneiss (sample 18LYB03).. 85
Figure 40. Plots of chemical composition of biotites from biotite gneiss (sample 18LYB03). (A) Classification diagram for biotite species (Wlodek et al., 2015). (B) $Si+Fe^{2+}+Mg$ plotted against total Al contents with Tschermak substitution line for comparison. 88
Figure 41. Plots of chemical composition of muscovite in the boudin of biotite gneiss (sample 18LYB03). 90
Figure 42. SEM-BSE images showing the mineral relationships between garnet, biotite, and plagioclase. 92

Figure 43. Six line profile analysis of garnet grains (Garnet1 to Garnet 6) in the boudin of biotite gneiss (sample 18LYB03). 93
Figure 44. Line profile analysis of feldspar chemical compositions of the amphibolite (sample 18TP01).. 96
Figure 45. Plots of chemical composition of biotites from amphibolite (sample 18TP01).. 97
Figure 46. Chemical compositional plot of amphibole compositions from amphibolite (sample 18TP01) on a classification diagram for calcium amphiboles (Hawthorne et al., 2012). 98
Figure 47. Line profile analysis of feldspar compositions in 18TP04 amphibolite.. 100
Figure 48. Chemical compositional plot of amphibole compositions from amphibolite (sample 18TP04) on a classification diagram for calcium amphiboles (Hawthorne et al., 2012). 101
Figure 49. Petrography and chemical mapping of line profiles of K-feldspar (Kfs_1, Kfs_2) and plagioclase (Pl_3, Pl_4) in tonalitic gneiss (sample 18TP04). 106
Figure 50. Petrography and chemical mapping of line profiles of K-feldspar (Kfs_3, Kfs_4) and plagioclase (Pl_5, Pl_6) in tonalitic gneiss (sample 18TP04). 107
Figure 51. Line profile analysis of feldspar chemical compositions in the tonalitic gneiss (sample 18TP04). 108
Figure 52. Plots of chemical composition of biotites in tonalitic gneiss (sample 18TP01). 110
Figure 53. Chemical compositional plot of amphibole compositions from tonalitic gneiss (sample 18TP04) on a classification diagram for calcium amphiboles (Hawthorne et al., 2012). 112
Figure 54. Results of Ti-in-biotite geothermometer. 117
Figure 55. Line profile analyses of hornblendes in tonalitic gneiss (sample 18TP04). 120
Figure 56. The estimated P-T ranges for each deformation event and the reconstructed P-T path of Kinmen Island. 129
Figure 57. Reconstructed cooling path of the Cretaceous granitoids of Kinmen Island revised from Huang and Yeh (2020). 143
Figure 58. Schematic diagram of the tectonic setting for the sustained high-grade metamorphism in a thinned continental crust in Kinmen Island. 147
Figure 59. A compiled diagram showing the structural and tectonic evolution of Kinmen Island revised from Huang and Yeh (2020). 150

doi:10.6342/NTU202202659

Table Contents

Table 1. Sample locations and their abbreviations, as well as corresponding lithology units. 8

Table 2. Calculation of the structural formula of a biotite from EPMA analysis. The biotite is No.122 from sample 18LYA01. 23

Table 3. Measured major and trace elements with their LOD. 27

Table 4. The interpreted Al_{total} contents in the core and rim of hornblende in each line profile. 120

Table 5. The result of estimated pressures from different muscovite compositions with one fixed biotite composition from sample 18LYA01. 122

Table 6. The mica compositions used for biotite-muscovite geobarometer of sample 18LYA01 with the results of the calculated pressure. 123

Table 7. The mica compositions used for biotite-muscovite geobarometer of sample 181117A01 with the results of the calculated pressure. 123

doi:10.6342/NTU202202659

1 Introduction

High-grade metamorphism usually occurs in a thickened continental crust within a collisional orogenic belt, such as the Cenozoic Himalaya-Tibet orogen, the Paleozoic Caledonian orogen and the Meso-Neoproterozoic Grenville orogen (Weller et al, 2021). Due to the thickened continental crust along with magmatic advection, pressure and temperature conditions are easily reached into amphibolite facies and granulite facies in a collisional orogen (Gao et al., 2012; Möller et al., 2015; Searle, 2022). With a thinned continental crust, however, the decreased crustal thickness hinders pressure conditions in reaching burial depth where such high-grade metamorphism occurs, more specifically the Barrovian facies series, which are the normal P-T conditions within the continental orogens (Aoki et al., 2014; Imayama et al., 2020). Otherwise, to attain such high-temperature conditions at a reduced crustal thickness, an elevated geothermal gradient is required (Zheng and Chen, 2017). These high-temperature and relatively low-pressure metamorphic conditions follow the Buchan facies series, which usually occurs in a collapsed orogen (Vanderhaeghe, 2012).

In a collapsed orogen, the crustal thinning history is recorded usually as the retrograde minerals partly overprint the previous peak metamorphic paragenesis (La Roche et al., 2015). However, such retrograde metamorphism barely completes to delineate the detailed retrograde P-T evolution of the crustal thinning history due to

doi:10.6342/NTU202202659

slow reaction rates and the limited rates of fluid supply (Jamtveit et al., 2021). This missing piece of metamorphic evidence impedes our understanding regarding the thinning processes of the continental crust. Nevertheless, the present study discovered an ideal region,— Kinmen Island, which is on the southeast continental margin of southeast Asia, to explore the thinning processes of the continental crust. The region is ideal not only because it simply experienced a crustal thinning history since the formation of its granitoid basement, but also that the retrograde P-T evolution is preserved (Huang and Yeh, 2020). Therefore, the present study conducted a combination of field structural analyses, microstructural analyses, and metamorphic petrology to explore the metamorphic evolution during the thinning processes of continental crust.

doi:10.6342/NTU202202659

2 Geological Background

The southeast region of the Eurasian plate is situated on a transition zone between the continental lithosphere into the oceanic lithosphere (Figure 1A), which is composed of two continental blocks (South China Block and Indochina Block) and two marginal seas (South China Sea and Philippine Sea). The South China Block consists of the Yangtze Block to the northwest and the Cathaysia Block to the southeast with Kinmen Island on the southeast edge of the Cathaysia Block. The southeast region of the Cathaysia Block is characterized by widespread Jurassic-to-Cretaceous volcanics and plutonics, abundant NE-trending and E-W trending to WNW-trending normal faults, the NE-trending sinistral Changle-Nanao Shear Zone and the NE-trending Pingtan-Dongshan Metamorphic Belt along the coast (Figure 1B; Zhou et al., 2006; Liu et al., 2012; Wang et al., 2013; Li J. et al., 2014). These Mesozoic geological features are the products of the tectono-magmatic events triggered by the multiple stages of subduction and rollback of the Paleo-Pacific plate under the southeast margin of the Cathaysia Block (Liu et al., 2012; Zhang et al., 2012; Wang et al., 2013; Li J. et al., 2014; Li Z. et al., 2014; Mao et al., 2014; Liu et al., 2016; Zhao et al., 2016; Huang and Yeh, 2020; Liu et al., 2020; Wang et al., 2020).

Two magmatic episodes are noted from the Jurassic to Cretaceous periods in southeast China: 170-130 Ma and 110-90 Ma, with the Cretaceous rocks more

doi:10.6342/NTU202202659

concentrated along the southeast coastal regions of the Cathaysia Block (Figure 1B; Liu et al., 2020). Along these coastal areas, three magmatic stages are further identified: 145-137Ma, 136-118 Ma and 107-86 Ma (Wang et al., 2020). These Cretaceous rocks are comprised of mainly high-K calc-alkaline I-type granitoids with minor A-type granitoids and gabbros as well as rhyolitic to basaltic volcanics (Li, 2000; Zhou et al., 2006; Li Z. et al., 2014; Zhao et al., 2015; Zhao et al., 2016; Yang et al., 2017; Wang et al., 2020; Xu et al., 2021). An extensional setting associated with these magmatisms is delineated by the intimate temporal-spatial relationships between the 115-95 Ma gabbros and surrounding I-type granitoids, 100-90 Ma A-type granitoids (Li Z. et al., 2014), and the 94-81 Ma rhyolite-dominated bimodal volcanism (Chen et al., 2004). All these Cretaceous rocks were intruded later by the NE-trending mafic dyke swarms (Lee, 1994; Zhao et al., 2007; Chen et al., 2014; Pan et al., 2014), which indicates a rifting stage of the continental crust (Huang and Yeh, 2020).

Similar magmatic evolution was also identified in Kinmen Island offshore from Fujian Province (Lin et al., 2011; Huang and Yeh, 2020), on the southeast leading edge of the continental margin of the Cathaysia Block. Five lithological units with four Cretaceous granitoids and one schist unit were mapped out (Figure 2A): the Taiwushan Granite (139 Ma, Yui et al., 1996), the Chenggong Tonalite (129 Ma, Lin et al., 2011), the Doumen Granite (120 Ma, Lin et al., 2011), the Tienpu Granite (100 Ma, Yui et al.,

doi:10.6342/NTU202202659

1996) and the Kingueishan Schist (early Mesozoic, Lin et al., 2011), all of which were intruded by the 90–76 Ma mafic dike swarms along the NE-trending fractures (Lee, 1994; Lan et al., 1995; Lan et al., 1997; Lin et al., 2011; Huang and Yeh, 2020). Lan et al (1997) inferred that these Cretaceous granitoids evolved from the same parental magma with different stages of fractional crystallization under a post-orogenic continental extension setting (Huang and Yeh, 2020). This tectonic interpretation was further supported by the shallowing intrusion depth of the younger granitoids (Lin, 1994; Lin et al., 2011), and the retrograding deformation history post the igneous crystallization from granulite-facies ductile deformation to brittle fracturing of the crust (Huang and Yeh, 2020). All this evidence demonstrates that the basement of Kinmen Island underwent crustal thinning from an original lower-crustal level at 28-30 km depth (Lo et al., 1993) to an upper-crustal level near the surface (Huang and Yeh, 2020). To further explore the crustal thinning history, the present study continued the previous work (Huang and Yeh, 2020) with new field and metamorphic petrological data on the meta-granitoids and the schist belt in Kinmen Island to establish the P-T evolution accompanying the crustal thinning and the strain pattern evolution related to the multiple stages of the subduction and rollback of the Paleo-Pacific plate.

doi:10.6342/NTU202202659

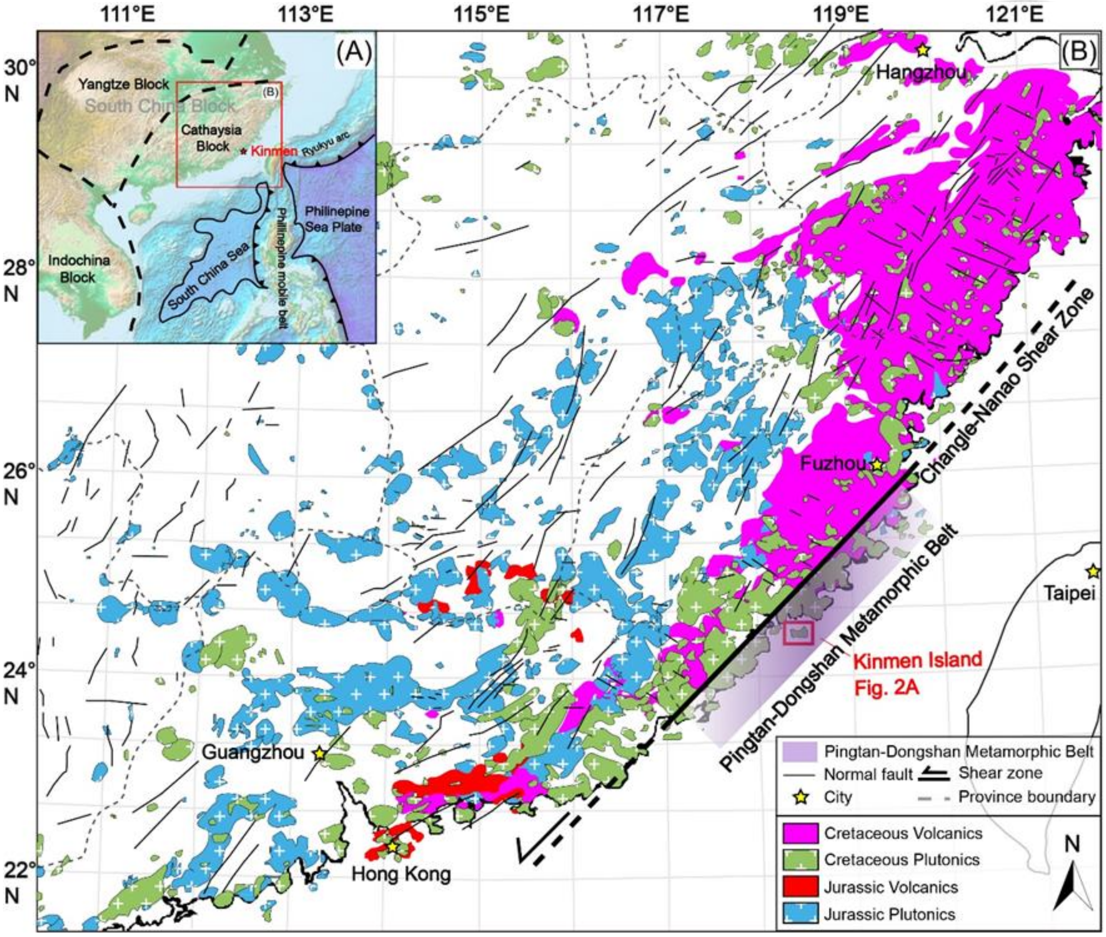

Figure 1. Simplified tectonic and geological map of southeast Asia from Huang and Yeh (2020). (A) Topography map showing tectonic components of southeast Asia under present-day configuration. The black dashed lines mark the boundaries of the tectonic blocks while the black solid lines mark the boundaries between continental crust and oceanic crust. Solid black lines with triangles indicate the subduction zones. (B) Geological map modified and compiled from Li J. et al. (2014) and Zhou et al. (2006) illustrating the distribution of the Jurassic and Cretaceous plutonics and volcanics, Mesozoic normal faults, Changle-Nanao Shear Zone (CNSZ), and the Pingtan-Dongshan Metamorphic Belt (PDMB). The red rectangle indicates the study site in the present study.

doi:10.6342/NTU202202659

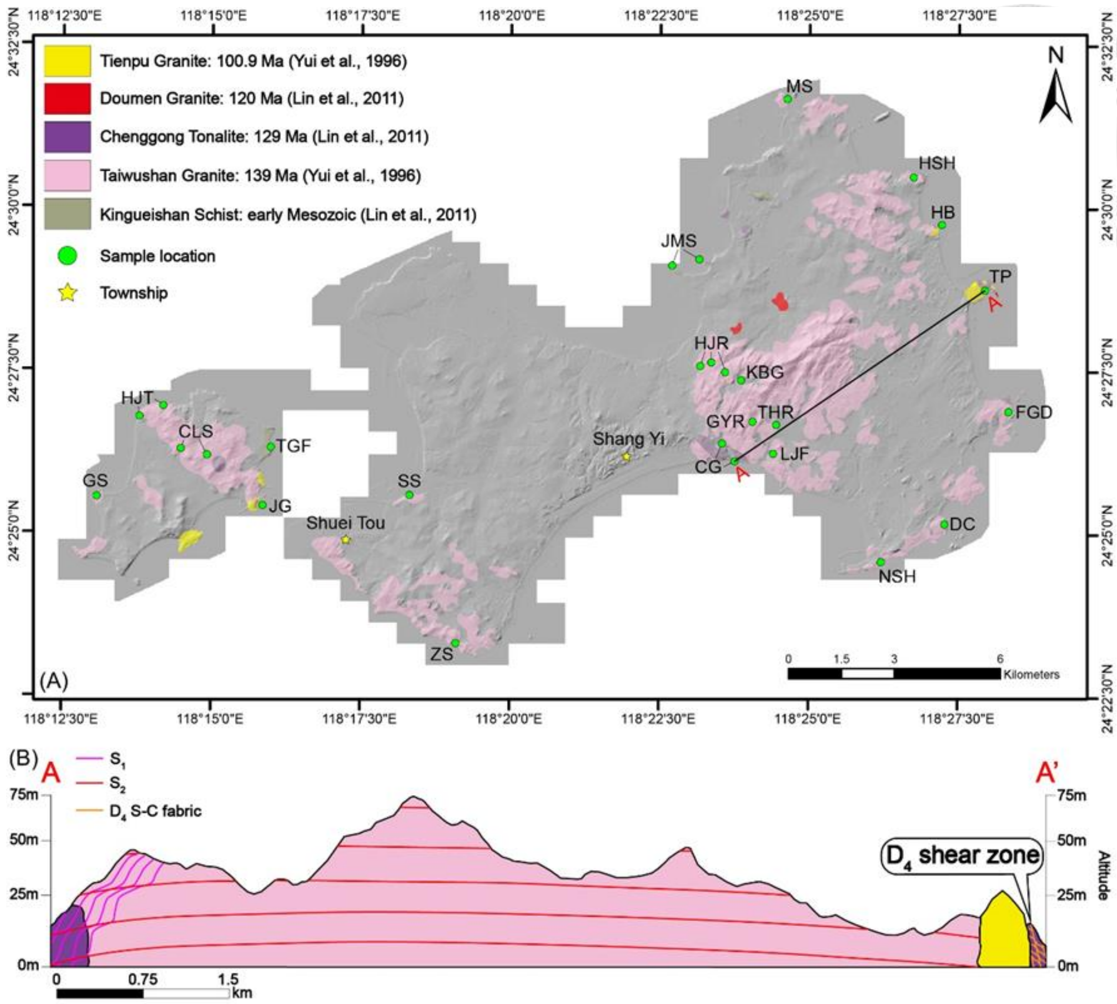

Figure 2. Simplified geological map of Kinmen Island showing the distribution of Mesozoic basement rocks and the sample locations. (A) Geological map modified from Lin et al. (2011) and Huang and Yeh (2020). The full name of sample locations and their longitudes and latitudes are summarized in Table 1. (B) Schematic diagram of reconstructed A-A' cross section. The pink line indicates the gneissic foliation (S_1) defining D_1 doming event. The red line indicates D_2 subhorizontal S-tectonite (S_2). The orange line indicates the locally developed D_4 shear belts (S/C fabric).

doi:10.6342/NTU202202659

Table 1. Sample locations and their abbreviations, as well as corresponding lithology units.

Lithology Unit	Sample Location	Abbreviation	Longitude (E°)[1]	Latitude (N°)
Chenggong Tonalite	Cheng Gong	CG	118.39625	24.43536
	Cheng Gong	CG	118.39252	24.44013
	Fu Guo Dun	FGD	118.47209	24.44786
	Ji Ming Shan	JMS	118.38830	24.48619
	Jiou Gong	JG	118.26265	24.42372
	Tien Pu	TP	118.46546	24.47895
Taiwushan Granite	Chi Lin Shan	CLS	118.24887	24.43629
	Chi Lin Shan	CLS	118.24139	24.43788
	Dong Cun	DC	118.45466	24.41940
	Gong Yuan Road	GYR	118.40114	24.44525
	Guei Shan	GS	118.21808	24.42606
	Han She Hua	HSH	118.44571	24.50800
	Hou Bian	HB	118.45250	24.49510
	Hu Jing Tou	HJT	118.23667	24.44882
	Hu Jing Tou	HJT	118.22990	24.44608
	Huan Jhong Road	HJR	118.38668	24.45938
	Huan Jhong Road	HJR	118.38946	24.46025
	Huan Jhong Road	HJR	118.39308	24.45787
	Kinmen Botanical Gardens	KBG	118.39788	24.45582
	Liang Jin Farm	LJF	118.40692	24.43752
	Ma Shan	MS	118.41065	24.52785
	Nan Shih Hu	NSH	118.43694	24.40980
	Sia Shu	SS	118.30538	24.42643
	Sin Hu	SH	118.41007	24.43202
	Tai Hu Road	THR	118.40802	24.44470
	Zhai Shan	ZS	118.31819	24.38856
Kingueishan Schist	Ji Ming Shan	JMS	118.37978	24.48353
	The General's Fortress	TGF	118.26625	24.43633

1: The coordinate system follows WGS84 (World Geodetic System 1984).

doi:10.6342/NTU202202659

3 Materials and Methods

3.1 Field Observation

Field observation of lithological relationships and structural measurement forms the basis for further lab-work analyses, including petrographic, microstructural, and metamorphic petrological analyses. The objective of field work is to clarify the lithological and structural evolution based on crosscutting relationships to establish a preliminary tectonic model responsible for these geological events, which is later refined according to the other analyses mentioned above.

The structural evolution is separated into different deformation phases (D_1, D_2, D_3, etc.) with the foliation (S_1, S_2, S_3, etc.) and lineation (L_1, L_2, L_3, etc.) named corresponding to each deformation phase. If different stages are identified for one deformation event, different stages are named in alphabetical order (D_{1a}, D_{1b}, D_{1c}, etc.), as are the foliations and lineations. All the identified ductile planar and linear structures are measured using a clinometer for further discussion of strain patterns and tectonic implications in the aid of equal-area southern hemisphere stereonet projection using the software —Stereonet (Allmendinger et al., 2012; Cardozo and Allmendinger, 2013). Each deformation phase and lithology unit were collected with (oriented) samples. To sample an oriented rock, a reference plane is marked with its orientation on a flat rock surface prior to sampling (Figure 3), which is used for reorientation in the lab. The field

doi:10.6342/NTU202202659

equipment used is summarized in Figure 4.

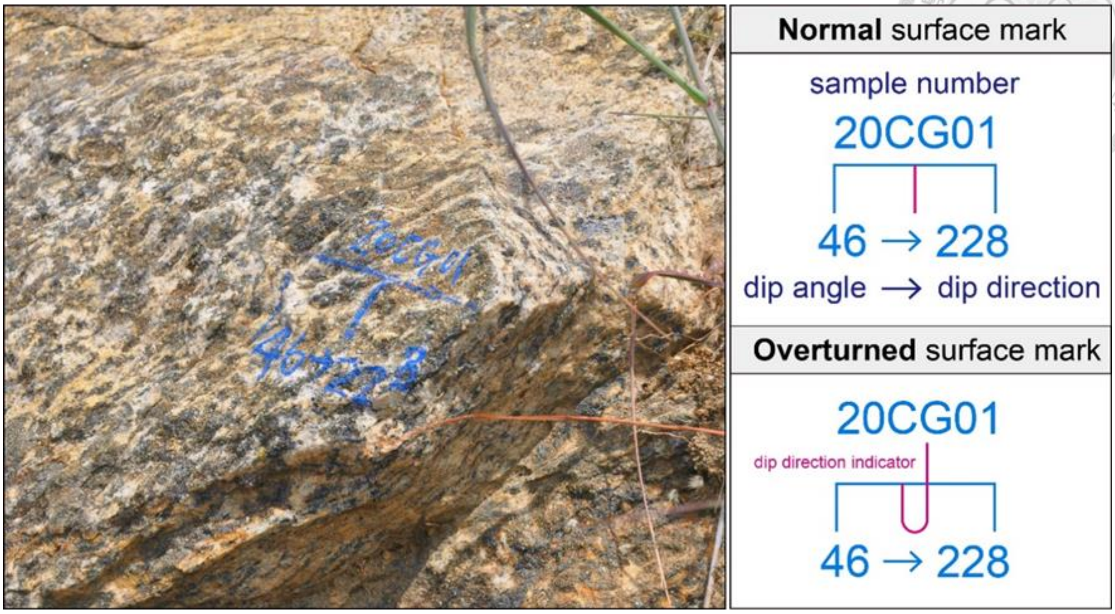

Figure 3. Oriented sample mark showing the orientation of the marked reference surface. The long line represents the horizontal line, and the pink line perpendicular to it shows the dip direction.

Figure 4. Field equipment used to conduct field measurement and sample collection.

doi:10.6342/NTU202202659

3.2 Oriented Thin Sections

Oriented thin sections have orientations consistent with the geographical directions. The orientations of all the microstructures on the oriented thin sections can be measured by image analysis software (e.g., Image-Pro Plus) and can be correlated to the mesoscale structures measured in the field (Yeh et al., 2013). Also, the shear sense or the movement direction of the rock bodies can be determined through observation of kinematic indicators from reconstructed microstructures (Hansen, 1990; Chiu et al., 2018).

To view three-dimensional (3-D) microstructures of deformed rocks, three oriented thin sections were made for each oriented sample in the present study with one horizontal thin section and two vertical thin sections. Two vertical thin sections intersect at a 45-degree angle with one perpendicular to major foliation identified on horizontal thin section and the other oblique to major foliation. The horizontal thin section can show the strike of all the foliations within the rocks. The vertical thin section perpendicular to major foliation not only displays the dip angles and the dip direction of the major foliation, but also apparent dip angles for the other foliations. The other vertical thin section oblique to major foliation better constrains the measured orientations of the microstructure and complements the reconstructed 3-D microstructures from a different angle of view. These chosen orientations for the three

doi:10.6342/NTU202202659

oriented thin sections follow the conclusion of Yeh et al (2013), in that: three orthogonal thin sections with section intervals ≤ 50° and one being a horizontal thin section are the most economically efficient setting for foliation reconstruction.

The oriented thin sections were made using the equipment at Department of Earth Sciences, National Taiwan Normal University. The procedures are summarized in Figure 5, including reorientation, sectioning, impregnation, polishing, and mounting. The detailed operation procedures are described in Appendix 8.1.

	Procedure	**Main Equipment**
1	Reorientation	orientometer, clinometer, sandbox, electronic laser level
2	Sectioning	double blade rock saw
3	Impregnation	oven, hot plate, Petropoxy 154 optional
4	Polishing	lapping machine with diamond grinding discs
5	Mounting	hot plate, Petropoxy 154, microscope slides
6	Sectioning	Buehler PetroThin™ Thin Section System
7	Polishing	lapping machine with diamond grinding discs

Figure 5. Procedures for making oriented thin sections with the equipment used in each step.

doi:10.6342/NTU202202659

3.3 Petrographic and Microstructural Analysis

Based on the mesoscale structural evolution established from the field observation and measurement, the oriented thin sections were made for petrographic and microstructural analysis to unravel the detailed deformation history and its relationships to the metamorphic evolution. The analytical results include:

(1) the mineral assemblages/parageneses for each lithology and each deformation event to infer the metamorphic condition (e.g., metamorphic facies) and its relationship to the deformation event;

(2) the textures of metamorphic mineral reaction to infer the P-T conditions according to petrogenetic grids;

(3) the deformation mechanisms of minerals to infer the deformation condition (e.g., ductile, or brittle deformation), and;

(4) the foliation styles and kinematic indicators to infer the tectonic movement, which gives rise to strain pattern.

doi:10.6342/NTU202202659

3.4 Scanning Electron Microscope

A scanning electron microscope (SEM) is used for more detailed petrographic analysis in micrometer scale, which is difficult to reach under ordinary petrographic microscopy. Apart from its higher resolution, the electron images can further provide chemical composition to identify mineral assemblages, especially back-scattered electron images (BSE image). In addition, when SEM is combined with an X-ray spectrometer such as energy-dispersive spectrometer (EDS) or wavelength-dispersive spectrometer (WDS), semi-quantitative or quantitative chemical analysis can be obtained to identify the mineral species using EDS or measure chemical composition of the minerals using WDS. The SEM equipped with WDS is the so-called electron probe microanalysis (EPMA). All these SEM works were done at Institute of Earth Sciences, Academia Sinica, and the details of analytical procedures are described as follows and referenced from Reed (2005).

3.4.1 BSE Image

When an incident electron is deflected back and emerges from the surface of the sample, it is called a back-scattered electron. The fraction of BSEs is dependent on atomic number (Z) with increasing probability of deflection for higher Z. The BSE detector thus detects different energies for different mineral species with minerals of the higher mean atomic number having higher energies. The minerals with higher mean

doi:10.6342/NTU202202659

atomic number will show brighter colors in the BSE image, and the mineral with lower mean atomic number appears gray or even dark in the BSE image (Figure 6). Thus, the BSE image could initially distinguish different mineral species according to their different chemical composition.

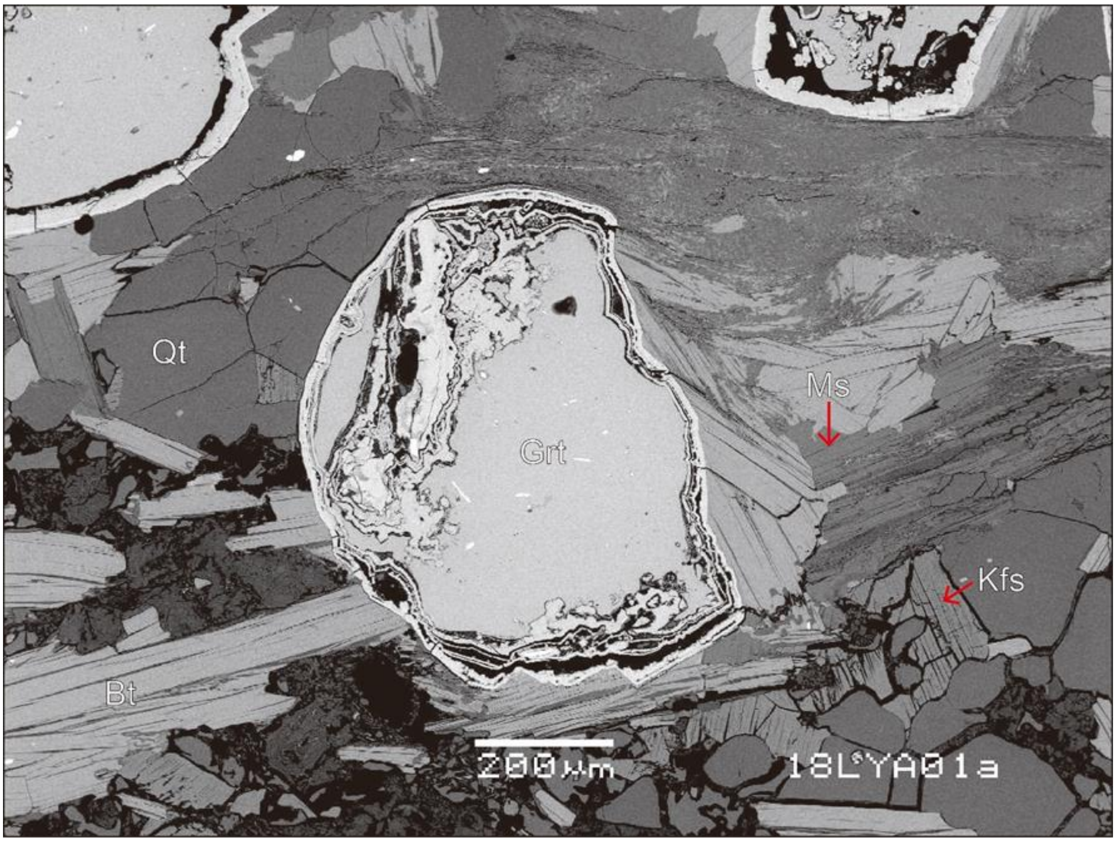

Figure 6. SEM-BSE image from sample 18LYA01. The identified minerals are marked to show their brightness contrast under the BSE image.

doi:10.6342/NTU202202659

3.4.2 SEM-EDS

The SEM-EDS can be used to quickly identify a mineral under the BSE image in around 30 seconds. Therefore, it is adopted to identify the mineral assemblages for each sample. When electron beams strike the sample, parts of the energy are transferred into the electrons within the samples. The energy-gaining electrons might jump to higher energy levels or even leave the original atom depending on the energy gained. Such atomic electron transition will leave a transient hole at the original place that would be filled by another electron at higher energy level. This electron transition will emit characteristic X-rays related to the energy difference between the two energy levels, which is characteristic to each element. Accordingly, the characteristic X-rays reflect the elements composing the samples, and the intensity of these characteristic X-rays imply the relative concentrations of these elements. As with the EDS, it collects X-rays of all energies simultaneously and produces an X-ray spectrum with the intensity versus X-ray photon energy. By comparing the X-ray spectrum of an analyzed mineral with the standard X-ray spectrum for each mineral (Severin, 2004), the mineral can be easily identified (Figure 7).

doi:10.6342/NTU202202659

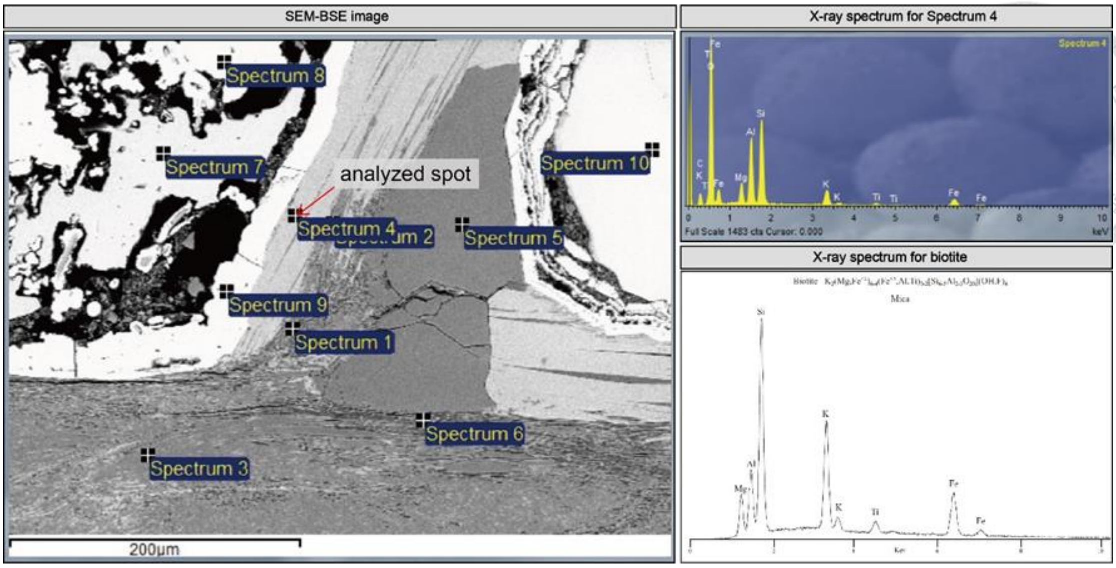

Figure 7. BSE image with marked analyzed spots for EDS analysis. The X-ray spectrum for Spectrum 4 is shown to compare with the standard biotite X-ray spectrum from Severin (2004).

3.4.3 EPMA

An electron probe micro-analyzer (EPMA) is an *in-situ*, non-destructive, analytical technique, which can quantify the chemical composition of minerals especially for the major elements. The purpose is not only to calculate mineral formulas for mineral species identification but also to calculate the equilibrium pressure and/or temperature condition for a certain mineral or mineral parageneses, which is the application of a geothermobarometer.

The mineral major element analyses were performed using a thermal emission EPMA (JEOL W-EPMA: JXA8900-R) with four channeled WDS. There were two operating conditions for analyses, including an acceleration voltage of 15.0 and 20.0 kV, a beam current of 12 nA and a beam diameter of 2μm. The calibration was done

doi:10.6342/NTU202202659

using natural and synthetic standard minerals, and raw data were corrected online with the ZAF correction. Each point analysis was performed for three minutes, and multiple points were analyzed within individual grains and throughout the selected regions to understand the degree of chemical heterogeneity. Line profiles within mineral grains (e.g., garnet, muscovite, feldspar, and amphibole) were also analyzed to determine the chemical variation from the interior to the rim. Line profiles are made up of multiple points with the distance at 10-25μm. For the mineral grains with line profile analyses, compositional maps were also obtained via an area scan at the same operating conditions as for point and line analyses to double check the chemical zoning.

3.5 Mineral Chemistry

The analytical results of mineral chemistry from EPMA measurement (weight percentage, wt.%) can be used to calculate the chemical formula of minerals (atom per formula unit, apfu), which is based on cation allocation to each crystallographic site. Such a derived structural chemical formula can be applied to classify mineral species, and to estimate the P-T conditions for the mineral growth in chemical equilibrium, including a conventional geothermobarometer and single-phase concentration thermobarometer.

doi:10.6342/NTU202202659

3.5.1 Mineral Formulae Recalculation

The chemical compositions of silicate minerals are commonly reported in wt.% of the oxides of the elements measured, due to the historic reason of using a gravimetric technique for chemical analysis. It is assumed that each mineral is electrically neutral, and that the positive charges of the cations are balanced by an appropriate quantity of oxygen anions. The steps for mineral formula calculation are described as follows and referenced from Spear (1993), which assumes that the Fe are all ferrous iron (Fe^{2+}) except for the feldspars being ferric iron (Fe^{3+}). The calculated example of a biotite is illustrated in the columns of Table 2. This mineral formula recalculation method is used for biotite, muscovite, garnet, K-feldspar, plagioclase, epidote, ilmenite and titanite, but not for amphibole. For amphibole formula calculation, the method established from Li et al (2020) is adopted.

Step 1: *Calculation of molecular proportions of cations*. The conversion of oxides from wt.% to molecular proportion is to divide the wt. % of oxide (column 1) by the formula weight of oxide (column 2) to yield the molecular proportions (column 3). Then, multiply the molecular proportions of oxides (column 3) by the number of cations per oxide (column 4) to yield molecular proportions of cations (column 5).

Step 2: *Normalization of molecular proportions*. The normalization is based on the charge balance, which means that the sum of the positive charges equals to the

doi:10.6342/NTU202202659

sum of the negative charges. For example, there are 22 oxygens in a biotite based on the oxide calculation without hydrogen measurement for the chemical formula, $K_2(Fe^{2+}, Mg)_6[Al_2Si_6O_{20}](OH)_4$, which equals to $1K_2O$ + 6(FeO or MgO) + $1Al_2O_3$ + $6SiO_2$. Thus, the cations should be normalized to 44 positive charges to balance the negative charges of 22 oxygens. First, the molecular proportions of cations (column 5) are multiplied by the charge per cation (column 6) to derive the equivalent positive charge (column 7) of each cation. The sum of all the positive charges of all cations is 4.8682, which should be normalized to 44 by a factor of 44/4.8682 = 9.0382. Multiplication of the molecular proportions of cations (column 5) by the normalization factor gives the normalized moles of each cation (column 8).

Step 3. *Assignment of cations to structural sites*. Calculation of a mineral formula requires assignment of cations to structural sites (columns 9 and 10). This is typically done based on the relative size of cations: K > Na > Ca > Mn > Fe^{2+} > Mg > Ti > Fe^{3+} > Al > Si. The structural formula of a biotite is $I_2M_{4\text{-}6}T_8O_{20}(OH,F)_4$, where I is mainly K, Na or Ca; M is mainly Al, Fe^{2+}, Mg but also Mn and Ti, and T is mainly Si or Al and possibly also Fe^{3+} and Ti. All Si is assigned to the T site (tetrahedral site) with sufficient Al assigned to the sum of 8.0 (Al^{IV} = 2.6693). The remaining Al is assigned to the M site (octahedral site; Al^{VI} = 1.0719). Fe^{2+}, Mg,

doi:10.6342/NTU202202659

Mn, Ti are all assigned to the M site, and K, Na, Ca is assigned to the I site.

Step 4. *Examination of calculated result*. To ensure that the calculated result of the mineral formula is reliable, the calculated result is compared with the accepted values provided within Deer et al (2013). The values include the total atoms per formula unit (apfu) of the I, M, T sites and the apfu of certain elements in specific cation sites, such as the Al in the T site and Si in the T site.

Step 5. *Estimation of Fe^{3+} by stoichiometric normalization*. The method for estimation of ferric iron content of a mineral is to normalize the cation number to an ideal stoichiometric number, which is a cation-based mineral formula calculation method in Schumacher (1991). For example, there are 16 cations in the structural formula of a biotite, which is the value used to normalize the molecular proportions of cations with the assumption of all ferrous iron (column 5) into an ideal stoichiometric number of cations (column 11). The total positive charges based on 16 cations are 45.6711 (column 12), which is larger than ideal negative charges of oxygen of 44, and the number of oxygens per oxide (column 13). In this case, the analysis cannot be corrected for ferric iron (Schumacher, 1991), and only calculates the mineral formula with the assumption of all ferrous iron. Biotite is nearly impossible to do a ferric iron correction only based only on an EPMA analysis, due to the possible vacancies at the 12-fold coordinated interlay sites and

doi:10.6342/NTU202202659

the octahedral sites as well as the minor interlayers of other sheet silicates (Schumacher, 1991). Thus, all biotites in this study were calculated with an all-ferrous iron assumption.

doi:10.6342/NTU202202659

Table 2. Calculation of the structural formula of a biotite from EPMA analysis. The biotite is No.122 from sample 18LYA01.

column	1	2	3	4		5	6	7	8		9	10		11	12	13
	Weight % of oxide	Formula weight[1]	Molecular proportions of oxides	Cations per oxide		Molecular proportions of cations	Charge per cation	Equivalent positive charge	Normalized moles of cations[2]		Cation structural positions	Cation site assignment		Cations normalized to 16[3]	Equivalent positive charge	Oxygen per oxide
SiO_2	35.435	60.08	0.5898	1	Si^{4+}	0.5898	4	2.3592	5.3307	Si^{4+}	Si(T)	5.3307	Si^{4+}	5.5332	22.1327	11.0664
TiO_2	2.417	79.88	0.0303	1	Ti^{4+}	0.0303	4	0.1210	0.2735	Ti^{4+}	Ti(M)	0.2735	Ti^{4+}	0.2839	1.1355	0.5677
Al_2O_3	21.102	101.96	0.2070	2	Al^{3+}	0.4139	3	1.2418	3.7412	Al^{3+}	Al^{IV}(T)	2.6693	Al^{3+}	3.8833	11.6498	5.8249
FeO	22.525	71.85	0.3135	1	Fe^{2+}	0.3135	2	0.6270	2.8335		Al^{VI}(M)	1.0719	Fe^{2+}	2.9411	5.8822	2.9411
MnO	0.314	70.94	0.0044	1	Mn^{2+}	0.0044	2	0.0089	0.0400	Fe^{2+}	Fe(M)	2.8335	Mn^{2+}	0.0415	0.0831	0.0415
MgO	6.318	40.30	0.1568	1	Mg^{2+}	0.1568	2	0.3135	1.4170	Mn^{2+}	Mn(M)	0.0400	Mg^{2+}	1.4708	2.9416	1.4708
CaO	0.000	56.08	0.0000	1	Ca^{2+}	0.0000	2	0.0000	0.0000	Mg^{2+}	Mg(M)	1.4170	Ca^{2+}	0.0000	0.0000	0.0000
Na_2O	0.239	61.98	0.0039	2	Na^+	0.0077	1	0.0077	0.0697	Ca^{2+}	Ca(I)	0.0000	Na^+	0.0724	0.0724	0.0362
K_2O	8.906	94.20	0.0945	2	K^+	0.1891	1	0.1891	1.7090	Na^+	Na(I)	0.0697	K^+	1.7739	1.7739	0.8870
										K^+	K(I)	1.7090				
Total	97.256					1.7055		4.8682	15.4146					16.0000	45.6711	22.8355

[1]The values of formula weight are from Spear (1993)

[2]Normalization factor = 44/4.8682 = 9.0382

[3]Normalization factor = 16/1.7055 = 9.3815

doi:10.6342/NTU202202659

3.5.2 Ti-in-biotite Geothermometer

The Ti-in-biotite geothermometer used in this study was developed by Henry et al. (2005), which is empirically calibrated Ti-saturation surface generated using considerable biotite data set from ilmenite- or rutile-bearing graphitic, peraluminous metapelites in western Maine and south-central Massachusetts (Ferry, 1981; Henry & Guidotti, 2002 and references therein). The Ti-saturation surface is calculated from the relationships between the Ti contents, $Mg/(Mg+Fe^{2+})$ value and the temperature based on 22-O atoms of the biotite formula. The surface-fit equation can be reformulated into a geothermometer expression: $T=\{[\ln(Ti)-a-c(X_{Mg})^3]/b\}^{0.333}$, in which T is temperature in degree Celsius (°C), Ti is the number of atoms per formula unit (apfu), X_{Mg} is $Mg/(Mg+Fe^{2+})$, a = -2.3594, b = 4.6482×10^{-9} and c = -1.7283. The calibration/applicable range for this geothermometer is T = 480-800 °C, Ti = 0.04-0.60 apfu and X_{Mg} = 0.275-1.000 with equilibrated pressure at about 3-6 kbar. The precision of estimated temperatures is within ±24 °C in the range of 480-600 °C, ±23 °C in the range of 600-700 °C, and ±12 °C in the range of 700-800 °C. Application of the geothermometer to metapelites without the Ti-saturating minerals (e.g., ilmenite, rutile) and/or graphite can cause minor-to-significant errors in estimated temperatures (Henry et al., 2005).

doi:10.6342/NTU202202659

3.5.3 Al-in-hornblende Geobarometer

The total Al content in magmatic calcic hornblende was discovered in a positive correlation to the crystallization depth of calc-alkalic plutonic rocks (Hammarstrom and Zen, 1986). Such relation has been developed into a geobarometer using the Al_{total} content in hornblende to calculate the emplacement pressure of plutonic rocks or the equilibration depth of the magma reservoir for volcanic rocks (Hammarstrom and Zen, 1986; Hollister et al., 1987; Johnson and Rutherford, 1989; Schmidt, 1992). The geobarometer is applicable to tonalitic rocks with an equilibrated mineral assemblage of hornblende + biotite + plagioclase + K-feldspar + quartz + titanite + Fe-Ti-oxide with calibration P-T ranges of 2.5-13 kbar and 655-700 °C (Schmidt, 1992). The calibrated equation is $P (\pm 0.6 \text{ kbar}) = -3.01 + 4.76Al_{total}$ (Schmidt, 1992), which is used in this study to calculate the emplacement pressure of the tonalitic basements of Kinmen Island.

doi:10.6342/NTU202202659

3.5.4 Biotite-Muscovite Geobarometer

Due to low Ca content, some metapelites are devoid of garnet and/or plagioclase, which makes the conventional garnet-plagioclase-related geobarometers unapplicable [e.g., garnet-Al_2SiO_5-plagioclase-quartz (GASP) geobarometer; Holdaway, 2001]. However, Wu (2020) established a biotite-muscovite geobarometer that can be applied to garnet- and/or plagioclase-deficient metapelites. The barometer was empirically calibrated using 270 natural garnet-and-plagioclase-bearing metapelites and the reaction of $KFe_3AlSi_3O_{10}(OH)_2 + 3\ TiO_2 + Al_2SiO_5 = 3\ FeTiO_3 + SiO_2 + KAl_2AlSi_3O_{10}(OH)_2$. The mineral phases include biotite, rutile, aluminosilicate, ilmenite, quartz, and muscovite. The chemical compositions of muscovite and biotite cover the natural chemical ranges of the micas within metapelites; thus, no chemical limitation is put on the application of the barometer. However, if ilmenite is present but rutile is absent in the rock, the estimated pressures can only provide the upper limit of the pressure conditions (Wu, 2020). The calibrated P-T conditions were determined simultaneously by a garnet-biotite geothermometer (Holdaway, 2000) and GASP geobarometer (Holdaway, 2001) with the ranges of 1-12 kbar and 470-760 ˚C. The pressure estimates are within error of ±1.5 kbar to the well-calibrated GASP geobarometer (Holdaway, 2001) with the total error estimated to be less than ±1.6 kbar. The calculation done was performed by the spreadsheet provided by Wu (2020).

doi:10.6342/NTU202202659

3.6 Whole-rock Geochemistry

Whole-rock major and trace element analysis was conducted on seven metamorphic rock samples at the lab of Australian Laboratory Services in Brisbane, Australia. Seven samples were analyzed including amphibolite (18TP01, 18TP04a), tonalitic gneiss (18TP04a), Crd-Kfs-Grt-Sill mica schist (18LYA01), sill-mica schist (181117A01), biotite gneiss (18LYB03m) and the garnet-biotite boudin within the biotite gneiss (18LYB03b). The analytical results are given in the Appendix 8.2. Major elements were measured by inductively coupled plasma atomic emission spectrometry (ICP-AES) excluding LOI (loss on ignition), which was done using thermogravimetric analysis (TGA). As for trace elements, measurement was carried out by inductively coupled plasma mass spectrometry (ICP-MS) with lithium borate fusion prior to acid dissolution. The measured elements and their limit of detection (LOD) are summarized in Table 3.

Table 3. Measured major and trace elements with their LOD.

	Analytes and LOD							
Major Element (wt%)	SiO_2	0.01	MgO	0.01	TiO_2	0.01	BaO	0.01
	Al_2O_3	0.01	Na_2O	0.01	MnO	0.01	LOI	0.01
	Fe_2O_3	0.01	K_2O	0.01	P_2O_5	0.01		
	CaO	0.01	Cr_2O_3	0.002	SrO	0.01		
Trace Element (ppm)	Ba	0.5	Hf	0.1	Sn	1	Y	0.1
	Ce	0.1	Ho	0.01	Sr	0.1	Yb	0.03
	Cr	10	La	0.1	Ta	0.1	Zr	2
	Cs	0.01	Lu	0.01	Tb	0.01		
	Dy	0.05	Nb	0.1	Th	0.05		
	Er	0.03	Nd	0.1	Tm	0.01		
	Eu	0.02	Pr	0.02	U	0.05		
	Ga	0.1	Rb	0.2	V	5		
	Gd	0.05	Sm	0.03	W	1		

doi:10.6342/NTU202202659

4 Results and Interpretation

4.1 Field Work

Field observation and structural measurement were carried out from 27 locations all around Kinmen Island (Figure 2A; Table 1), including 14 locations from the previous study (Huang and Yeh, 2020). The results are presented in two sections, the first being the complex lithologies identified and their field relationships (section 4.1.1; Figure 8), and second being the structural evolution of these complex lithologies (section 4.1.2; Figure 9-21).

4.1.1 Reconstructed Lithological Evolution

The crystalline basement of Kinmen Island contains much more complex lithologies than the geological map can show. There are four highly deformed and metamorphosed rocks surrounding the granite core, including tonalitic gneiss, amphibolite, biotite gneiss, and sillimanite mica schist (Figure 8). In these highly deformed rocks, leucogranite was commonly found not only intruding the granitoid basements and spatially related to shear zones (Huang and Yeh, 2020), but also appeared in biotite gneiss and sillimanite mica schist in this study (Figure 11). Leucogranites within these complex basements were accompanied with multiple deformation events, which implies their syn-deformation origins and their long-lasting generation during crustal deformation (Figure 11, 13, 16, 18). Moreover, amphibolite

doi:10.6342/NTU202202659

was all identified within the shear zone in the granitoid basements and had the same shear fabrics as the host rocks. There are two kinds of occurrence for amphibolite in the field, one being a dike and the other appearing to be xenoliths or enclaves (Figure 14, 18). The dike was found both within the granitic and tonalitic basement, but the xenolith or enclave ones were found only within the tonalitic basement. Despite different possible origins for these amphibolites, the concordant shear fabrics and spatial confinement to the shear zone suggest its close relationship with the shear zone development. Finally, mafic dykes crosscut all these highly deformed and metamorphosed lithologies (Figure 21). The other contact relationships between these complex lithologies, however, were not apparent. Therefore, structural correlation between these rocks was conducted to compare their geological histories since their protolith formed. The age constraints and assumptions followed the previous studies (Lin et al., 2011; Huang and Yeh, 2020).

doi:10.6342/NTU202202659

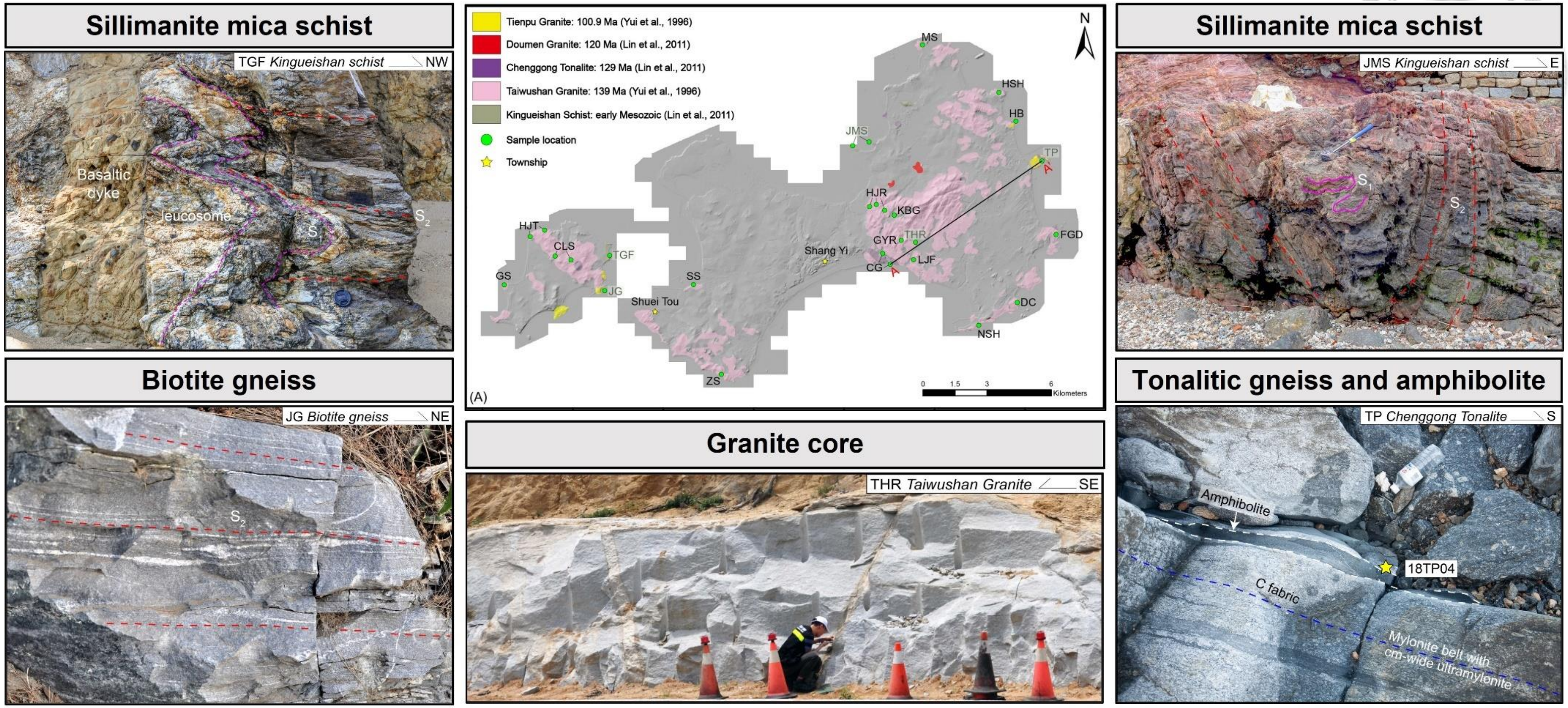

Figure 8. Complex lithologies in Kinmen Island. Field photos with sketch of interpreted structures show that these complex lithologies are highly deformed compared with the granite core. The locations for these field photos are marked by shaded green rectangles on the geological map.

doi:10.6342/NTU202202659

4.1.2 Reconstructed Structural Evolution

These complexes are classified into three types for comparison of their geological histories. The first type is Kingueishan Schist, which includes the sillimanite mica schist. The second type is Taiwushan Granite, which forms the granite core of Kinmen Island. The third type is Chenggong Tonalite, which contains tonalitic gneiss and biotite gneiss. The sample locations for each exhumed basement are summarized in Table 1. A total of 1068 structural measurements were taken from these basements, including the 568 measurements from Huang and Yeh (2020) (Figure 9 and Appendix 8.3). Six deformation events were reconstructed, which revised the original five in the previous study (Huang and Yeh, 2020). These six deformation events can be correlated within different basements, which indicates that they experienced a similar deformation history since the granitoid basements crystallized. The deformation events went from ductile (D_1, D_2, D_3, and D_4) to brittle ones (D_5 and D_6), which suggests a decreasing temperature condition accompanying the structural evolution. The details of deformation events are summarized in the following sections.

doi:10.6342/NTU202202659

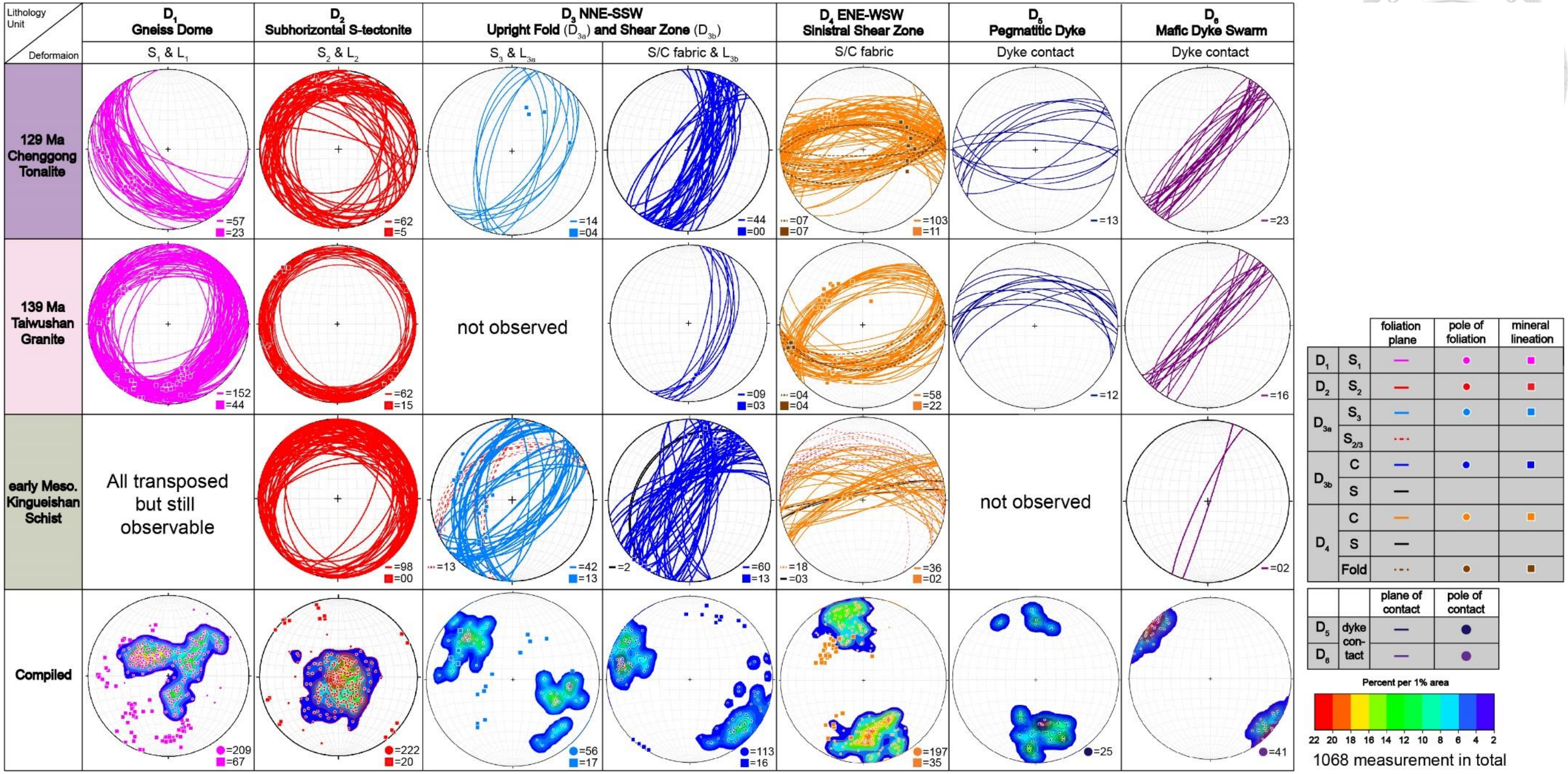

Figure 9. Compiled field structural measurement data from three basement rocks in Kinmen Island. Each deformation event is marked by different colors as shown in the legend. The compiled row shows the pole of foliation and lineation together with 1% area contour.

doi:10.6342/NTU202202659

4.1.2.1 D_1 Gneiss dome

D_1 formed a kilometer scale gneiss dome structure with the core being Taiwushan Granite surrounded by Chenggong Tonalite and Kingueishan Schist at the margin. Moderately- to shallowly- dipping gneissic foliations (S_1) were formed around the margin of Taiwushan Granite and within Chenggong Tonalite, all of which were dipping away from the core of Taiwushan Granite (Figure 10). Within Kingueishan Schist, however, S_1 were folded and transposed by later deformation events (Figure 8). The degree of foliation development varies a lot in different limbs of the gneiss dome with the southwest to the southeast limb having developed the best, evidenced by the more penetrative foliations throughout the rock. The moderately- to shallowly- down-dipping mineral stretching lineation was mainly developed from the west to south limb of the dome, which is characterized by L-S tectonite with W-, SW- to S-plunging lineation indicative of a plane strain. In contrast, S-tectonite is the feature at the east limb of the dome suggestive of a flattening strain (Davis et al., 2011). Such a difference in strain patterns and degrees of foliation development implies strong strain partitioning at different limbs of the dome with the southwest limb having the best-developed structure.

In the D_1 domain of Taiwushan Granite and Chenggong Tonalite, these granitoids were deformed without metamorphic neocrystallization. Even if the granitoid reached the migmatitic condition with *in-situ* partial melting in a few places (Huang and Yeh,

doi:10.6342/NTU202202659

2020), there was only compositional differentiation into quartzofeldspathic-rich and mafic mineral rich domains. In Kingueishan Schist, instead, not only compositional differentiation but also widespread leucosome and melanosome are identified (Figure 8), which provides direct evidence of high-grade metamorphism during D_1. In addition, such distinct metamorphic phenomena for different lithologies indicate their different metamorphic behaviors during the same deformation event.

doi:10.6342/NTU202202659

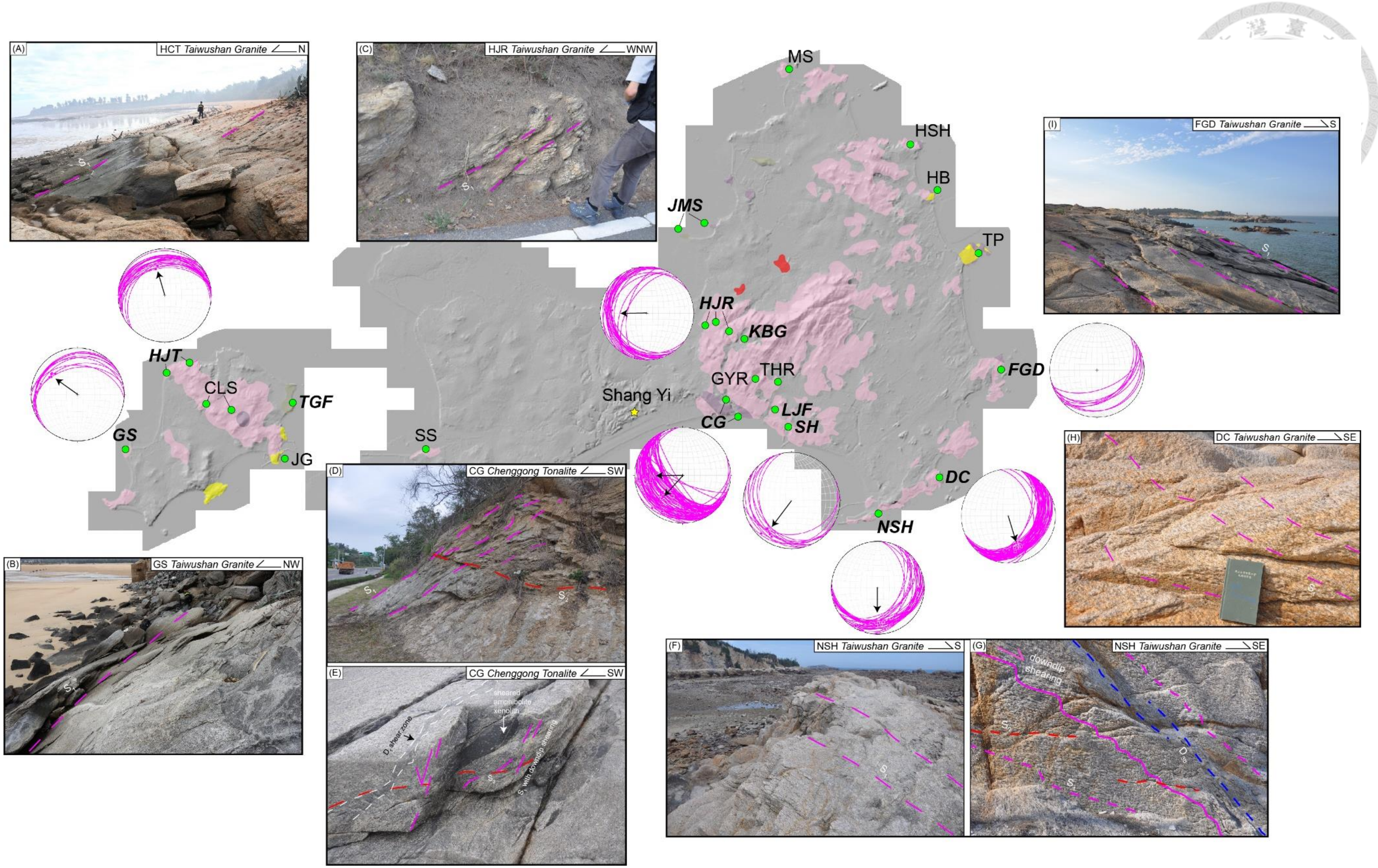

doi:10.6342/NTU202202659

Figure 10. The 20-meter digital terrain model map overlaid by the geological map showing outcrop photos with measured S_1 gneissic foliation and L_1 mineral lineation to demonstrate D_1 gneiss dome. The bold italic words indicate the sample locations with S_1 fabrics identified. Photos from C to I are compiled from Huang and Yeh (2020). (A) The shallowly NNW dipping gneissic foliation with poorly developed lineation at HCT. (B) The shallowly NNW-dipping gneissic foliation with NW-plunging lineation at GS. (C) The N-S striking and shallowly W-dipping gneissic foliation with poorly- to no- mineral lineation developed at HJR. (D, E) The NW-SE striking, shallowly to moderately SW-dipping gneissic foliation with well-developed W and SW plunging lineation at CG. The S_1 is deformed into a wavy form due to the subhorizontal S_2 foliation. The sheared amphibolite xenolith indicates the down-dip shearing along the S_1 foliation. (F, G) The NE-SW striking, shallowly to moderately SE-dipping gneissic foliation with well-developed S plunging lineation at NSH. The kinking of S_1 foliation is due to the weak development of the subhorizontal S_2 foliation, both of which are crosscutted by D_3 shear zone. (H) The NE-SW striking, moderately SE-dipping gneissic foliation with well-developed SSE plunging lineation at DC. (I) The ENE-WSW striking, moderately SE-dipping gneissic foliation with no lineation developed at FGD.

4.1.2.2 D_2 Subhorizontal S-tectonite

D_2 formed subhorizontal S-tectonite (S_2) with few lineations developed as the D_1 gneiss dome collapsed. The S_2 foliation was well developed within all the deformed basements, yet with distinct deformation styles in different lithologies. In Taiwushan Granite and Chenggong Tonalite, the S_2 gneissic foliation distorted the S_1 doming fabrics into wavy foliations indicative of ductile crustal flow from the core of the gneiss dome to the margin (Figure 10D, G and Figure 11A, B). In addition, S_2 was spaced and developed around the same height level across the granitoids. However, within Kingueishan Schist, S_2 deformed S_1 fabric into a recumbent fold and was penetratively developed throughout the schist belt (Figure 11C). The subhorizontal S-tectonite reflects a flattening strain for D_2, which deformed under a stress setting of vertical

doi:10.6342/NTU202202659

shortening and horizontal extension. Such a strain pattern is typically found in a thinned continental crust under gravitational collapse.

In the D_2 domain of Taiwushan Granite and Chenggong Tonalite, the granitoids were mostly deformed without metamorphic neocrystallization as the D_1 event. Only mineral realignment and grain flattening was identified, except for Taiwushan Granite at the SS location and biotite gneiss at the JG location. Taiwushan Granite at the SS location was deformed into not only L-tectonite with compositional differentiation but also L-S tectonite with centimeter-thick, garnet-rich metamorphic layering (Figure 11D). Furthermore, biotite gneiss formed during the D_2 event, which not merely metamorphosed its protolith into biotite gneiss but triggered the in-situ partial melting and leucogranite formation as well (Figure 11E). In Kingueishan Schist, S_2 was defined by well-developed, mica-rich schistosity. Also, leucogranite concordant to the schistosity was commonly identified (Figure 11F), which suggests a migmatitic condition for the schist belt during D_2. Such distinct metamorphic features for different lithologies unveiled their different metamorphic behaviors during the same deformation event, which is the same result as the D_1 event.

doi:10.6342/NTU202202659

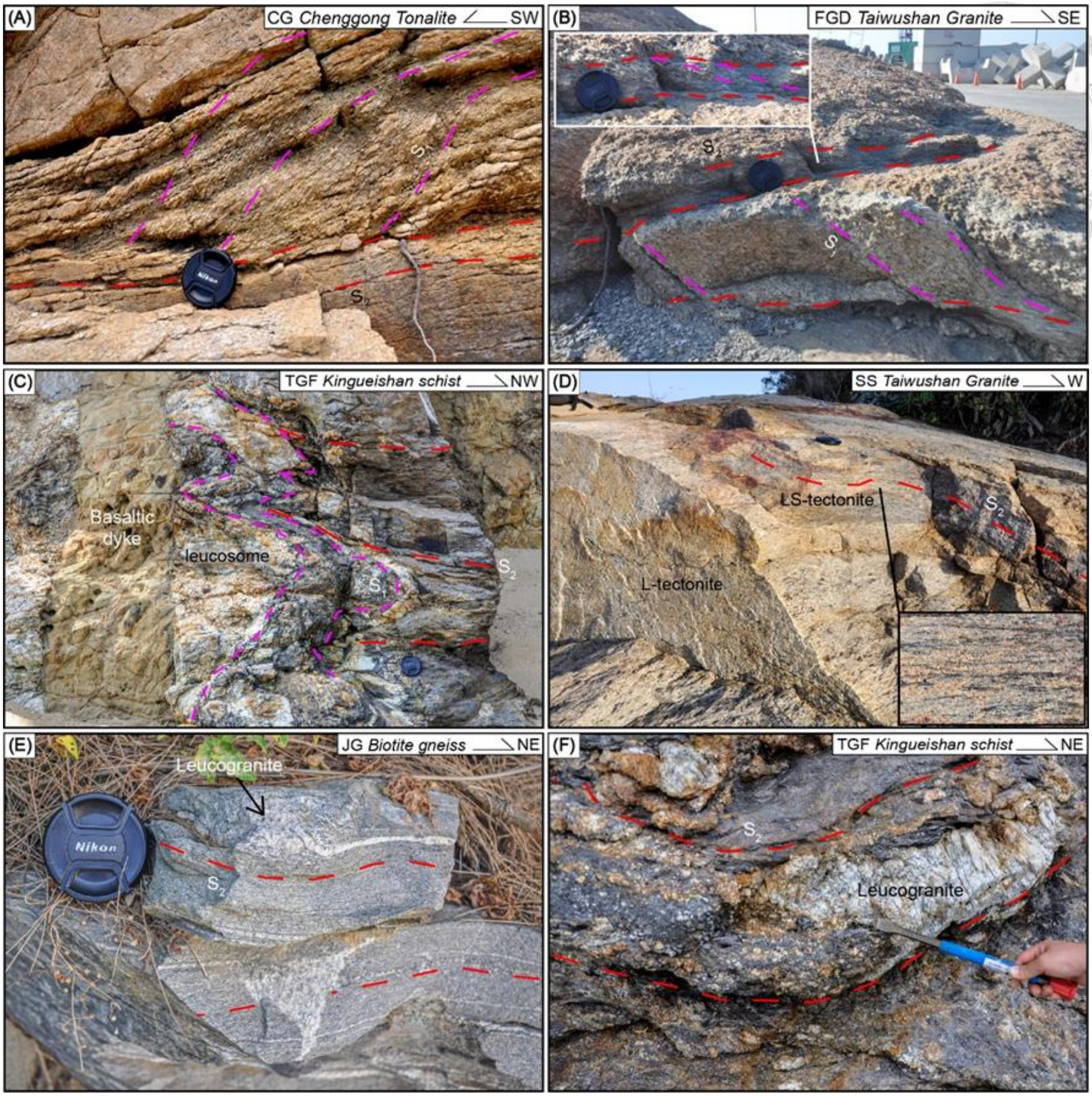

Figure 11. Outcrop photos and sketches showing D_2 domain within different lithologies. Figure A and B are compiled from Huang and Yeh (2020). (A) Wavy S_1 foliation due to the development of subhorizontal S_2 foliation in Chenggong Tonalite at CG. (B) Subhorizontal S_2 foliation crosscuts the S_1 doming fabric in Taiwushan Granite at FGD. (C) D_1 domain leucosome and S_1 foliation is folded in a recumbent fold with penetrative fold axial schistosity (S_2) in Kingueishan Schist at TGF, all of which are truncated by basaltic dyke. (D) L-tectonite and LS-tectonite developed during D_2 event with garnet-rich metamorphic layering within the LS-tectonite in Taiwushan Granite at SS. (E) In-situ partial melting and leucogranite generation during D_2 domain in biotite gneiss at JG. (F) Leucogranite concordant to the S_2 in Kingueishan Schist at TGF.

doi:10.6342/NTU202202659

4.1.2.3 D_3 NNE-SSW Shear Fold Belt

D_3 formed an NNE-SSW trending shear fold belt with the fold (D_{3a}) developing first and the shear zone (D_{3b}) initiating along the fold limbs later. These D_3 structures were all formed at the margin of the gneiss dome, especially at the east and west limbs, with varying scales from a centimeter to one hundred meters (Figure 12). The D_{3a} folding event was mainly developed within Kingueishan Schist and biotite gneiss while the D_{3b} shear zone penetrated all the lithological units (Figure 9), which shows strain partitioning between different deformation styles and lithologies. The D_{3a} folding event formed NNE-SSW to NE-SW trending spaced S_3 crenulation schistosity, which doubly dips to the NW and SE. The mineral lineation (L_{3a}) obliquely plunges to the dip directions of S_{3a} with moderate plunging angles. The S_3 crenulation schistosity shows opposite shear sense on the opposite side of the fold limbs (Figure 13), which indicates that the folding mechanism is shear folding. The D_{3b} shearing event formed NNE-SSW striking S/C fabrics, which doubly dips to the NW and SE. The mineral lineation (L_{3b}) plunges nearly parallel to the strike of C fabrics with horizontal to shallow plunging angles. Such lineation pattern suggests a strike-slip shear zone during the D_{3b} shearing event. Furthermore, the D_{3b} shear zone has opposite shear sense on different sides of the gneiss dome with the west side being a dextral shear (e.g., TGF location; Figure 13E) and the east side being a sinistral shear [e.g., TP location; Figure 8A in Huang and

doi:10.6342/NTU202202659

Yeh (2020)]. Such opposite shear senses on opposite sides of the structure (e.g., fold limbs or dome limbs) with the shear zone dominating the structural development are both identified in the D_{3a} folding and D_{3b} shearing event, which suggests that D_3 was a shear folding event with progressive deformation from folding to shearing.

In the D_3 domain of Kingueishan Schist, the schist was deformed not only with in-situ shear melting but also sillimanite neocrystallization along the mineral lineation (Figure 13C, E), which suggests a sillimanite grade metamorphism along with anatexis during the D_{3b} shearing event. As for Taiwushan Granite and Chenggong Tonalite, these granitoids were deformed into a mylonite belt with heterogeneous deformation ranging from augen gneiss to ultramylonite with augen gneiss being the main lithology (Figure 14A, B). Within Chenggong Tonalite, amphibolite dikes subparallel to the S/C fabrics was abundant at the TP location (Figure 14C), which indicates an amphibolite facies metamorphism during the D_{3b} shearing event. Also, the concordant relationships between amphibolite and the matrix augen gneiss implies that the protolith of the amphibolite could be mafic magma intruding the Chenggong Tonalite at nearly the same stress field as the formation of D_{3b} shear zone.

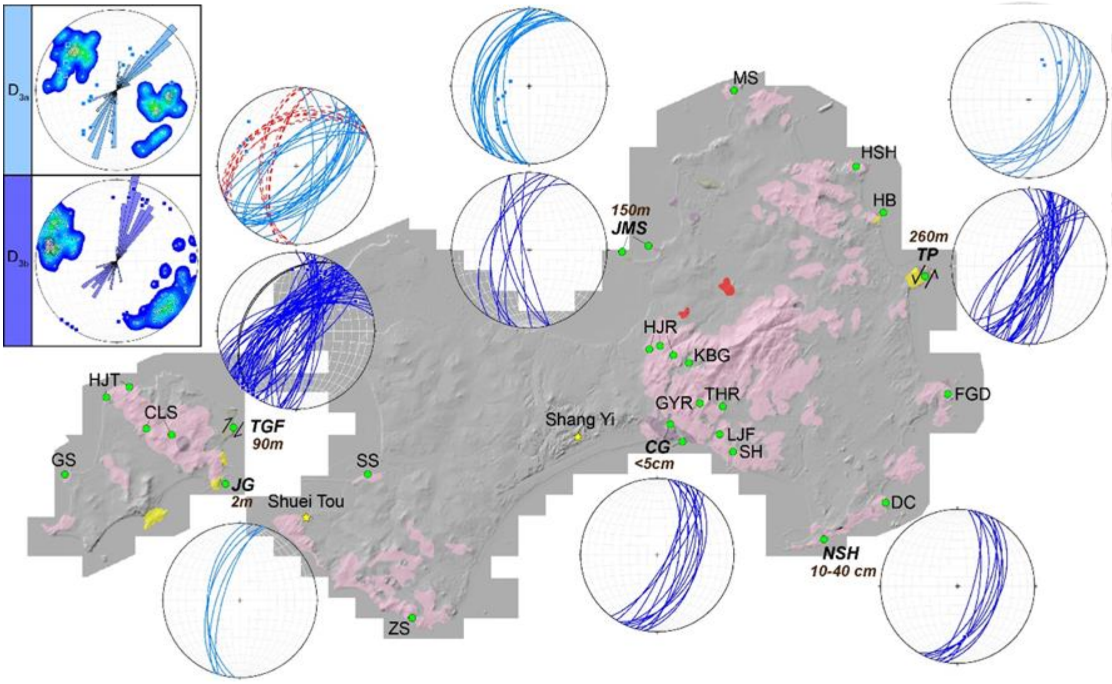

Figure 12. Topographic map overlaid by the geological map showing measured D_3 structures. The bold italic words indicate the sample locations with D_3 structures measured. The brown bold italic words next to the locations are estimated horizontal width of the D_{3b} shear zone.

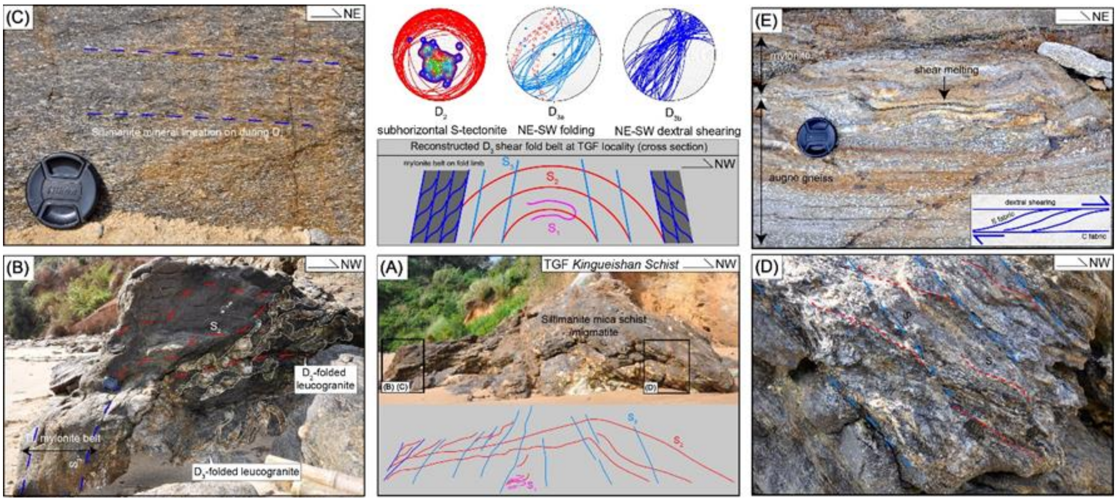

Figure 13. Outcrop photos and sketches showing D_3 structures within Kingueishan Schist at TGF location with a schematic diagram illustrating the structural relationships between D_1, D_2 and D_3. (A) An overall view shows that S_2 subhorizontal foliation was folded by S_3 crenulation schistosity with many leucogranites deformed within. (B) A D_{3b} mylonite belt was developed at SE limb of the fold with twice folded leucogranites within. (C) Sillimanite mineral lineation grew on the SE limb of the fold. (D) S_{3a} crenulation schistosity sheared the S_2 foliation. (E) Dextral S/C fabrics was developed within the shear zone with in-situ shear melting.

doi:10.6342/NTU202202659

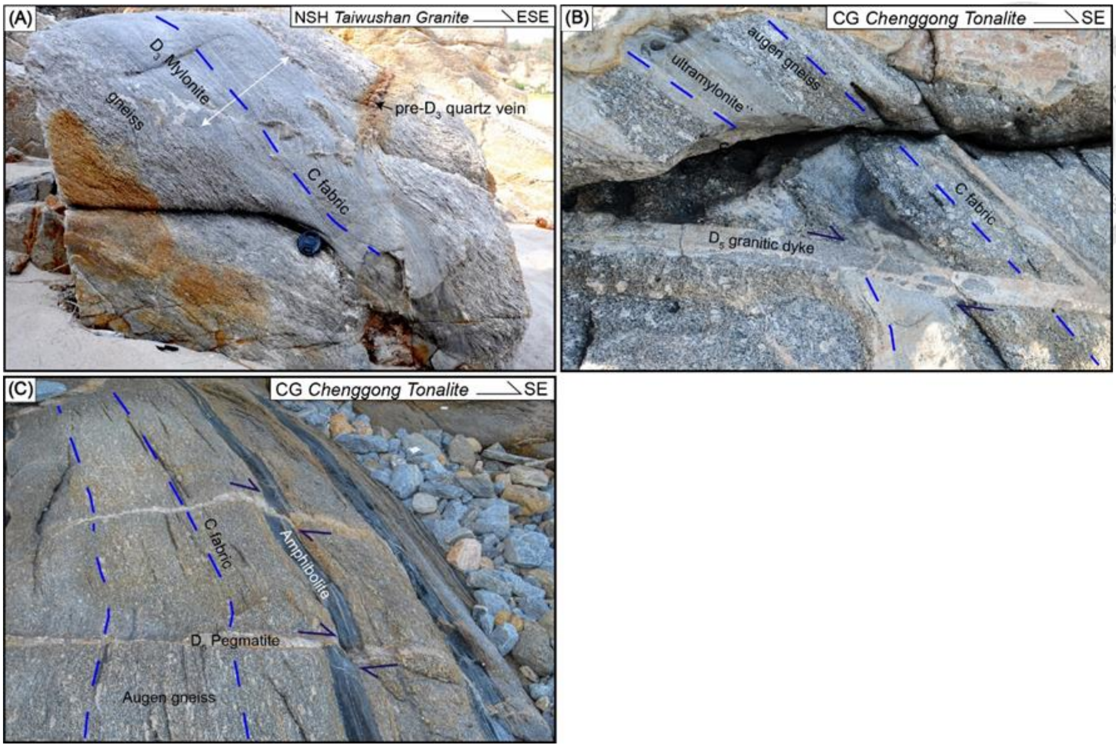

Figure 14. Outcrop photos and sketches showing D_{3b} shear zones within Taiwushan Granite and Chenggong Tonalite. (A) D_{3b} shear zone transformed the original granitic gneiss into mylonite within Taiwushan Granite at NSH. (B) Heterogeneous shear zone deformation was developed within the Chenggong Tonalite at TP, shown as the coexistence of augen gneiss and ultramylonite, both of which were crosscutted by D_5 granitic dyke with dextral displacement. (C) Amphibolite of dike occurrence within the augen gneiss in Chenggong Tonalite at TP, both of which were crosscutted by D_5 granitic dyke with dextral displacement.

doi:10.6342/NTU202202659

4.1.2.4 D_4 ENE-WSW Sinistral Transtensional Shear Zone

D_4 formed an ENE-WSW trending transtensional sinistral shear zone. The D_4 shear zone not only penetrated all the lithological units but also was formed across the gneiss dome from the core to the margin with varying scales from a centimeter to hundreds of meters (Figure 15). The D_4 shearing event formed E-W to NE-SW trending S/C fabrics, which doubly dips toward the N and S. The mineral lineation obliquely plunges to the dip directions of S/C fabrics with moderate plunging angles. Most S/C fabrics and related mineral lineation suggest a sinistral transtensional deformation of the D_4 shear zone, except for the HSH location with transpressional deformation [Figure 15; Figure 7F, G in Huang and Yeh (2020)].

Compared with Taiwushan Granite and Chenggong Tonalite, the size of the D_4 shear zone is much smaller within Kingueishan Schist with only a centimeter scale. Otherwise, the deformation was mainly manifested by shear folding with the shear plane (C fabric) developed as the fold axial plane (Figure 16). As for Taiwushan Granite and Chenggong Tonalite, these granitoids were deformed into mylonite with heterogenous deformation ranging from protomylonite to ultramylonite (Figure 17). Within Chenggong Tonalite, amphibolite enclaves or xenoliths subparallel to the S/C fabrics was commonly identified at the TP location (Figure 18A). One amphibolite dike concordant to the matrix foliation (Figure 18B), similar to the ones in Chenggong

doi:10.6342/NTU202202659

Tonalite in D_{3b} domain, was identified within Taiwushan Granite at the HSH location, which indicates an amphibolite facies metamorphism during the D_4 shearing event. In the D_4 domain, metamorphic neocrystallization was only identified within the amphibolite with the other lithologies mainly undergoing shear zone deformation and dynamic recrystallization. In addition, leucogranites was identified from pre-, syn-, to post-D_4 shearing at both the transtensional shear zone at the TP location and transpressional shear zone at the HSH location (Figure 18). Lastly, a post-D_4 folding event with pegmatitic vein along the fold axial cleavage was firstly discovered locally within Chenggong Tonalite at JMS location (Figure 19A). Chloritization was found accompanying the pegmatitic veins, including the regions where D_4 shear fabrics were folded and a chloritization layering parallel to D_4 shear fabrics (Figure 19B, C). It is suggested that the post-D_4 folding event was formed under greenschist facies conditions with chloritization triggered by the pegmatitic veins. The pegmatitic veins formed not only along the original D_4 shear fabrics but also along the fold axial cleavage, indicating that the post-D_4 event reactivated the D_4 shear fabrics and then deformed into a fold.

doi:10.6342/NTU202202659

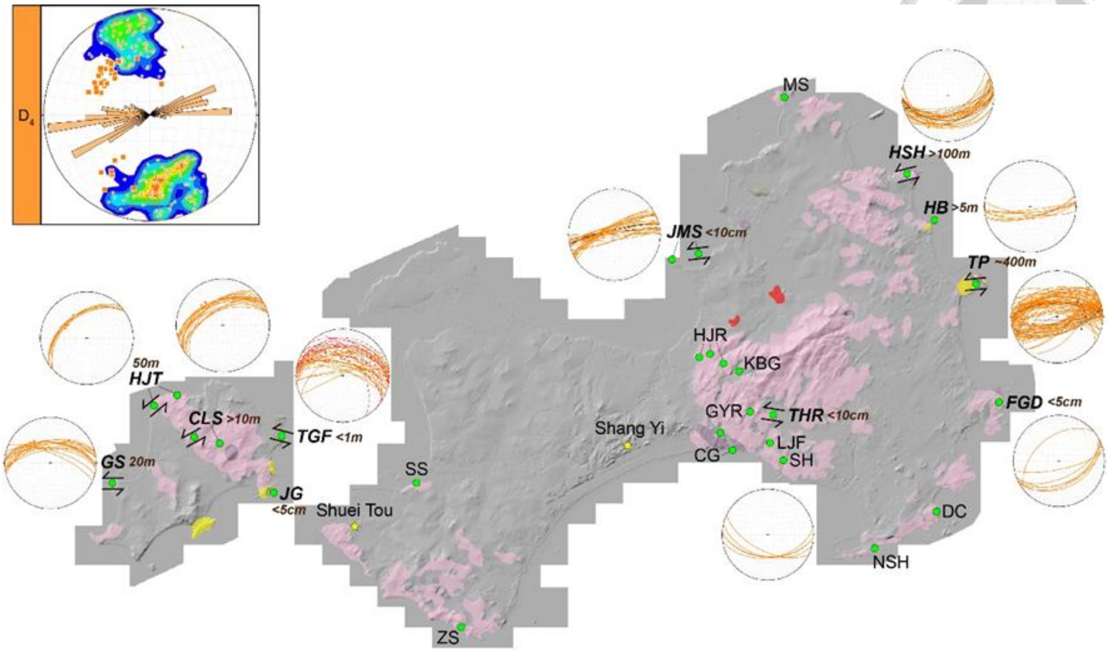

Figure 15. Topographic map overlaid by the geological map showing measured D_4 structures. The bold italic words indicate the sample locations with D_4 structures measured. The brown bold italic words next to the locations are estimated horizontal width of the D_4 shear zone.

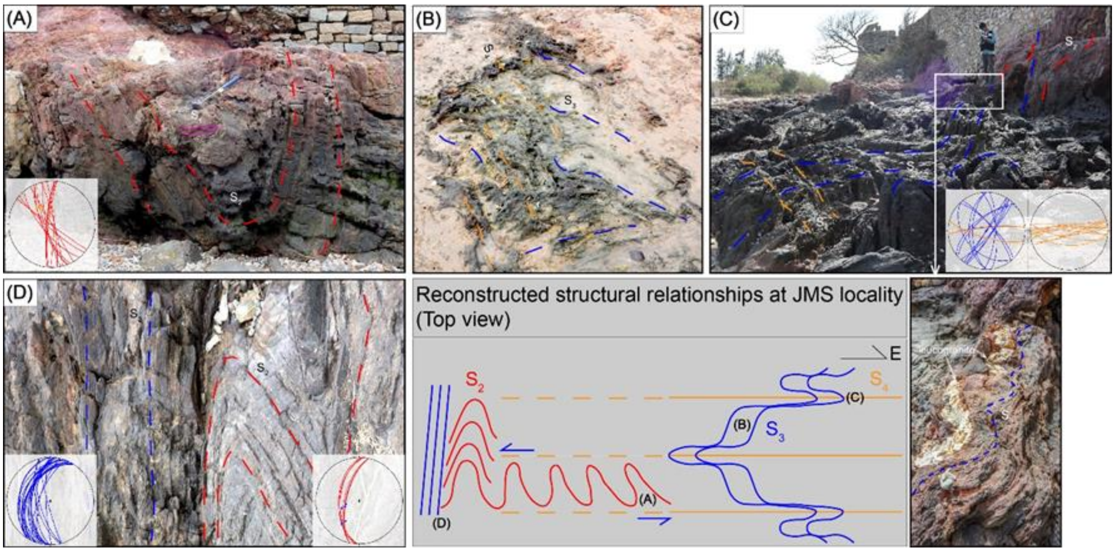

Figure 16. Outcrop photos, sketches, measured structures, and a schematic diagram to show interpreted structural relationships (D_1-D_4) within Kingueishan Schist at the JMS location. (A) The original subhorizontal S_2 foliation is folded into an upright fold due to D_{3a} folding event, whose orientation was later rotated into NW-SE striking by the D_4 event. (B) Shear folding of the S_3 foliation by the S_4 foliation. (C) Crosscutting relationships between S_2, S_3 and S_4 with calculated fold axial plane of folded S_3 foliation parallel to the S_4 foliation. The inset shows the close-up photos of folded S_3 and the leucogranites within. (D) S_2 foliation is folded into an upright fold by S_3 foliation.

doi:10.6342/NTU202202659

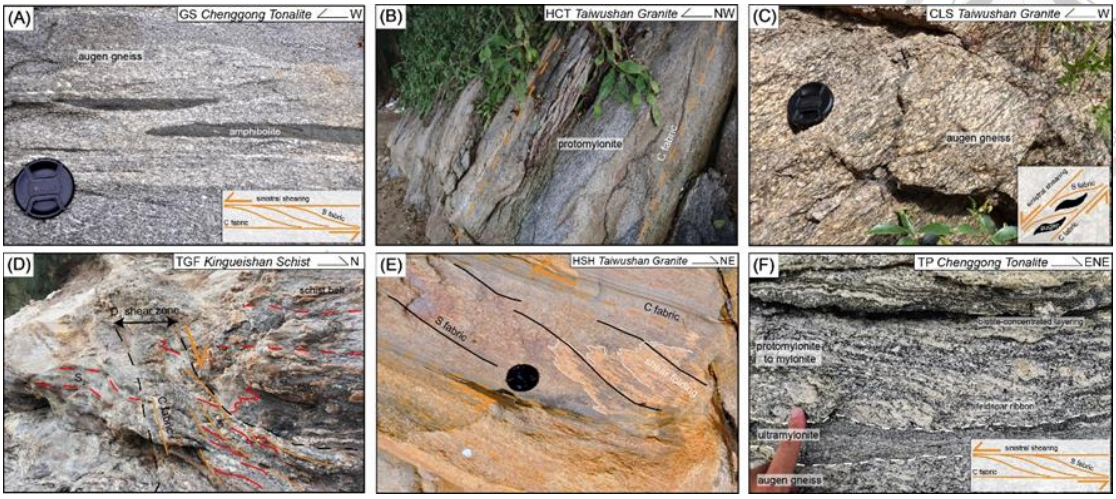

Figure 17. Outcrop photos and sketches showing interpreted D_4 structures within different lithologies. Figure E and F are from Huang and Yeh (2020). (A) Augen gneiss and amphibolite with sinistral S/C fabrics within Chenggong Tonalite at the GS location. (B) A protomylonite belt with penetrative shear fabric was developed within Taiwushan Granite at the HCT location. (C) An augen gneiss belt with normal sense of shear and sinistral S/C fabrics formed within Taiwushan Granite at the CLS location. (D) A shear zone with normal shear sense was developed within Kingueishan Schist at the TGF location. (E) A mylonite belt with sinistral S/C fabric and folded leucocratic dyke formed within Taiwushan Granite at the HSH location. (F) Heterogeneous shear zone deformation from augen gneiss, protomylonite, mylonite to ultramylonite with sinistral S/C fabrics was developed within Chenggong Tonalite at the TP location.

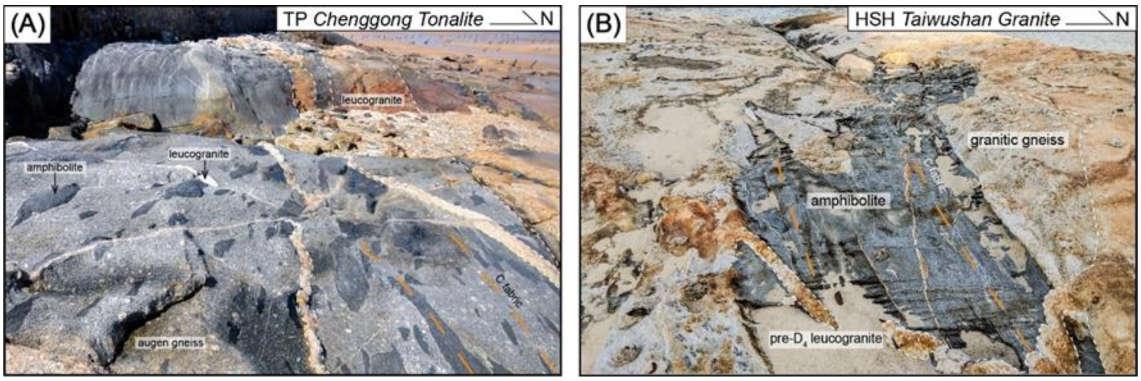

Figure 18. Outcrop photos and sketches showing interpreted D_4 structures and lithological relationships between amphibolite, leucogranite and the granitoids. Figure A is from Huang and Yeh (2020). (A) The amphibolite of enclave or xenolith occurrence within Chenggong Tonalite was deformed with the host augen gneiss, both of which were truncated by syn- to post-D_4 leucogranite. (B) The amphibolite of dike occurrence within Taiwushan Granite was deformed with the host granitic gneiss, both of which were intruded by the pre-D_4 leucogranite.

doi:10.6342/NTU202202659

Figure 19. Outcrop photos and sketches showing interpreted post-D_4 structures within Chenggong Tonalite at the JMS location. (A) The matrix sinistral S/C fabrics were folded by a later deformation event with pegmatitic veins along the fold axial cleavage. (B) Pegmatitic veins were found confined in the post-D_4 folding regions not only parallel to the matrix shear fabrics but also along the fold axial cleavage. Besides, chloritization was found where these pegmatitic veins are. (C) The chloritization metamorphic layering was developed parallel to the matrix shear fabrics where pegmatitic veins are within.

doi:10.6342/NTU202202659

4.1.2.5 D_5 E-W Pegmatitic Dyke

D_5 is defined by the intrusion of Tienpu Granite followed by E-W striking and both N and S steeply dipping pegmatites (Figure 20). Tienpu Granite and E-W striking pegmatites intruded both Taiwushan Granite and Chenggong Tonalite (Figure 20A, B), but did not crosscut Kingueishan Schist. After the intrusion of Tienpu Granite, ductile deformation is not apparent, but brittle deformation can be easily identified. Also, the pegmatite intrusion is accompanied by sinistral displacement as they sinistrally offset the D_4 mylonite belts (Figure 20D).

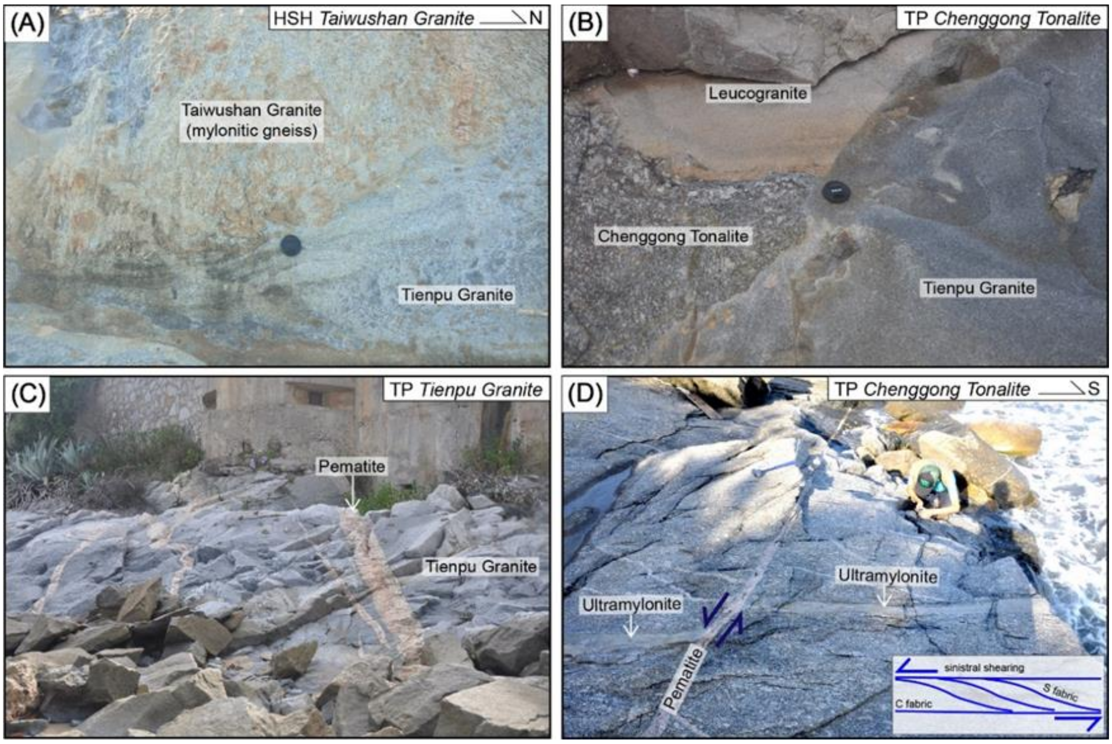

Figure 20. Outcrop photos and sketches showing the crosscutting relationships between D_5 Tienpu Granite, pegmatite and granitoid basements (Taiwushan Granite and Chenggong Tonalite). Figure B, C, D are revised from Huang and Yeh (2020). (A) The mylonitic Taiwushan Granite is truncated by undeformed Tienpu Granite. (B) Chenggong Tonalite is intruded by leucogranite, both of which are truncated by Tienpu Granite. (C) Pegmatites intrude Tienpu Granite. (D) Pegmatite crosscuts the D_4 S/C fabrics within Chenggong Tonalite with sinistral displacement, shown by the offset ultramylonite.

doi:10.6342/NTU202202659

4.1.2.6 D_6 NE-SW Mafic Dyke Swarm

The youngest deformation event (D_6) formed NE-SW striking subvertical mafic dikes, which crosscuts all the crystalline basements and D_1–D_5 structures (Figure 21). This mafic dike intrusion is accompanied by dextral displacement shown by the displaced D_5 pegmatite (Figure 21D). The brittle nature of the basaltic dike intrusion indicates the temperature condition for D_6 should be at least lower than the greenschist facies condition and was close to the ground surface.

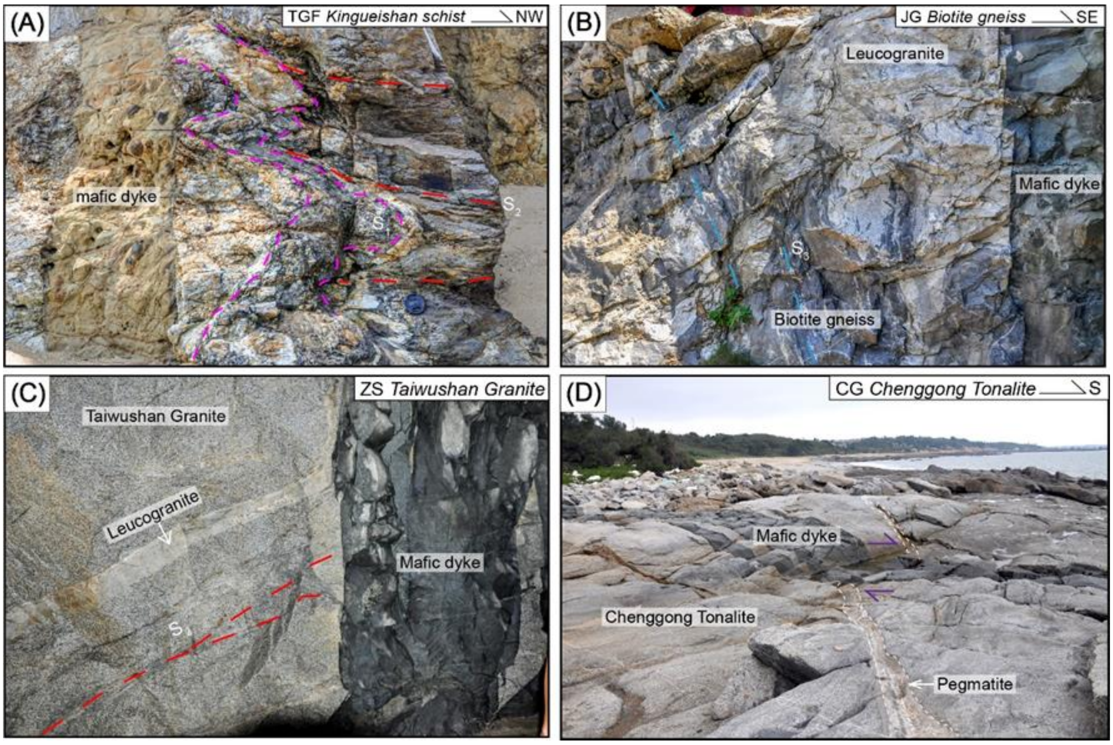

Figure 21. Outcrop photos and sketches showing the crosscutting relationships between D_6 mafic dyke and the crystalline basements. Figure D is revised from Huang and Yeh (2020). (A) Mafic dyke intrudes Kingueishan Schist and truncates S_1 and S_2 foliation. (B) Mafic dyke truncates both the leucogranite and biotite gneiss with S_3 foliation. (C) Mafic dyke intrudes Taiwushan Granite with S_2 foliation and syn-D_2 leucogranite. (D) Mafic dyke intrudes Chenggong Tonalite and dextrally offset the D_5 pegmatite

doi:10.6342/NTU202202659

4.2 Petrography and Microstructural Analysis

4.2.1 Sillimanite Mica Schist

4.2.1.1 181117A01 Sample

The sample was collected from JMS, with S_3 shallowly dipping to the NW, which was folded during D_4. In the vertical thin section, three deformation events are identified (D_2, D_3, D_4; Figure 22A). The major foliation corresponds to S_3 with S_2 in the microlithon domain, both of which were later folded and sheared by D_4 event with very weak foliation. S_3 is defined by fibrolite, which grew over decussate muscovite porphyroblasts. Aside from the decussate biotite relicts within the microlithon domain, subhedral biotite folia was found defining S_2 (Figure 22B). In the D_4 domain, muscovite were ductilely sheared and broke down into sillimanite as well (Figure 22C, D). Aside from the fibrolite in the matrix foliation, small acicular- to prismatic- sillimanite inclusions were found within coarse-grained muscovite porphyroblasts and coarse quartz grains in the matrix (Figure 22E, F). These sillimanite inclusions also showed folded patterns different from S_3 matrix foliation, which indicates that such sillimanite inclusion trails formed prior to D_3. Then, muscovite porphyroblasts grew intertectonically and enclosed this folded sillimanite. In the horizontal thin section, the major foliation is N-S striking and was folded by the E-W striking foliation, which corresponds to D_3 and D_4 respectively. Both these two foliations were defined by

doi:10.6342/NTU202202659

fibrolite (Figure 23A, B), suggesting that sillimanite grew during both D_3 and D_4. Most biotite has small grain sizes and exhibits decussate texture dispersing in the microlithon domain. This indicates that both biotite and some sillimanite formed pre-D_3 with biotite forming earlier than sillimanite as inferred from its relict texture.

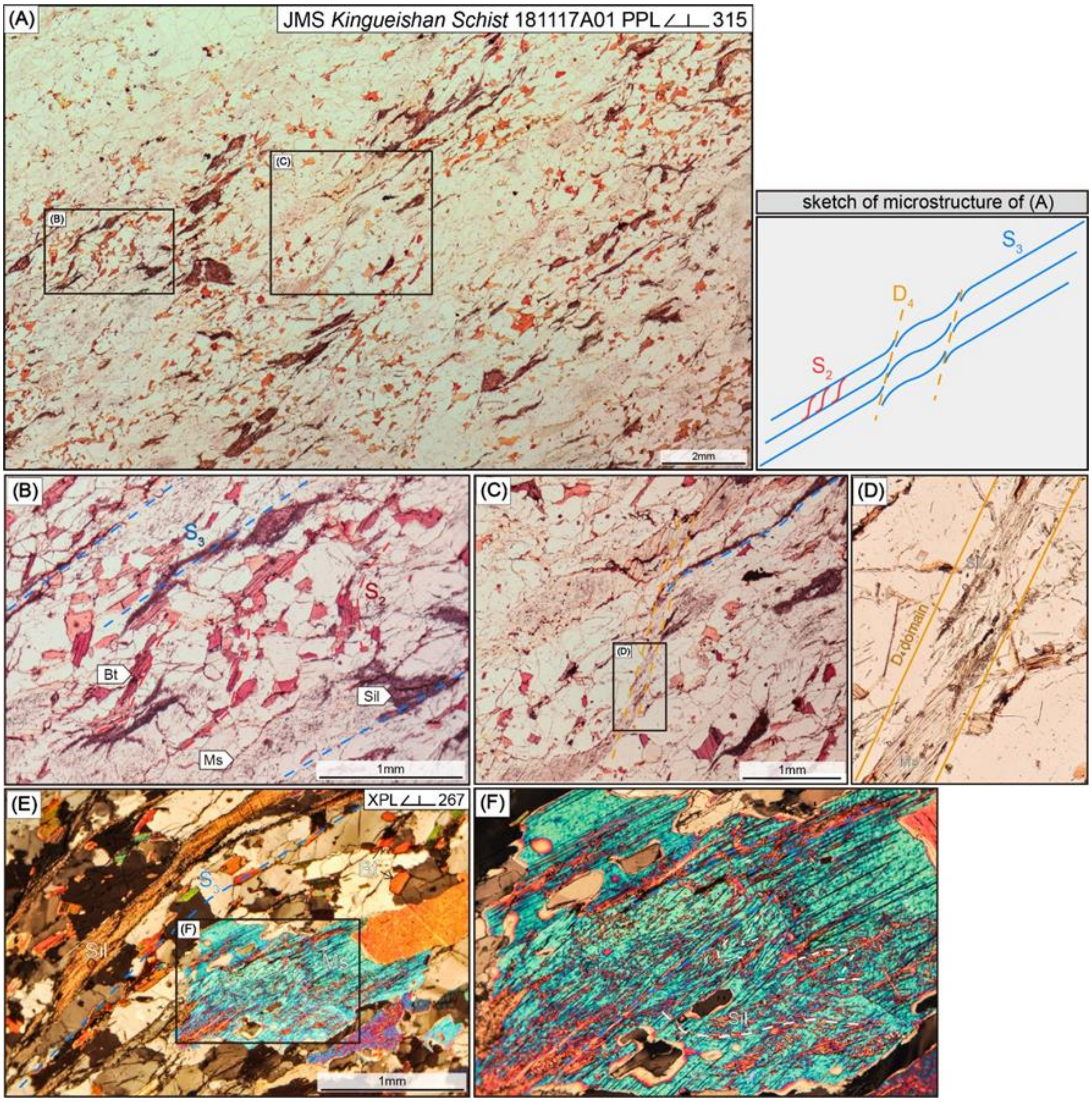

Figure 22. Microphotographs showing microstructures and petrographic relationship of D_2, D_3, D_4 in 181117A01 sillimanite mica schist. (A) Photo with sketch of interpreted foliations showing crosscutting relationships between D_2, D_3 and D_4. (B) S_2 is defined by subhedral biotite folia within the microlithon domain of S_3. (C, D) Weak D_4 fibrolite folia formed where muscovite porphyroblast was sheared. (E, F) Sillimanite inclusion trails within muscovite porphyroblast defining earlier foliation.

doi:10.6342/NTU202202659

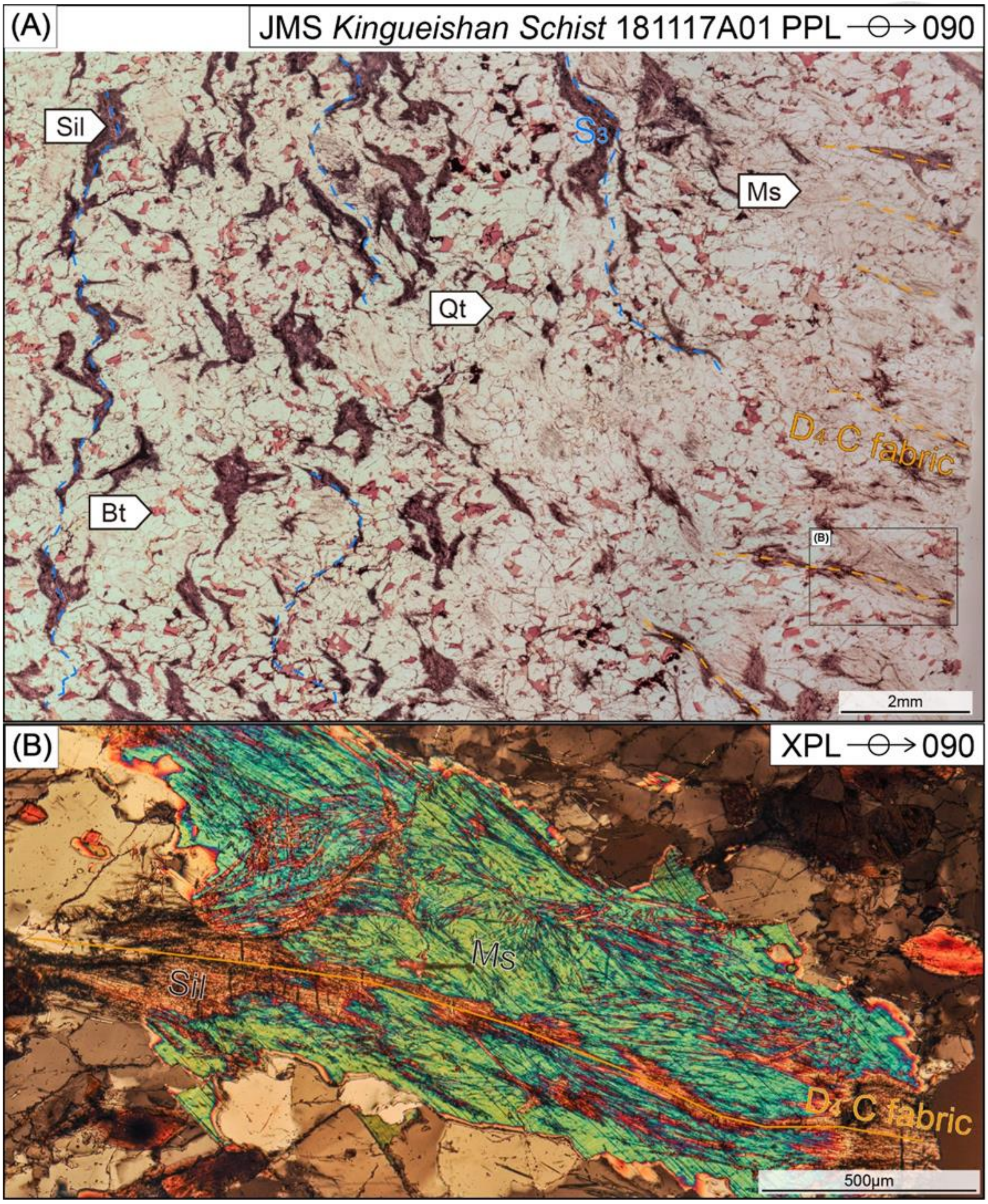

Figure 23. Microphotographs showing microstructures and petrographic relationship of D_3 and D_4 in 181117A01 sillimanite mica schist. (A) Horizontal thin section showing D_4-folded S_3 fibrolite folia. (B) D_4 fibrolite folia formed over muscovite porphyroblast.

doi:10.6342/NTU202202659

4.2.1.2 18LYA01 Sample

The sample was collected from the southeast limb of the D_3 fold at the TGF location (Figure 13B), where D_2 foliation was folded with the D_{3b} shear zone initially developed. From the oriented thin section perpendicular to the L_{3b} mineral lineation, the folded S_2 foliation dips moderately to steeply to the southeast with weak crenulation fibrolite schistosity developing along the fold axial plane (Figure 24A). The L_{3b} mineral lineation is shown as the sillimanite nodules in this vertical thin section. The S_2 is defined by lepidoblastic biotite, which truncates the coarser-grained muscovite porphyroblasts (Figure 24B). Apart from the S_2 biotite folia, a coarser-grained biotite porphyroblast was found crosscutted by muscovite, and small biotite inclusions were identified within the same muscovite grain (Figure 24C). Such microstructures indicate that biotite grew not only during D_2 but also prior to D_2 and the growth of muscovite. The muscovite porphyroblasts are dispersed in the schist without preferred orientation, which suggests that this muscovite formed before D_2. Most muscovite shows breakdown microstructure with overgrown sillimanite and biotite in the vicinity. Also, poikiloblastic K-feldspar with matrix-fabric-aligned biotite inclusions were found in the muscovite broken-down region (Figure 24D). The L_{3b} mineral lineation is defined by sillimanite, suggesting that the sillimanite and K-feldspar were formed during D_3.

doi:10.6342/NTU202202659

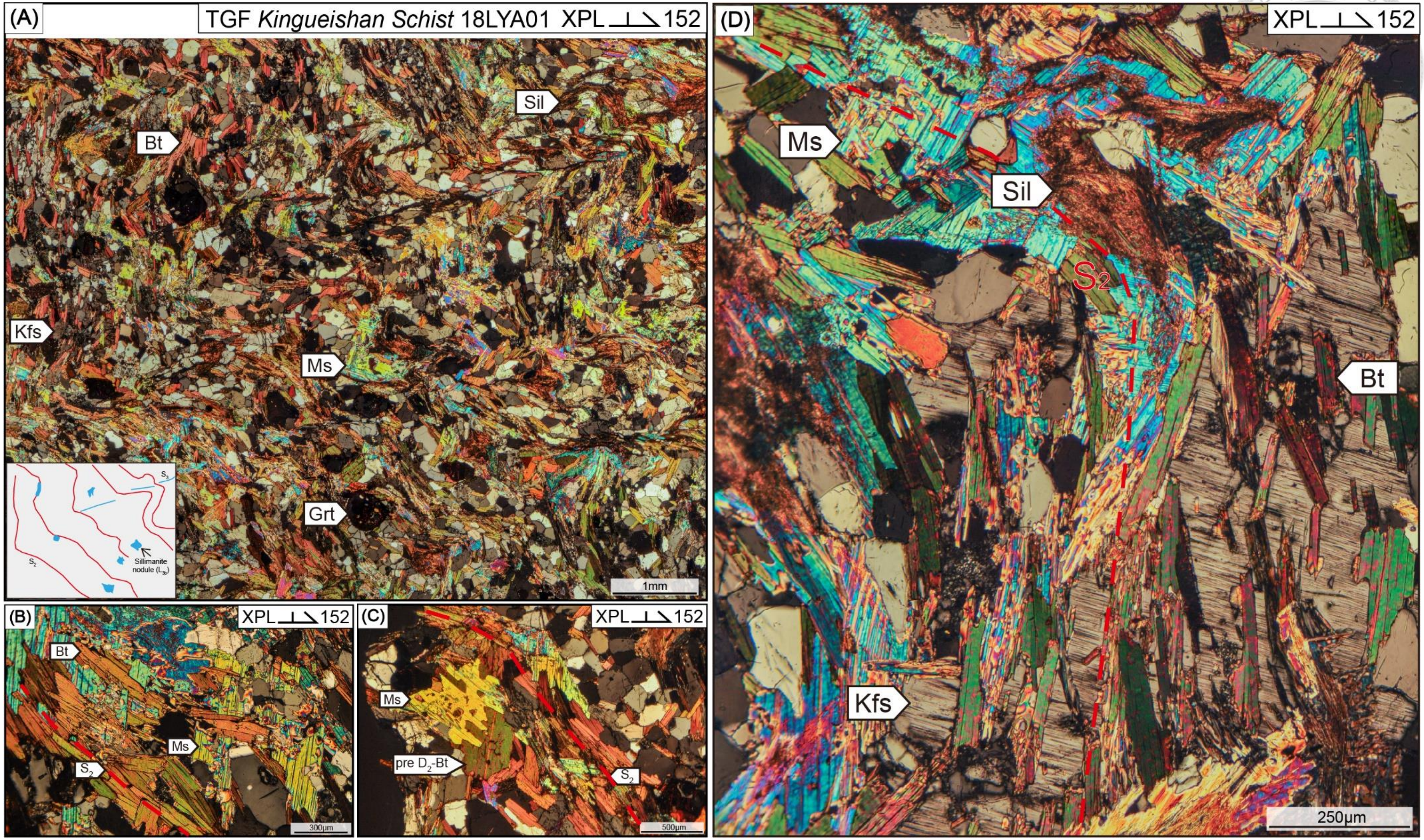

doi:10.6342/NTU202202659

Figure 24. Microphotographs showing microstructures and petrographic relationship of D_2 and D_3 in 18LYA01 sillimanite mica schist. (A) Photo with sketch of interpreted S_2 and S_3 as well as the fibrolite nodules defining L_{3b} mineral lineations. (B) S_2 lepidoblastic biotite folia truncating muscovite porphyroblast. (C) Muscovite porphyroblast grows over pre-D_2 biotite porphyroblast. (D) Muscovite breaks down into sillimanite and poikiloblastic K-feldspar, which encloses the S_2 biotite folia.

4.2.1.3 20LYB11 Sample

The sample was collected from the D_{3b} shear zone at the JMS location. In the oriented thin sections, foliations are dextral S/C fabrics with C fabrics striking NNE-SSW, which moderately dip to the ESE with a normal shear sense. Mineral-concentrated layers are well developed along C fabrics, including quartz, biotite, and sillimanite (Figure 25A, B, C). Sillimanite- and biotite-concentrated layers define the S/C fabrics with quartz filling the microlithon domain (Figure 25B, C). Sillimanite grew as fibrolite over biotite and muscovite (Figure 25D). Apart from the fibrolite defining S/C fabrics, folded inclusion trails of prismatic sillimanite within muscovite were also identified (Figure 25E). Such petrographic evidence suggests sillimanite grew not only during the syn-D_{3b} shearing event but also prior to the growth of muscovite. Despite biotite-concentrated layers defining the S/C fabrics, two generations of biotite are identified based on their orientation, grain size and deformation features. The first generation is the older biotite forming before the D_{3b} shearing event. This biotite has larger grain sizes and was folded and kinked during the D_{3b} shearing event. The second

doi:10.6342/NTU202202659

generation formed during the D_{3b} shearing, which is parallel to the C fabric and grew over the older biotite where the kink formed (Figure 25F).

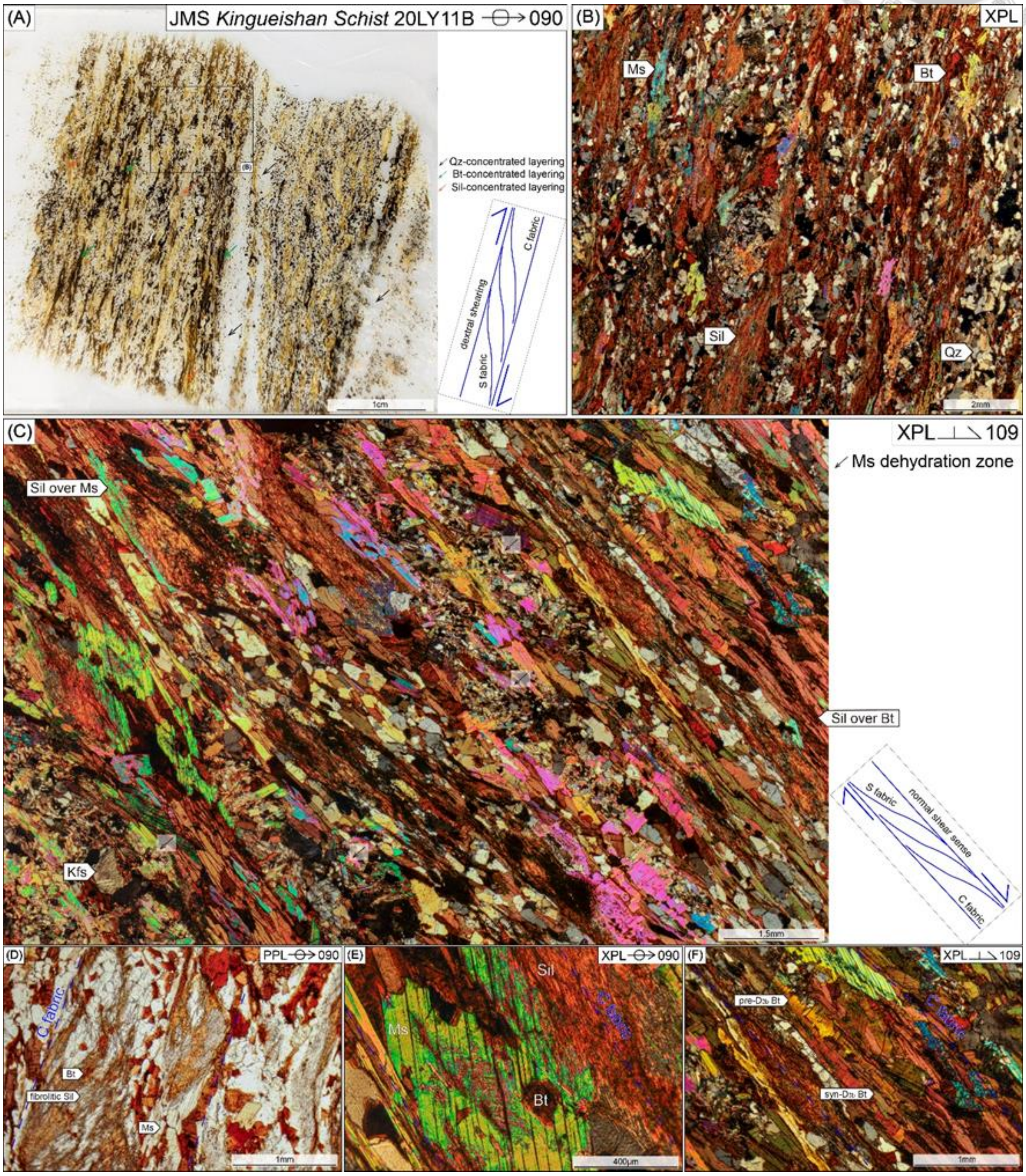

Figure 25. Microphotographs showing microstructural relationship of D_3 in 20LYB11 sillimanite mica schist. (A) Horizontal thin section showing dextral S/C fabrics and mineral concentrated layers. (B) Cross-polarized light image showing part of the figure A. (C) Dextral S/C fabrics showing normal shear sense on the vertical thin section. Also, the muscovite dehydration zone is parallel to the S/C fabrics. (D) Fibrolite grows over both muscovite and biotite with biotite relicts within the fibrolite. (E) Folded inclusion trail of prismatic sillimanite within muscovite porphyroblast, which is truncated by D_{3b} fibrolite folia. (F) Syn-D_{3b} biotite grows over pre-D_{3b} biotite porphyroblast, which is folded during D_{3b}.

doi:10.6342/NTU202202659

4.2.2 Biotite gneiss

18LYB03 biotite gneiss was collected from the D_2 domain at the JG location. Syn-D_2 leucogranite formation was identified in the field, which was boudinaged parallel to S_2 (Figure 26A). The boudinaged leucogranite is mainly composed of Grt + Bt + Pl + Qt + Chl + Ms + Sulfur-bearing opaque mineral. The intergrowth of Grt, Bt, and Pl within the boudin suggests that they were mineral paragenesis in equilibrium during D_2 (Figure 26B). The host biotite gneiss exhibits a simpler mineral assemblage of Bt + Pl + Qt. The major foliation (S_2) is defined by subhedral and anhedral biotites with granoblastic polygonal quartz and plagioclase in the microlithon domain (Figure 26C). Anhedral biotite shows a dehydration melting texture especially near the leucogranite, which suggests that syn-D_2 leucogranite was derived from biotite dehydration melting (Figure 26D, E). Chlorite is identified along the cleavage of biotite, and muscovite forms all along the fractures of plagioclase, which would indicate a retrograde overprint after the peak metamorphism.

doi:10.6342/NTU202202659

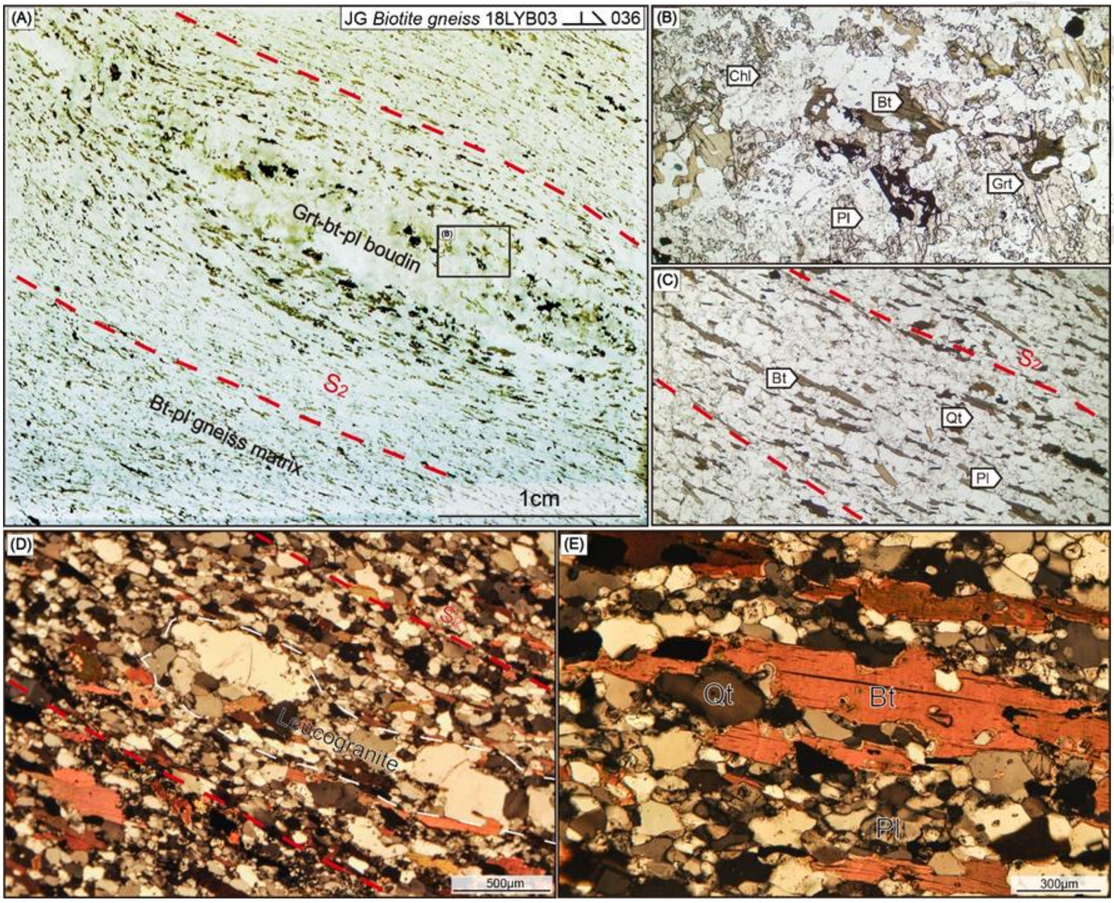

Figure 26. Microphotographs showing microstructures and petrographic relationship of D_2 in 18LYB03 biotite gneiss. (A) Vertical thin section showing Grt-Bt-Pl boudin parallel to the S_2 matrix foliation of the biotite gneiss. (B) Intergrowth of coarse-grained biotite, plagioclase, and garnet within the boudin under PPL. (C) S_2 foliation is defined by mainly subhedral biotite with minor anhedral biotite, granoblastic polygonal quartz and plagioclase in the microlithon domain under PPL. (D) Syn-D_2 leucogranite parallel to S_2 matrix foliation under XPL. (E) Biotite dehydration melting texture with coarsening quartz grains migrating into biotite and fine-grained plagioclase dispersed within the quartz grains under XPL.

doi:10.6342/NTU202202659

4.2.3 Amphibolite

Two amphibolites (sample 18TP01, 18TP04) were collected from the D_{3b} shear zone at the TP location. The major foliation is the sinistral S/C fabrics defined mainly by hornblende (Figure 27A, B, C), which suggests amphibolite facies conditions during the D_{3b} shearing event. Mimetic growth of biotite folia over original hornblende-defining S/C fabrics indicates a P-T change from a hornblende into biotite grade in the end of the D_{3b} shearing (Figure 27B). Besides, a local folding event was identified from the folded D_{3b} C fabric (Figure 27D, E). The folding was accompanied by a breakdown of hornblende into epidote along the fold axial plane (Figure 27E), which indicates a retrograde path from amphibolite facies into epidote-amphibolite facies conditions. Granoblastic polygonal plagioclase and quartz fill the microlithon domain (Figure 27C, E), which suggests sustained high temperature conditions (>450 °C) for static recrystallization after the D_{3b} shearing.

doi:10.6342/NTU202202659

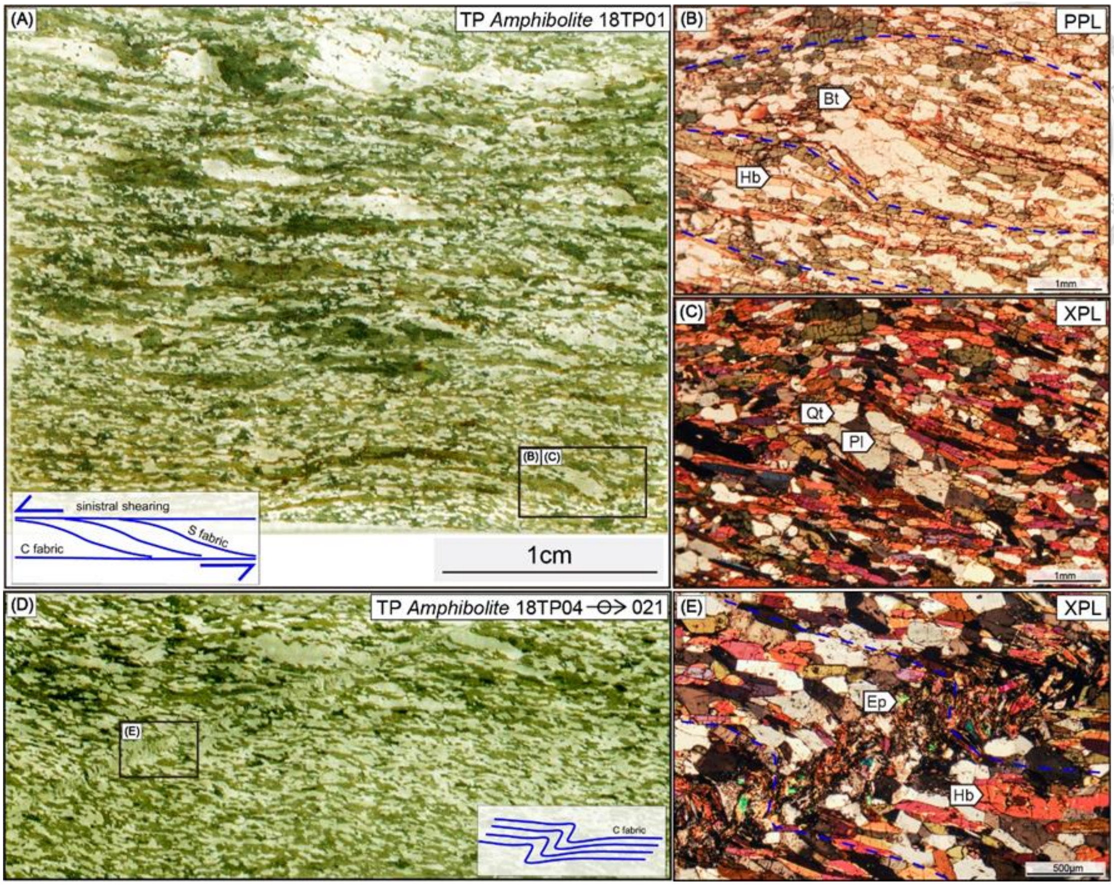

Figure 27. Microphotographs showing microstructures and petrographic relationship of D_{3b} in amphibolite (sample 18TP01, 18TP04). (A) Scanning photo of 18TP01 XZ plane thin section with sketch of sinistral S/C fabrics. (B) Sinistral S/C fabrics are defined by euhedral to subhedral hornblende, which are grown over by mimetic biotite along the S/C fabrics. (C) Granoblastic polygonal quartz and plagioclase fill the microlithon domain. (D) Scanning photo of 18TP04 horizontal thin section with sketch of folded D_{3b} C fabrics. (E) Hornblende is broken down into epidote along the fold axial plane.

doi:10.6342/NTU202202659

4.2.4 Tonalitic gneiss

One tonalitic gneiss sample (18TP04) was collected from the D_{3b} shear zone at the TP location. The major foliation is sinistral S/C fabrics defined by concentrated hornblende and quartzofeldspathic layering (Figure 28A). In the thin section, coarse- and fine-grained compositional layering define the S/C fabrics (Figure 28B). Coarse-grained layering is composed of concentrated anhedral hornblende, quartz ribbon and anhedral K-feldspar of grain boundary migration, subhedral plagioclase and a few biotite. Fine-grained layering consists of granoblastic polygonal quartz and plagioclase with a few subhedral resorbed biotite relicts. Such a microstructure relationship suggests that the compositional differentiation was developed during the shearing. Quartz and feldspar suffered from the strongest grain size reduction during the shearing, while hornblende remained undeformed and became concentrated when quartz and feldspar dissolved and reprecipitated. The grain boundary migration of quartz and K-feldspar into hornblende along with the anhedral shape suggest that hornblende was dissolved during the shearing event (Figure 28C).

doi:10.6342/NTU202202659

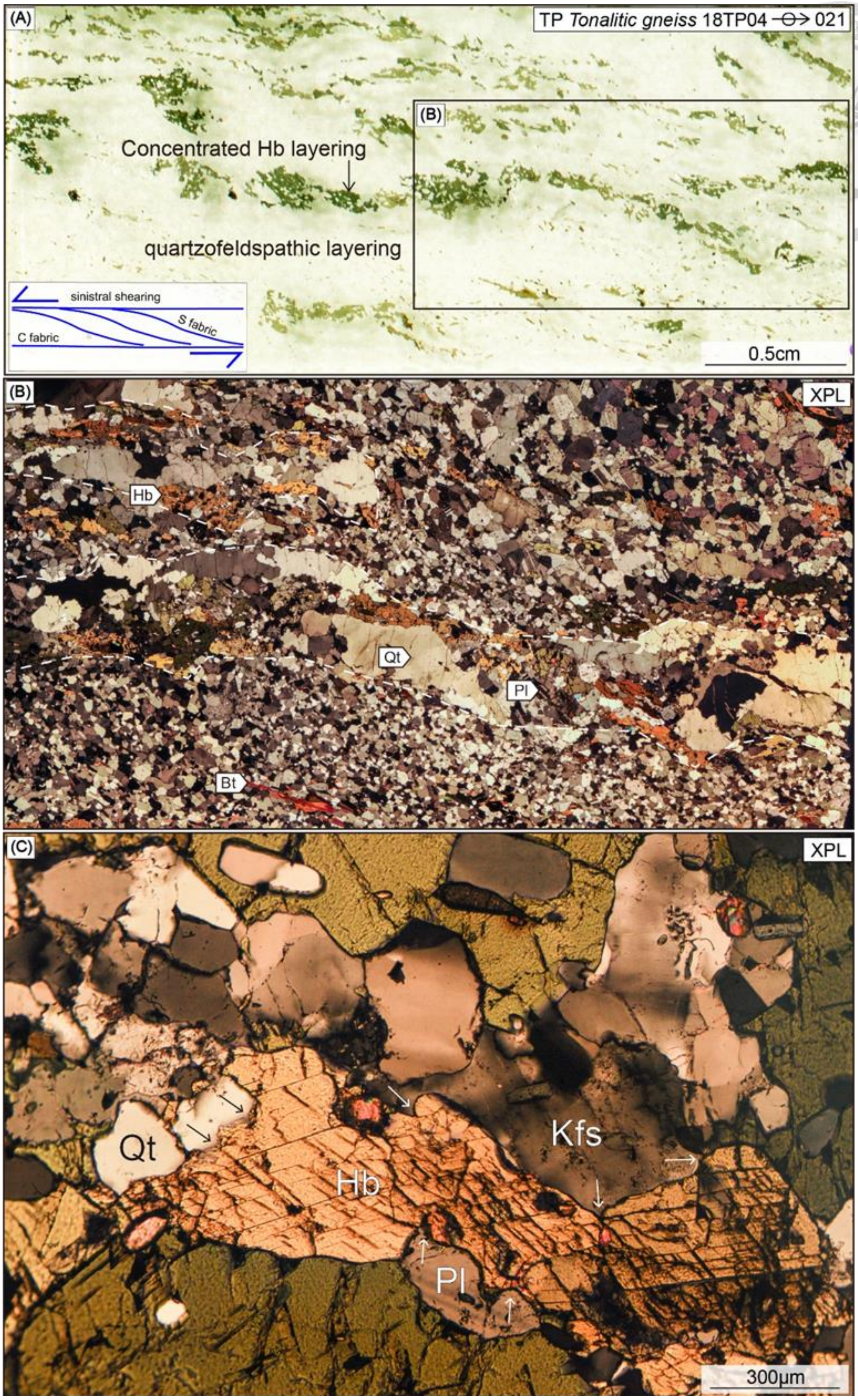

Figure 28. Microphotographs showing microstructures and petrographic relationship of D_{3b} in tonalitic gneiss (sample 18TP04). (A) Scanning photo of 18TP04 horizontal thin section with sketch of sinistral S/C fabrics. The hornblende-concentrated and quartzofeldspathic layering is parallel to the S/C fabrics. (B) The coarse-grained layering is circled by white dashed line, which is parallel to the matrix foliation. (C) Grain boundary migration of quartz and feldspar into hornblende as indicated by the arrows.

doi:10.6342/NTU202202659

4.2.5 Summary

Based on microstructural and petrography analysis from seven samples, the relationship between metamorphic mineral growth and deformation events of Kinmen Island can be summarized in Figure 29.

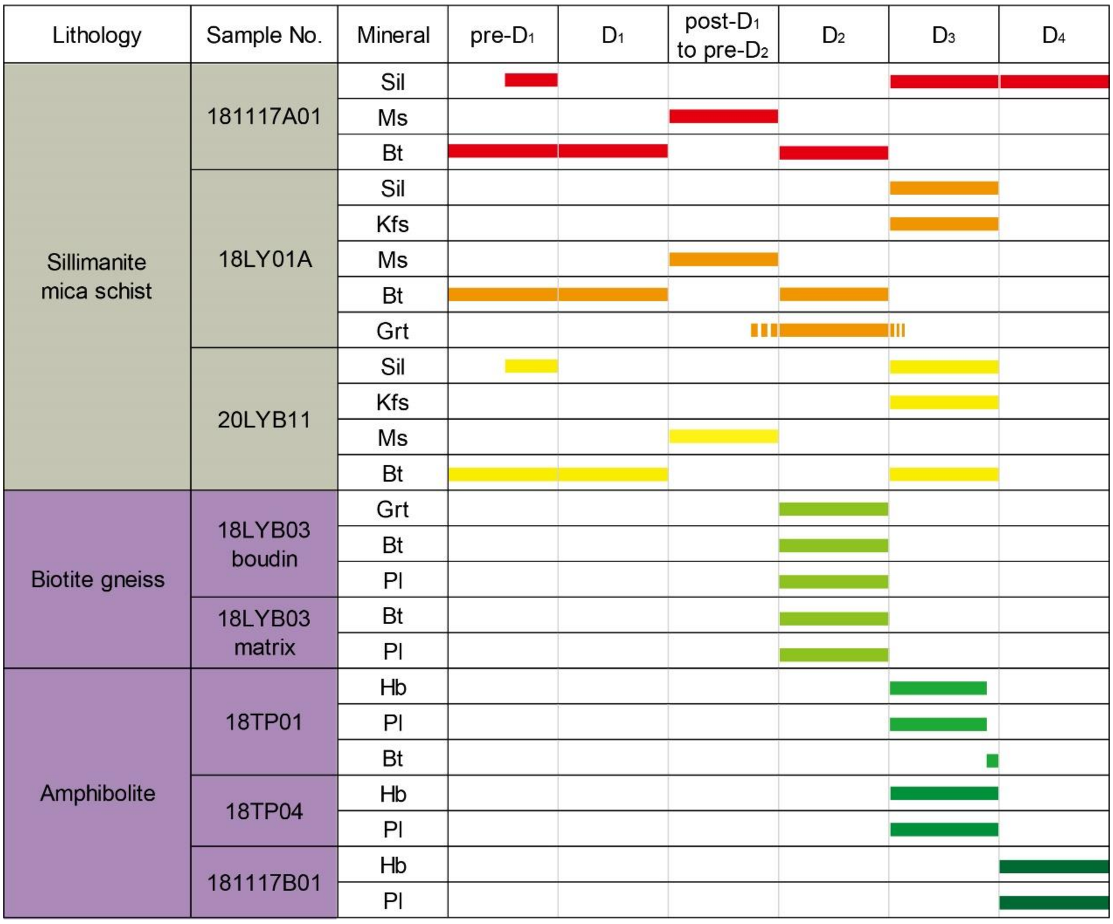

Figure 29. Relationship between metamorphic mineral growth and deformation events. The shaded colors beneath the lithology and sample number corresponds to the lithological unit on the geological map (green: Kingueishan Schist; purple: Chenggong Tonalite). Each color represents one rock sample, and the length of the color bar stands for the possible duration of the mineral growth. Sample 181117B01 is compiled from Huang and Yeh (2020). The mineral abbreviation is as follows: Sil-sillimanite; Ms-muscovite; Bt-biotite; Kfs-K-feldspar; Grt-garnet; Pl-plagioclase; Hb-hornblende.

doi:10.6342/NTU202202659

4.3 Mineral Chemistry

The BSE images marked with the positions of analytical spots are provided in the Appendix 8.4. The calculated mineral chemistry results are classified into three categories, including “best”, “acceptable” and “not good”, based on the reference values from Deer et al (2013), which is compiled in the Appendix 8.5. If the measured major element compositions (wt.%) and the calculated mineral formula (apfu) nearly fall in the range of the reference values, these data belong to “best”, and are considered to be reliable. If only the total wt.% is a little lower than the reference value with other measurement and calculation results in the range, these data are “acceptable”. If the calculated mineral formula is in acceptable range yet with measured wt.% out of the reference values, these data fall into “not good”. The reason for using the “not good” data is because the calculated result of the mineral formula is in the acceptable range. As long as such data are not utilized for calculation involving the absolute values like wt.%, they can still be used for ratio calculation (e.g., end-member compositions). All the analytical and calculation results of the mineral chemistry are summarized in Appendix 8.5 and will be discussed in the following sections.

doi:10.6342/NTU202202659

4.3.1 18LYA01 Sillimanite Mica Schist

Feldspar

Feldspars include both alkali feldspars and plagioclase feldspars (Figure 30A). Alkali feldspars are all K-feldspars, yet with large composition variations from Or_{93} to Or_{49}. Most of the K-feldspar have compositions ranging from Or_{93} to Or_{86}. Plagioclase feldspars include albite and oligoclase compositions. Petrographically, K-feldspars are coarse-grained poikiloblasts growing as muscovite breaks down into sillimanite (Figure 24D & Figure 30B). Nearby these high-temperature metamorphic K-feldspars, fine-grained anhedral plagioclase and clay-like minerals grow together and replace the K-feldspars (Figure 30B). Accordingly, the high-temperature metamorphic K-feldspars (Or_{93} to Or_{86}) become more sodium rich (Or_{78} to Or_{49}) during the growth of albite and clay-like minerals in the low-temperature environment. Such a reaction of K-feldspars into albite and clay-like minerals requires a Na-rich fluid to induce hydrolysis of K-feldspar, which is a chemical weathering reaction occurring at the surface.

doi:10.6342/NTU202202659

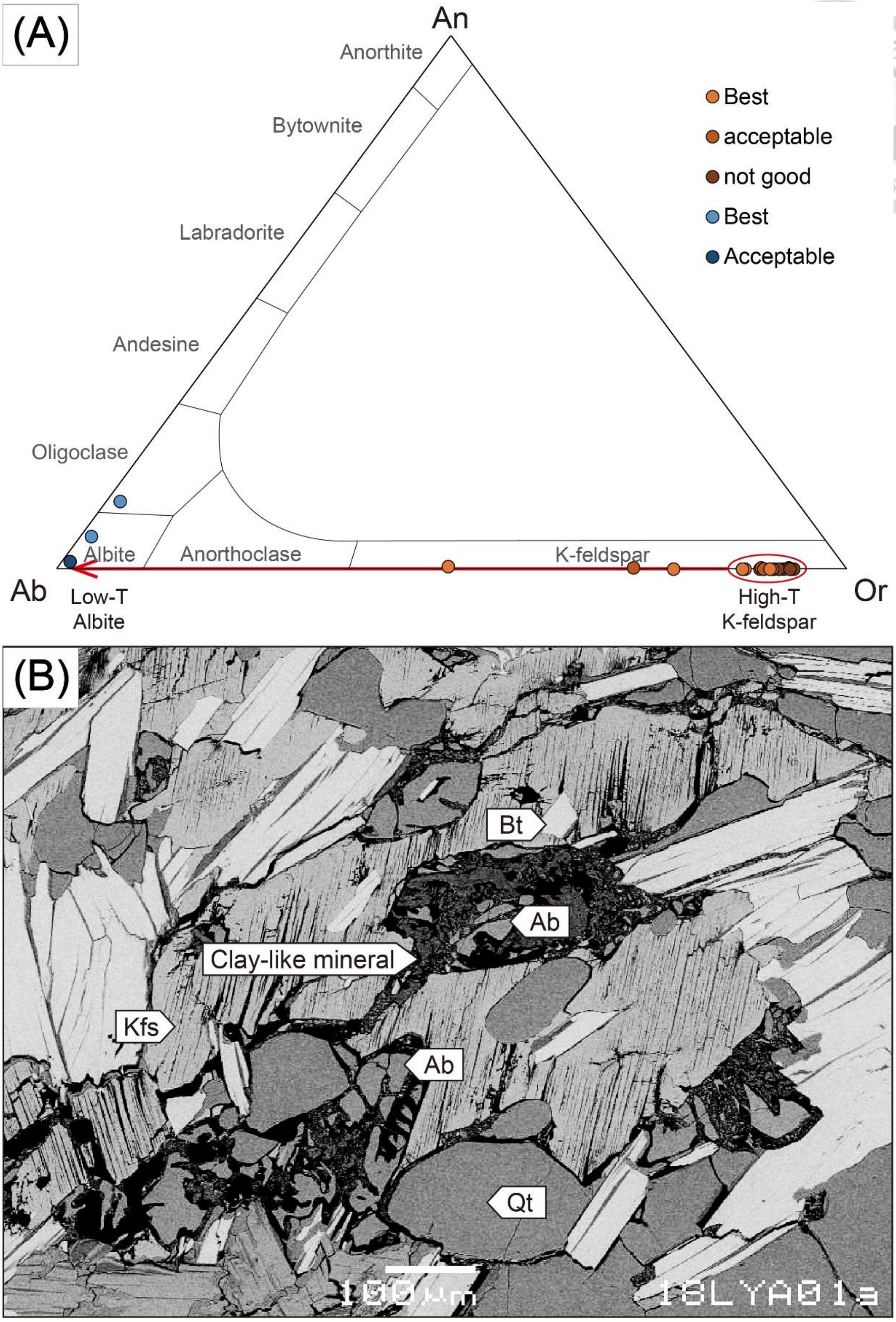

Figure 30. Feldspar composition and SEM-BSE image showing mineral relationship of feldspar in sample 18LYA01. (A) Ternary composition diagram for feldspar classification (Harrison et al., 2019) with the red arrow showing the interpreted compositional change from high-temperature K-feldspar into low-temperature albite. (B) K-feldspar poikiloblast with multiple biotite inclusions, which is replaced by anhedral albite and clay-like mineral.

doi:10.6342/NTU202202659

Biotite

The biotites measured are matrix S_2 biotite folia, which is folded during D_3. Low Al_{total} contents (3.58-3.85 apfu) and its closeness to 2 suggests that these biotites are close to the annite-phlogopite solid solution series, $K_2(Fe^{2+},Mg)_6[Al_2Si_6O_{20}](OH)_4$. Along with a slightly high X_{Fe} ratios (0.64-0.68), these biotites are close to annite compositions (Figure 31A). A certain degree of substitution of Al^{VI} (0.91-1.12) for Fe^{2+}+Mg in octahedral sites shows that Tschermak substitution occurs between the siderophyllite and annite solid solution series (Figure 31B). The limited ranges of measured major element compositions except for Ti and the finite X_{Mg} values of 0.32-0.35 show their quite homogenous compositions, which suggests that these biotites formed in one metamorphic episode. However, the concentrations of Ti vary a lot from 0.22 to 0.38 apfu. Ti substitution into an octahedral site of biotites is temperature sensitive and favors higher temperatures. Thus, such a Ti variation indicates local equilibrium or re-equilibration of biotite chemistry, which could be the older lower temperature records, re-equilibrated temperatures by later events, or the local heterogeneity of chemical equilibrium. The Ti variation does not show any pattern with the microstructures or selected regions within biotite grains. Thus, local heterogeneity of chemical equilibrium may have occurred in the sample.

doi:10.6342/NTU202202659

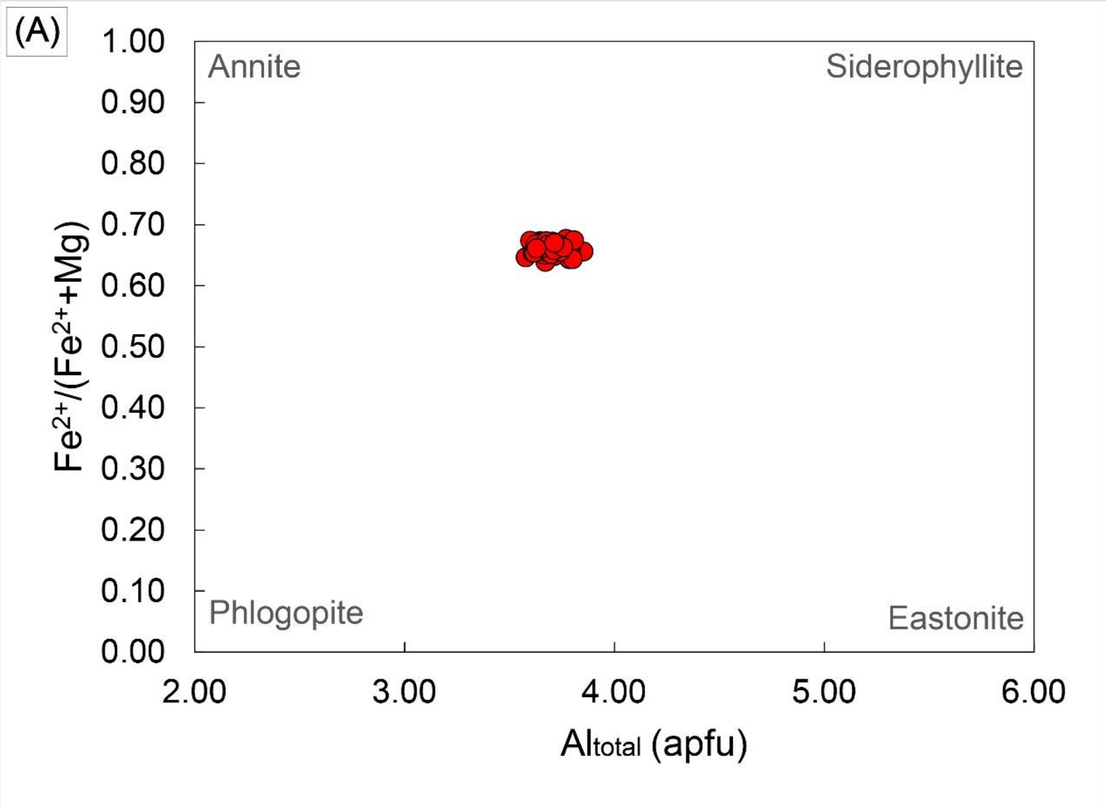

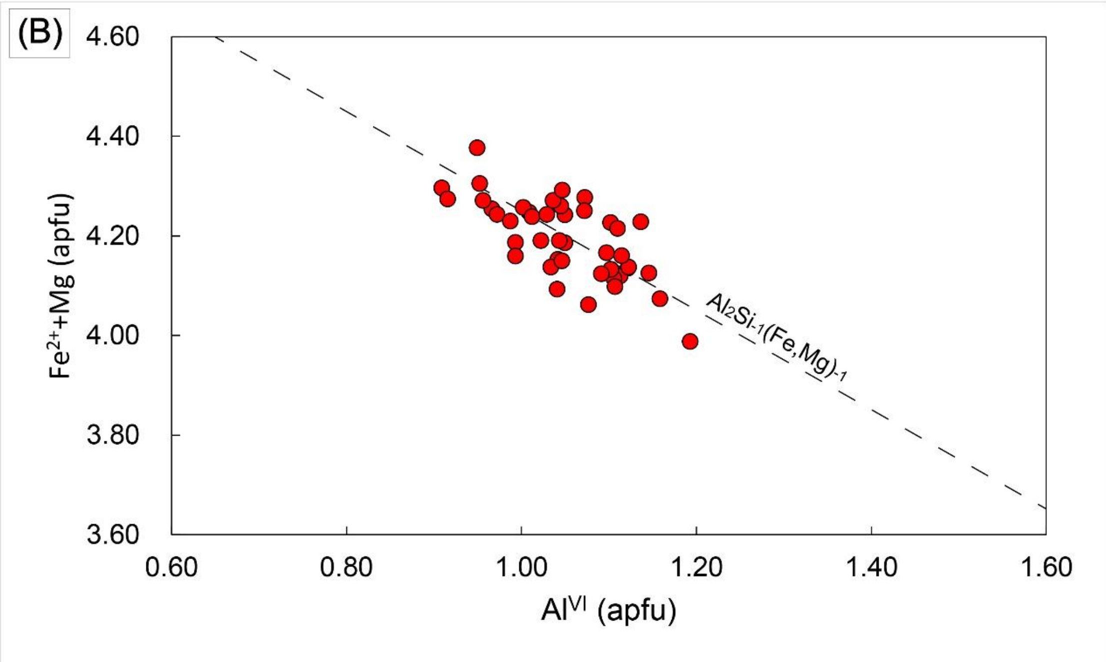

Figure 31. Plots of chemical composition of biotite from sillimanite mica schist (sample 18LYA01). (A) Classification diagram for biotite (Wlodek et al., 2015). (B) Divalent cations (Fe, Mg) plotted against Al contents in octahedral sites to show Tschermak substitution within the biotite.

doi:10.6342/NTU202202659

Muscovite

Muscovites are coarse-grained porphyroblasts with decussate texture in sillimanite mica schist, which can grow intertectonically between D_1 and D_2. The limited and very low Na/Na+K (0.08-0.10) and Fe^{2+}+Mg/Fe^{2+}+Mg+Ti+Al^{VI} (0.04-0.05) values show almost no paragonite and caledonite composition. The low Si/Al ratios (mostly 1.05-1.07 with one 1.12) excludes phengite composition. The lack of phengite composition indicates that muscovite does not crystallize at high-pressure conditions (Deer et al., 2013). On the plot of Si+Fe^{2+}+Mg vs. Al^{VI} (Figure 32), muscovite roughly follows the Tschermak substitution line with Al^{VI} contents higher than the sillimanite and sillimanite + K-feldspar zone described by Duke (1994). Such high Al^{VI} (3.74-3.85), low Si (6.04-6.11) and low Fe^{2+}+Mg (0.17-0.23) contents suggests that these muscovites were formed under high-grade metamorphic conditions (Duke ,1994; Deer et al., 2013). The sustained sillimanite growth from the inclusion trails within these muscovite porphyroblasts and the fibrolite folia crosscutting these muscovites supports the longstanding sillimanite grade, when these muscovites formed. The limited major element compositions infer that this muscovite formed in similar P-T conditions, except for No. A35 having higher Si contents expressed as an outlier in Figure 32, which needs more analysis to confirm.

doi:10.6342/NTU202202659

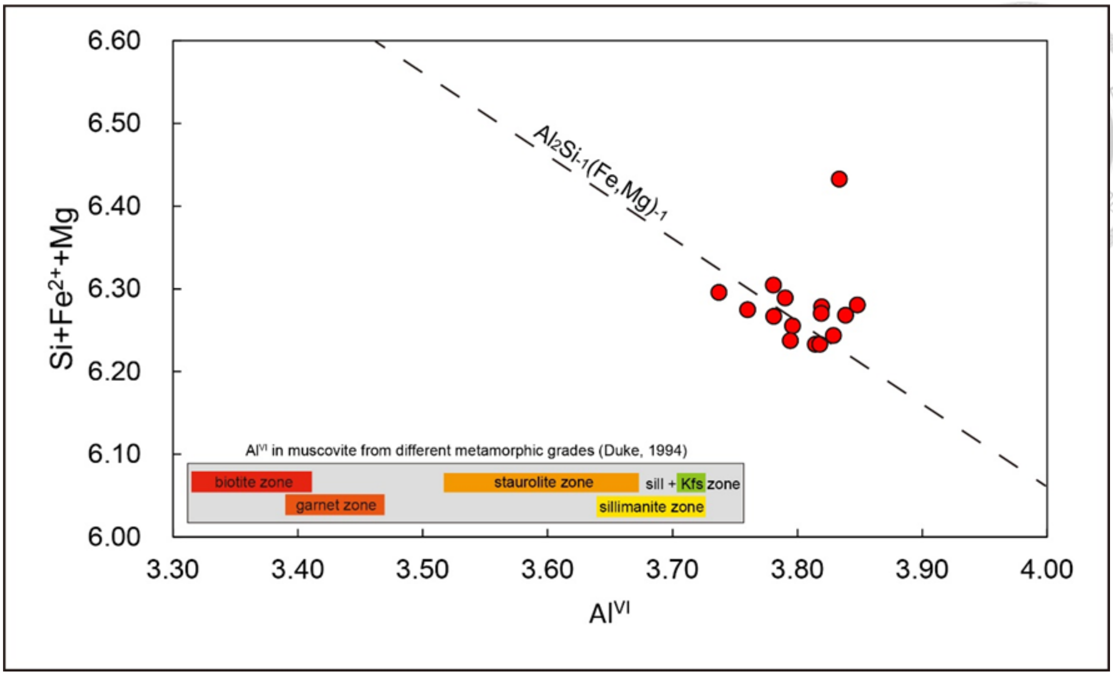

Figure 32. Plot of Al^{VI} vs. $Si+Fe^{2+}+Mg$ based on 22 oxygens of muscovite of sample 18LYA01. The dashed line is the Tschermak substitution line ($Al_2Si_{-1}(Fe,Mg)_{-1}$). The Al^{VI} contents in muscovite from different metamorphic grades (Duke, 1994) are shown for comparison with different color bars representing different metamorphic zones.

Garnet

Garnets appear in a concentrated zone oblique to all the foliations and lineations in the sillimanite mica schist. This garnet-rich zone is subparallel to the L_{3b} mineral lineation defined by fibrolite. Local distribution within the schist suggests their possible origins of original compositional layering, crystallization from the melt or other intricate nucleation and/or metamorphic differentiation mechanisms. In thin sections, most garnets exhibit an inclusion-rich core, a comparatively inclusion-free rim and a strongly altered Fe-rich crust (Figure 33). Accessory minerals dominate the inclusions including ilmenite, apatite, and zircon with minor biotite, a few quartzes and

doi:10.6342/NTU202202659

aluminosilicate. These inclusion-rich garnets show complex internal patterns from foliation free, simple orientation to folded inclusion trails. Such complex inclusion trail orientations along with the wrapping of L_{3b} sillimanite lineation around the garnet porphyroblasts indicate that these garnets formed before D_3. The inclusion trail patterns are also different from the S_2 biotite folia, which suggests that these internal foliations are earlier deformation fabrics with respect to S_2 (probably S_1). The direct contact between the S_2 biotite folia and garnet porphyroblasts implies their growth in the same period. Accordingly, these garnet porphyroblasts grew at least from S_1 to S_2.

Five transects of chemical analyses were conducted on three garnet grains (Grt1, Grt2, Grt3; Figure 34). The line profiles are composed of multiple point analyses with a 10-μm distance between the points. The data reduction is done excluding the total wt. % values out of 99.00-102.00 wt.%. These three garnet grains have similar major chemical compositions, and all fall within almandine compositional ranges (Grt1: $Alm_{70\text{-}76}Py_{8\text{-}10}Sp_{11\text{-}19}Gro_{2\text{-}5}$; Grt2: $Alm_{72\text{-}77}Py_{7\text{-}10}Sp_{11\text{-}16}Gro_{3\text{-}5}$; Grt3: $Alm_{72\text{-}75}Py_{7\text{-}10}Sp_{11\text{-}16}Gro_{3\text{-}5}$). Almost no compositional zoning is identified for the major elements (Fe, Mg, Ca) of garnets except for the increase of Mn in the rim (Figure 34). Such relatively homogeneous composition of Fe, Mg and Ca of garnets with a Mn-rich rim are also identified in the line profile analysis. However, some subtle chemical variations are noted. Grt1 has a core of homogenous composition ($Alm_{74\text{-}76}Py_{9\text{-}10}Sp_{11\text{-}12}Gro_{3\text{-}5}$) with a

doi:10.6342/NTU202202659

Mn-rich rim ($Alm_{70-75}Py_{8-9}Sp_{12-19}Gro_{2-5}$). The increase of spessartine composition from Sp_{11-12} to Sp_{19} is accompanied by a slight decrease of almandine content to Alm_{70-72} with a subtle decrease of pyrope and grossular content of 0.01 mol. %. Grt2 has a relatively homogenous compositional profile than Grt1. The core composition is $Alm_{74-77}Py_{7-10}Sp_{11-13}Gro_{3-5}$, and the rim is $Alm_{72-74}Py_{8-9}Sp_{13-16}Gro_{3-5}$. The same pattern of spessartine content increase (Sp_{11-13} to Sp_{16}) and almandine content decrease (Alm_{74-77} to Alm_{72}) is identified with pyrope and grossular compositions remaining constant. Grt3 has an asymmetric compositional profile with only one side of the rim showing Mn increase. The homogenous part exhibits composition of $Alm_{73-75}Py_{7-9}Sp_{11-14}Gro_{4-5}$, and the rim has $Alm_{72-73}Py_{9-10}Sp_{14-16}Gro_{3-4}$. Grt3 shows hardly any compositional variations of almandine, pyrope and grossular compositions except for an increase of spessartine content from Sp_{11-14} to Sp_{16}. In summary, these garnet porphyroblasts have quite homogenous core compositions of $Alm_{73-77}Py_{7-10}Sp_{11-14}Gro_{3-5}$. The rim shows mainly spessartine content increase to Sp_{14-19} and a slight almandine content decrease to Alm_{70-73} with pyrope and grossular content remaining the same.

The bell shape of Mn zoning is very common in metamorphic garnets (Tracy et al., 1976). Such compositional zonation is due to slow element diffusion rates which hinders chemical homogenization, especially in the medium-grade metamorphism. However, garnets in this sample show a flat compositional profile in the core with a

doi:10.6342/NTU202202659

Mn-rich rim (Figure 35A). The flat compositional profile indicates that the garnets experienced diffusional modification to homogenize the chemical compositions, which requires elevated temperatures (>600 °C) under high-grade metamorphic conditions (Yardley, 1977; Nyström and Kriegsman, 2003; Tirone and Ganguly, 2010; Deer, 2013). An increase of Mn contents toward the rim suggests a retrograde condition during garnet growth following the peak metamorphism (Tracy et al., 1976). On the plot of CaO+MnO vs. FeO+MgO (Nandi, 1967; Sturt, 1962), garnet compositions change from close to the sillimanite zone in the core to the kyanite zone in the rim (Figure 35D). Combined with the microstructures, the garnet core should form during the folding of S_1 foliation and development of S_2 biotite folia. A retrograde rim could have formed during the D_3 event, and probably was caused by garnet-melt back reaction due to muscovite dehydration melting (Nyström and Kriegsman, 2003).

doi:10.6342/NTU202202659

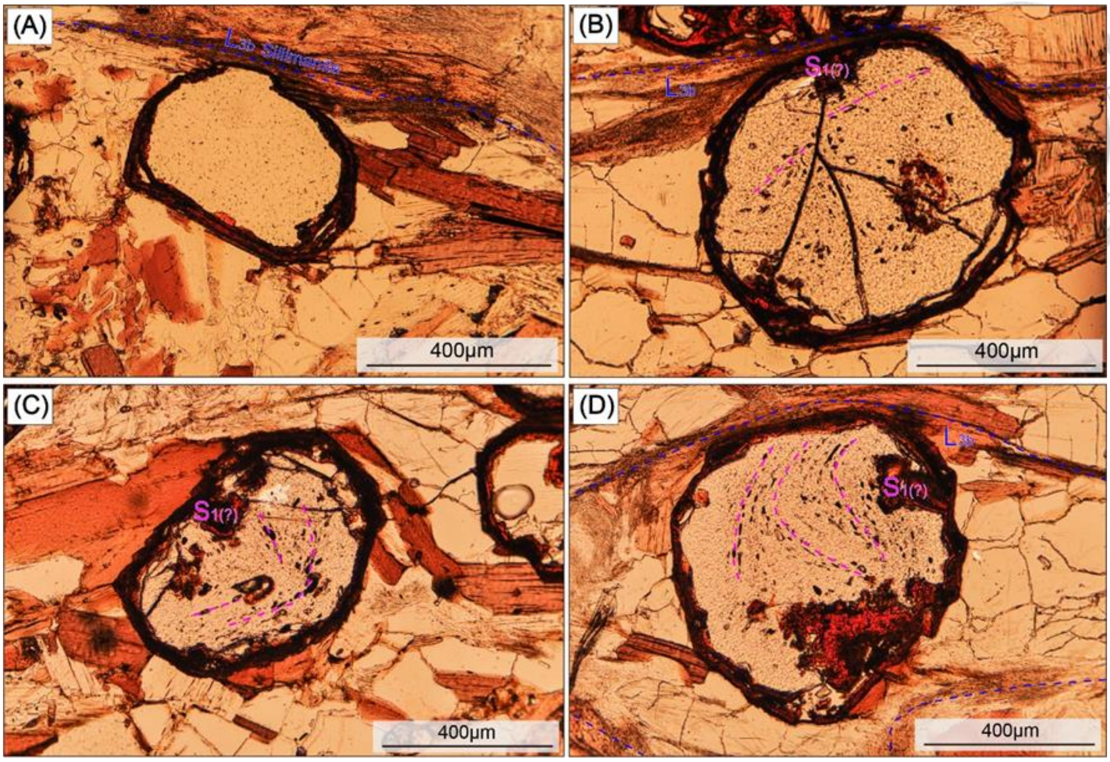

Figure 33. Microphotographs of sillimanite mica schist (sample 18LYA01) showing complex inclusion patterns within garnet porphyroblasts under plane-polarized light. The thin section is a vertical plane parallel to L_{3b} mineral lineation defined by fibrolite. (A) An inclusion rich garnet without internal foliation. (B) A garnet grain with weak to no inclusion trail alignment. (C) A garnet porphyroblast with folded inclusion trail. The inclusion trail orientation is different from the matrix S_2 biotite folia and L_{3b} fibrolite, which indicates that the internal foliation is older deformation fabric, and probably is S_1. The direct contact of the matrix S_2 biotite with the garnet implies that garnet and biotite grew in the same period. (D) A folded inclusion trail within a garnet porphyroblast. The wrapping of fibrolite around the garnet suggests that the garnet formed before the sillimanite formation.

doi:10.6342/NTU202202659

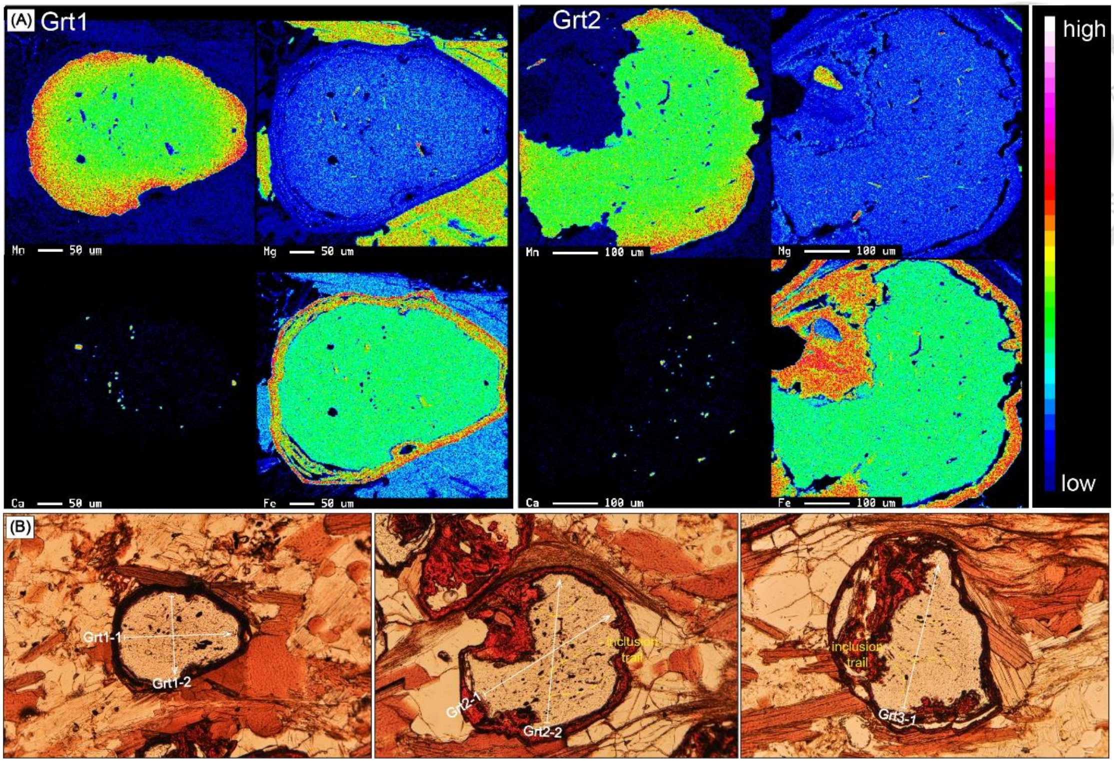

Figure 34. Three garnet grains (Grt1, Grt2, Grt3) in sillimanite mica schist (sample 18LYA01) with EPMA chemical mapping and line profile analysis. (A) Chemical mapping of divalent major element (Mn, Mg, Ca, Fe) distribution in Grt1 and Grt2. (B) Locations of line profile analyses in three garnet grains. The arrow indicates the moving direction of the analytical spots.

doi:10.6342/NTU202202659

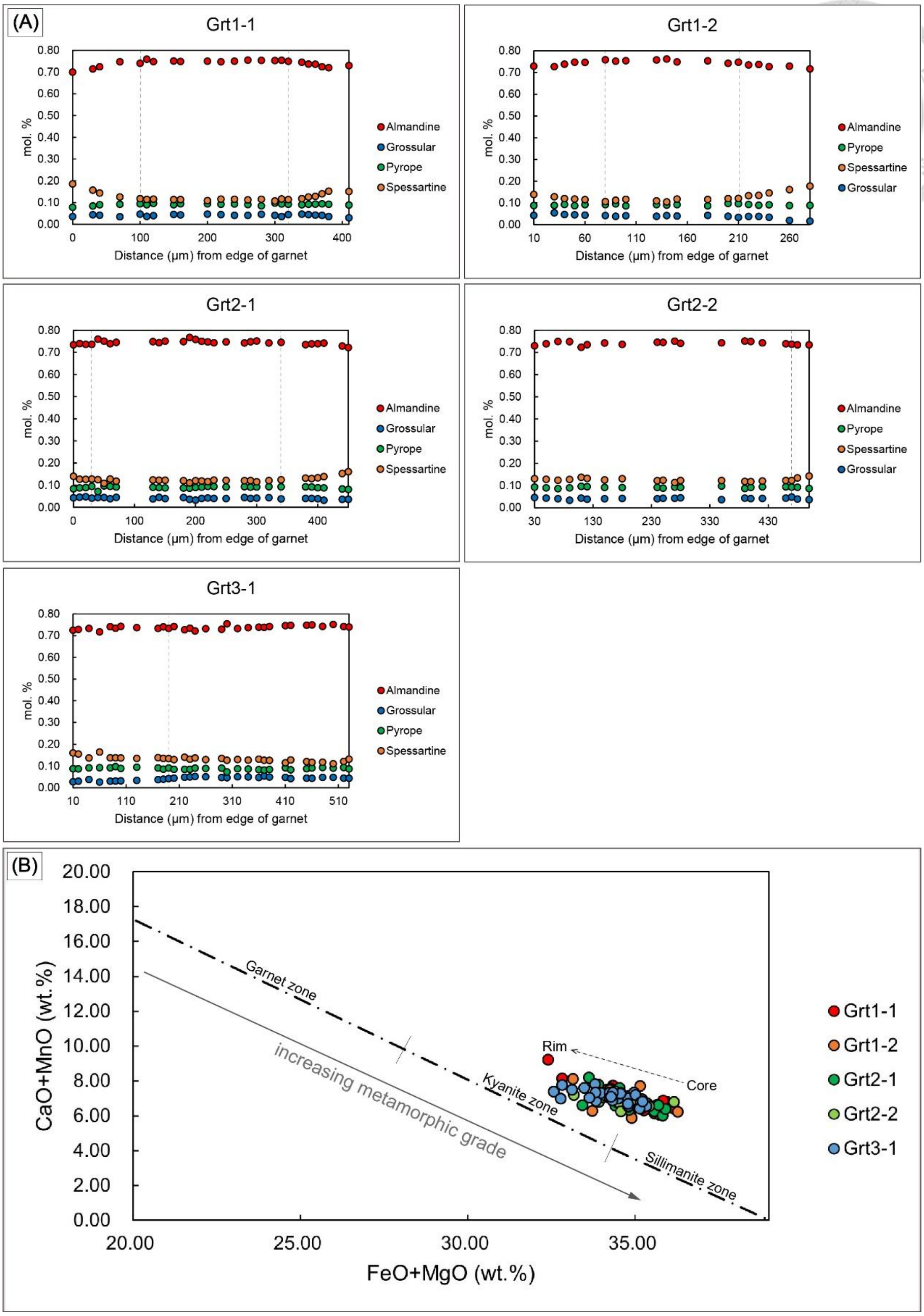

Figure 35. Garnet compositional profiles and variations of (FeO+MgO) with (CaO+MnO) in garnets from different metamorphic grades (Nandi, 1967). The garnets are from sillimanite mica schist (sample 18LYA01). (A) Garnet compositional profiles with gray dashed lines marking the interpreted boundaries between the core and the rim. The discontinuous line profile is due to the exclusion of bad-quality data with total wt.% out of 99-102 wt.%. (B) The gray dashed line with arrow shows the compositional change from garnet core toward rim.

doi:10.6342/NTU202202659

4.3.2 181117A01 Sillimanite Mica Schist

Biotite

The biotites in this sample are subhedral to anhedral in matrix residing within the microlithon domain of the D_3 fibrolite folia (Figure 22A). The closeness of Fe^{2+}+Mg (3.89-4.64 apfu) values to 4 shows that these biotites are close to siderophyllite-eastonite solid solution series, $K_2(Fe^{2+},Mg)_4Al_2[Al_4Si_4O_{20}](OH)_4$. However, due to relatively lower Al_{total} contents (3.27-3.58 apfu) along with the high X_{Fe} ratios (0.69-0.74), these biotites are close to annite compositions (Figure 36A). A certain degree of substitution of Al^{VI} (0.72-1.06) for Fe^{2+}+Mg in octahedral sites reveals that Tschermak substitution occurs between the siderophyllite and annite solid solution series (Figure 36B). Aside from the chemical variation due to Tschermak substitution, Ti contents (0.21-0.37) also vary a lot. No clear patterns of Ti variation with their microstructural domain or selected regions within biotite grains are identified. Hence, local heterogeneity of chemical equilibrium might be responsible for the variation of chemical composition. Such single biotite species and confined major element ranges suggests that these biotites were formed in one metamorphic episode.

doi:10.6342/NTU202202659

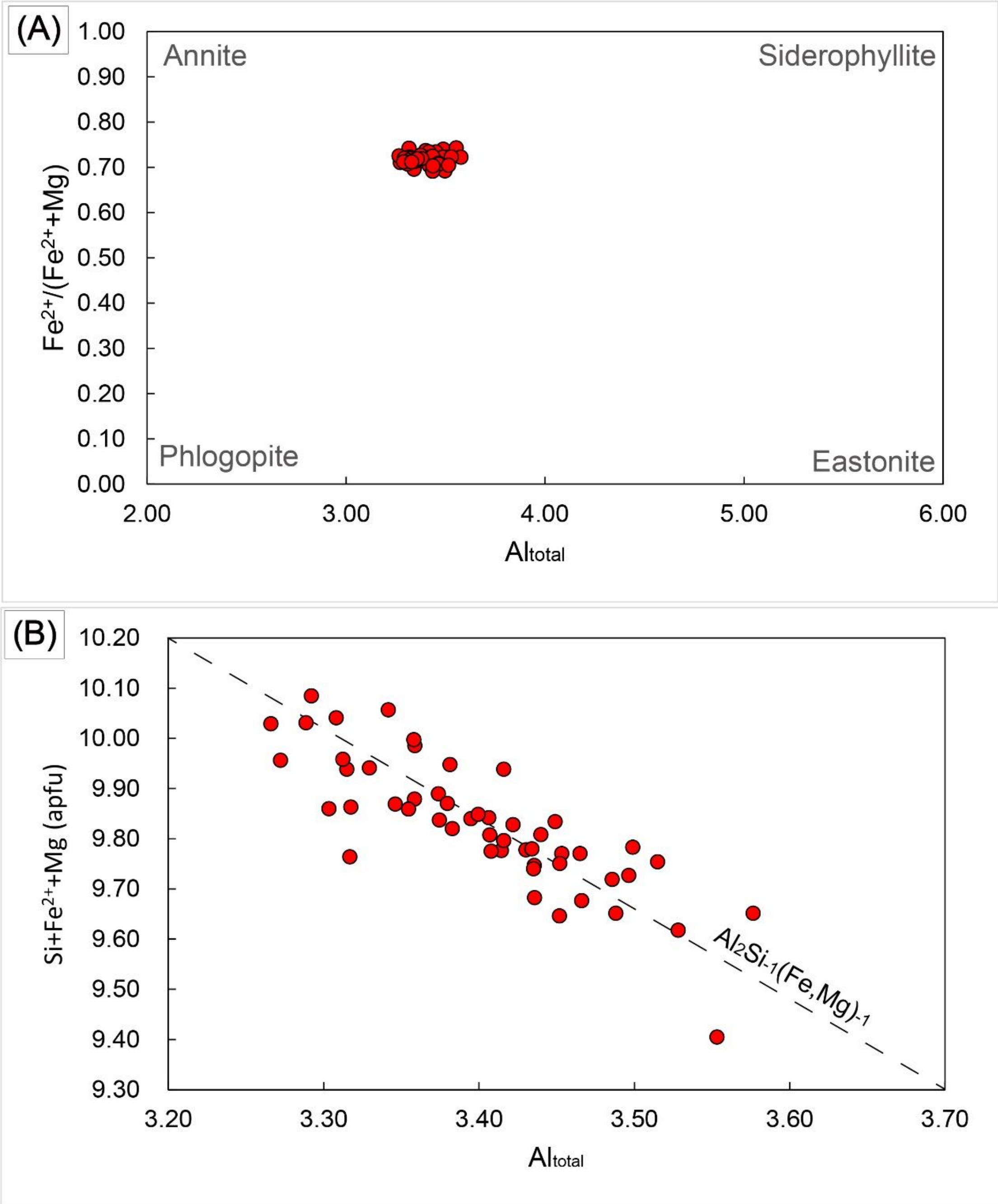

Figure 36. Plots of chemical composition of biotite from sillimanite mica schist (sample 181117A01). (A) Classification diagram for biotite (Wlodek et al., 2015). (B) Si+Fe^{2+}+Mg plotted against total Al contents to show Tschermak substitution within the biotite.

doi:10.6342/NTU202202659

Muscovite

Muscovites appear as coarse-grained porphyroblasts with decussate texture in this sillimanite mica schist, which might grow intertectonically between D_1 and D_2. The limited and very low Na/Na+K (0.08-0.11) and Fe^{2+}+Mg/Fe^{2+}+Mg+Ti+Al^{VI} (0.07-0.09) values show almost no paragonite and caledonite composition. The low Si/Al ratios (mostly 1.07-1.17) excludes phengite composition. The lack of phengite composition indicates that muscovite does not crystallize in a high-pressure environment (Deer et al., 2013). On the plot of Si+Fe^{2+}+Mg vs. Al^{VI}, muscovite roughly follows the Tschermak substitution line with Al^{VI} contents spreading from staurolite zone into sillimanite + K-feldspar zone (Figure 37). Such relatively high Al^{VI} (3.59-3.74), low Si (6.08-6.26) and low Fe^{2+}+Mg (0.28-0.36) contents suggests these muscovites formed in high-grade metamorphic condition (Deer et al., 2013).

doi:10.6342/NTU202202659

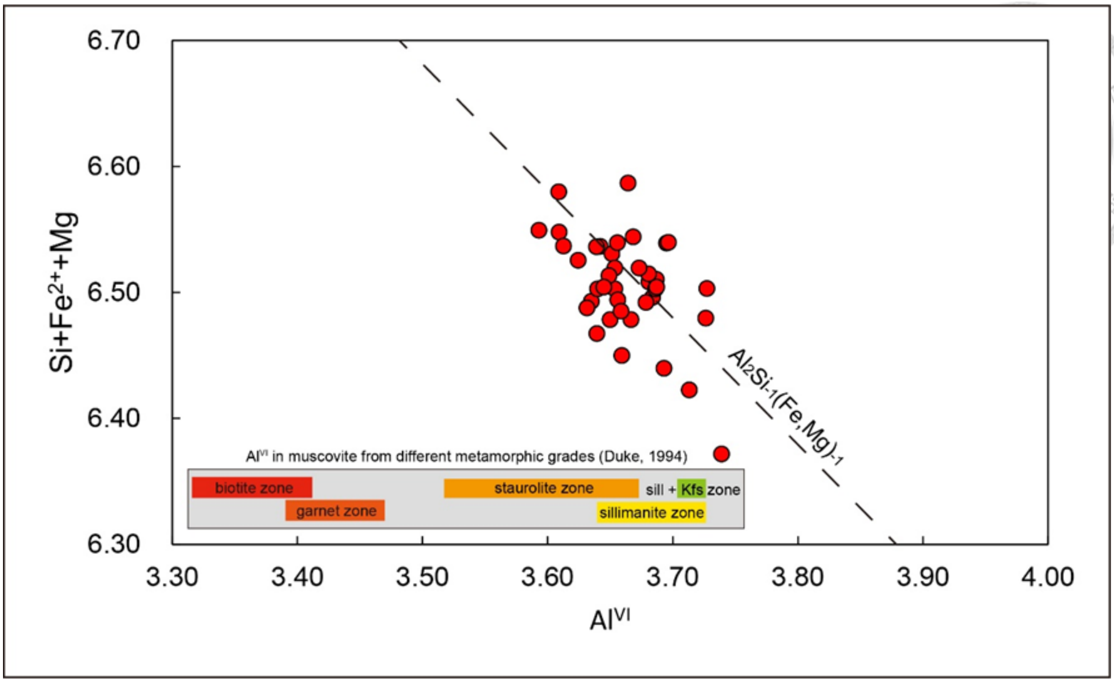

Figure 37. Plot of Al^{VI} vs. $Si+Fe^{2+}+Mg$ based on 22 oxygens of muscovite in sample 181117A01. The dashed line is the Tschermak substitution line ($Al_2Si_{-1}(Fe,Mg)_{-1}$). The Al^{VI} contents in muscovite from different metamorphic grades (Duke, 1994) are shown for comparison with different color bars representing different metamorphic zones.

4.3.3 18LYB03 Biotite Gneiss

Feldspar

Six line profile analyses of feldspars were conducted in the boudin (Pl1, Pl2, Pl3, Pl4, Pl5, and Pl6) and two were performed in the host gneiss (Pl7 and Pl8; Figure 38). Feldspar and garnet within the boudin mostly show anhedral shapes with high mobility of grain boundaries. Such lobate grain boundaries suggests that the boudin assemblages formed in high-grade metamorphism (>600 °C; Passchier and Trouw, 2005). Host feldspars show multiple recrystallized fine-grains and somewhat polygonal granoblastic texture, indicative of dynamic recrystallization by subgrain rotation

doi:10.6342/NTU202202659

recrystallization during D_2 followed by sustained high-temperature of static recrystallization (Figure 38). Despite different microstructures in the boudin and host gneiss, feldspars show nearly the same chemical composition ranging from bytownite to labradorite, An_{51}-An_{89} for the boudin and An_{57}-An_{86} for the host (Figure 39A).

The line profile of Pl1 and Pl2 show similar patterns of An contents variation oscillating between $An_{79.7}$-$An_{88.0}$ in Pl1 and $An_{77.9}$-$An_{86.9}$ in Pl2 (Figure 39B). Despite the relatively low An content ($An_{77.4}$) in the rim of Pl1, no obvious trend can be ascertained considering the lowest An value of 77.9 in Pl2. In the thin section, Pl1 is a single plagioclase grain of lobate grain boundaries with multiple inclusions and some fractures. Pl2 is composed of three plagioclase grains of polygonal grain boundaries with one plagioclase overgrown by muscovite (Figure 38). In spite of such different microstructural features, they show similar chemical compositions and variation patterns. It is suggested that the chemical composition of plagioclase can be preserved even though static recrystallization is initiated to reduce the grain boundary area and change the geometry of mineral grains.

The line profile of Pl3 have similar An content ranges ($An_{78.3-86.8}$) as Pl1 and Pl2 but with less oscillatory variation (Figure 39B). Pl3 is a single plagioclase grain of a little curved to polygonal grain boundary, which is similar to the grains within Pl2. The line profile of Pl4 transects a plagioclase grain of lobate grain boundaries with its core

doi:10.6342/NTU202202659

overgrown by anhedral muscovite. The An contents decrease from $An_{78.4-82.5}$ in the rim to $An_{64.7-70.7}$ in the core. The muscovite growth in the plagioclase core without in the rim part indicates that the decrease of An contents is caused by muscovite growth over the plagioclase.

The line profile of Pl5 transects one plagioclase grain of lobate grain boundaries and complex extinction patterns with subgrain boundaries in the rim. The plagioclase is also grown over by muscovite and chlorite within the grains and along the fractures. The An compositional profile shows two distinct chemical domains: a limited An content ranges ($An_{52.4-54.4}$) of a flat profile within a subgrain in the rim, and a complex oscillatory variation ($An_{65.3-85.6}$) in the core of complex extinction pattern (Figure 39B). The line profile of Pl6 transects two plagioclase grain of lobate grain boundaries, with one grain clearly overgrown by muscovite. Thus, the line profile plotted is mainly within the plagioclase grain without much muscovite overprint. The An contents show a comparatively flat profile from $An_{80.9}$ to $An_{89.2}$ with an a 20-μm width interval of lower An values of $An_{72.9-78.3}$. Such muscovite overgrowth over plagioclase and the decrease of An content is similar to the one identified in Pl4.

The line profile of Pl7 is made up of multiple recrystallized fine-grained plagioclases, which are also overgrown by muscovite (Figure 38). The An compositional profile shows two distinct An content ranges, $An_{82.8-86.4}$ and $An_{60.8-64.0}$

doi:10.6342/NTU202202659

(Figure 39B). The lower An content side is close to the regions where muscovite forms. The line profile of Pl8 transects one plagioclase grain of lobate grain boundaries. The An compositional profile shows a limited variation ranges of $An_{75.5-83.4}$ in the most part of the plagioclase only with the rim as low as $An_{57.5}$ (Figure 39B).

In summary, the feldspars in both boudin and host gneiss have composition varying from bytownite to labradorite. The decrease of An contents is accompanied by growth of muscovite as suggested by their intimate spatial relationship. Accordingly, plagioclase of bytownite composition ($An_{75.5-89.2}$) formed together with garnet and biotite in the peak metamorphism followed by muscovite growth and re-equilibration of plagioclase composition into labradorite ($An_{52.4-66.9}$). The same chemical compositional ranges and variation patterns of the feldspars in the boudin and the host gneiss suggests that these feldspars formed in the same P-T conditions and recorded the same geological histories.

doi:10.6342/NTU202202659

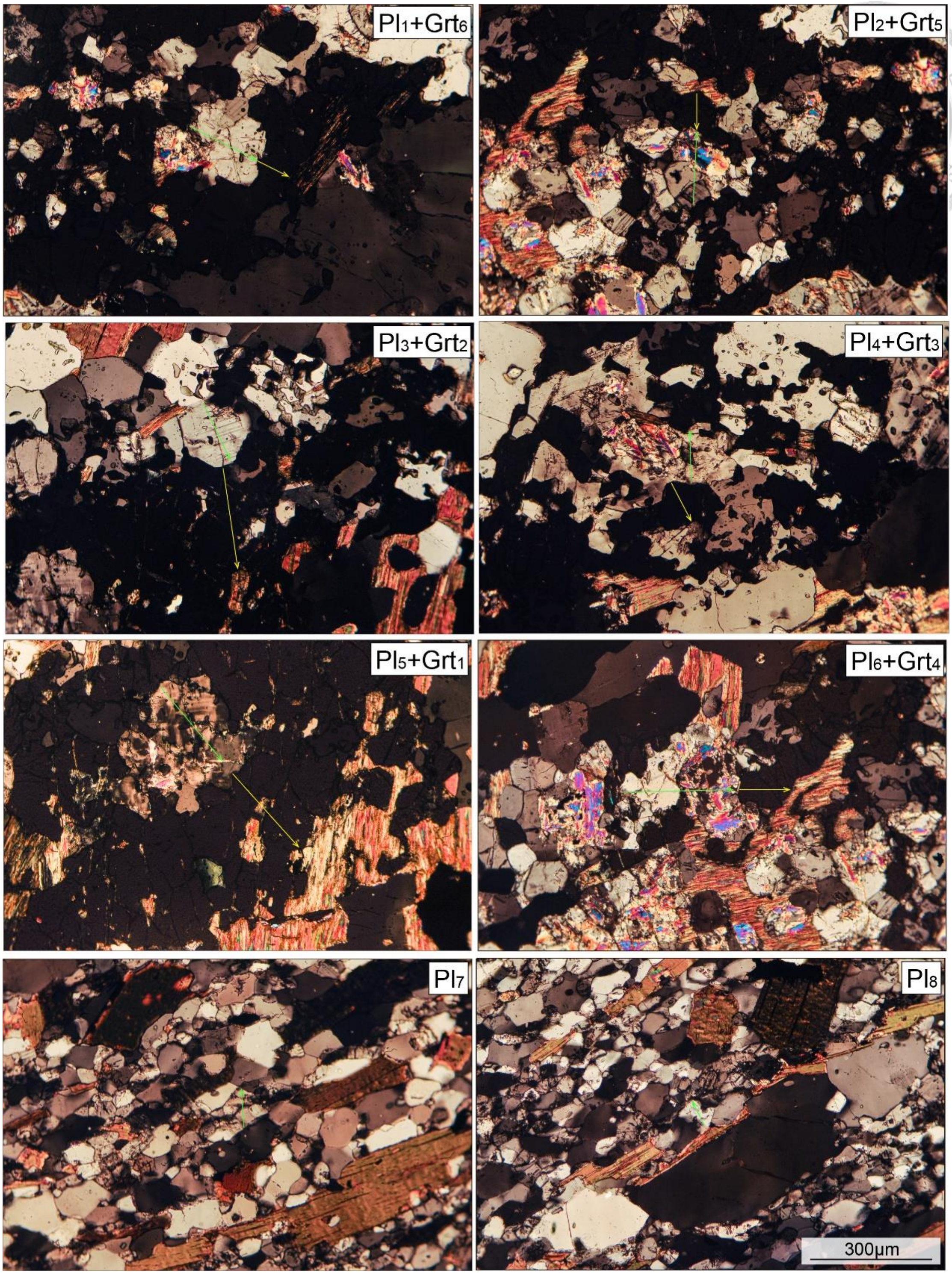

Figure 38. Thin section photos under cross-polarized light with green and yellow arrows marking the position of line profile analysis for feldspars and garnets respectively.

doi:10.6342/NTU202202659

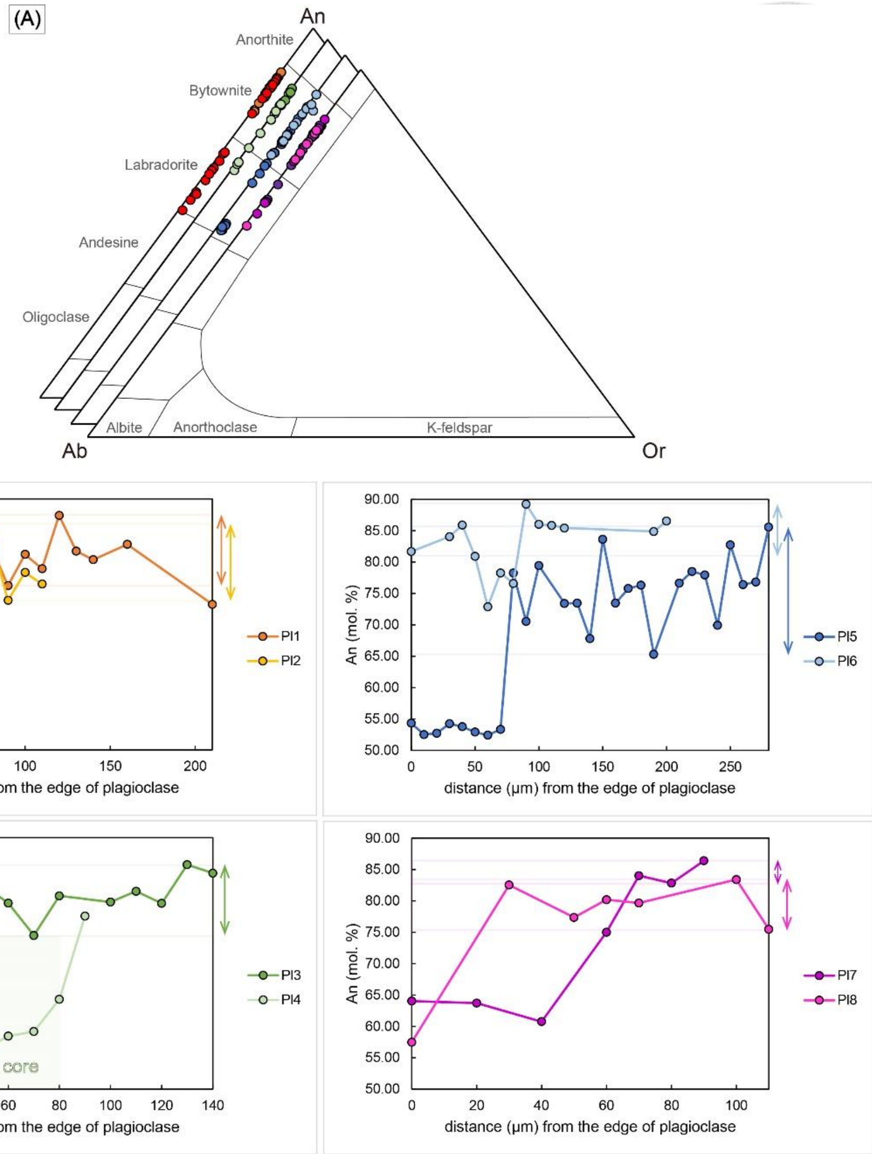

Figure 39. Line profile analysis of feldspar chemical compositions in the boudin and host rock of the biotite gneiss (sample 18LYB03). (A) Ternary An-Ab-Or diagram for feldspar classification (Harrison et al., 2019). Legends are the same in Figure B. (B) Compositional profile of An contents (mol. %) plotted against the distance from the edge/starting analytical point of plagioclase. The double-arrow line marks out the interpreted high An contents parts of the plagioclase.

Biotite

Biotite in the boudin shows decussate texture intergrowing with garnet, plagioclase, and quartz. Besides, chlorite growth along the biotite cleavage is widely identified. The biotites in the host gneiss are usually anhedral to subhedral, and roughly S_2-parallel with anhedral shapes showing dehydration melting texture. The Fe^{2+}+Mg (4.38-4.97 apfu) values of biotites spread between siderophyllite-eastonite and annite-phlogopite solid solution series. Due to a relatively low Al_{total} contents (2.97-3.34 apfu) along with high X_{Fe} ratios (0.70-0.75), these biotites are close to annite compositions (Figure 40A). In the Si+Fe^{2+}+Mg vs. Al_{total} plot, no Tschermak substitution trend is identified (Figure 40B). These two biotites with different structural domains show similar major chemical compositions (Si, Fe, Mg) except slight difference in Al and K. The biotites in boudin have higher Al (3.17-3.34 apfu) and lower K (1.64-1.90 apfu) than the host biotites (Al:2.97-3.20; K:1.78-1.95). Such compositional differences could be explained by the different mineral assemblages in the two structural domains. The boudin is a garnet-concentrated zone, and all the biotites exhibit chlorite overgrowth along cleavage. The highly garnet-concentrated boudin reflects that the bulk composition of boudin is peraluminous. Therefore, the minerals growing from such peraluminous bulk rock would have elevated Al contents than usual, as evidenced by the lack of garnet in the host gneiss forming the lower-Al contents biotites.

doi:10.6342/NTU202202659

Formation of chlorite from biotite requires removal of potassium from biotites, which could further decrease the K contents of the biotite left. Such chlorite-forming reaction along the cleavage of biotite is only identified in the boudin but not in the host gneiss, which explained the reason why biotites in boudin have lower K contents. In addition, the biotites in the boudins exhibit lower Ti contents (0.23-0.34 apfu) with respect to biotites in host gneiss (0.32-0.51 apfu), which indicates that biotite chemistry in the boudins re-equilibrated in lower temperature conditions. This further supports that the chlorite-forming reaction in the boudin changes the biotite chemistry during retrograde metamorphism.

doi:10.6342/NTU202202659

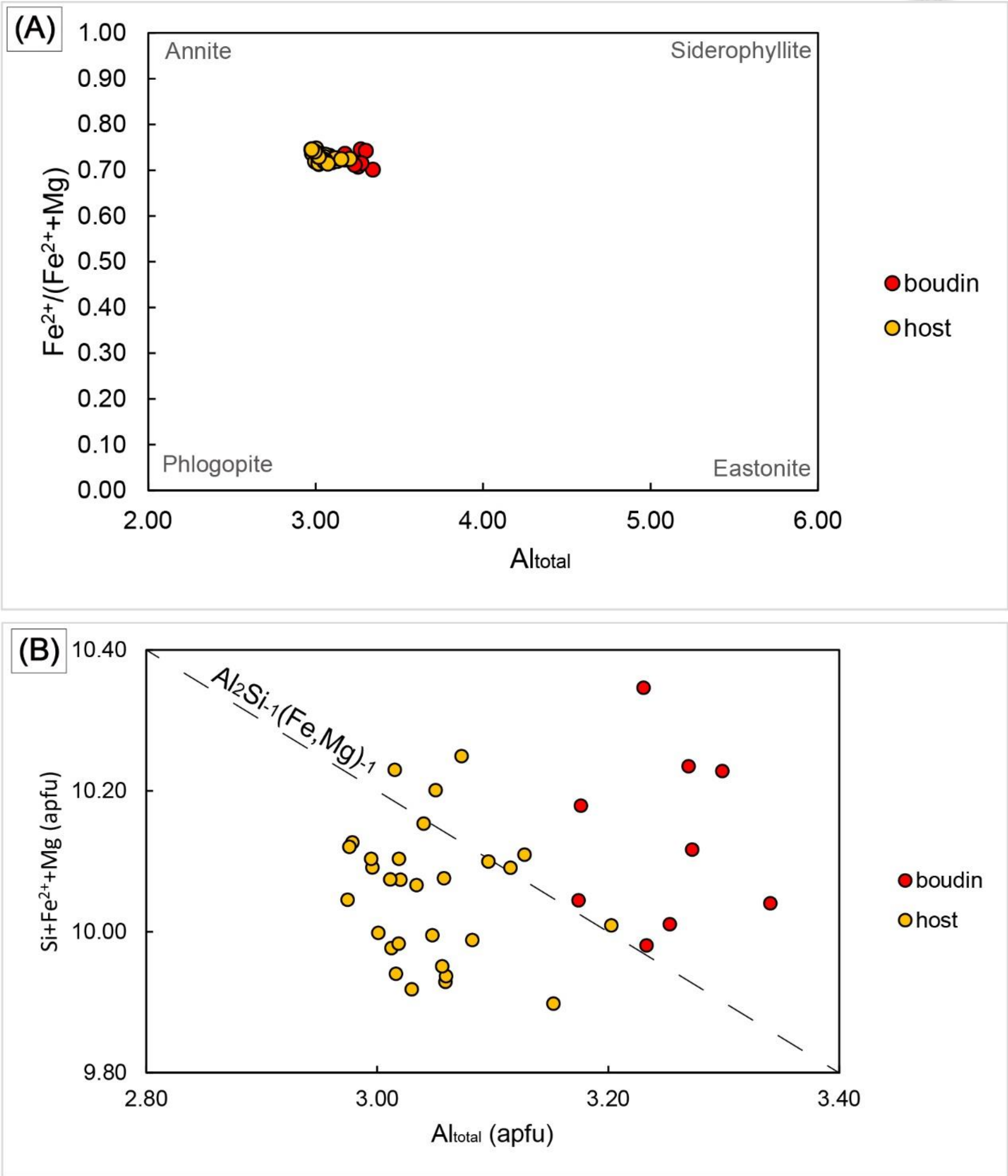

Figure 40. Plots of chemical composition of biotites from biotite gneiss (sample 18LYB03). (A) Classification diagram for biotite species (Wlodek et al., 2015). (B) Si+Fe^{2+}+Mg plotted against total Al contents with Tschermak substitution line for comparison.

doi:10.6342/NTU202202659

Muscovite

All the muscovites in this sample are mostly anhedral crystals growing over the plagioclase in the boudin, which is after the D_2 peak metamorphism. The limited and very low Na/Na+K (0.00-0.03) and Fe^{2+}+Mg/Fe^{2+}+Mg+Ti+Al^{VI} (0.06-0.12) values show almost no paragonite and caledonite composition. Besides, the low Si/Al ratios (mostly 1.14-1.34) excludes phengite composition. The lack of phengite composition indicates that muscovite does not crystallize in a high-pressure environment. On the plot of Si+Fe^{2+}+Mg vs. Al_{total}, muscovite follows the Tschermak substitution line (Figure 41A). Furthermore, Al^{VI} contents spreads from staurolite zone into and above sillimanite + K-feldspar zone (Figure 41B). Such wide-ranged and relatively high Al^{VI} (3.52-3.78) contents suggests that these muscovites formed from high- to medium-grade metamorphic conditions followed the D_2 peak metamorphism. Therefore, the crustal P-T condition is still maintained at least in the staurolite zone (500-650°C; Borisova and Baltybaev, 2021) during the post-D_2 muscovite growth.

doi:10.6342/NTU202202659

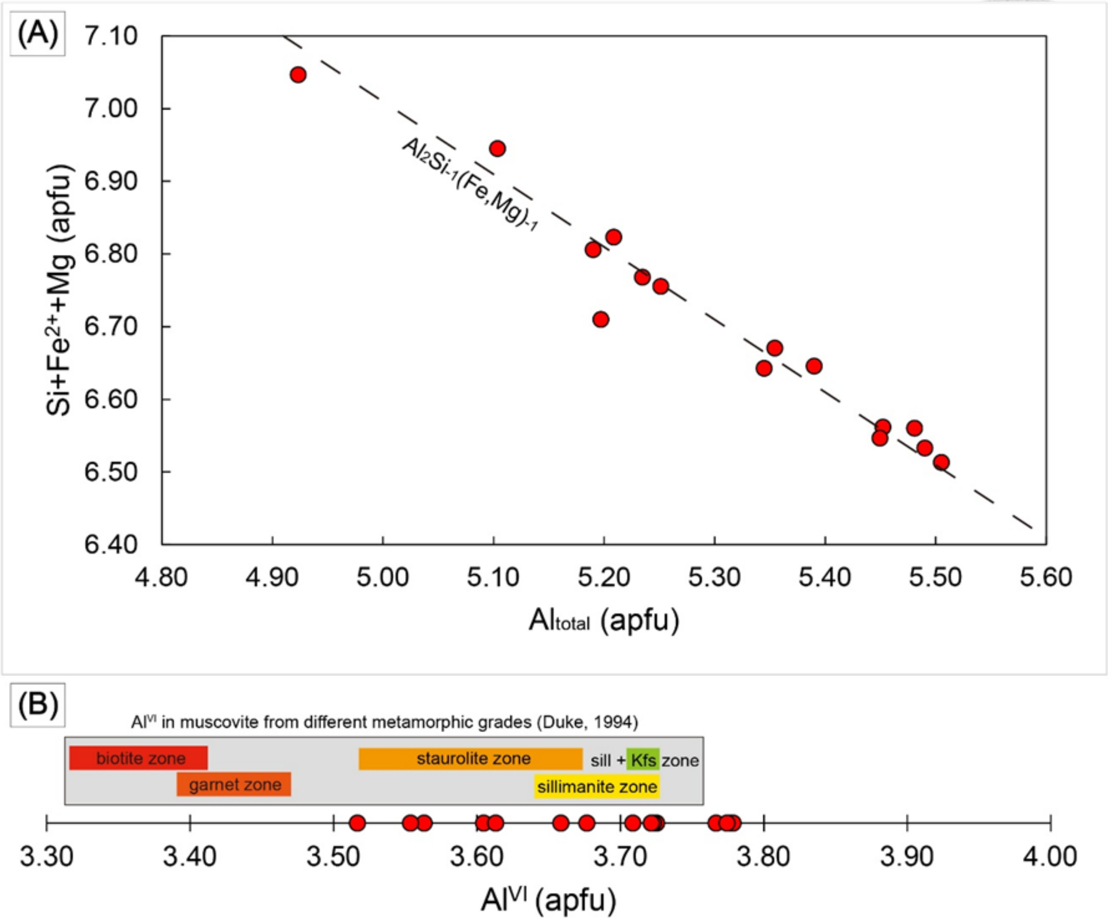

Figure 41. Plots of chemical composition of muscovite in the boudin of biotite gneiss (sample 18LYB03). (A) Plot of Si+Fe^{2+}+Mg vs. Al_{total} based on 22 oxygens of muscovite. The dashed line is the Tschermak substitution line ($Al_2Si_{-1}(Fe,Mg)_{-1}$). (B) Plot of Al^{VI} contents in muscovites compared with muscovites from different metamorphic grades (Duke, 1994).

Garnet

All the garnets measured are within the boudin of the host biotite gneiss. In the SEM-BSE images, garnets grow truncating the cleavages of biotite, and enclose the biotite relicts as inclusions (Figure 42). Such microstructural relationship suggests that biotites are reactants consumed for garnet formation. The geometry and the migration of grain boundaries from plagioclase into garnet shows that plagioclase forms by the

doi:10.6342/NTU202202659

consumption of garnets, as also supported by multiple garnet relict inclusions within the plagioclase. However, grain boundaries of some garnets migrate into plagioclase, which indicates that garnet also forms through the consumption of plagioclase. Such inter-crosscutting relationship between garnet and plagioclase suggests that these two minerals grow during the same period in an equilibrium state. Due to faster crystal-growth rates, nevertheless, plagioclase will enclose the garnets within and makes them become the inclusions. Accordingly, garnet and plagioclase are peak metamorphic assemblage of D_2 with biotite being the reactants formed prior to D_2.

Six line profiles of chemical composition measurement were conducted on garnet (Grt1, Grt2, Grt3, Grt4, Grt5, and Grt6), which are all next to the line profile analyses of plagioclase (Figure 38). The line profiles are composed of multiple point analyses with a 10-μm distance between the points. All the garnet exhibits similar and limited major chemical compositions within the range of $Alm_{55-60}Py_{4-5}Sp_{19-25}Gro_{14-21}$. The compositions show dominant almandine compositions with minor spessartine and grossular components and very low pyrope content. In the compositional profiles, spessartine and grossular compositions show antipathetic relationships with periodic chemical variations similar to a flatten sinusoidal wave (Figure 43). Such repetitive pattern and limited variation ranges suggest that these garnets have multiple growth stages under similar chemical environments. Almandine composition also shows a

doi:10.6342/NTU202202659

variation of wave-like pattern, but the variation pattern is not the same as the spessartine and grossular components. It is suggested that different mechanisms control the Fe and Mn+Ca contents in the garnet. Finally, there is no chemical variation in the pyrope composition. On the plot of CaO+MnO vs. FeO+MgO (Nandi, 1967; Sturt, 1962), garnet compositions all plot within the garnet zone.

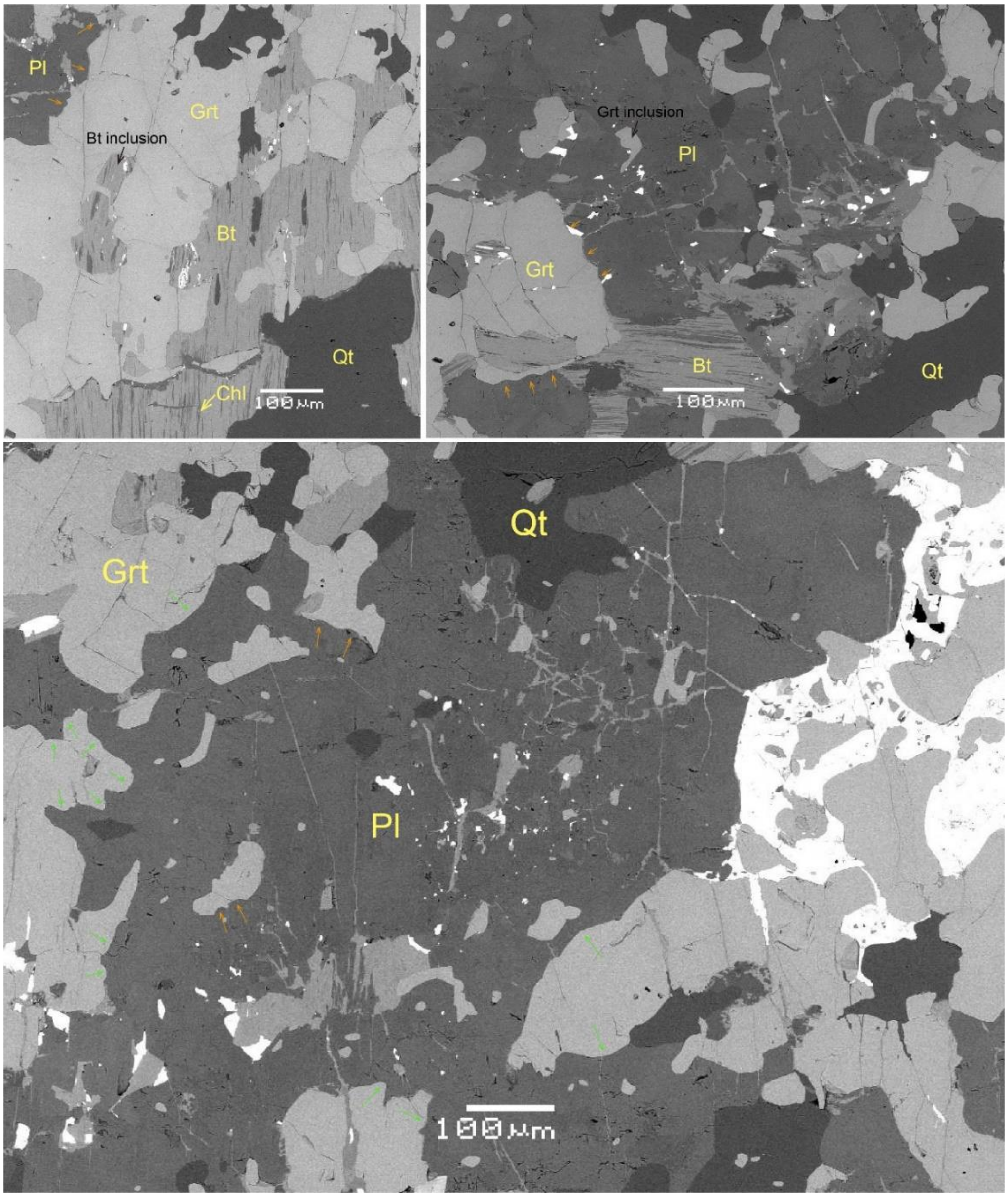

Figure 42. SEM-BSE images showing the mineral relationships between garnet, biotite, and plagioclase. Orange and green arrows indicate the migration directions of the grain boundaries of plagioclase and garnets respectively.

doi:10.6342/NTU202202659

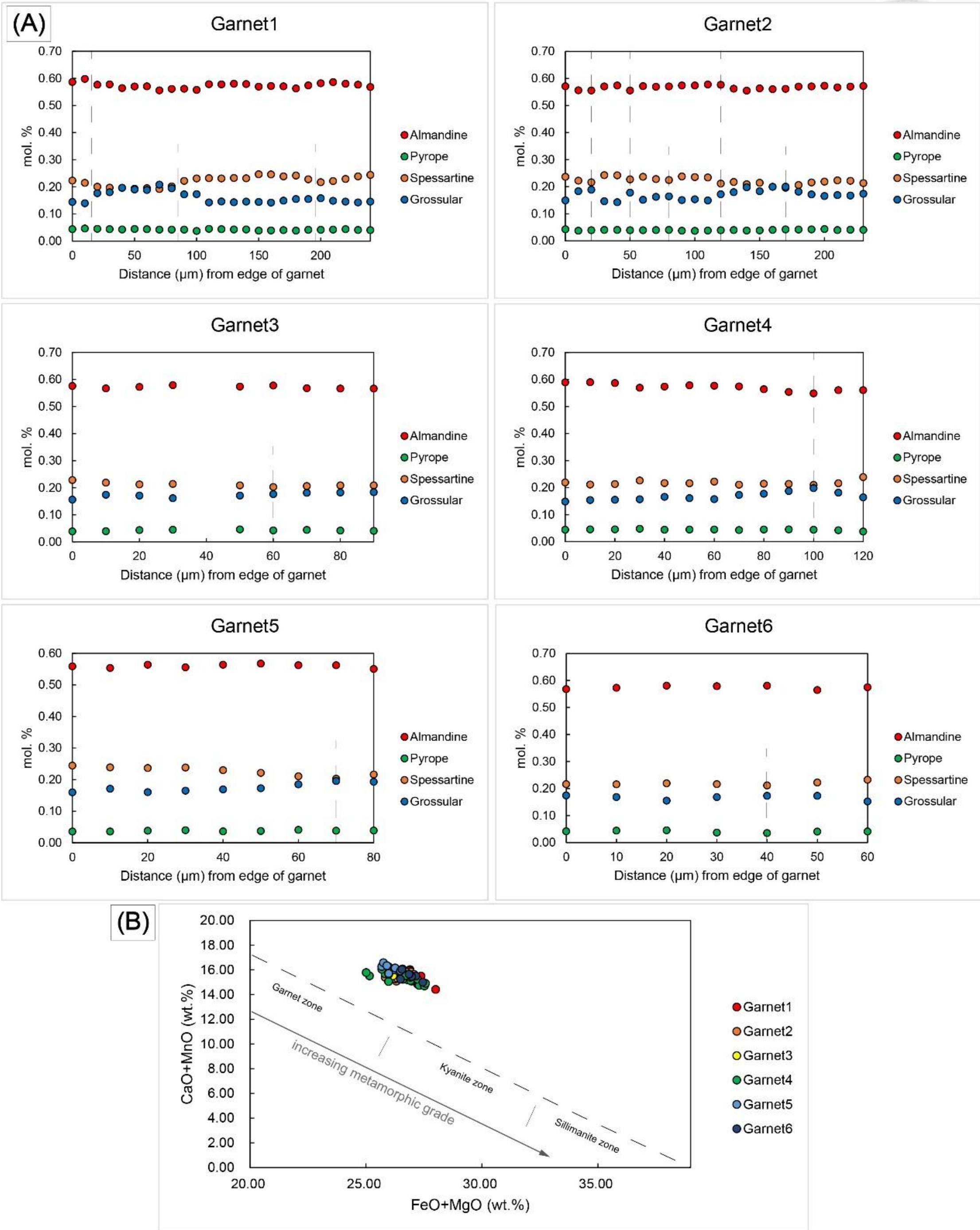

Figure 43. Six line profile analysis of garnet grains (Garnet1 to Garnet 6) in the boudin of biotite gneiss (sample 18LYB03). (A) Garnet compositional profiles with gray dashed lines marking the interpreted boundaries between the different garnet growth stage, which is mainly based on the spessartine and grossular compositions. If the boundaries can be linked to the almandine composition, the dashed line will penetrate through the line profile of almandine. (B) A plot of weight percentages of CaO+MnO vs. FeO+MgO to show the variation of garnet compositions with metamorphic grades. The garnet compositional ranges from different metamorphic zones are from Nandi (1967).

doi:10.6342/NTU202202659

4.3.4 18TP01 Amphibolite

Feldspar

Four line profile analyses (Pl1, Pl2, Pl3, Pl4) were performed on two plagioclase grains. The selected line profiles within each plagioclase are nearly perpendicular to each other and along the long and short axis of the mineral grain (Figure 44A). Two measured plagioclases have polygonal granoblastic grain boundaries suggestive of sustained high temperatures after deformation to initiate static recrystallization. Besides, some tiny minerals along the fractures within the plagioclase are identified, which should occur after the annealing process. These two plagioclases show similar chemical compositions within the range of andesine ($An_{41-46}Ab_{53-57}Or_{1-2}$) with Pl3 and Pl4 having larger compositional variation (Figure 44B). In the composition profiles, Pl1 and Pl2 show homogeneous composition from the core to the rim. However, Pl3 and Pl4 show complex variation especially along the long axis of Pl3 (Figure 44C). The chemical profile of Pl3 have periodic sinusoidal wave-like and antipathetic variation of An and Ab contents. In the thin section, Pl3 transects multiple fractures with tiny dusty minerals in the plagioclase. Comparing the compositional variation with those fractures and tiny minerals, it is indicated that these plagioclases appear to re-equilibrate during the fracturing and growth of these minerals, and usually show increase of An contents and decrease of Ab contents. In summary, the relatively original plagioclase composition

doi:10.6342/NTU202202659

formed during the amphibolite facies metamorphism is close to $An_{42-43}Ab_{55-57}Or_{1-2}$ as suggested by the Pl1 and Pl2. The later fracturing and mineral growth changed the composition a little into more Ca-rich ($An_{41-46}Ab_{53-57}Or_{1-2}$).

Biotite

Biotites measured are mimetic growth over the hornblendes defining D_3 S/C fabrics. Thus, this biotite composition will reflect the metamorphic conditions after the cessation of D_3 shearing event. The Fe^{2+}+Mg (4.58-5.06 apfu) values of biotites spread between siderophyllite-eastonite and annite-phlogopite solid solution series. Due to a relatively low Al_{total} contents (3.06-3.34 apfu) along with a little low X_{Fe} ratios of 0.42-0.47, these biotites have closer compositions to phlogopite (Figure 45A). According to the plot of Si+Fe^{2+}+Mg vs. Al_{total}, Tschermak substitution did occur in these biotites (Figure 45B). In addition, Ti contents vary from 0.19 to 0.28 apfu indicative of the local chemical heterogeneity during the biotite formation.

doi:10.6342/NTU202202659

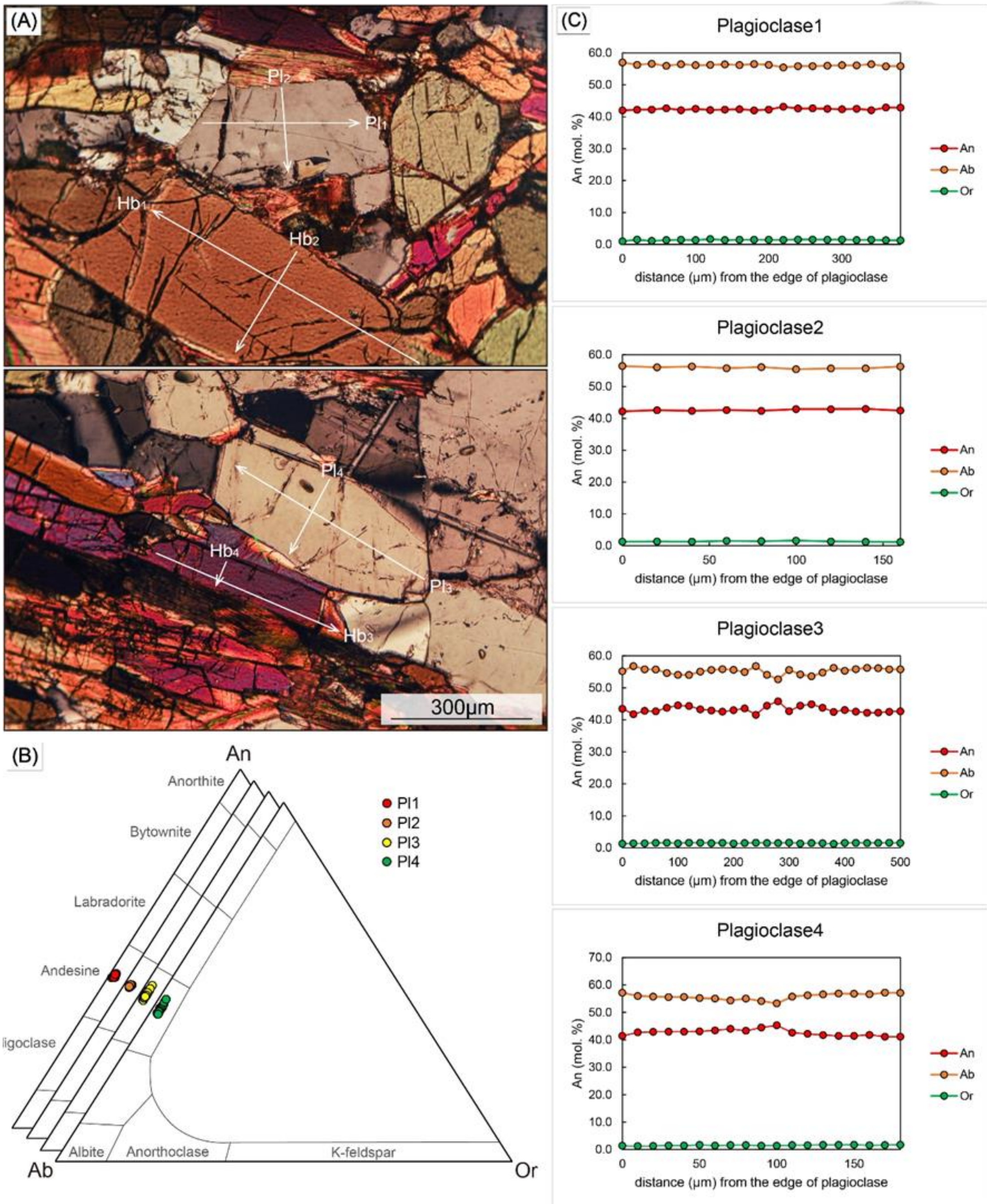

Figure 44. Line profile analysis of feldspar chemical compositions of the amphibolite (sample 18TP01). (A) Thin section photos under cross-polarized light with white arrows marking the position of line profile analysis for feldspars and hornblendes respectively. (B) Ternary An-Ab-Or diagram for feldspar classification (Harrison et al., 2019). (C) Compositional profile of An, Ab and Or contents (mol. %) plotted against the distance from the edge/starting analytical point of plagioclase.

doi:10.6342/NTU202202659

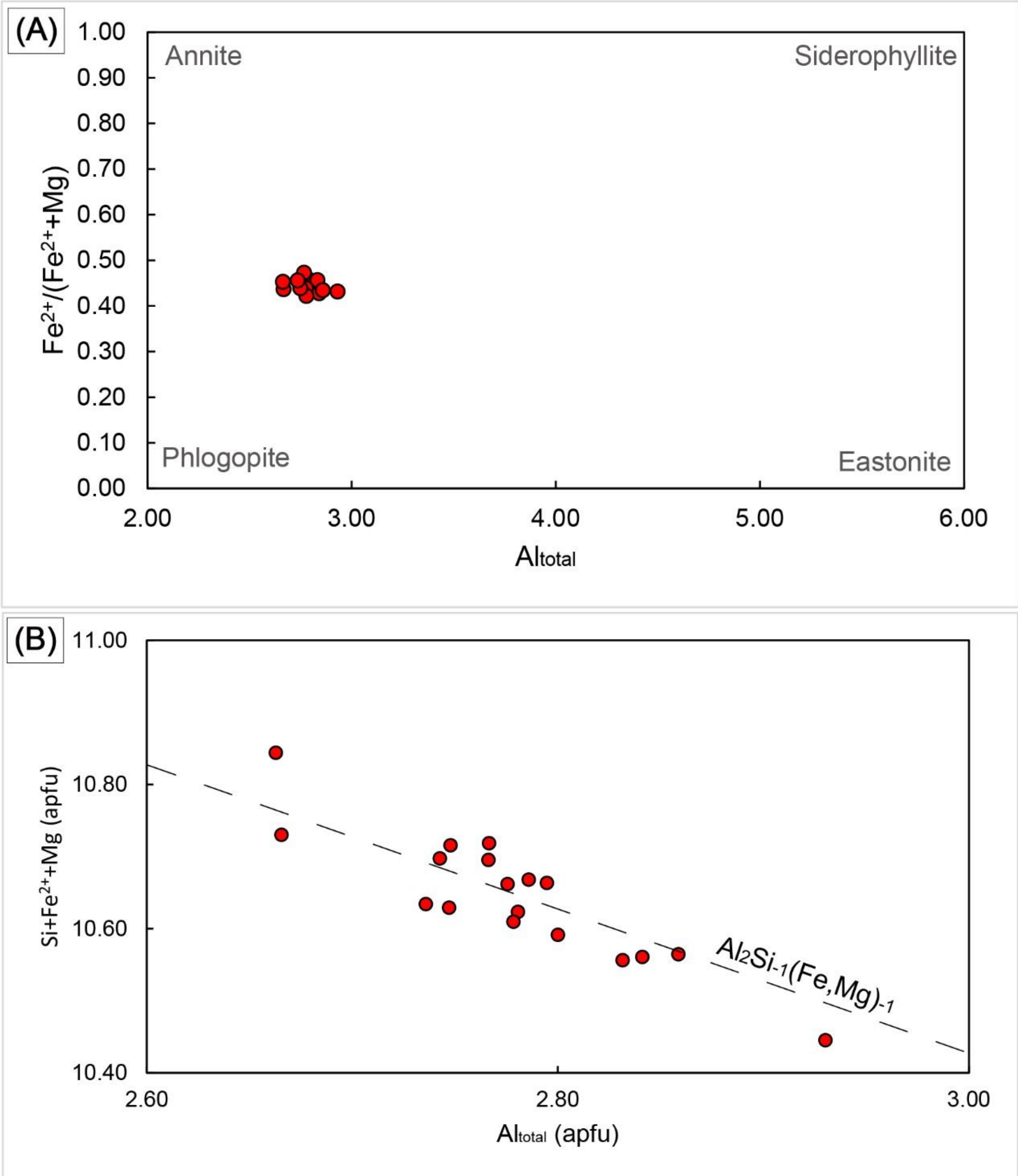

Figure 45. Plots of chemical composition of biotites from amphibolite (sample 18TP01). (A) Classification diagram for biotite (Wlodek et al., 2015). (B) Si+Fe^{2+}+Mg plotted against total Al contents with Tschermak substitution line for comparison.

doi:10.6342/NTU202202659

Amphibole

Amphiboles define the D_3 S/C fabrics in the amphibolite. Two amphibole grains were measured with four line profile analyses (Hb_1, Hb_2, Hb_3, Hb_4). The selected line profiles in each amphibole are nearly perpendicular and along the long and short axis of the mineral grain to check the chemical zonation from the core to the rim. The ratios of B-group cations show that all the amphiboles are calcium amphiboles [$^{B}(Ca+Mg+Fe^{2+}+Mn)/B_{total}$ = 0.91-0.98 > 0.75, $^{B}Ca/B_{total}$ = 0.89-0.97 > $^{B}(Fe^{2+}+Mg+Mn)/B_{total}$ = 0.00-0.04]. On the plot of $^{A}(Na+K+2Ca)$ vs. $^{C}(Al+Fe^{3+}+2Ti)$ for calcium amphibole classification (Hawthorne et al., 2012), most amphiboles fall within magnesio-hornblende with some in the pargasite field (Figure 46).

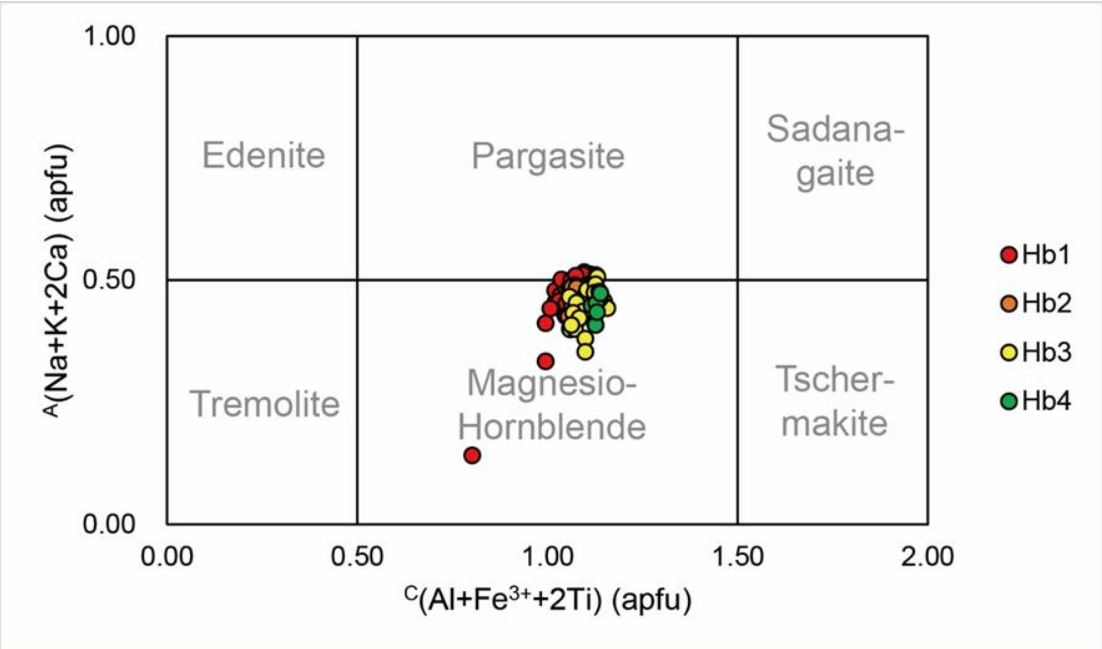

Figure 46. Chemical compositional plot of amphibole compositions from amphibolite (sample 18TP01) on a classification diagram for calcium amphiboles (Hawthorne et al., 2012).

doi:10.6342/NTU202202659

4.3.5 18TP04 Amphibolite

Feldspar

Feldspars in the amphibolite are all plagioclase of polygonal granoblastic grain boundaries suggestive of sustained high temperatures for static recrystallization. Accessory minerals are identified within the plagioclase and along their grain boundaries, including titanite and apatite. Later fracturing and alteration is also identified by the tiny dusty minerals. Two transects (Pl1, Pl2) were conducted on the plagioclase. Each line profile is composed of multiple point analyses with 20-μm distance between the points. The line profile of Pl1 transects multiple plagioclase grains with Pl2 nearly perpendicular to Pl1 and only crossing one plagioclase grain (Figure 47A). On the ternary feldspar diagram (Figure 47B), all plagioclases are plotted within the andesine region with limited compositional ranges of $An_{37-45}Ab_{54-61}Or_{1-2}$. The major chemical variation lies in the Ca and Na substitution with fixed K contents. In the chemical compositional profiles (Figure 47C), most line segments show quite homogenous compositions ($An_{37-40}Ab_{59-61}Or_{1-2}$) except for three segments of a 160-μm, 60-μm and, a 40-μm intervals in the middle of the line. These three intervals all show the same compositional variation trend of increasing An contents and decreasing Ab contents with the most extreme composition of $An_{45}Ab_{54}Or_{1}$. Only the 160-μm interval shows the gradual compositional change with the other two narrower intervals of

doi:10.6342/NTU202202659

sudden chemical change. In thin sections, some plagioclases show zoning extinction patterns reflective of their compositional variation. Such zonation can be the cause for chemical change identified from the compositional profiles, as evidenced by one zoned plagioclase in the line profile of Pl1. The position of higher An contents and lower Ab contents corresponds to the core of the zoned plagioclase. Accordingly, plagioclase has two growth stages from higher An contents in the core to lower An contents in the rim. Most plagioclase compositions have lower and consistent An contents with only a few places preserving the higher Ca core. It is suggested that the consistent and lower An compositions in the rim of plagioclase grew as the amphibolite formed, and the higher Ca core grew during the protolith formation.

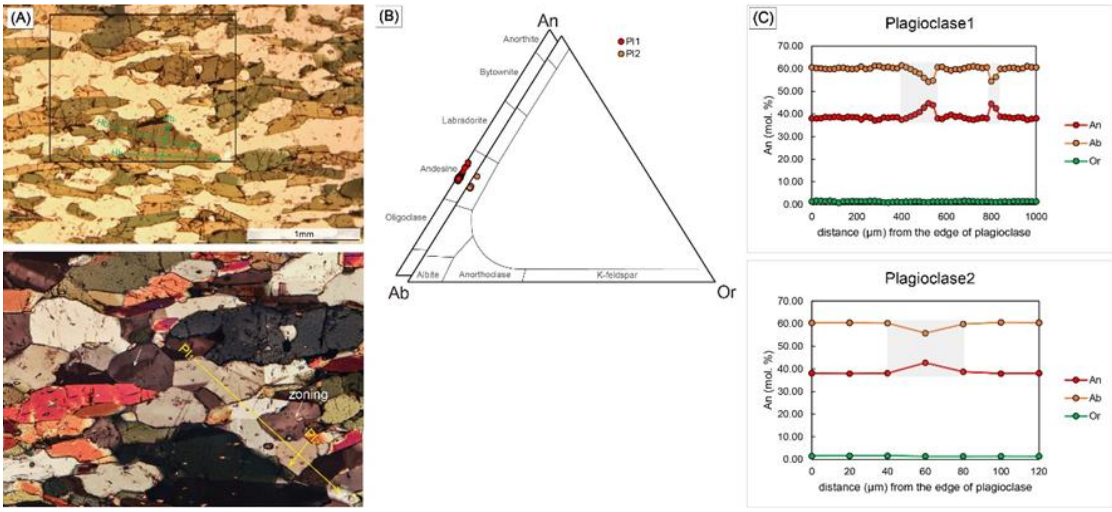

Figure 47. Line profile analysis of feldspar compositions in 18TP04 amphibolite. (A) Thin section photos under plane- and cross-polarized light with green and yellow arrows marking the position of line profiles for hornblendes and feldspars respectively. The black rectangle region is enlarged to show the microstructures of plagioclase. (B) Ternary feldspar classification diagram (Harrison et al., 2019). (C) Compositional profile of An, Ab and Or contents (mol. %) plotted against the distance from the edge/starting analytical point of plagioclase.

doi:10.6342/NTU202202659

Amphibole

Amphiboles define the D_3 S/C fabrics in the amphibolite. Two amphibole grains were measured with three line profile analyses (Hb_1, Hb_2, Hb_3). The selected line profiles in each amphibole are along the long and short axis of the minerals to check the chemical zonation from the core to the rim. The ratios of B-group cations show that all the amphiboles are calcium amphiboles [$^{B}(Ca+Mg+Fe^{2+}+Mn)/B_{total}$ = 0.94-1.00 > 0.75, $^{B}Ca/B_{total}$ = 0.89-0.96 > $^{B}(Fe^{2+}+Mg+Mn)/B_{total}$ = 0.00-0.06]. On the plot of $^{A}(Na+K+2Ca)$ vs. $^{C}(Al+Fe^{3+}+2Ti)$ for calcium amphibole classification (Hawthorne et al., 2012), all amphiboles fall across the boundaries between magnesio-hornblende and the pargasite (Figure 48).

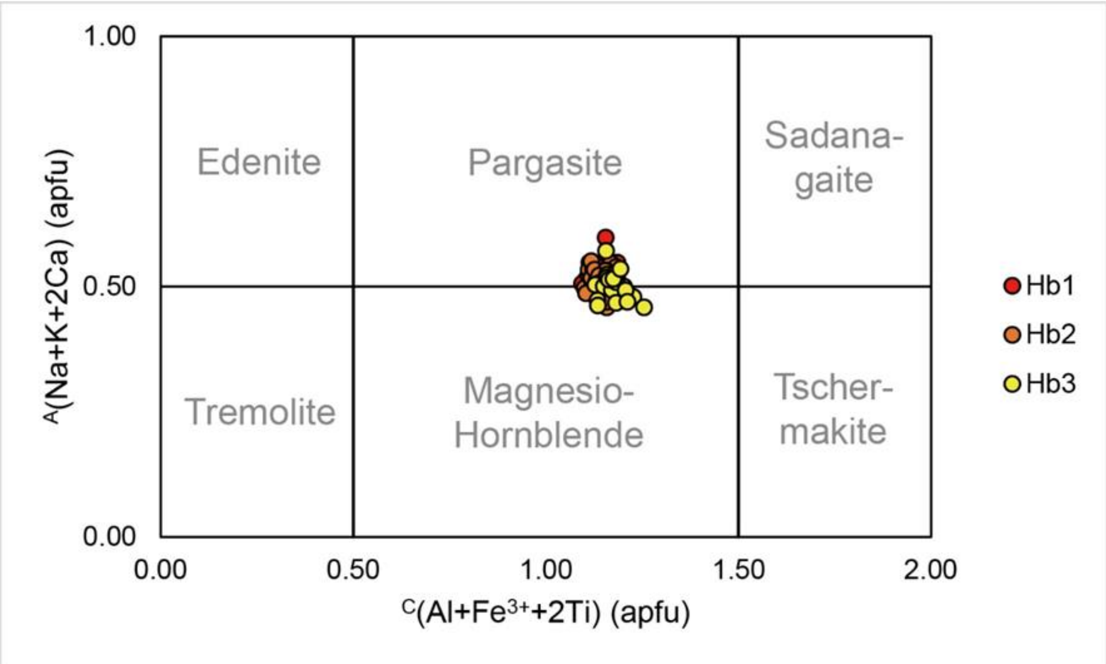

Figure 48. Chemical compositional plot of amphibole compositions from amphibolite (sample 18TP04) on a classification diagram for calcium amphiboles (Hawthorne et al., 2012).

doi:10.6342/NTU202202659

4.3.6 18TP04 Tonalitic Gneiss

Feldspar

Both K-feldspar and plagioclase coexist in tonalitic gneiss with plagioclase dominating over the K-feldspar in amount. All the K-feldspars show irregular grain boundaries, and most of them are concave inward suggestive of consumption of the K-feldspar by recrystallized quartz and plagioclase. However, some places show reverse migration directions of grain boundaries from K-feldspar into plagioclase. It is suggested that K-feldspar and plagioclase grow at the same time during metamorphism and element distribution occurs between them. Thus, the chemical composition of these feldspars can reflect the conditions during the metamorphism of D_{3b} shear zone event. Most plagioclase show polygonal granoblastic texture indicative of sustained high temperature of static recrystallization after the D_{3b} shearing event. In addition, plagioclases also show irregular grain boundaries but comparatively straight and polygonal compared to K-feldspar. Strong grain boundary migration into the other minerals, including K-feldspar, quartz, and hornblende, suggests that plagioclase undergoes strong crystal growth and recrystallization during metamorphism. Besides, Na-rich myrmekite is identified formed from the rim of plagioclase extruding into the K-feldspar, which indicates the reaction of Na-bearing fluids with K-feldspar. Four line profile analyses for K-feldspar and plagioclase have been conducted to check chemical

doi:10.6342/NTU202202659

zonation (Kfs1, Kfs2, Kfs3, Kfs4; Pl3, Pl4, Pl5, Pl6; Figure 49, 50). Each line profile is composed of multiple point analyses with 20-μm distance between the points, and two line profiles are conducted for each mineral grain.

On the ternary diagram for feldspar classification, all the plagioclases exhibit small compositional ranges of $An_{33-41}Ab_{58-66}Or_{1-2}$ (Figure 51A). The major chemical variation lies in the Ca and Na substitution with fixed K content. In the compositional profiles, line profiles of Pl3 and Pl4 show repetitive variation pattern of first increasing and then decreasing An contents in an antipathetic relationships with Ab contents (Figure 51B). However, line profile of Pl5 and Pl6 have relatively homogenous compositions except for a 60-μm width interval of sudden compositional change. This segment has higher An and lower Ab contents compared to the neighboring consistent part of the plagioclase. In the thin section, the line profile of Pl3 is composed of multiple plagioclase grains of polygonal granoblastic textures, and Pl4 only contains one plagioclase grain. Line profiles of Pl5 and Pl6 are within a big plagioclase grain with Pl6 transecting the twinning pattern. Compared with the chemical mapping of Pl5 and Pl6, plagioclase has a Ca-rich core with a band of Ca-rich zone, which can be corresponded to the growth twinning observed. Therefore, this Ca-rich core and the Ca-rich twinning should form before the metamorphism of D_{3b} shearing event and probably during the crystallization of the tonalite, and the other lower-Ca regions formed during

doi:10.6342/NTU202202659

the metamorphism. Based on this interpretation, the higher An content regions in the line profile of Pl3 and Pl4 also correspond to the earlier magmatic compositions with the lower An content compositions in the rim related to those formed by metamorphism. Thus, the repetitive chemical variation patterns within the line profile of Pl3 is due to the existence of multiple plagioclase grains with a decreasing Ca content from the core to the rim. Even though these plagioclase grains undergo static recrystallization, their chemical information is still preserved.

On the ternary diagram, all the K-feldspar is plotted within K-feldspar region with limited compositional ranges of $An_0Ab_{4-9}Or_{91-96}$ (Figure 51C). The major chemical variation lies in the K and Na substitution with no Ca. In the compositional profiles, both two K-feldspar grains show the same compositional variation pattern (Figure 51D). For the longer compositional profiles of Kfs1 and Kfs3, repetitive variation pattern of first decreasing and then increasing Or contents in an antipathetic relationship with Ab contents is identified. Along the shorter line profiles of Kfs2 and Kfs4, a slight increase of Or contents from the core to rim (Or_{91} to Or_{96} in Kfs4; Or_{92} to Or_{94} in Kfs2) is accompanied by the decrease of An contents (An_9 to An_4 in Kfs4; An_8 to An_6 in Kfs2). Such repetitive compositional variation pattern is similar to the one identified in the plagioclase. From the image of chemical mapping of these K-feldspar especially the Na distribution map, these coarse-grained K-feldspar seems to be composed of multiple

doi:10.6342/NTU202202659

subgrains with the Na content decreasing from the core to the rim, which cannot be identified under the thin section alone. Hence, the cause for such repetitive compositional variation pattern in one coarse-grained feldspar is that the coarse-grained feldspar consists of multiple subgrains. These subgrains are connected into one large coarse grain during the metamorphism while the chemical composition is still preserved. In addition, the variation of Ab contents in plagioclase and K-feldspar show inverse trend, which indicates that Na distribution within these two minerals is affected by their simultaneous growth. Based on their microstructural features and compositional variation pattern, it is implied that K-feldspar and plagioclase grow at the same period under a quite consistent chemical environment during metamorphism.

doi:10.6342/NTU202202659

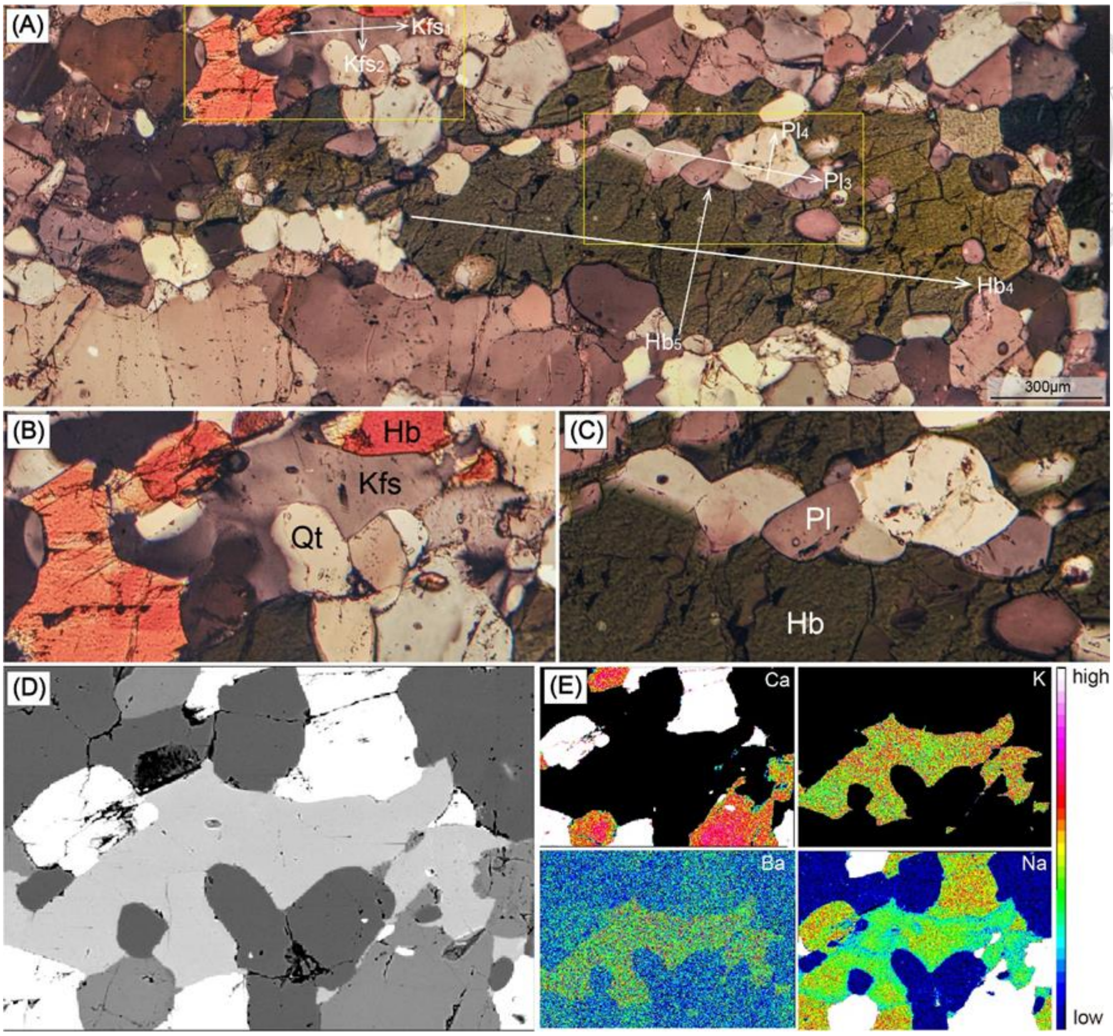

Figure 49. Petrography and chemical mapping of line profiles of K-feldspar (Kfs_1, Kfs_2) and plagioclase (Pl_3, Pl_4) in tonalitic gneiss (sample 18TP04). (A) A thin section photo under cross-polarized light with marked positions of line profile analyses (Hb_4, Hb_5, Pl_3, Pl_4, Kfs_1, Kfs_2). The yellow rectangle regions are enlarged to show detailed microstructures in figure B and C. (B,C) Microphotographs showing the microstructures of the measured K-feldspar and plagioclase. (B) K-feldspar shows undulous extinction and irregular grain boundaries, intruded by the recrystallized quartz. (C) Plagioclase shows polygonal granoblastic textures with grain boundaries migrating into the neighboring hornblende. (D) SEM-BSE image of the measured K-feldspar (Kfs_1, Kfs_2). Nearly all the minerals have grain boundaries migrate into the K-feldspar, including quartz, plagioclase, and hornblende. (E) Chemical mapping of Ca, K, Ba and Na of the same area in figure D. Weak K and Na chemical zonation is identified for K-feldspar with higher K and lower Na contents in the rim.

doi:10.6342/NTU202202659

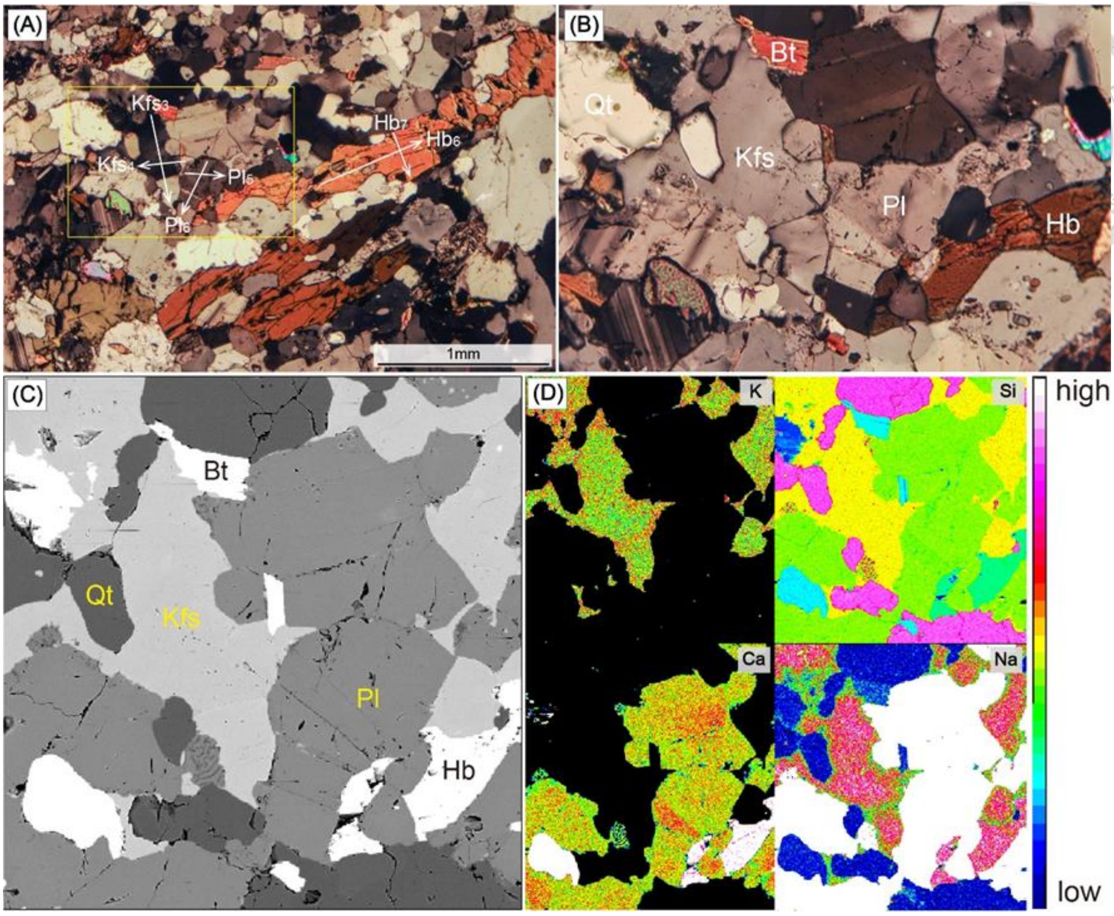

Figure 50. Petrography and chemical mapping of line profiles of K-feldspar (Kfs_3, Kfs_4) and plagioclase (Pl_5, Pl_6) in tonalitic gneiss (sample 18TP04). (A) A thin section photo under cross-polarized light with marked positions of line profile analyses (Hb_6, Hb_7, Pl_5, Pl_6, Kfs_3, Kfs_4). The yellow rectangle region is enlarged to show detailed microstructures in figure B. (B) A microphotograph showing the microstructures of the measured K-feldspar and plagioclase. K-feldspar has irregular grain boundaries with recrystallized subgrain. The grain boundaries of K-feldspar are intruded by the recrystallized quartz, plagioclase and myrmekite. (C) SEM-BSE image of the measured K-feldspar and plagioclase. Myrmekite is formed from the rim of plagioclase into the K-feldspar nearby. (D) Chemical mapping of K, Si, Ca, and Na of the same area in figure C. K and Na chemical zonation is identified for K-feldspar with higher K and lower Na contents in the rim. Ca chemical zonation is identified for the plagioclase with the higher Ca contents in the core. Besides, a high-Ca concentrated zone reflects the growth twinning of plagioclase.

doi:10.6342/NTU202202659

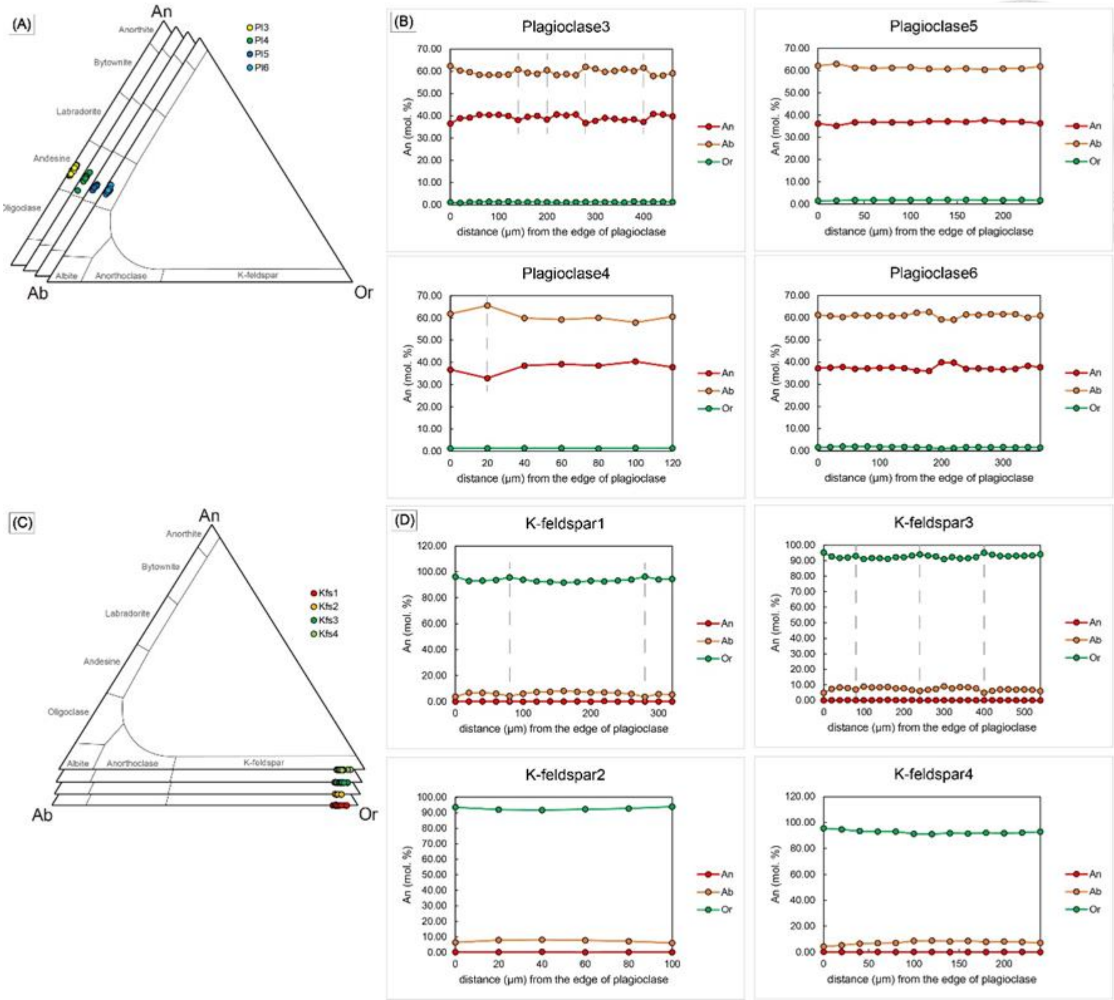

Figure 51. Line profile analysis of feldspar chemical compositions in the tonalitic gneiss (sample 18TP04). (A, C) Ternary An-Ab-Or diagram for feldspar classification (Harrison et al., 2019). (B, D) Compositional profile of An, Ab and Or contents (mol. %) plotted against the distance from the edge/starting analytical point of plagioclase and K-feldspar.

doi:10.6342/NTU202202659

Biotite

Biotite in the tonalitic gneiss defines the D_3 S/C fabrics. The Fe^{2+}+Mg (4.96-5.33 apfu) values of biotites spread between annite-phlogopite and siderophyllite-eastonite solid solution series with compositions close to annite-phlogopite. Due to the low Al_{total} contents (2.58-2.84 apfu) along with the X_{Fe} ratios (0.52-0.61), these biotites sit in the middle of the annite-phlogopite solid solution series and slightly close to annite compositions (Figure 52A). In the plot of Si+Fe^{2+}+Mg vs. Al_{total}, biotites roughly follow the Tschermak substitution line (Figure 52B). The Ti contents vary a lot from 0.21 to 0.35 apfu suggestive of local chemical heterogeneity. A small decreasing trend of Ti content from the core to rim is identified for one biotite grain, which indicates the biotite composition may have been re-equilibrated in a decreasing temperature environment.

doi:10.6342/NTU202202659

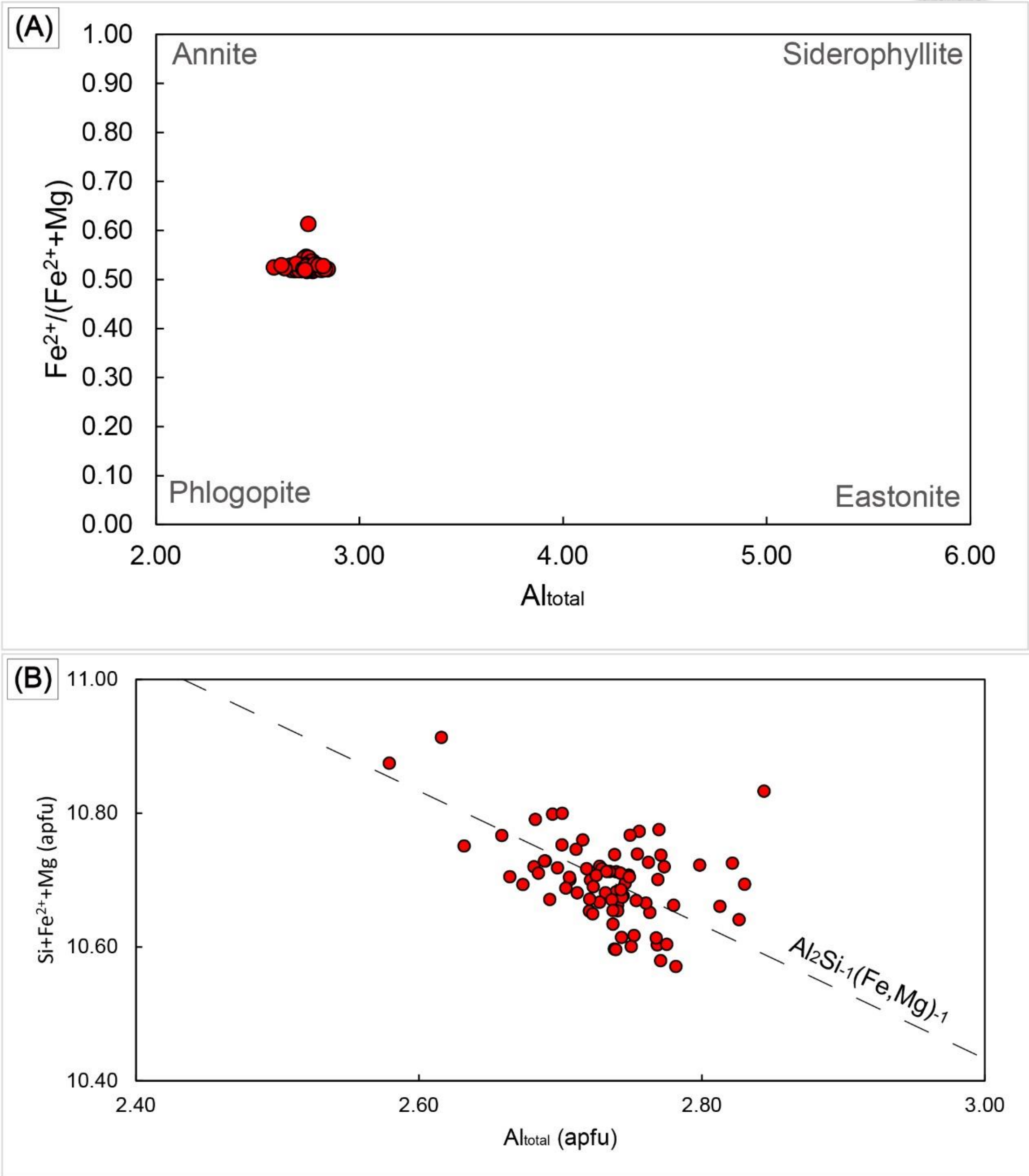

Figure 52. Plots of chemical composition of biotites in tonalitic gneiss (sample 18TP01). (A) Classification diagram for biotite species (Wlodek et al., 2015). (B) Si+Fe^{2+}+Mg plotted against total Al contents with Tschermak substitution line for comparison.

doi:10.6342/NTU202202659

Amphibole

Amphiboles are concentrated into an amphibole rich layer in the tonalitic gneiss, and this layering defines the D_3 S/C fabrics. All the amphiboles are anhedral in shape with concave inward grain boundaries, consumed by the other minerals, including quartz, plagioclase, and K-feldspar, suggesting that amphibole is concentrated without crystal growth or recrystallization during the metamorphism. Thus, their composition should reflect their crystallization from the tonalitic melt with possible re-equilibration of the composition in the rim. Two amphibole grains were measured with four line profile analyses (Hb_4, Hb_5, Hb_6, Hb_7). The selected line profiles in each amphibole are along the long and short axes of the minerals to check the chemical zonation from the core to the rim. The ratios of B-group cations show that all the amphiboles are calcium amphiboles [$^{B}(Ca+Mg+Fe^{2+}+Mn)/B_{total}$ = 0.93-1.00 > 0.75, $^{B}Ca/B_{total}$ = 0.90-0.95 > $^{B}(Fe^{2+}+Mg+Mn)/B_{total}$ = 0.00-0.16]. On the plot of $^{A}(Na+K+2Ca)$ vs. $^{C}(Al+Fe^{3+}+2Ti)$ (Hawthorne et al., 2012), nearly all amphiboles fall in the pargasite with some plotted on the boundaries between pargasite and magnesio-hornblende (Figure 53).

doi:10.6342/NTU202202659

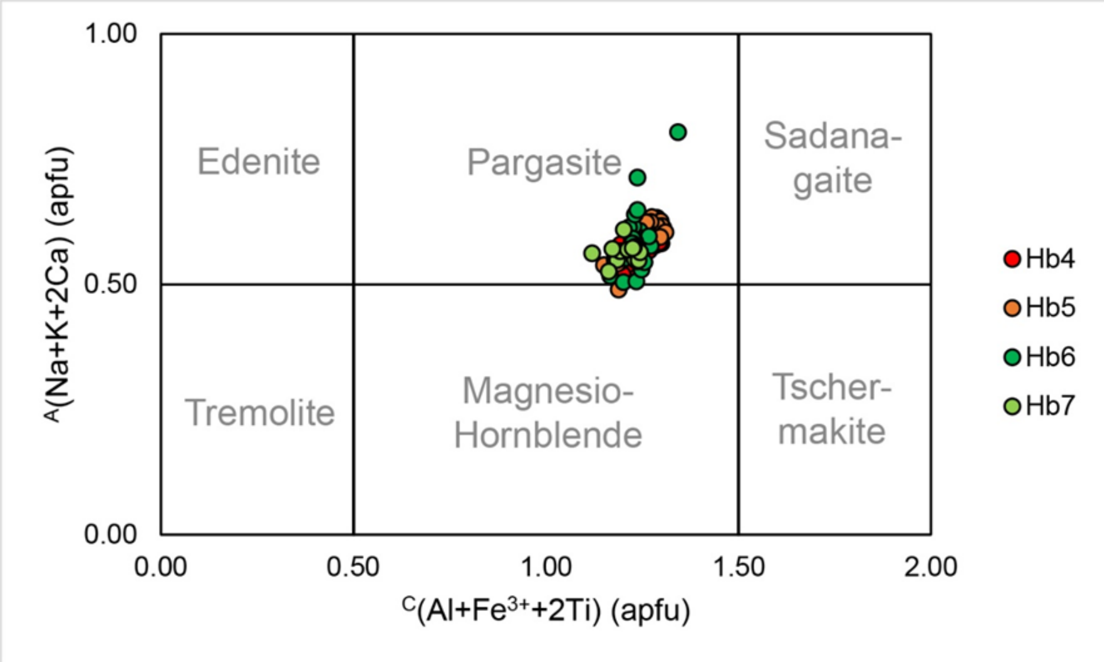

Figure 53. Chemical compositional plot of amphibole compositions from tonalitic gneiss (sample 18TP04) on a classification diagram for calcium amphiboles (Hawthorne et al., 2012).

4.3.7 Ti-in-biotite Geothermometer

Despite diverse metamorphic lithologies, biotites are ubiquitous in all these metamorphic rocks and exist in different structural domains, spanning from pre-D_1, D_1, D_2 to D_3. Therefore, biotites are suitable materials for exploring the differences of metamorphic conditions among different lithologies and deformation events. To understand these different metamorphic conditions, a Ti-in-biotite geothermometer (Henry et al., 2005) was utilized to calculate the metamorphic temperatures. The calculation results are compiled in the Appendix 8.5. The samples used for calculation mostly contain Ti-bearing minerals, except for the boudin within the biotite gneiss. Both sillimanite mica schist and biotite gneiss have ilmenite, while amphibolite and tonalitic

doi:10.6342/NTU202202659

gneiss have titanite within.

The calculation results show that nearly all the temperatures fall between 600 ˚C and 700 ˚C with a few points in the range of 550-600 ˚C and above 700 ˚C (Figure 54A). If compiling the maximum and minimum biotite temperatures for each lithology, a temperature gap larger than the errors appears (Figure 54B), suggesting that local re-equilibration of biotite chemistry occurred during the retrograde metamorphism, which can be supported by the lower temperature ranges of the biotites in the boudin (551-676 ˚C) compared to its host biotite gneiss (620-725 ˚C) in the sample 18LYB03. The biotites in the boudin have chlorite overgrowth along the cleavages (Figure 42), while the biotites in the host gneiss do not have such microstructure evidence of retrograde reactions. The lack of ilmenite within the boudin of biotite gneiss will underestimate the temperatures derived (Henry et al., 2005). Accordingly, to explore the peak metamorphic temperatures of each deformation event, the maximum temperature derived from the calculation along with the error was used to represent the possible peak temperatures for biotites in different structural domains.

The biotites in sillimanite mica schist (sample 181117A01) formed from pre-D_1 to D_1 and during D_2, and the maximum temperature range was 644-690 ˚C (Figure 54B). These temperatures are similar to the range of 650-696 ˚C from another sillimanite mica schist (sample 18LYA01), whose biotite mainly defines S_2 foliation with only a

doi:10.6342/NTU202202659

few coarse porphyroblasts forming pre-D_2. This indicated that biotites in the schist belt formed in a very consistent temperature ranges of 644-696 °C spanning from pre-D_1 to D_1 and during D_2. The biotites in biotite gneiss and the boudin within formed (sample 18LYB03) during D_2 with the biotite in gneiss defining S_2 foliation, and with maximum temperature ranges of 701-725 °C and 630-676 °C, respectively. This temperature difference can be explained by the retrograde overgrowth of chlorite along the biotite cleavage in the boudin (Figure 42), which reequilibrated the biotite composition in a lower temperature condition, as shown by the lower Ti contents of the boudin in Figure 54A. Therefore, the peak temperature range adopted for the biotite gneiss during D_2 should be around 701-725 °C derived from the host gneiss rather than the reequilibrated biotites in the boudin. In tonalitic gneiss (sample 18TP04), biotites define D_3 sinistral S/C fabrics, and the derived peak temperatures range from 658 °C to 704 °C. For the amphibolite (18TP01) collected from the same outcrop as the tonalitic gneiss, biotites has mimetic growth over the hornblende defining D_3 sinistral S/C fabrics, and the peak temperature range was estimated to be 636-682°C. This indicated that the temperatures were still sustained at approximately the same range after the cessation of the D_3 shearing event. The minimum temperatures reflect the local re-equilibration of biotite composition after the peak metamorphism of each deformation event during the retrograde conditions. Thus, the compiled minimum temperature ranges from these

doi:10.6342/NTU202202659

rocks were used to represent the temperature conditions after the D_3 deformation event. The derived retrograde temperature range is 534-622 °C, which is still in the amphibolite facies condition. In summary, all the above information suggests that the crustal temperatures may have been sustained at medium to high-grade temperature conditions for a long period of time from pre-D_1 to post-D_3. The interpreted peak temperatures for each deformation event are summarized in Figure 54C.

doi:10.6342/NTU202202659

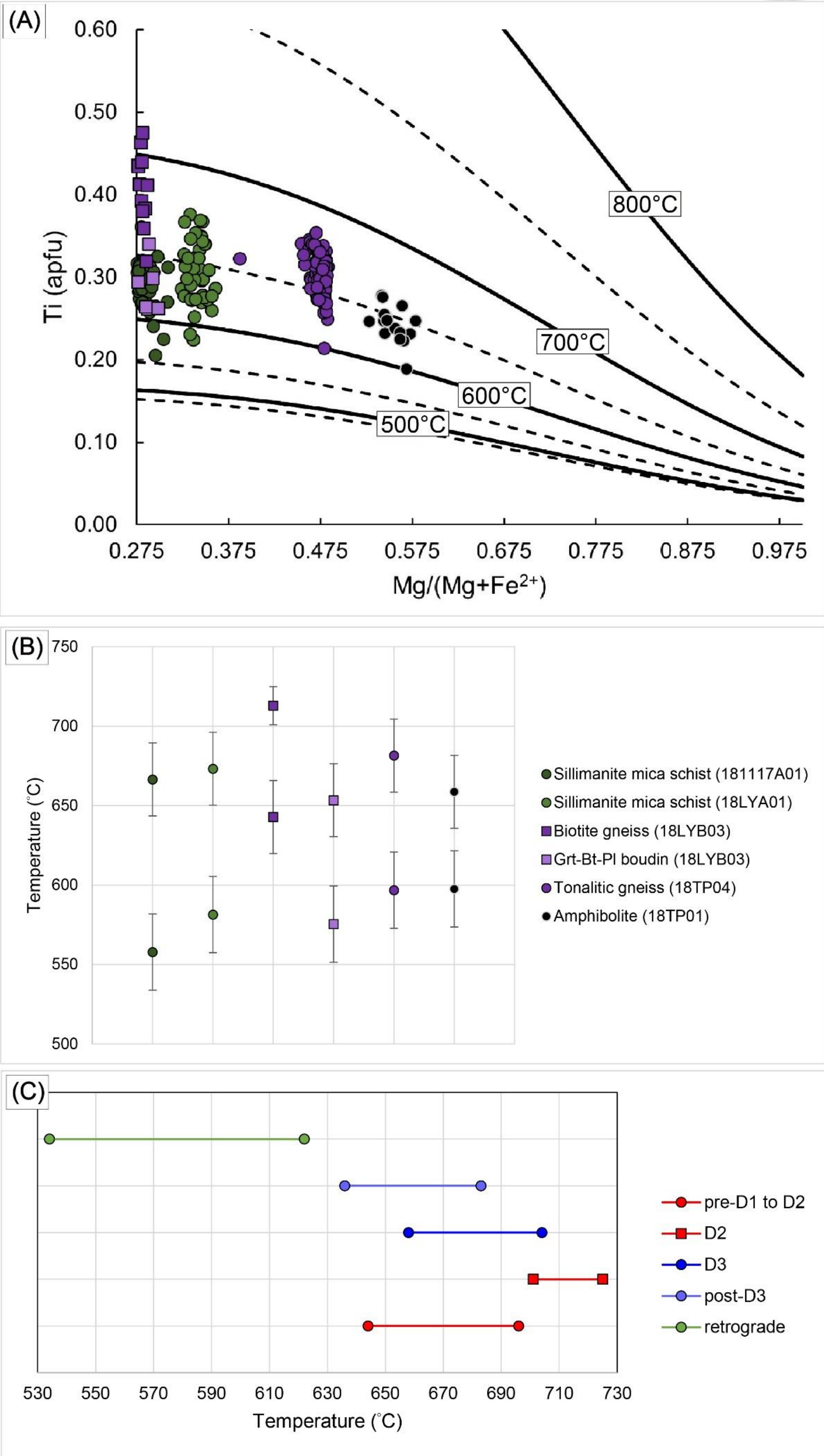

doi:10.6342/NTU202202659

Figure 54. Results of Ti-in-biotite geothermometer. (A) Two-dimensional projection plot of the Ti-saturation surface used for calibration of the Ti-in-biotite geothermometer. The Ti contents (apfu) of biotites is plotted against the X_{Mg} values to show the temperature distribution of the biotites. The dashed curves represent the 50°C interval isotherms. The legend is the same as figure B. (B) Compiled maximum and minimum temperatures of biotites from different lithologies. (C) The interpretation of biotite temperature results on the relationship between the metamorphic temperatures and the deformation events.

4.3.8 Al-in-hornblende Geobarometer

Based on petrographic analysis, coarse-grained anhedral hornblende within the tonalitic gneiss (sample 18TP04) formed during magmatic crystallization (Figure 28 and Figure 55A), which was later concentrated into a mineral-concentrated layer and re-equilibrated during D_3 sinistral shearing event. If such interpretation works, the hornblende compositions should reflect both original magmatic features and the later metamorphism during deformation. Accordingly, the chemical composition of hornblende from magmatic crystallization with Al-in-hornblende geobarometer developed by Schmidt (1992) can be used to estimate the emplacement pressures of the tonalite.

Two grains of hornblende in tonalitic gneiss were analyzed with four line profiles, Hb_4 and Hb_5 for one grain and Hb_6 and Hb_7 for the other. On the compositional profile, two distinct compositional domains can be identified from the values and the variation patterns (Figure 55B). One is the core region with smaller ranges of variation and higher

doi:10.6342/NTU202202659

Al_{totol} contents. The other one is the rim showing a larger range of variation and decreasing Al_{total} contents from the core to the edge of the hornblende. There are two possibilities for forming such compositional patterns in the hornblende. The first is the continual crystallization of hornblende from the core to the rim due to a changing composition of magma. The second is that the hornblende formed previously from magmatic crystallization and was later re-equilibrated during metamorphism. Petrographically, all hornblende shows a homogenous color of green to yellowish green in plane-polarized light without growth zoning, which is typical of episodic magmatic growth (Barnes et al., 2017). However, re-equilibration textures along the rim and fractures are commonly identified (Figure 55A). In the classification diagram of calcic amphibole, all hornblendes are plotted in a confined region except two points (Figure 53), which suggests one episode growth for hornblende. Therefore, the higher Al_{total} contents preserved in the core of hornblende may reflect the P-T condition during magmatic crystallization, and the lower, decreasing Al_{total} contents in the rim represent the re-equilibration of metamorphism during D_3 shearing event.

The Al_{total} contents on the magmatic core and re-equilibrated rim are summarized in Table 4. The core and rim compositional domains are more clearly distinguished in the line profiles of Hb_4 and Hb_5, which show evident decreasing Al_{total} contents from a relatively flat compositional profile in the core towards the rim, except for some sudden

doi:10.6342/NTU202202659

drops at some points. The sudden decrease of the Al_{total} contents can be correlated to the re-equilibrated regions along the fractures in hornblende. In contrast, line profiles of Hb_6 and Hb_7 show very weak differentiation between the core and the rim. In addition, the Al_{total} contents of Hb_6 and Hb_7 (1.91-2.15 apfu) are mostly within, and some are even lower than the range of the re-equilibrated rim of Hb_4 and Hb_5 (1.96-2.20 apfu). This suggested that the measured hornblende with line profiles of Hb_6 and Hb_7 was totally re-equilibrated during the metamorphism, and only the core from Hb_4 and Hb_5 preserved the magmatic chemistry (2.20-2.24 apfu). Hence, the Al_{total} contents of 2.20-2.24 apfu were used to calculate the emplacement pressure of the tonalite, indicating pressure conditions at 7.5-7.7 kbar ± 0.6 kbar (6.9-8.3 kbar, corresponding to 24.9-29.9 km in depth). The declining Al_{total} contents in the re-equilibrated rim from 2.20 to 1.91 apfu suggest that these hornblendes re-equilibrated at a lower pressure condition (<6.9-8.3 kbar), but still high temperature conditions for Al diffusion to occur. Along with the consistent and limited ranges of Ti contents from the core to rim (mostly 0.10-0.12 apfu), these hornblendes do re-equilibrate at lower pressure, but at a similar temperature condition as hornblende crystallizes. The same barometer applied to the re-equilibrated compositions of hornblende would indicate the pressure conditions of 6.1 ± 0.6 -6.9 kbar (5.5-6.9 kbar, corresponding to 19.8-24.9 km in depth).

doi:10.6342/NTU202202659

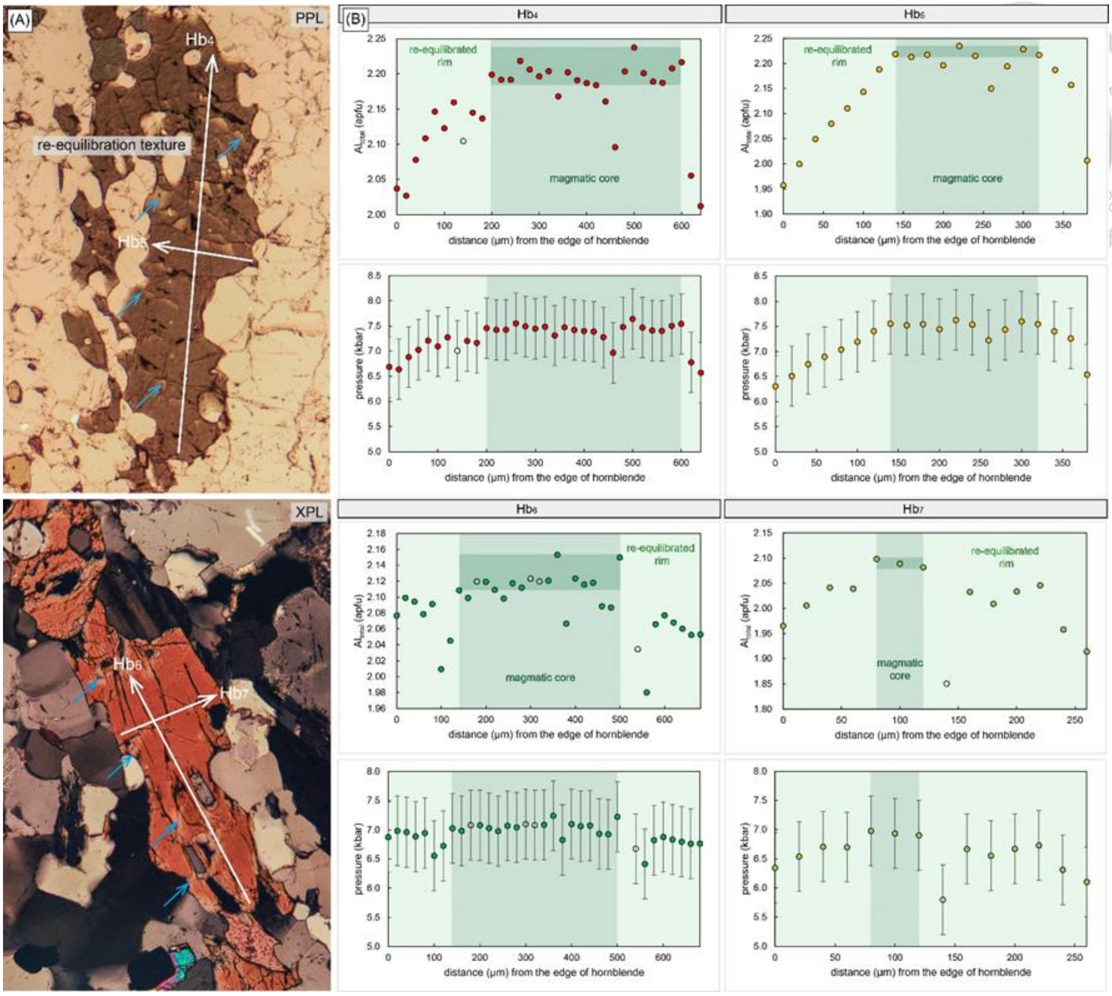

Figure 55. Line profile analyses of hornblendes in tonalitic gneiss (sample 18TP04). (A) Microphotographs showing the positions for line profile analyses of hornblende with the blue arrows indicating the re-equilibration textures along the rim and fractures in the hornblende. (B) Compositional profiles of Al_{total} contents in hornblende and the results of Al-in-hornblende geobarometer with error bars. The hollow circles are bad-quality data. The green shaded regions from the lightest to the darkest mark the interpreted re-equilibrated rims, magmatic cores, and the selected magmatic compositions in each profile.

Table 4. The interpreted Al_{total} contents in the core and rim of hornblende in each line profile.

Line profile	Magmatic core	Re-equilibrated rim
Hb4	2.18-2.24	2.01-2.17
Hb5	2.21-2.23	1.96-2.20
Hb6	2.11-2.15	1.98-2.10
Hb7	2.08-2.10	1.91-2.05

doi:10.6342/NTU202202659

4.3.9 Biotite-Muscovite Geobarometer

The biotite-muscovite geobarometer (Wu, 2020) was applied to two sillimanite mica schists due to the deficiency of plagioclase and/or garnet hindering the usage of the GASP geobarometer (Holdaway, 2001). Both samples lack rutile in the mineral assemblage, which causes the estimated pressures to be the maximum pressure during the biotite-muscovite reaction (Wu, 2020). The biotite compositions whose estimated temperatures from Ti-in-biotite geothermometer (Henry et al., 2005) are within the range of the interpreted peak temperatures were used for calculation. The results show that no matter what muscovite composition was used for calculation, the variation of the estimated pressure is smaller than 0.1 kbar (e.g., 6.075-6.084 kbar in Table 6), which is still smaller than the total errors of 1.6 kbar of the barometer (Wu, 2020). Therefore, muscovite composition is randomly chosen for the barometric calculation.

For sample 18LYA01, the estimated peak temperature range is 650-696 ˚C with a margin of error of ±23˚C for the Ti-in-biotite geothermometer (Henry et al., 2005). Therefore, the biotite compositions with calculated temperatures of 650-673 ˚C and one randomly chosen muscovite composition were used for barometric calculation. The results show that the estimated pressures range from 5.8 to 6.6 kbars with the possible maximum pressure within 5.0-8.2 kbars (Table 5). For sample 181117A01, the estimated peak temperature range is 644-690 ˚C with a margin of error of ±23˚C for

doi:10.6342/NTU202202659

the Ti-in-biotite geothermometer (Henry et al., 2005). Therefore, the biotite compositions with estimated temperatures of 644-673 ˚C and one randomly chosen muscovite composition were used for barometric calculation. The results of the barometer suggest similar estimated pressures roughly at 5.1-6.5 ±1.6 kbars with the possible maximum pressure within 4.9-8.1 kbars (Table 7).

Table 5. The result of estimated pressures from different muscovite compositions with one fixed biotite composition from sample 18LYA01.

	No.	SiO_2	TiO_2	Al_2O_3	FeO	MnO	MgO	CaO	Na_2O	K_2O	T(°C)	P(bar)
Biotite	116	34.94	3.31	20.32	22.52	0.25	6.30	0.00	0.18	9.28	673	-
Muscovite	A-32	45.28	0.32	36.66	1.22	0.04	0.37	0.00	0.73	9.83	-	6083
	A-35	47.00	0.32	35.55	0.94	0.01	0.36	0.00	0.57	9.49	-	6081
	A-47	45.83	0.48	36.77	1.02	0.00	0.46	0.03	0.72	9.90	-	6082
	A-48	45.60	0.56	36.33	1.03	0.07	0.47	0.00	0.62	10.18	-	6079
	A-74	45.57	0.88	36.79	1.33	0.02	0.42	0.00	0.62	9.75	-	6079
	A-110	45.58	0.50	36.59	1.12	0.02	0.37	0.00	0.71	9.94	-	6082
	A-111	45.35	0.64	36.48	0.83	0.08	0.38	0.00	0.62	10.09	-	6081
	A-112	45.68	0.68	36.30	1.12	0.03	0.48	0.00	0.67	9.90	-	6079
	A-123	46.34	0.41	37.02	0.90	0.00	0.40	0.04	0.66	9.85	-	6084
	A-129	45.55	0.92	36.39	0.94	0.03	0.38	0.01	0.70	9.51	-	6080
	A-130	46.35	1.15	36.25	0.97	0.01	0.41	0.01	0.63	10.01	-	6075
	A-131	46.21	0.82	37.26	0.96	0.00	0.35	0.00	0.62	9.91	-	6082
	A-132	46.09	0.51	37.50	1.06	0.01	0.45	0.03	0.74	9.97	-	6083
	A-133	46.02	0.85	37.11	1.08	0.05	0.36	0.02	0.66	9.97	-	6080
	A-134	46.41	1.08	36.96	1.09	0.05	0.46	0.00	0.69	9.75	-	6077

doi:10.6342/NTU202202659

Table 6. The mica compositions used for biotite-muscovite geobarometer of sample 18LYA01 with the results of the calculated pressure.

	No.	SiO_2	TiO_2	Al_2O_3	FeO	MnO	MgO	CaO	Na_2O	K_2O	T(°C)	P(bar)
Biotite	7	34.79	2.90	20.50	21.52	0.21	6.30	0.08	0.22	8.96	655	6054
	23	35.00	2.84	19.93	22.35	0.31	6.08	0.03	0.18	9.07	650	5763
	55	34.99	3.04	20.33	20.91	0.38	6.17	0.00	0.17	9.07	663	6348
	71	35.09	2.96	20.33	21.04	0.32	6.34	0.00	0.27	8.86	659	6210
	73	34.50	3.03	20.37	21.85	0.21	6.46	0.00	0.22	9.18	662	5982
	100	34.64	2.93	20.35	20.95	0.17	6.29	0.00	0.27	8.78	659	6234
	105	35.40	3.01	20.17	21.54	0.23	6.40	0.00	0.16	9.21	660	6089
	106	34.58	3.20	20.06	21.95	0.27	6.53	0.00	0.19	9.18	671	6016
	107	34.64	3.08	20.33	22.29	0.17	6.40	0.04	0.22	8.74	664	5983
	116	34.94	3.31	20.32	22.52	0.25	6.30	0.00	0.18	9.28	673	6088
	117	35.09	3.23	20.91	20.96	0.21	6.17	0.05	0.14	8.91	671	6645
	118	34.48	3.17	20.22	21.70	0.25	5.92	0.03	0.15	9.12	669	6279
	120	34.87	3.03	20.54	22.16	0.20	6.22	0.01	0.19	9.14	660	6046
	121	35.08	2.81	20.57	21.18	0.28	6.18	0.00	0.18	8.61	650	6187
Muscovite	A-32	45.28	0.32	36.66	1.22	0.04	0.37	0.00	0.73	9.83	-	-

Table 7. The mica compositions used for biotite-muscovite geobarometer of sample 181117A01 with the results of the calculated pressure.

	No.	SiO_2	TiO_2	Al_2O_3	FeO	MnO	MgO	CaO	Na_2O	K_2O	T(°C)	P(bar)
Biotite	28	33.97	3.14	18.77	24.08	0.42	4.75	0.02	0.28	8.97	667	5711
	40	35.50	3.13	19.42	22.29	0.41	4.32	0.04	0.27	9.26	663	6532
	61	35.45	3.09	18.10	23.52	0.37	5.13	0.00	0.31	9.31	663	5619
	42	35.47	2.95	18.96	23.58	0.41	4.88	0.02	0.30	9.17	653	5748
	117	35.29	2.78	18.76	22.71	0.37	5.39	0.00	0.29	9.38	647	5572
	32	34.26	2.71	18.15	24.20	0.39	5.09	0.00	0.21	9.43	644	5091
Muscovite	1	46.56	0.97	34.72	1.87	0.07	0.67	0.07	0.66	9.41	-	-

doi:10.6342/NTU202202659

5 Discussion

5.1 P-T Evolution during Crustal Deformation of Kinmen Island

5.1.1 Estimated P-T Conditions for each Deformation Event

Based on the results of reconstructed structural evolution, the deformed granitoids and its associated metamorphic complexes in Kinmen Island experienced the same deformation history after the crystallization of the granitoids (Taiwushan Granite and Chenggong Tonalite). The high-grade mineral assemblages of the metamorphic rocks and the high-temperature deformation microstructures of the granitoids show that these rocks appear to be deformed under similar P-T conditions under at least amphibolite facies (Huang and Yeh, 2020). Therefore, the P-T conditions derived from the metamorphic rocks can be used to estimate/represent the P-T conditions during deformation of the granitoids after their emplacement. By compiling the results of mineral chemistry, geothermobarometers and the identified metamorphic reactions from these complex granitoid and metamorphic basements, the P-T evolution during the crustal deformation of the granitoid basements of Kinmen Island can be inferred, as shown in Figure 56.

According to the Al-in-hornblende geobarometer, the granitoid core of Taiwushan Granite may have crystallized at 7.9-8.4 kbar (Lo et al., 1993), which is around 28.3-30.4 km in depth by assuming mean continental crust density of 2830 kg/m^3

doi:10.6342/NTU202202659

(Christensen and Mooney, 1995). Chenggong Tonalite emplaced at 6.9-8.3 kbar (around 24.9-29.9 km). From the strain state of the D_1 gneiss dome and D_2 subhorizontal S-tectonite (Figure 9, 10), the crystalline basement of Kinmen Island had been continually exhumed in a crustal thinning setting during deformation. Besides, all the deformation events appear to have occurred after the crystallization of the granitoids. Therefore, the maximum confining pressure of the basement during D_1 and D_2 should be lower than the emplacement pressure of the granitoids (at least < 28.3-29.9 km). The interpreted crustal thinning setting during deformation is supported by the contemporaneous opening of extensional basins in the upper crust in the South China Block (Li et al., 2014). The biotites in sillimanite mica schist and biotite gneiss formed from pre-D_1 to D_2, and the range of peak metamorphic temperatures derived from Ti-in-biotite thermometers is at 644-725 °C (Figure 54C). The maximum pressures estimated from biotite-muscovite geobarometer is 4.9-8.2 kbar for sillimanite mica schist. Besides, the D_1-folded sillimanite inclusion trails within muscovite porphyroblast growing intertectonically between D_1 and D_2 show that the metamorphic conditions were within the sillimanite stability field during pre-D_1. In sum, the P-T conditions from pre-D_1 to D_2 should fall in the range of around 644-725 °C with a maximum pressure of 8.2 kbar (around 29.4km). The consistency of the estimated maximum pressure of 8.2 kbar for sillimanite mica schist and the emplacement pressure of 7.9-8.4 kbar for Taiwushan

doi:10.6342/NTU202202659

Granite suggests that the schists were the country rock during the intrusion of the granitoid complex.

As for D_3 the shear folding event, the biotites in tonalitic gneiss define the D_3 shearing fabrics with the estimated peak metamorphic temperatures falling between 658 °C and 704 °C (Figure 54C). In sillimanite mica schist, the stretching lineation of the D_3 shear zone was defined by the growth of fibrolite and poikiloblastic K-feldspar with the dehydration melting of muscovite porphyroblasts. In addition, *in-situ* crustal anatexis during the shear zone development was commonly identified in the schist belt. Such a typical metamorphic reaction, Muscovite + Quartz → Sillimanite + K-feldspar + Melt, commonly occurs in metapelite above middle amphibolite facies. Considering the D_3 biotite metamorphic temperatures and the identified muscovite dehydration reaction, the P-T conditions during the D_3 shear folding event are estimated at 658-704 °C with a maximum pressure of 5.5 kbar (around 19.8 km). After the cessation of the D_3 shearing event, post-kinematic mimetic growth of biotite over the hornblende defining D_3 S/C fabrics in the amphibolite were identified. The calculated metamorphic temperatures from these biotites are estimated to be in the lower ranges of 636-682 °C (Figure 54C). During this tectonic quiescence period, the rocks should stay at probably the same level without much vertical movement. With the constraint from the biotite metamorphic temperatures and the similar sillimanite stability field as D_3, the P-T

doi:10.6342/NTU202202659

conditions when D_3 shearing ceased would be around 636-682 ˚C with a maximum pressure of 4.6 kbar (around 16.7 km).

Despite a lack of mineral composition data from the samples in the D_4 domain, the P-T ranges can still be constrained by evidence from the deformation features, petrography, and the mineral chemistry information from the available samples. D_4 formed a transtensional shear zone throughout the basement of Kinmen Island, which suggests that the continental crust was thinned under extension. Such a crustal thinning setting will decrease the confining pressure of the basements, which should be at least lower than the maximum pressure of D_3 (<4.6 kbar). The ductile deformation of feldspar-quartz aggregates in the tonalitic gneiss and the amphibolite with D_4 shearing fabrics showing that the P-T conditions during D_4 shearing event were still within amphibolite facies. By compiling the re-equilibrated metamorphic temperatures of biotites from all the lithologies, the temperature condition is estimated at 534-622 ˚C (Figure 54C), which is apparently lower than the temperature ranges from pre-D_1 to D_{3end} (636-725 ˚C). However, these temperatures are still high enough in the amphibolite facies to initiate ductile deformation. This is consistent with the field and petrography observations. Besides, the continental crust was deformed by brittle fracturing with dyke intrusion during D_5 and D_6, when the crustal temperatures should have been as low as around <300 ˚C. Thus, the derived metamorphic temperatures from

doi:10.6342/NTU202202659

re-equilibrated biotites should reflect the temperature conditions after D_{3end} and before D_5. This interpretation is also supported by the chemical compositions of the retrograde overprint of muscovite over plagioclase within the boudin of biotite gneiss (Figure 38; Figure 41B). This retrograde muscovite has chemical compositions characteristic of muscovite from the staurolite zone into the sillimanite and K-feldspar zone (Figure 41B). This suggests that the muscovite formed at temperature conditions within, at least, the staurolite zone (500-650°C; Borisova and Baltybaev, 2021). Overall, the P-T conditions from post-D_{3end} to pre-D_5 can be constrained within the temperature range of 534-622 ˚C with the pressure lower than D_3.

doi:10.6342/NTU202202659

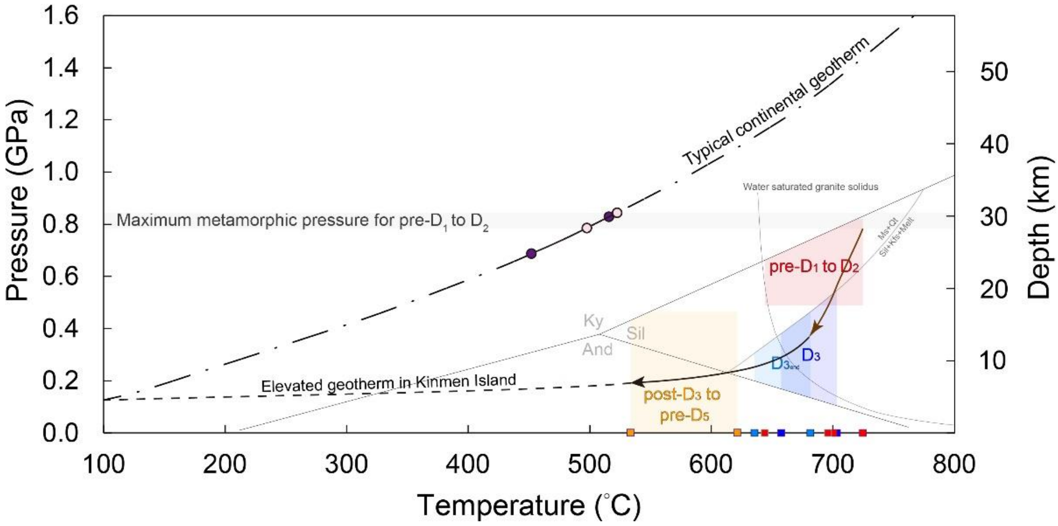

Geothermobarometer	Lithology	Temperature	Pressure (depth)
Al-in-Hornblende Barometer	○ Taiwushan Granite	498-523°C	7.9-8.4 kbar (28.3-30.4km)[1]
	● Chenggong Tonalite	452-516°C	6.9-8.3 kbar (24.9-29.9km)
Ti-in-Biotite Thermometer	■ Sillimanite mica schsit (pre-D_1 to D_2)	644-696°C	11.6-13.3 kbar (41.8-48.0km)
	■ Biotite gneiss (D_2)	701-725°C	13.5-14.4 kbar (48.7-51.9km)
	■ Tonalitic gneiss (D_3)	658-704°C	12.0-13.6 kbar (43.3-49.0km)
	■ Amphibolite (D_{3end})	636-682°C	11.4-12.8 kbar (41.1-46.2km)
	■ Re-equilibrated biotite (post-D_3 to pre-D_5)	534-622°C	8.7-11.0 kbar (31.4-39.7km)

Note: The temperatures and pressures in brown color are derived from the typical continental geotherm for comparison.
[1]Compiled from Lo et al (1993).

Figure 56. The estimated P-T ranges for each deformation event and the reconstructed P-T path of Kinmen Island. The typical continental geotherm represents the continental crust without heat perturbation due to tectonic events, and the geotherm is from Winter (2013). The calculated temperatures and pressures from geothermobarometers are plotted onto the typical continental geotherm to derive the corresponding temperatures and pressures. It is suggested that Kinmen Island had an elevated geotherm compared with the typical continental geotherm.

doi:10.6342/NTU202202659

5.1.2 Reconstructed P-T path and Elevated Geotherm in Kinmen Island

To reveal the P-T evolution accompanying the deformation of the granitoids in Kinmen Island, the P-T path should pass through the inferred P-T regions for each deformation event (Figure 56). All the deformation events occurred after the crystallization of the granitoid basements; thus, their P-T conditions are the starting point for later geological events. Due to the development of D_2 subhorizontal S-tectonite indicating an already thinned crust, the maximum pressure of D_2 should be lower than the crystallization depth of the granitoid basements (<7.9 kbar). Therefore, the peak temperature and pressure of 725 °C and 7.9 kbar is set to be the initial point for the P-T path. The peak metamorphic temperatures of D_3 are within the values of pre-D_1 to D_2 but have a narrower range, and the maximum pressure is 5.5 kbar constrained by the muscovite dehydration reaction and the maximum biotite metamorphic temperatures (704 °C). Accordingly, the basements of Kinmen Island should be exhumed from 7.9-8.4 kbar to at least 5.5 kbar or an even shallower crustal level during D_3. The P-T path is thus placed passing through the point at peak temperature and pressure of D_3 at 704 °C and 5.5 kbar. At the end of D_3, mimetic growth of biotite over the hornblende defining D_3 shear fabrics suggests there was no tectonic movement to significantly displace the basements vertically in the crust, so a similar pressure condition as D_3 can be assumed. However, a lower temperature range shows

doi:10.6342/NTU202202659

that the crustal temperature was on the decrease. Although no available geothermobarometers can be applied on samples collected from the D_4 domain, the sillimanite-over-muscovite reaction was also identified in the D_4 domain. It is assumed that the P-T conditions during D_4 were still in the lower pressure side of the muscovite -into-sillimanite reaction line. The transtensional movement of the D_4 shear zone also indicates a lower pressure condition with respect to D_3. Thus, the P-T path is set to pass from the D_{3end} region to the intersection point of the muscovite into sillimanite reaction line and the univariant line of andalusite and sillimanite. Finally, the P-T path should go through the post-D_3 to pre-D_5 regions, which can be confined by the metamorphic temperatures of the re-equilibrated biotites.

It can therefore be concluded that, the reconstructed P-T path of Kinmen Island shows two distinct stages of P-T change. The first stage is a near isothermal decompression path from 725˚C and 7.9 kbar to 704 ˚C and 5.5 kbar, since the crystallization of the granitoid complexes until D_3. It is then followed by a large temperature drop from 704 ˚C to 534 ˚C with smaller decline of pressure over temperature change from D_3 to pre-D_5. Furthermore, by projecting the metamorphic temperatures of Kinmen Island onto a typical continental geotherm, such high temperatures from pre-D_1 to D_{3end} can only be reached at deep crustal levels of 41.1-51.9 km in depth. However, these high temperatures were achieved at relatively

doi:10.6342/NTU202202659

shallower crustal depths (<28.3 km during D_2, <19.8 km during D_3 and <16.7 km during D_{3end}) and were sustained through four deformation events, thus indicating that Kinmen Island had an elevated geotherm during these deformation events, and the apparent geothermal gradient was around 918°C/GPa or 25.6 °C/km.

5.2 Heat Source for the Sustained High-grade Metamorphism in Shallow Crust

According to field observations, all the ductile deformation occurred after the emplacement of the deformed granitoids, including Taiwushan Granite (139 Ma; Yui et al., 1996) and Chenggong Tonalite (129 Ma; Lin et al., 2011). The intrusion of Tienpu Granite at 100 Ma (Lin et al., 2011) marked the end of ductile deformation and so did the accompanying high-grade metamorphism. Therefore, the high-grade metamorphism accompanying the ductile deformation of Kinmen Island had been sustained for 29 million years. Compared with the typical continental geotherm (Winter, 2013), the elevated geotherm established from the reconstructed P-T path of Kinmen Island requires heat perturbation of the crustal thermal structures to achieve amphibolite to granulite facies temperatures (534-725 °C) in the shallower crust (<28.3 km). To maintain the increased geothermal gradients for a long-lasting time (e.g., 29 million years), heat should be continually and stably supplied to the crust, which can first exclude the possibility of contact metamorphism caused by magmatic intrusion. Magmatic intrusion is a single geological event, and the cooling rates of plutons to the

doi:10.6342/NTU202202659

ambient wall rock temperatures are mostly within 2 million years (Nabelek et al., 2012), which makes it unlikely to be a stable heat supplier for tens of millions of years.

Another possible mechanism is to bury the rocks into a deeper depth where the high temperatures can be reached, which commonly occurs in an orogenic belt during crustal thickening (Zhang et al., 2015). However, the reconstructed P-T evolution of Kinmen Island shows a decompression path since the crystallization of the granitoid basements. Moreover, the ductile-to-brittle deformation along with the extensional strain patterns, and the mafic dyke swarms crosscutting all the geological events indicate a continually thinned crust in Kinmen Island (Huang and Yeh, 2020). Therefore, the possibility of deep burial of the rocks during crustal thickening can be ruled out. The other possibility is the advective heat transferred from hot materials, including magma, hot crustal units, or an upwelling asthenosphere (Miyazaki, 2004; Berger et al., 2011; Santosh et al., 2012). From the field observations, multiple episodes of crustal anatexis producing leucogranitic melts accompanying the deformation events were commonly identified within the metamorphic rocks in Kinmen Island from D_1 to D_3. Such migmatitic crustal conditions are consistent with the estimated P-T regions mostly above the water-saturated granite solidus. The widespread melt migration throughout the schist belts can effectively transport the heat from the deeper to the shallower crust and produce a high dP/dT thermal profile in the deeper crust, as suggested by the

doi:10.6342/NTU202202659

numerical thermal modelling from Miyazaki (2004). Also, the syntectonic intrusion of mafic magma into middle to upper crustal levels during D_3, D_4 and D_6 suggests that there was a continual partial melting of the underlying asthenosphere for a long time. The derived mafic magma could underplate to contribute the conductive heat to trigger the high-grade metamorphism in the above continental crust (Bohlen and Mezger, 1989). Such continual and widespread melt migration throughout the continental crust as the basements exhumed to the upper crust shows that advective heat transfer of melt migration plays an important role in providing the heat to initiate the high-grade metamorphism at the shallow crust. The migration of these mafic magma from the base of the lithosphere upward to the upper crustal levels indicates that the continental lithosphere was highly attenuated to an almost rifting stage (Zheng and Chen, 2017). The accompanying upwelling asthenosphere during the lithospheric thinning can displace the 600 °C isotherm to shallow crustal levels at around 10 km at a continental margin under a longstanding extension (at least 16 million years; Brune et al., 2014), which is quite consistent with the estimated P-T ranges of Kinmen Island. In conclusion, the heat source for the sustained high-grade metamorphism in the shallower crustal levels may be attributed to the continual and long-lasting melt production and migration throughout the continental crust, and the upwelling asthenosphere due to tens of millions of years of lithospheric thinning.

doi:10.6342/NTU202202659

5.3 Thermochronological Constraints on Reconstructed Structural Evolution

5.3.1 Timing for Deformation Events

Based on the crosscutting relationship observed in the field and oriented thin sections, six deformation events have been reconstructed from Taiwushan Granite, Chenggong Tonalite and Kingueishan Schist, which revises the original five deformation events proposed by the previous study (Huang and Yeh, 2020). Four ductile deformation events (D_1, D_2, D_3, and D_4) were followed by two magmatic intrusions under brittle conditions (D_5 pegmatitic dyke and Tienpu Granite, and D_6 mafic dyke swarm). From the crystallization ages of these magmas, the timing of D_1-D_4, D_5 and D_6 can be roughly constrained. The deformed 144-139 Ma Taiwushan Granite (Yui et al., 1996; Chen et al., 2020) and 134-129 Ma Chenggong Tonalite (Lin et al., 2011; Chen et al., 2020) were intruded by the 100 Ma Tienpu Granite (D_5; Yui et al., 1996), which suggests that D_1-D_4 occurred within 129-100 Ma. The intrusion of the 90-76 Ma mafic dyke swarm (D_6; Lee, 1994) sets the timing for D_5 within 100-90 Ma. With the P-T estimation for four ductile deformation events from petrographic analysis and the Ti-in-biotite geothermometer used in this study, the cooling path of the ductilely deformed Taiwushan Granite and Chenggong Tonalite reconstructed by Huang and Yeh (2020) can be revised (pink dashed line in Figure 57).

The zircon saturation temperature (T_{Zr}) can provide minimum estimates of the

doi:10.6342/NTU202202659

magma temperatures for Zr-undersaturated rocks (Miller et al., 2003), which is the case of the granitoids (e.g., Taiwushan Granite and Chenggong Tonalite) in Kinmen Island with whole-rock Zr concentration smaller than 150 ppm (Chen et al., 2020). The calculated T_{Zr} of 746-712 ˚C for Taiwushan Granite and Chenggong Tonalite (Chen et al., 2020) is used to constrain the crystallization temperatures of these granitoids (gray rectangle behind the zircon symbol in Figure 57). The maximum temperature for pre-D_1 to D_2 estimated from Ti-in-biotite geothermometer is 725 ˚C, which is within the range of T_{Zr} of the granitoids. It is reasonable to expect a similar temperature condition for metamorphism just after the granitoid crystallization; thus, 725 ˚C is set at 129 Ma just after the crystallization of Chenggong Tonalite (Figure 57). Despite having difficulty in differentiating the temperature conditions of pre-D_1 to D_2 and D_3 due to estimated overlapping temperature ranges, the possible maximum temperature of 704 ˚C of D_3 is set at the boundary if considering that the continual exhumation of the granitoids would gradually lower the temperature conditions (Huang and Yeh, 2020). As the reconstructed cooling curve is correlated to 704 ˚C, the timing of 117 Ma at the boundary between pre-D_1 to D_2 and D_3 can be derived (Figure 57). The possible minimum temperature of D_3 (636 ˚C) is set at the boundary between D_3 and D_4 because of a small temperature gap between the temperature ranges of D_3 and the re-equilibrated biotites interpreted to be post-D_3 to pre-D_5. As the reconstructed cooling curve is

doi:10.6342/NTU202202659

correlated to 636 ˚C, a time range of 117 to 110 Ma can be inferred for D_3. Finally, the possible minimum temperature of post-D_3 to pre-D_5 is 534 ˚C, which should not be the temperature condition for D_5, when the continental crust was deformed by brittle fracturing. This estimated minimum temperature is considerably consistent with the closure temperature of 557 ± 7°C for the 100.2 ± 0.9 Ma hornblende separates from Taiwushan Granite (Lo et al., 1993). Therefore, the temperature of 534 ˚C is set at 100 Ma marking the termination of all ductile deformation events (Figure 57). Combining the results above, the Ar-Ar age of hornblende from Taiwushan Granite is the cooling age. The metamorphic temperatures of four ductile deformation events should be higher than the estimated closure temperature of 557 ± 7°C. Such interpretation is consistent with the results of the Ti-in-biotite geothermometers in this study with a possible minimum temperature of 534 ˚C (Figure 56). In summary, the estimated timing for pre-D_1 to D_2 is 129-117 Ma, for D_3 is 117-110 Ma, for D_4 is 110-100 Ma, for D_5 is 100-90 Ma, and for D_6 is 90-76 Ma.

5.3.2 Estimated Cooling Rates and their Tectonic Implication

Four stages of different cooling rates can be recognized from the reconstructed cooling path for the deformed Taiwushan Granite and Chenggong Tonalite in this study (Figure 57). The first stage is featured by having had the slowest cooling rate of 1.8 °C/Ma from 725 °C at 129 Ma to 704 °C at 117 Ma during pre-D_1 to D_2, which shows

doi:10.6342/NTU202202659

that the high temperature condition (>700 °C) was sustained during the exhumation and gravitational collapse of the gneiss dome in Kinmen Island. The second stage had a faster but still relatively slow cooling rate of 8.6 °C/Ma from 704 °C at 117 Ma to 557 °C at 100 Ma. This faster cooling rate corresponds to the initiation of D_3 shear folding and D_4 transtensional shear zone, which can trigger a more rapid exhumation of the basement, compared with D_1 and D_2, into shallower levels with lower crustal temperatures. If using the apparent geotherm (25.6 °C/km) to transform the cooling rates into uplift rates, the cooling rate of 1.8 °C/Ma and 8.6 °C/Ma equals to 0.07 mm/yr and 0.34 mm/yr respectively. Such uplift rates are extremely slow compared with the expected exhumation rates for normal exhumation of most mountain ranges (> 1mm/yr; Burbank, 2002). If using the estimated uplift rates to calculate the vertical movement of the basement, the basement of Kinmen Island would be exhumed to the depth of 21.7 km after all the ductile deformation events. However, this depth is deeper than the possible maximum pressure of D_3 (5.5 kbar; 19.8 km; Figure 56), suggesting that the actual uplift rates are higher than that inferred from the cooling rates, namely that the cooling rates cannot reflect the vertical movement of the basement in Kinmen Island. Such discrepancy can be explained by the changing thermal structure of the continental crust during crustal thinning, more specifically the displacement of the isotherms into shallower depths [e.g., Figure 3 in Brune et al. (2014)]. Due to the shallowing depths

doi:10.6342/NTU202202659

of the isotherms, the high temperature conditions can be achieved at shallower levels to retard the decrease of temperature during the continual exhumation of the crust as evidenced by the very slow cooling rates from pre-D_1 to D_4.

The third stage had the fastest cooling rate of 88.3 °C/Ma cooling from 557 °C at 100.2 Ma to 292 °C at 97.2 Ma (Figure 57; Lo et al., 1993), which passes through the brittle-ductile transition of the continental crust (Fossen, 2016), as supported by the initiation of brittle fracturing of the crust (D_5 and D_6) after 100 Ma. Such a fast-cooling rate can be explained by passing through the densely concentrated isotherms nearby the brittle-ductile transition zone due to the shallowing depths of the isotherms [Figure 4 in Li et al. (2019)]. This scenario is supported by the fast-cooling rate of >61.1 °C/Ma cooling from >700 °C at 100 Ma (Yui et a., 1996) to 333 °C at 94.1 Ma (Lin, 1994) derived from the cooling path of Tienpu Granite (yellow dashed line in Figure 57). Such a fast-cooling rate can be ascribed to the cooling of pluton to an ambient crustal temperature, which was <300-350 °C as Tienpu Granite emplaced into the crust. Finally, a slow cooling rate of 5.6 °C/Ma followed the fastest cooling stage until the end of D_6. By converting the cooling rate into the uplift rate, 0.22 mm/yr is derived. For tectonically stable regions regardless of climate conditions, the long-term erosion rates are generally smaller than 0.1 mm/yr (Granger, 2007). Therefore, such uplift rate is a consequence of erosion facilitated by the continual opening of fractures (D_5 and D_6)

doi:10.6342/NTU202202659

within the upper continental crust.

5.3.3 Comparison to Pingtan-Dongshan Metamorphic Belt

The Pingtan-Dongshan Metamorphic Belt (PDMB) is a NE-striking tectonic unit along the southeast coast of Cathaysia Block (Figure 1), in which Kinmen Island is in the middle part of the PDMB. To better constrain the timing of the reconstructed deformation events of Kinmen Island, the available geochronological data (e.g., $^{40}Ar/^{39}Ar$ and U-Pb) from the PDMB are discussed below.

Li et al. (2015) analyzed the U-Pb zircon ages of four mica schists from Putian and Dongshan Islands, in the northern and southern section of the PDMB. The mineral assemblage is Ms + Qt ± Sil ± Rt ± Mag, which seems similar to the sillimanite mica schist in Kinmen Island (Ms + Qt + Sil + Bt + Kfs + Ilm ± Grt), but with varying metamorphic grades. The ages of the metamorphic zircon growth within the sillimanite mica schists range from 128.3 ± 1.9 Ma to 99.4 ± 2.4 Ma, which is consistent with the interpreted ages of deformation and related metamorphism at 129-100 Ma in Kinmen Island. Such a coincidence of timing further verifies that sustained high-grade metamorphism with a duration of ca. 30 million years did occur in Kinmen Island or even the whole metamorphic belt (PDMB) during the Cretaceous.

Wang and Lu (2000) conducted a $^{40}Ar/^{39}Ar$ geochronological analysis on five mylonitized samples from the southern section of the PDMB [Figure 1 in Wang and Lu

doi:10.6342/NTU202202659

(2000)]. The outcrops where these five samples were collected are characterized by NE-striking shearing fabrics of both sinistral and dextral shear senses and tight folds within. The stretching lineation plunges horizontally to gently towards NE and SW, which is defined by strongly elongated and recrystallized quartz aggregates. Petrographically, quartz is ductily deformed while feldspar is fractured. Despite the lower temperature condition, similar structural features can still be correlated to the D_3 shear folding event in Kinmen Island. The $^{40}Ar/^{39}Ar$ plateau ages from the biotite and muscovite show a range of 118-107 Ma. Considering the greenschist-facies condition during the shearing event, Wang and Lu (2000) interpreted this age to be the ductile deformation and mylonitization, which is consistent with the estimated timing of 117-110 Ma for D_3 in this study. Such timing is also supported by the crystallization age of syn-tectonic granitoid intrusion at Dongshan Island (121.5 ± 2.8 Ma; Tong and Tobisch, 1996), in the southern section of the PDMB. The granitoid is deformed with NE-striking sinistral shearing fabrics and subhorizontal stretching lineation, which can also be correlated to the D_3 shear folding event in Kinmen Island. Besides, the Al-in-hornblende geobarometer and fluid inclusion analysis suggests that the P-T conditions during the shearing are 700-740 ˚C and 4.2-4.9 kbar. Such P-T conditions are found to be similar to the P-T estimation of 658-704 °C and <5.5 kbar for D_3 in Kinmen Island as discussed in the present study.

doi:10.6342/NTU202202659

Chen et al. (2002) reconstructed the cooling curves for the entire metamorphic belt (PDMB) from $^{40}Ar/^{39}Ar$ thermochronology. Their results showed that the most rapid cooling from hornblende to biotite closure temperature occured within 110-85 Ma except for Pingtan Island within 132-126 Ma, sitting in the most northern part of the PDMB [Figure 5 in Chen et al. (2002)]. Such a time gap suggests that Pingtan Island had a different tectonic history during Cretaceous compared with the other regions within the PDMB. The rapid cooling of 110-85 Ma of the other regions within the PDMB corresponds to the timing of D_4 transtensional shear zone and D_5 brittle fracturing in Kinmen Island, when the continental crust passed through the brittle-ductile transition zone. If considering the slow cooling rates during crustal deformation of D_4 and D_5 are 8.6 °C/Ma and 5.6 °C/Ma, respectively, such fast-cooling rates of > 40-50 °C/Ma (Chen et al., 2002) cannot be attributed to the tectonic exhumation. Instead, the passing through densely-concentrated isotherms in the shallower crust due to upwelling mantle (Brune et al., 2014) may be responsible for the case.

doi:10.6342/NTU202202659

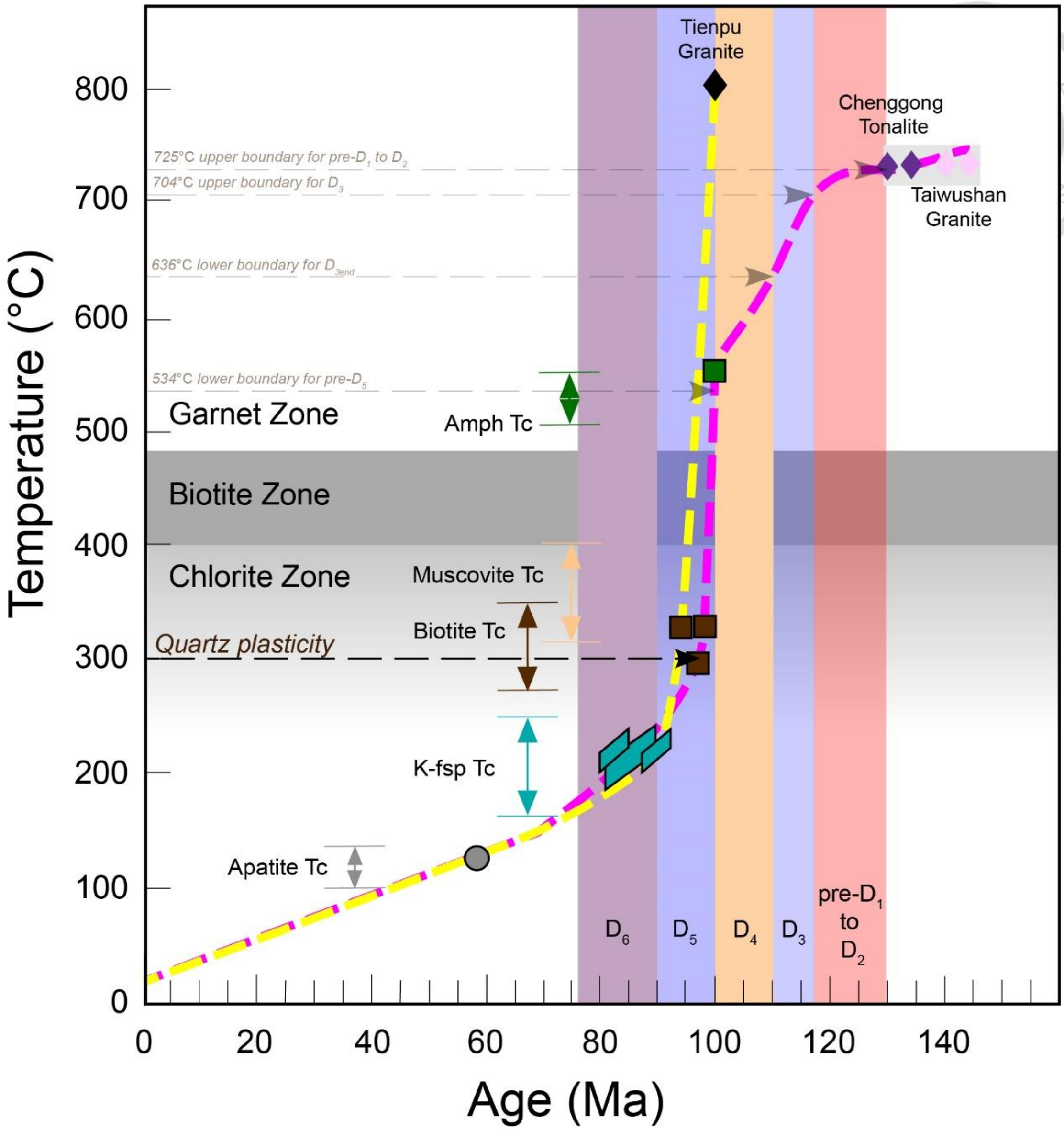

Figure 57. Reconstructed cooling path of the Cretaceous granitoids of Kinmen Island revised from Huang and Yeh (2020). The cooling path is established based on previously published geochronological results (Lo et al., 1993; Lin, 1994; Yui et al., 1996; Lin et al., 2011; Chen et al., 2020). The dashed pink line describes the cooling path for 144-139 Ma Taiwushan Granite and 134-129 Ma Chenggong Tonalite, while the dashed yellow line delineates the cooling path of 100 Ma Tienpu Granite. The closure temperature ranges for different mineral systems are as followed: U-Pb zircon (>700–900°C; solid black, purple, pink diamond; Lee et al., 1997), Ar-Ar amphibole (Amph; solid green square 500–550°C; Harrison, 1982), Ar-Ar muscovite (350 ± 50°C; McDougall and Harrison, 1999), Ar-Ar biotite (275–350°C; solid brown square Döpke, 2017), Ar-Ar K-feldspar (K-fsp; solid green parallelogram 250–150°C; Harrison and McDougall, 1982), apatite fission track (110 ± 10°C; solid gray circle Gleadow and Duddy, 1981). The timing for the six deformation events (D_1–D_6) are distinguished by correlating the metamorphic temperature conditions estimated in this study to the reconstructed cooling path.

doi:10.6342/NTU202202659

5.4 Tectonic Setting for Sustained High-temperature in Shallow Crust

The reconstructed P-T path for the basement complexes in Kinmen Island shows similar P-T ranges to the Buchan metamorphic facies series from kyanite-absent granulite (pre-D_1 to D_2), amphibolite (D_3, D_4), into greenschist facies (D_5, D_6). The absence of kyanite and andalusite in the schist belt along with the longstanding sillimanite-forming reactions from muscovite identified from pre-D_1 to D_4 shows that the continental crust had long stayed at a relatively high-temperature and low-pressure environments. Kyanite is usually produced by prograde metamorphism in Alpine- or Barrovian-type facies series in a compressional tectonic setting with low- to medium-dT/dP ratios (Carosi et al., 2015; Zheng and Chen, 2021), where continental crust is thickened with elevated lithostatic pressure into the kyanite stability field. The lack of kyanite suggests that no crustal thickening triggered kyanite-grade metamorphism during the crustal deformation (D_1-D_4) in Kinmen Island. Andalusite usually forms by prograde metamorphism in a nearly isobaric heating setting due to magmatism in an orogenic belt and can also be produced in the retrograde metamorphism during exhumation of the deep-seated rocks (Skrzypek et al., 2011; Nakano et al., 2021). If andalusite formed first and was later transformed into sillimanite without preservation, prograde metamorphism by burial would be required to reach the estimated maximum pressure and temperature conditions. However, the reconstructed P-T path shows a

doi:10.6342/NTU202202659

retrogressive trajectory in a totally opposite way to those expected for prograde reactions. Besides, the P-T conditions of the crust were all in the sillimanite stability field during all the ductile deformation events. Even though the retrogressive P-T trajectory passes through the andalusite stability field afterwards, a large temperature drop from 534-622 ˚C at the end of ductile deformation to <300 ˚C during brittle fracturing of the crust (D_5, D_6) will inhibit the growth of andalusite because of drastic P-T changes unpreferable to chemical equilibrium. This is supported by the fast-cooling rates of the granitoid basements in Kinmen Island at around >61.1 °C/Ma when the deformation mechanism switched from a ductile into brittle regime. In summary, no crustal thickening induced prograde metamorphism occurred during the deformation of the basements in Kinmen Island. In contrast, an extensional setting is preferred for the decompressional, and regressive P-T path established by the present study.

The apparent geothermal gradient from the reconstructed P-T path is 918 ˚C/GPa (around 25.6 ˚C/km) if considering the possible maximum temperature and pressure at 725 ˚C and 7.9 kbar. The high apparent metamorphic thermal gradients (dT/dP > 775 ˚C/GPa) are typical features for Buchan-type metamorphism, which can be linked to a rifting stage of an orogen (Zheng and Chen, 2017; Zheng and Chen, 2021). Compared with the geotherm from different tectonic settings, the reconstructed apparent geotherm of Kinmen Island is similar to that expected for a collapsed orogen (Vanderhaeghe,

doi:10.6342/NTU202202659

2012). Collapse of an orogenic belt represents a tectonic switch from crustal thickening to thinning, which can be caused by the change of plate interactions from convergence to divergence (e.g., retreating convergent plate boundaries). Kinmen Island is located along the southeast coast of South China, where Cretaceous igneous rocks and extensional basins are widely distributed. These Cretaceous magmatism and extensional basins were formed during the subduction and rollback of the Paleo-Pacific plate underneath the South China Block (Li, et al., 2014), and so did the crystallization, deformation, and metamorphism of the granitoid basement in Kinmen Island (Lin et al., 2011; Huang and Yeh, 2020). The complex extensional strain pattern evolution of the granitoid basements in Kinmen Island is also ascribed to the long-lasting crustal extension caused by the changing rollback directions of the Paleo-Pacific plate (Huang and Yeh, 2020). Due to the same deformation histories and similar metamorphic P-T conditions, the metamorphic rocks in Kinmen Island should also form in the same tectonic setting as the granitoid basement. Accordingly, the sustained high-grade metamorphism of the crystalline basements in Kinmen Island formed in a thinned continental crust, which was attributed to the continual slab rollback of the Paleo-Pacific plate (Figure 58).

doi:10.6342/NTU202202659

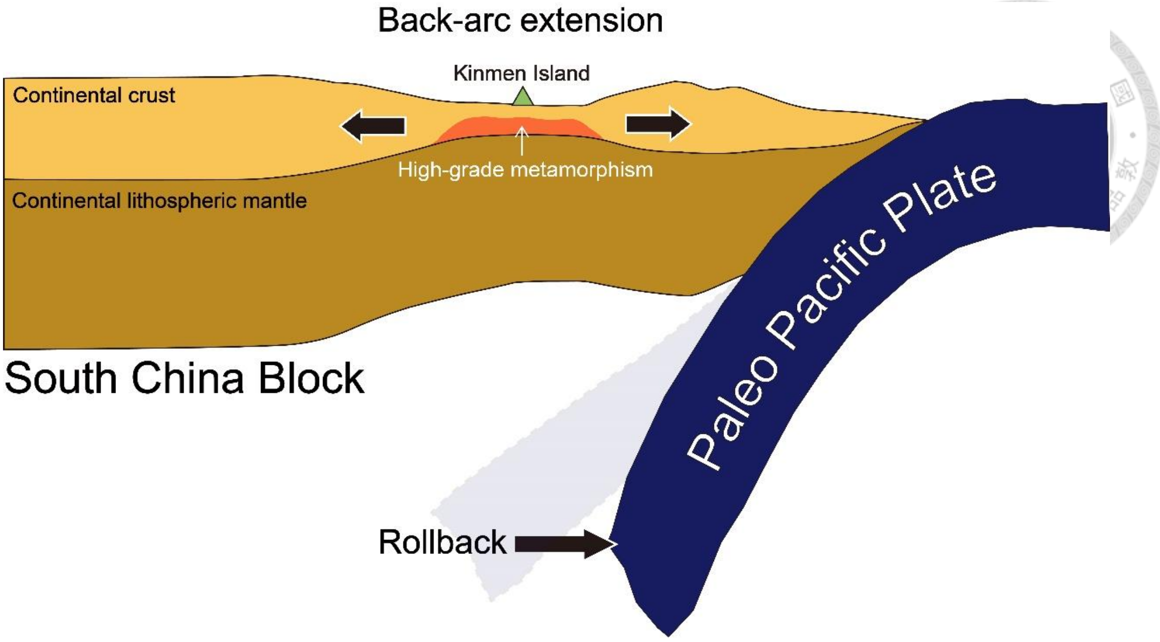

Figure 58. Schematic diagram of the tectonic setting for the sustained high-grade metamorphism in a thinned continental crust in Kinmen Island. The crustal thinning is caused by the continual slab rollback of the Paleo-Pacific plate, which triggered extensive back-arc extension on the South China Block.

5.5 Tectonic and Crustal Evolution of Kinmen Island

On the bases of the reconstructed structural evolution of Kinmen Island in the present study and the previous studies on structural evolution within the Cathaysia Block (Shi, 2011; Li et al., 2014; Huang and Yeh, 2020), the plate kinematics of the Paleo-Pacific plate linked to the tectonic evolution of Kinmen Island can be delineated more completely (Figure 59A). Huang and Yeh (2020) proposed that the Paleo-Pacific plate changed from NE-ward rollback during 129-107 Ma to SE-ward rollback during 107-76 Ma. With the identification of D_3 shear folding event and the revised estimated timing for each deformation event based on P-T estimation in this study, a stage of tectonic switch between the NE-ward to SE-ward slab rollback during 117-110 Ma is

doi:10.6342/NTU202202659

identified. This tectonic switch is featured by pure shear deformation with ESE-WNW compression (σ_1) and NNE-SSW extension (σ_3), which shows different stress fields and strain patterns from the other deformation events (e.g., pre-D_1 to D_2 and D_4-D_6). The inferred timing of 117-110 Ma for the tectonic switch is also consistent with the magmatic quiescence period of 118-107 Ma within the Cathaysia Block (Li et al., 2014), which further supports the idea of tectonic switch during this time. In addition, the generation of magmatism under an extensional setting during 107-86 Ma (Wang et al., 2020) corresponds to the initiation of D_4 transtensional shear zone during 110-100 Ma as well as D_5 and D_6 transtensional fracturing of the crust during 100-76 Ma. Thus, the estimated timing and stress setting for each deformation event is quite consistent with and supported by the regional geology within the Cathaysia Block during the Cretaceous time.

In conclusion, abundant granitoid batholiths intruded along the coast of SE Asia during early Cretaceous (Wang et al., 2011; Li et al., 2015; Dong et al., 2018), including those in Kinmen Island (e.g., Taiwushan Granite and Chenggong Tonalite; Yui et al., 1996; Lin et al., 2011; Chen et al., 2020). The northeastward rollback of the Paleo-Pacific plate initiated the extension of continental crust and post-orogenic magmatism in Kinmen Island (e.g., Taiwushan Granite; Lan et al., 1997; Huang and Yeh, 2020). This northeastward slab rollback triggered the bulk extension of the crust, as evidenced by the opening of widespread extensional basins within the Cathaysia Block (Li et al., 2014). This bulk extension generated the kilometer-scale gneiss dome and subhorizontal S-tectonite (D_{1-2}; 129–117 Ma) in Kinmen Island. The further exhumation of the basement complexes due to the tectonic adjustment of the Paleo-Pacific plate with ESE-WNW compression caused the NNE-SSW striking shear fold belt (D_3; 117–110 Ma) with decompressional melting of muscovite. As the Paleo-Pacific plate changed to southeastward rollback, an ENE-WSW striking sinistral transtensional shear zone was developed (D_4; 110-100 Ma) with syntectonic mafic dykes, which were later metamorphosed into amphibolite during D_4. The continually thinning crust and advected heat from the upwelling asthenosphere produced the longstanding leucogranite magmatism from D_1 to D_4, and related amphibolite facies metamorphism. Under the same stress setting of southeastward slab rollback as D_4, the basement of Kinmen Island was continually uplifted into the upper crust with the intrusion of Tienpu Granite and later pegmatites along E-W striking transtensional fractures (D_5 ;100–90 Ma) marking the end of ductile deformation (Huang and Yeh, 2020). The final D_6 (90–76 Ma) formed NE-SW striking mafic dike swarms sourced from the upwelling asthenosphere, which demonstrates the almost rifting stage of the continental crust (Huang and Yeh, 2020; Figure 59B).

doi:10.6342/NTU202202659

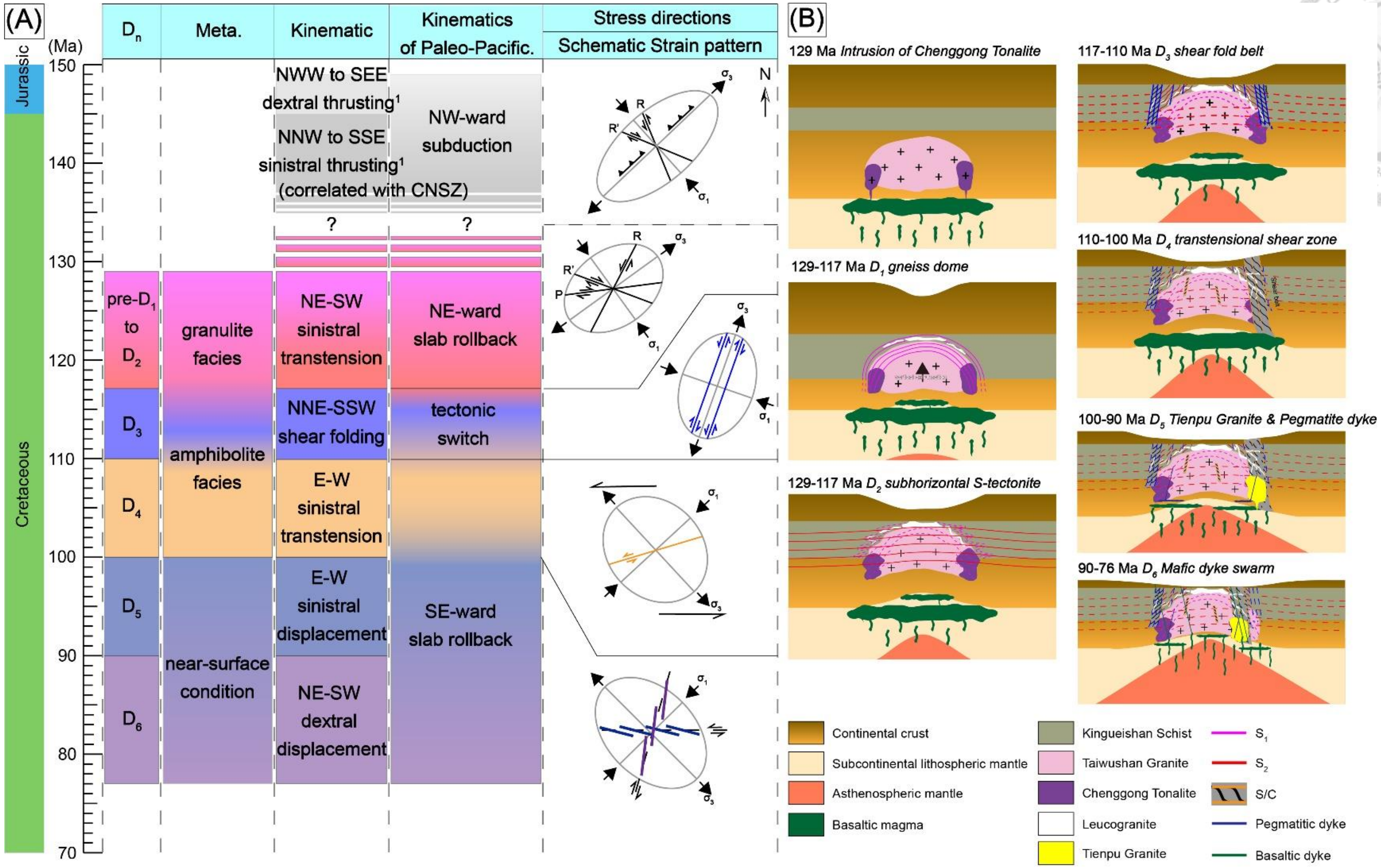

Figure 59. A compiled diagram showing the structural and tectonic evolution of Kinmen Island revised from Huang and Yeh (2020). (A) Composite diagram showing the reconstructed structural evolution and the associated plate kinematics and the schematic strain pattern. The structural evolution of Kinmen is correlated to the regional-scale Changle-Nanao Shear Zone (superscript 1; Shi, 2011). The normal fault systems of the extensional basins within the Cathaysia Block (Li et al., 2014) is also compiled to constrain the stress field during pre-D_1–D_2. (B) Schematic diagram of the tectonic evolution of Kinmen Island between 129 and 76 Ma. Both horizontal and vertical dimensions are not to scale.

doi:10.6342/NTU202202659

6 Conclusion

The crystalline basements of Kinmen Island experienced sustained high-grade metamorphism as continental crust was thinned during the long-lasting slab rollback of the Paleo Pacific plate during the Cretaceous. The basement is composed of a granite core surrounded by sillimanite-mica schist, biotite gneiss, tonalitic gneiss, and amphibolite with sillimanite-mica schist and biotite gneiss firstly reported by the present study. Based on the reconstructed structural evolution, petrographic analysis, and mineral chemistry, these complexes underwent the same deformation history under similar P-T conditions after the crystallization of the granitoids. Six deformation events were successfully identified as the deep-seated crystalline basements exhumed from 28.3-30.4 km (pre-D_1) to <6.9 km (D_5-D_6), which revised the proposed five deformation events by the previous study. A kilometer-scale gneiss dome (D_1) formed after the intrusion of the granitoid basements into the schist belt at 644-725 ˚C/<7.9 kbar. A similar temperature range was maintained with pressure decreasing during the gravitational collapse of the continental crust associating with generation of subhorizontal S-tectonite (D_2). Further exhumation of the crystalline basements due to continual crustal thinning formed a NNE-SSW striking shear fold belt (D_3) along the east and west limbs of the gneiss dome at 658-704 ˚C/<5.5 kbar. With further crustal extension and exhumation into the middle to upper crust, an ENE-WSW striking

doi:10.6342/NTU202202659

sinistral transtensional shear zone was developed throughout the basement at 534-682 ˚C/<4.6 kbar. Due to the continual exhumation into shallow levels (<1.9 kbar), the continental crust was deformed by brittle fracturing with intrusion of pegmatitic dykes (D_5) and mafic dyke swarm (D_6).

By compiling the results of petrographic analysis, using the Ti-in-biotite geothermometer and Al-in-hornblende geobarometer, a decompressional and regressive P-T path was revealed accompanying the crustal deformation from granulite-facies (pre-D_1 to D_2), amphibolite-facies (D_3 to pre-D_5) into near-surface conditions (D_5-D_6). The reconstructed P-T trajectory shows a stable temperature range and decompressional path from 725˚C/<7.9 kbar (pre-D_1 to D_2) to 704 ˚C/<5.5 kbar (D_3), followed by a continual decompression but a large temperature drop from 682 ˚C/<4.6 kbar (D_{3end}), 534 ˚C/1.9 kbar (pre-D_5) to <300 ˚C/<1.9 kbar (D_5 to D_6). The initiation of these sustained high-grade metamorphism in shallower crust are ascribed to the advective heat transfer from the upwelling asthenosphere beneath a prolonged thinned continental lithosphere, and the continual bimodal magma production and migration throughout the continental crust. The tectonic mechanism to thin the continental lithosphere for such a long period is the continual slab rollback of the Paleo-Pacific plate throughout most of the Cretaceous period.

doi:10.6342/NTU202202659

7 Reference

Allmendinger, R. W., Cardozo, N., & Fisher, D. (2012). Structural geology algorithms: Vectors and tensors in structural geology. Cambridge University Press, 302pp.

Aoki, K., Windley, B. F., Maruyama, S., & Omori, S. (2014). Metamorphic P–T conditions and retrograde path of high-pressure Barrovian metamorphic zones near Cairn Leuchan, Caledonian orogen, Scotland. Geological Magazine, 151(3), 559-571.

Barnes, C. G., Berry, R., Barnes, M. A., & Ernst, W. G. (2017). Trace element zoning in hornblende: Tracking and modeling the crystallization of a calc-alkaline arc pluton. American Mineralogist, 102(12), 2390-2405.

Berger, A., Schmid, S. M., Engi, M., Bousquet, R., & Wiederkehr, M. (2011). Mechanisms of mass and heat transport during Barrovian metamorphism: A discussion based on field evidence from the Central Alps (Switzerland/northern Italy). Tectonics, 30(1), TC1007.

Bohlen, S. R., & Mezger, K. (1989). Origin of granulite terranes and the formation of the lowermost continental crust. Science, 244(4902), 326-329.

Borisova, E. B., & Baltybaev, S. K. (2021). Petrochemical Criteria of Staurolite Stability in Metapelites at Medium-Temperature Low-and Medium-Pressure Metamorphism. Petrology, 29(4), 336-350.

doi:10.6342/NTU202202659

Brune, S., Heine, C., Pérez-Gussinyé, M., & Sobolev, S. V. (2014). Rift migration explains continental margin asymmetry and crustal hyper-extension. Nature Communications, 5(1), 1-9.

Burbank, D. W. (2002). Rates of erosion and their implications for exhumation. Mineralogical Magazine, 66(1), 25-52.

Carosi, R., Montomoli, C., Langone, A., Turina, A., Cesare, B., Iaccarino, S., Fascioli, L., Visonà, D., Ronchi, A., & Rai, S.M. (2015). Eocene partial melting recorded in peritectic garnets from kyanite-gneiss, Greater Himalayan Sequence, central Nepal. Geological Society, London, Special Publications, 412(1), 111-129.

Cardozo, N., & Allmendinger, R.W. (2013). Spherical projections with OSXStereonet: Computers & Geosciences, 51, 193-205.

Chen, C. H., Lee, C. Y., Tien, J. L., Xiang, H., Walia, M., & Lin, J. W. (2020). Post-orogenic thermal reset of the Pingtan-Dongshan metamorphic belt (SE China): Insights from zircon fission track and U-Pb double dating. Journal of Asian Earth Sciences, 201, 104512.

Chen, C. H., Lin, W., Lan, C. Y., & Lee, C. Y. (2004). Geochemical, Sr and Nd isotopic characteristics and tectonic implications for three stages of igneous rock in the Late Yanshanian (Cretaceous) orogeny, SE China. Earth and Environmental Science Transactions of the Royal Society of Edinburgh, 95, 237–248.

doi:10.6342/NTU202202659

Chen, N. H., Dong, J. J., Chen, J. Y., Dong, C. W., & Shen, Z. Y. (2014). Geometry and emplacement of the Late Cretaceous mafic dyke swarms on the islands in Zhejiang Province, Southeast China: Insights from high-resolution satellite images. Journal of Asian Earth Sciences, 79, 302-311.

Chen, W. S., Yang, H. C., Wang, X., & Huang, H. (2002). Tectonic setting and exhumation history of the Pingtan–Dongshan Metamorphic Belt along the coastal area, Fujian Province, Southeast China. Journal of Asian Earth Sciences, 20(7), 829-840.

Chiu, Y. P., Yeh, M. W., Wu, K. H., Lee, T. Y., Lo, C. H., Chung, S. L., & Iizuka, Y. (2018). Transition from extrusion to flow tectonism around the Eastern Himalaya syntaxis. Geological Society of America Bulletin, 130(9-10), 1675-1696.

Christensen, N. I., & Mooney, W. D. (1995). Seismic velocity structure and composition of the continental crust: A global view. Journal of Geophysical Research: Solid Earth, 100(B6), 9761-9788.

Davis, G. H., Reynolds, S. J., & Kluth, C. F. (2011). Structural geology of rocks and regions (third edition). John Wiley & Sons, 839pp.

Deer, W. A., Howie, R. A., & Zussman, J. (2013). An introduction to the rock-forming minerals, third edition. The Mineralogical Society, London, 498 pp.

Döpke, D. (2017). Modelling the Thermal History of Onshore Ireland, Britain and Its

doi:10.6342/NTU202202659

Offshore Basins Using Low-temperature Thermochronology. Doctoral dissertation, Trinity College Dublin, Ireland, 279 pp.

Dong, S., Zhang, Y., Li, H., Shi, W., Xue, H., Li, J., Huang, S., & Wang, Y. (2018). The Yanshan orogeny and late Mesozoic multi-plate convergence in East Asia—Commemorating 90th years of the "Yanshan Orogeny". Science China Earth Sciences, 61(12), 1888-1909.

Duke, E. F. (1994). Near infrared spectra of muscovite, Tschermak substitution, and metamorphic reaction progress: Implications for remote sensing. Geology, 22(7), 621-624.

Ferry, J. M. (1981). Petrology of graphitic sulfide-rich schists from south-central Maine: an example of desulfidation during prograde regional metamorphism. American Mineralogist, 66(9-10), 908-930.

Fossen, H. (2016). Structural Geology (second edition). Cambridge university press.

Gao, L., Zeng, L., & Xie, K. (2012). Eocene high-grade metamorphism and crustal anatexis in the North Himalaya Gneiss Domes, Southern Tibet. Chinese Science Bulletin, 57(6), 639-650.

Gleadow, A. J. W., & Duddy, I. R. (1981). A natural long-term track annealing experiment for apatite. Nuclear Tracks 5, 169–174.

Granger, D. E. (2007) Cosmogenic nuclide dating: landscape evolution. Encyclopedia

doi:10.6342/NTU202202659

of Quaternary Science, Elsevier, pp. 445-452.

Hammarstrom, J. M., & Zen, E. A. (1986). Aluminum in hornblende: an empirical igneous geobarometer. American Mineralogist, 71(11-12), 1297-1313.

Hansen, V. L. (1990). Collection and preparation of thin sections of oriented samples. Journal of Geological Education, 38(4), 294-297.

Harrison, A. D., Whale, T. F., Carpenter, M. A., Holden, M. A., Neve, L., O'Sullivan, D., Temprado, J. V., & Murray, B. J. (2016). Not all feldspars are equal: a survey of ice nucleating properties across the feldspar group of minerals. Atmospheric Chemistry and Physics, 16(17), 10927-10940.

Harrison, T. M. (1982). Diffusion of 40Ar in hornblende. Contributions to Mineralogy and Petrology. 78, 324–331.

Harrison, T. M., & McDougall, I. (1982). The thermal significance of potassium feldspar K-Ar ages inferred from 40Ar39Ar age spectrum results. Geochimica et Cosmochimica Acta 46, 1811–1820.

Hawthorne, F. C., Oberti, R., Harlow, G. E., Maresch, W. V., Martin, R. F., Schumacher, J. C., & Welch, M. D. (2012). Nomenclature of the amphibole supergroup. American Mineralogist, 97(11-12), 2031-2048.

Henry, D. J., Guidotti, C. V., & Thomson, J. A. (2005). The Ti-saturation surface for low-to-medium pressure metapelitic biotites: Implications for geothermometry

doi:10.6342/NTU202202659

and Ti-substitution mechanisms. American Mineralogist, 90(2-3), 316-328.

Henry, D. J., & Guidotti, C. V. (2002). Titanium in biotite from metapelitic rocks: Temperature effects, crystal-chemical controls, and petrologic applications. American Mineralogist, 87(4), 375-382.

Holdaway, M. J. (2000). Application of new experimental and garnet Margules data to the garnet-biotite geothermometer. American Mineralogist, 85(7-8), 881-892.

Holdaway, M. J. (2001). Recalibration of the GASP geobarometer in light of recent garnet and plagioclase activity models and versions of the garnet-biotite geothermometer. American Mineralogist, 86(10), 1117-1129.

Hollister, L. S., Grissom, G. C., Peters, E. K., Stowell, H. H., & Sisson, V. B. (1987). Confirmation of the empirical correlation of Al in hornblende with pressure of solidification of calc-alkaline plutons. American Mineralogist, 72(3-4), 231-239.

Huang, T. H., & Yeh, M. W. (2020). Structural Evolution of Extended Continental Crust Deciphered From the Cretaceous Batholith in SE China, a Kinmen Island Perspective. Frontiers in Earth Science, 330.

Imayama, T., Uehara, S., Sakai, H., Yagi, K., Ikawa, C., & Yi, K. (2020). The absence of high-pressure metamorphism in the inverted Barrovian metamorphic sequences of the Arun area, eastern Nepal and its tectonic implication. International Journal of Earth Sciences, 109(2), 465-488.

doi:10.6342/NTU202202659

Jamtveit, B., Dunkel, K. G., Petley-Ragan, A., Austrheim, H., Corfu, F., & Schmid, D. W. (2021). Rapid fluid-driven transformation of lower continental crust associated with thrust-induced shear heating. Lithos, 396, 106216.

Johnson, M. C., & Rutherford, M. J. (1989). Experimental calibration of the aluminum-in-hornblende geobarometer with application to Long Valley caldera (California) volcanic rocks. Geology, 17(9), 837-841.

La Roche, R. S., Gervais, F., Tremblay, A., Crowley, J. L., & Ruffet, G. (2015). Tectono-metamorphic history of the eastern Taureau shear zone, Mauricie area, Québec: Implications for the exhumation of the mid-crust in the Grenville Province. Precambrian Research, 257, 22-46.

Lan, C. Y., Chung, S. L., Mertzman, S. A., & Chen, C. H. (1995). Mafic dikes from Chinmen and Liehyu islands off SE China, petrochemical characteristics and tectonic implication. Journal of the Geological Society of China, 38, 183-214.

Lan, C. Y., Chung, S. L., & Mertzman, S. A. (1997). Mineralogy and geochemistry of granitic rocks from Chinmen, Liehyu and Dadan Islands, Fujian. Journal of the Geological Society of China, 40, 527-558.

Lee, C. Y. (1994). Chronology and Geochemistry of Basaltic Rocks from Penghu Islands and Mafic Dykes from East Fujian: Implications for The Mantle Evolution of SE China Since Late Mesozoic. Doctoral dissertation, National Taiwan

doi:10.6342/NTU202202659

University, Taipei, 243pp.

Lee, J. K., Williams, I. S., & Ellis, D. J. (1997). Pb, U and Th diffusion in natural zircon. Nature 390, 159–162.

Li, F., Sun, Z., Pang, X., Liao, J., Yang, H., Xie, H., Zhuo, H., & Zhao, Z. (2019). Low-viscosity crustal layer controls the crustal architecture and thermal distribution at hyperextended margins: modeling insight and application to the northern South China Sea Margin. Geochemistry, Geophysics, Geosystems, 20(7), 3248-3267.

Li, J., Zhang, Y., Dong, S., & Johnston, S. T. (2014). Cretaceous tectonic evolution of South China: A preliminary synthesis. Earth-Science Reviews, 134, 98-136.

Li, X., Zhang, C., Behrens, H., & Holtz, F. (2020). Calculating amphibole formula from electron microprobe analysis data using a machine learning method based on principal components regression. Lithos, 362, 105469.

Li, X. H. (2000). Cretaceous magmatism and lithospheric extension in Southeast China. Journal of Asian Earth Sciences, 18(3), 293-305.

Li, Y., Ma, C. Q., Xing, G. F., & Zhou, H. W. (2015). The Early Cretaceous evolution of SE China: Insights from the Changle–Nan'ao Metamorphic Belt. Lithos, 230, 94-104.

Li, Z., Qiu, J. S., & Yang, X. M. (2014). A review of the geochronology and geochemistry of Late Yanshanian (Cretaceous) plutons along the Fujian coastal area of southeastern China: Implications for magma evolution related to slab break-off and rollback in the Cretaceous. Earth-Science Reviews, 128, 232-248.

Lin, W. (1994). Geochemistry and thermal history of Late Yanshanian granites from Chinmen area. Master thesis, National Taiwan University, Taipei., 108pp. (in Chinese).

Lin, W., Lee, C. Y., Yang, H. C., & Chen, C. H. (2011). Geological Map of Taiwan scale 1:50000, Kinmen Area. Central Geological Survey, MOEA, ROC, 57pp.

Lin, W. (2001). Late Yanshanian intrusive magmatism in coastal region of South China and tectonic implications. Ph. D. Thesis, National Taiwan University, Taipei., 237pp. (in Chinese).

Liu, J. X., Wang, S., Wang, X. L., Du, D. H., Xing, G. F., Fu, J. M., Chen, X., & Sun, Z. M. (2020). Refining the spatio-temporal distributions of Mesozoic granitoids and volcanic rocks in SE China. Journal of Asian Earth Sciences, 201, 104503.

Liu, L., Xu, X., & Xia, Y. (2016). Asynchronizing paleo-Pacific slab rollback beneath SE China: Insights from the episodic Late Mesozoic volcanism. Gondwana Research, 37, 397-407.

Liu, Q., Yu, J. H., Wang, Q., Su, B., Zhou, M. F., Xu, H., & Cui, X. (2012). Ages and geochemistry of granites in the Pingtan–Dongshan Metamorphic Belt, Coastal South China: new constraints on Late Mesozoic magmatic evolution. Lithos, 150, 268-286.

Lo, C. H., Onstott, T. C., & Lee, C. M. (1993). 40Ar/39Ar dating of plutonic/metamorphic rocks from Chinmen Island off Southeast China and its tectonic implications. Journal of Geological Society of China, 36(1), 35-55.

Mao, J., Li, Z., & Ye, H. (2014). Mesozoic tectono-magmatic activities in South China: retrospect and prospect. Science China Earth Sciences, 57, 2853–2877.

McDougall, I., & Harrison, T. M. (1999). Geochronology and Thermochronology by the $^{40}Ar/^{39}Ar$ Method. Oxford: Oxford University Press, 269 pp.

Miller, C. F., McDowell, S. M., & Mapes, R. W. (2003). Hot and cold granites? Implications of zircon saturation temperatures and preservation of inheritance. Geology, 31(6), 529-532.

Miyazaki, K. (2004). Low-P–high-T metamorphism and the role of heat transport by melt migration in the Higo Metamorphic Complex, Kyushu, Japan. Journal of Metamorphic Geology, 22(9), 793-809.

Möller, C., Andersson, J., Dyck, B., & Lundin, I. A. (2015). Exhumation of an eclogite terrane as a hot migmatitic nappe, Sveconorwegian orogen. Lithos, 226, 147-168.

Nabelek, P. I., Hofmeister, A. M., & Whittington, A. G. (2012). The influence of temperature-dependent thermal diffusivity on the conductive cooling rates of plutons and temperature-time paths in contact aureoles. Earth and Planetary

doi:10.6342/NTU202202659

Science Letters, 317, 157-164.

Nakano, N., Osanai, Y., Jargalan, S., Adachi, T., Dolzodmaa, B., Kundyz, S., Owada, M., & Satish-Kumar, M. (2021). Petrology and geochronology of andalusite-and sillimanite-bearing kyanite metapelites from the Gobi Altai Mountains: Evidence for prolonged convergent tectonics in the Central Asian Orogenic Belt. Lithos, 400, 106362.

Nandi, K. (1967). Garnets as indices of progressive regional metamorphism. Mineralogical Magazine and Journal of the Mineralogical Society, 36(277), 89-93.

Nyström, A. I., & Kriegsman, L. M. (2003). Prograde and retrograde reactions, garnet zoning patterns, and accessory phase behaviour in SW Finland migmatites, with implications for geochronology. Geological Society, London, Special Publications, 220, 213-230.

Passchier, C. W., & Trouw, R. A. (2005). Microtectonics (second edition). Springer Science & Business Media, 366pp.

Pan, X., Shen, Z., Roberts, A. P., Heslop, D., & Shi, L. (2014). Syntectonic emplacement of Late Cretaceous mafic dyke swarms in coastal southeastern China: Insights from magnetic fabrics, rock magnetism and field evidence. Tectonophysics, 637, 328-340.

Reed, S. J. B. (2005). Electron microprobe analysis and scanning electron microscopy

doi:10.6342/NTU202202659

in geology (second edition). Cambridge University Press, 232pp.

Santosh, M., Liu, S. J., Tsunogae, T., & Li, J. H. (2012). Paleoproterozoic ultrahigh-temperature granulites in the North China Craton: implications for tectonic models on extreme crustal metamorphism. Precambrian Research, 222, 77-106.

Schmidt, M. W. (1992). Amphibole composition in tonalite as a function of pressure: an experimental calibration of the Al-in-hornblende barometer. Contributions to Mineralogy and Petrology, 110(2), 304-310.

Schumacher, J. C. (1991). Empirical ferric iron corrections: necessity, assumptions, and effects on selected geothermobarometers. Mineralogical Magazine, 55(378), 3-18.

Searle, M. P. (2022). Tectonic evolution of the Caledonian orogeny in Scotland: a review based on the timing of magmatism, metamorphism and deformation. Geological Magazine, 159, 124-152.

Severin, K. P. (2004). Energy dispersive spectrometry of common rock forming minerals. Dordrecht, The Netherlands: Kluwer Academic, 225.

Shi, J. J. (2011). Dividing of deformation and metamorphic stages and determination of its ages in Changle-Nanao tectonic zone. Geology of Fujian 3, 189–199.

Skrzypek, E., Štípská, P., Schulmann, K., Lexa, O., & Lexova, M. (2011). Prograde and retrograde metamorphic fabrics–a key for understanding burial and exhumation in orogens (Bohemian Massif). Journal of Metamorphic Geology, 29(4), 451-472.

doi:10.6342/NTU202202659

Spear, F. S. (1993). Metamorphic phase equilibria and pressure-temperature-time paths. Mineralogical Society of America Monograph, 799pp.

Sturt, B. A. (1962). The composition of garnets from pelitic schists in relation to the grade of regional metamorphism. Journal of Petrology, 3(2), 181-191.

Tirone, M., & Ganguly, J. (2010). Garnet compositions as recorders of P–T–t history of metamorphic rocks. Gondwana Research, 18(1), 138-146.

Tong, W. X., & Tobisch, O. T. (1996). Deformation of granitoid plutons in the Dongshan area, southeast China: constraints on the physical conditions and timing of movement along the Changle-Nanao shear zone. Tectonophysics, 267(1-4), 303-316.

Tracy, R. J., Robinson, P., & Thompson, A. B. (1976). Garnet composition and zoning in the determination of temperature and pressure of metamorphism, central Massachusetts. American Mineralogist, 61(7-8), 762-775.

Vanderhaeghe, O. (2012). The thermal–mechanical evolution of crustal orogenic belts at convergent plate boundaries: A reappraisal of the orogenic cycle. Journal of Geodynamics, 56, 124-145.

Wang, F. Y., Ling, M. X., Ding, X., Hu, Y. H., Zhou, J. B., Yang, X. Y., Liang, H. Y., Fan, W. M., & Sun, W. (2011). Mesozoic large magmatic events and mineralization in SE China: oblique subduction of the Pacific plate. International

doi:10.6342/NTU202202659

Geology Review, 53(5-6), 704-726.

Wang, Y., Fan, W., Zhang, G., & Zhang, Y. (2013). Phanerozoic tectonics of the South China Block: Key observations and controversies. Gondwana Research, 23(4), 1273-1305.

Wang, Z., Zhao, X., Yu, S., Li, S., Peng, Y., & Liu, Y. (2020). Cretaceous granitic intrusions in Fujian Province, Cathaysia Block: Implications for slab rollback and break-off of the Paleo-Pacific plate. Journal of Asian Earth Sciences, 190, 104164.

Wang, Z. H., & Lu, H. F. (2000). Ductile deformation and 40Ar/39Ar dating of the Changle–Nanao ductile shear zone, southeastern China. Journal of Structural Geology, 22(5), 561-570.

Weller, O. M., Mottram, C. M., St-Onge, M. R., Möller, C., Strachan, R., Rivers, T., & Copley, A. (2021). The metamorphic and magmatic record of collisional orogens. Nature Reviews Earth & Environment, 2(11), 781-799.

Wlodek, A., Grochowina, A., Gołębiowska, B., & Pieczka, A. (2015). A phosphate-bearing pegmatite from Lutomia and its relationships to other pegmatites of the Góry Sowie Block, southwestern Poland. Journal of Geosciences, 60(1), 45-72.

Winter, J. D. (2013). Principles of igneous and metamorphic petrology (second edition). Pearson education, 738pp.

Wu, C. M. (2020). Calibration of the biotite-muscovite geobarometer for metapelitic assemblages devoid of garnet or plagioclase. Lithos, 372, 105668.

Xu, X., Zhao, K., He, Z., Liu, L., & Hong, W. (2021). Cretaceous volcanic-plutonic magmatism in SE China and a genetic model. Lithos, 402, 105728.

Yang, Y. L., Ni, P., Yan, J., Wu, C. Z., Dai, B. Z., & Xu, Y. F. (2017). Early to late Yanshanian I-type granites in Fujian Province, SE China: Implications for the tectonic setting and Mo mineralization. Journal of Asian Earth Sciences, 137, 194-219.

Yardley, B. (1977). An empirical study of diffusion in garnet. American Mineralogist, 62(7-8), 793-800.

Yeh, M. W., Lin, Y. L., Lee, T. Y., & Ji, J. Q. (2013). Microfabric reconstruction via quantitative digital petrographic image analysis for weakly foliated gneisses. Tectonophysics, 587, 107-118.

Yui, T. F., Heaman, L., & Lan, C. Y. (1996). U-Pb and Sr isotopic studies on granitoids from Taiwan and Chinmen-Lieyu and tectonic implications. Tectonophysics 263, 61–76.

Zhang, Y. Q., Dong, S. W., Li, J. H., Cui, J. J., Shi, W., Su, J. B., & Li, Y. (2012). The new progress in the study of Mesozoic tectonics of South China. Acta Geoscientica Sinica, (3), 257-279.

Zhang, Z., Xiang, H., Dong, X., Ding, H., & He, Z. (2015). Long-lived high-temperature granulite-facies metamorphism in the Eastern Himalayan orogen, south Tibet. Lithos, 212, 1-15.

Zhao, J. H., Hu, R., Zhou, M. F., & Liu, S. (2007). Elemental and Sr–Nd–Pb isotopic geochemistry of Mesozoic mafic intrusions in southern Fujian Province, SE China: implications for lithospheric mantle evolution. Geological Magazine, 144(6), 937-952.

Zhao, J. L., Qiu, J. S., Liu, L., & Wang, R. Q. (2016). The Late Cretaceous I-and A-type granite association of southeast China: Implications for the origin and evolution of post-collisional extensional magmatism. Lithos, 240, 16-33.

Zhao, J. L., Qiu, J. S., Liu, L., & Wang, R. Q. (2015). Geochronological, geochemical and Nd–Hf isotopic constraints on the petrogenesis of Late Cretaceous A-type granites from the southeastern coast of Fujian Province, South China. Journal of Asian Earth Sciences, 105, 338-359.

Zheng, Y. F., & Chen, R. X. (2021). Extreme metamorphism and metamorphic facies series at convergent plate boundaries: Implications for supercontinent dynamics. Geosphere, 17(6), 1647-1685.

Zheng, Y. F., & Chen, R. X. (2017). Regional metamorphism at extreme conditions: Implications for orogeny at convergent plate margins. Journal of Asian Earth Sciences, 145, 46-73.

doi:10.6342/NTU202202659

Zhou, B. X., Sun, T., Shen, W., Shu, L., & Niu, Y. (2006). Petrogenesis of Mesozoic granitoids and volcanic rocks in South China: a response to tectonic evolution. Episodes 29:26.

doi:10.6342/NTU202202659

8 Appendices

8.1 Procedures for Making Oriented Thin Sections

8.1.1 Reorientation

Reorientation is a procedure that reorients rock samples back into their orientation at outcrops using the orientation of the marked reference surface. An orientometer along with an electronic laser level, a clinometer, and a sandbox are used in this procedure (Appendix figure. 1). Firstly, the clinometer is used to orient the platform of the orientometer into a horizontal plane and ajust the machine into a northern direction. To adjust the horizontal orientation of the platform, four height adjustment screws under each side of the orientometer are used. Secondly, the samples are reoriented back into the orientation in the field using the marked reference plane, the sandbox, and the clinometer. Finally, the reorientation is accomplished by marking the horizontal plane and the north-south line on the sample with the aid of the electronic laser level and marker pen. If there are oriented planes needed for analysis other than horizontal and north-south striking vertical planes, the orientation of the oblique planes can also be marked during the reorientation or after the sectioning.

doi:10.6342/NTU202202659

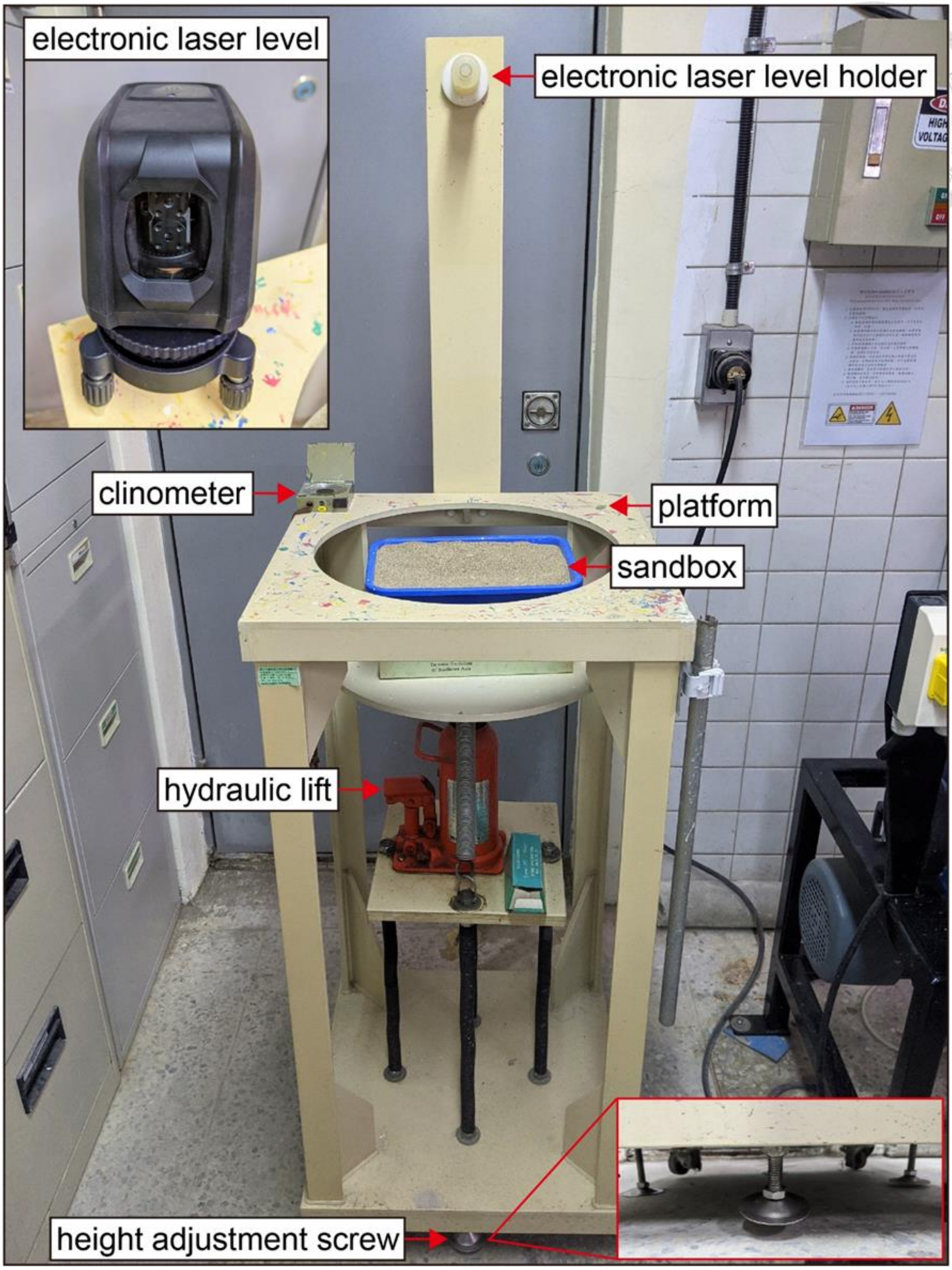

Appendix figure. 1. The equipment for reorientation with some parts of the orientometer marked.

doi:10.6342/NTU202202659

8.1.2 Sectioning

The oriented samples are cut along the orientation plane (e.g., the horizontal plane and the north-south striking vertical plane) using the double blade rock saw (Appendix figure. 2). The rock saw is equipped with sintered rim diamond saw blades, which are dedicated cutting tools for rocks. The saw blades are rotated at high speed by the dual-speed buffing motor to cut the rocks by grazing them into fine mud with the help of the diamonds embedded in the rim of the blades. Before sectioning rocks, inspection of all the rims of the blade is conducted by rotating blades by hand to check if the blade is fractured or bent. If it is, the blade must be replaced with a new one. During the sectioning, a water regulating valve is always turned on to cool down the temperature of the blade and lubricate the contact surface between the rock and the blade. Also, the water level within the water box must be maintained above the half height of the water pump motor in case the motor burns out. Finally, during rock sectioning, samples are pushed straight ahead into the blade and not in an oblique direction to the blade to prevent bending the blade and injuring the user.

doi:10.6342/NTU202202659

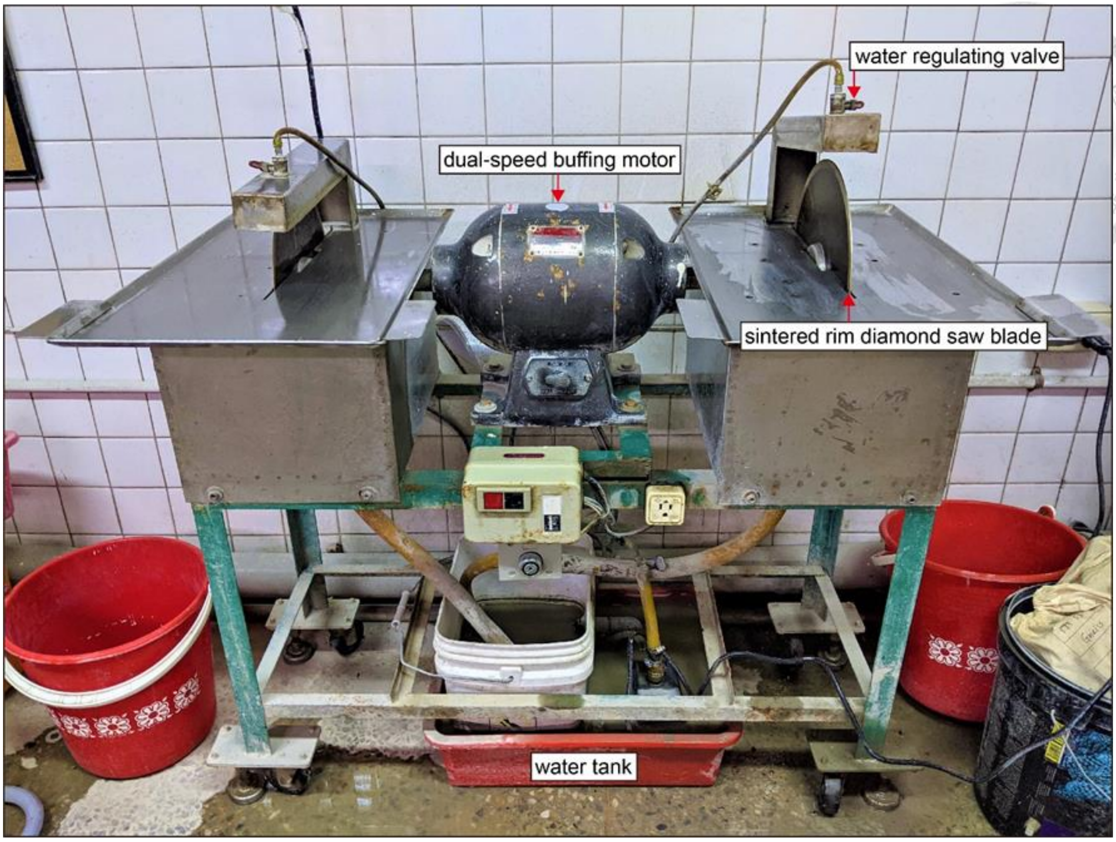

Appendix figure. 2. The double blade rock saw with some of the parts marked.

8.1.3 Impregnation

Impregnation is an optional procedure to prevent failure of thin section making, which embeds rock samples with epoxy to fill the pores and cracks. The purpose is to prevent bubble generation between rock samples and microscope slides during mounting, which will cause the microscope slides to separate from samples. The equipment used involves an oven, a hot plate, aluminum foil and a Petropoxy 154 standard kit (Appendix figure. 3). The Petropoxy 154 standard kit includes resin and a curing agent, a disposable beaker and syringes, plastic stirring rods, and a resin bottle spout. The detailed procedures for impregnation are described as follows.

doi:10.6342/NTU202202659

Step 1. Bake rock samples in an oven at 100 ˚C overnight to expel the moisture within the pores and cracks in the rocks.

Step 2. Wrap the hot plate completely with aluminum foil and place another layer underneath rock samples in case of epoxy spill. Then, heat rock samples on a hot plate at 135 ˚C for one day to increase the temperatures of rock samples as close to 135 ˚C as possible, which is the best cure temperature for Petropoxy 154.

Step 3. Prepare the epoxy in the mixing beakers using the mixing ratio by volume with 10 resin to 1 curing agent.

Step 4. Impregnate the rock surfaces needed for making thin sections with Petropoxy 154 on a hot plate at 135 ˚C until the epoxy is no longer absorbed into the rocks due to the epoxy- unfilled pores or cracks.

Step 5. Heat the impregnated rock samples on a hot plate at 135 °C until the epoxy is cured/hardened. The curing time can be as fast as one hour or longer depending on the temperatures reached for the epoxy and the actual ratio for making the epoxy.

doi:10.6342/NTU202202659

Aside from the impregnation procedures, the safety precautions for using Petropoxy 154 should be noted:

1. Petropoxy 154 contains significant amounts of Boron and should be avoided if preparing samples for Boron isotope analysis.
2. As with any organic chemical, use ventilation sufficient to avoid prolonged breathing of vapors.
3. Avoid contact with your skin. When handling Petropoxy 154, use vinyl or latex gloves.
4. In case of Petropoxy 154 contact with skin, wash with soap and water. Ethanol and isopropanol are low toxicity solvents that perform well for general cleanup.
5. Covered with foil in the freezer section of a refrigerator, the pot life is extended indefinitely. After more than two weeks in a refrigerator, the beaker should be placed in an airtight jar with a desiccant.

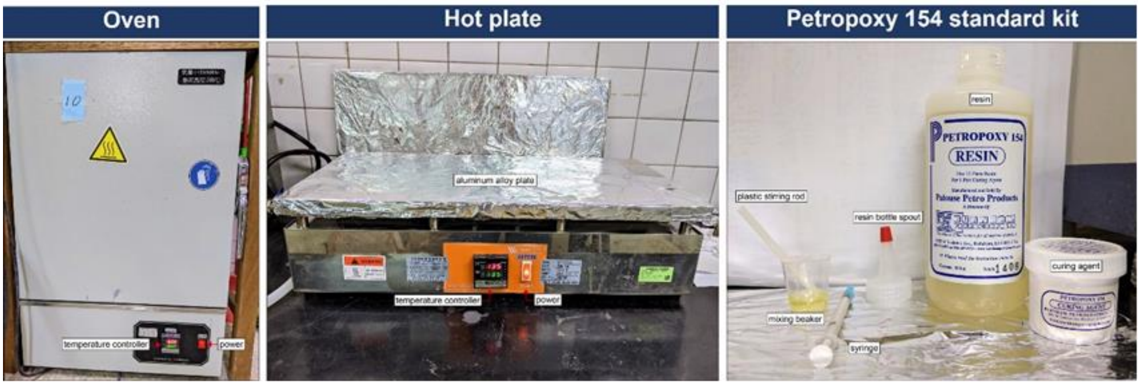

Appendix figure. 3. Equipment for impregnation.

doi:10.6342/NTU202202659

8.1.4 Polishing

The rock surfaces for making thin sections are polished using a lapping machine with diamond grinding discs of different grit sizes (Appendix figure. 4). There are five different grit sizes (ANSI particle size; ANSI stands for American National Standards Institute) used for polishing rock surfaces: 80, 120, 220, 500 and 1200 (Appendix figure. 5). All the rock surfaces should be polished from the coarser grit size to the finer one in order with a final grit size of 500. The polishing of microscope slides is optional, which depends on the epoxy used to mount. In this study, Petropoxy 154 is used for mounting, which does not require microscope-slide polishing due to its high-bond strength. If microscope-slide polishing is needed, a grit size of 500 is directly used. The detailed procedures for polishing are described as follows.

Step 1. Clean the diamond grinding discs using tap water to rinse the remaining fine particles or use an ultrasonic cleaner if needed.

Step 2. Place the diamond grinding discs on the magnetic turntable and cover the turntable controller with a rag in case of short circuit before opening the water cooling system and the power.

Step 3. Open the water cooling system and the power, and then determine the rotation speed (0-600 rpm) of the magnetic turntable.

Step 4. Polish rock samples from coarser grit sizes to the smaller ones (80, 120, 220,

doi:10.6342/NTU202202659

500). It takes about five to seven minutes to polish each sample. Remember to polish the discs evenly from the outer rim to the inner, and constantly change the sample orientation during polishing.

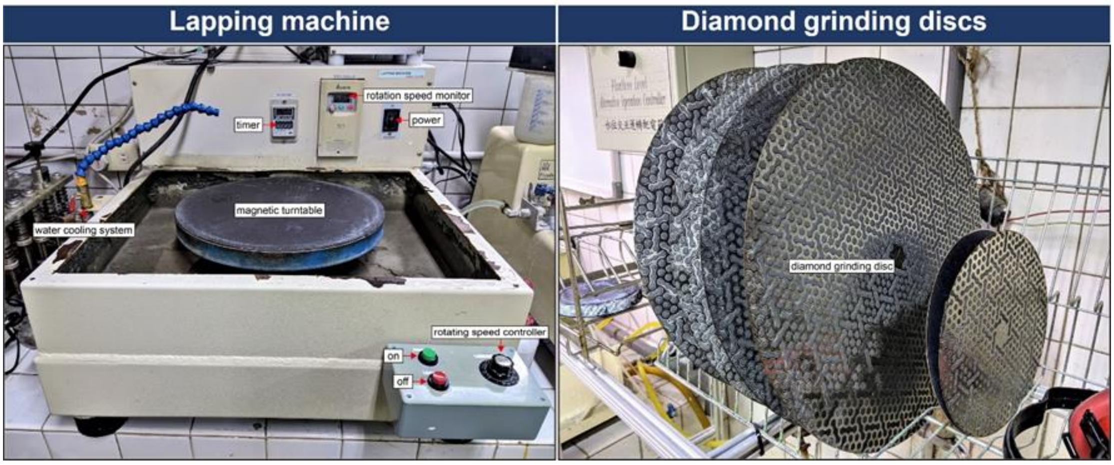

Appendix figure. 4. Polishing equipment.

Grit size	micron
80	180
120	106
220	53
500	13.9
1200	3.8

Appendix figure. 5. ANSI grit size and its corresponding micron sizes.

doi:10.6342/NTU202202659

8.1.5 Mounting

Mounting is the procedure used to mount microscope slides onto the rock surfaces needed for making thin sections. Petropoxy 154 is the mounting medium used, which is the same as the impregnation medium. The detailed procedures for mounting are described as follows.

Step 1. Before mounting the rock samples onto the microscope slides, all the samples and slides should be cleaned in an ultrasonic cleaner to get rid of the fine particles and dried on a hot plate at 135 °C for one day.

Step 2. Prepare the Petropoxy 154 by mixing the resin and the curing agent with the volume ratio of 10 to 1.

Step 3. Add some Petropoxy 154 on rock samples, and then cover the rock surfaces with the microscope slide.

Step 4. During the curing process, care should be taken to remove the bubbles between the microscope slides and the rock samples to avoid separation of the slides and rocks.

Step 5. When the bubbles are all cleared, and no bubbles are generated, the samples are left on the hotplate at 135 °C for at least one hour to cure the epoxy.

doi:10.6342/NTU202202659

8.1.6 Final Sectioning and Polishing

Final sectioning and polishing reduce the thickness of rock samples on the microscope slides to the standard thickness of 30μm. The PetroThin machine (Appendix figure. 6) along with the lapping machine as well as diamond grinding discs are used to complete the final sectioning and polishing. The detailed procedures for final sectioning and polishing are described as follows. First, the PetroThin machine is used to section rock samples thinner and polish them into a transparent material to light.

Step 1. Hand-inspection of all the rims of the blade and rotation of the blade is required to check if the blade is fractured or bent. If so, the blade must be replaced.

Step 2. Clean the sample holder with paper towels in case dirt or dust has been sucked into the vacuum system.

Step 3. Put the microscope slide side onto the sample holder, and then open the vacuum system to suck the samples tightly onto the holder, which can be checked by the vacuum gauge. It is better to have pressure conditions displayed smaller than -60 kPa.

Step 4. Use the precision micrometer to adjust the distance between the diamond blade and the microscope slide to determine the sectioning thickness.

Step 5. Turn on the motor and section the rock samples slowly, which usually takes several minutes up to one hour depending on the lithologies.

doi:10.6342/NTU202202659

Step 6. Use the precision micrometer to adjust the distance between the grinding wheel and the rock samples, and then gradually polish the rock samples into a transparent state with minerals of approximately third-order interference color under the microscopes.

Finally, the lapping machine with diamond grinding discs of grit sizes of 500 and 1200 is used to polish the thin sections into the standard thickness of 30 μm. The standard thickness of 30 μm is checked by the interference color of quartz and feldspar, which is at about first-order gray.

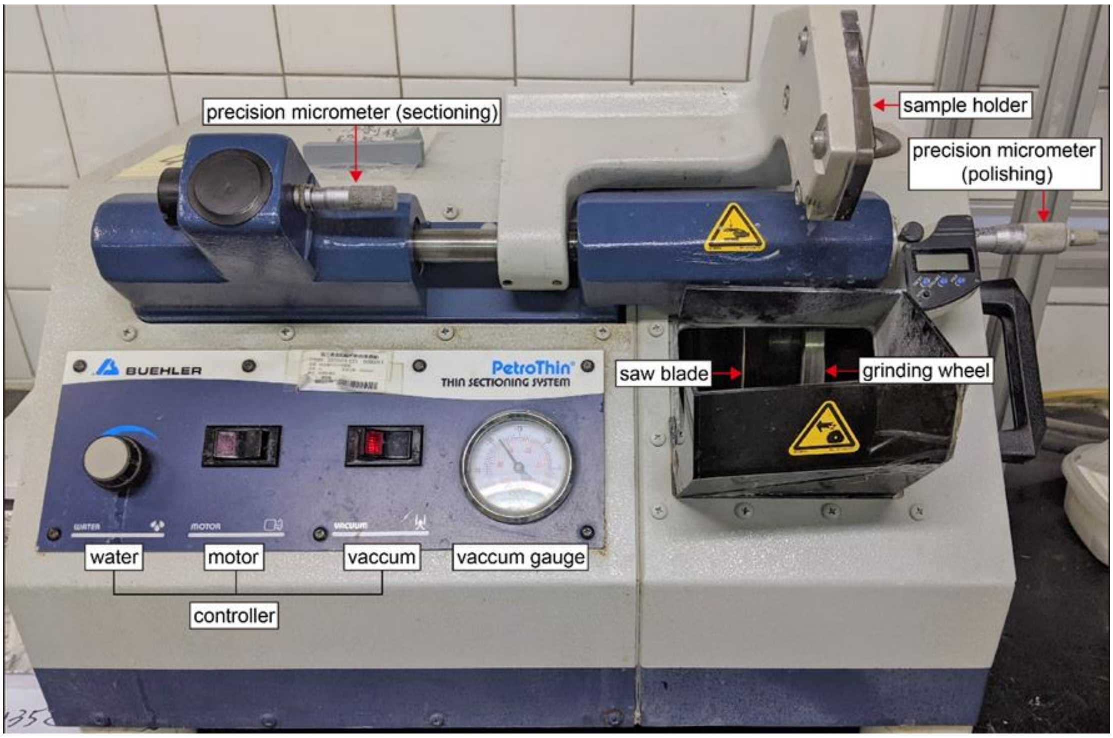

Appendix figure. 6. The PetroThin machine.

doi:10.6342/NTU202202659

8.2 Analytical Results of Major and Trace elements

	Analytes	18TP01	18TP04a	18TP04t	18LYA01	18117A01	18LYB03m	18LYB03b
Major Element (wt%)	SiO_2	47.50	49.40	66.30	62.10	77.20	66.10	65.10
	Al_2O_3	17.40	16.65	16.25	20.10	14.70	16.30	15.65
	Fe_2O_3	12.50	12.05	3.43	7.15	2.97	5.52	7.21
	CaO	10.70	10.80	5.08	0.03	0.01	5.44	5.80
	MgO	6.78	5.91	1.22	1.57	0.60	0.92	0.93
	Na_2O	2.96	3.41	3.67	0.44	0.22	2.36	1.18
	K_2O	1.24	0.90	2.37	4.63	2.96	1.65	1.60
	Cr_2O_3	0.019	0.007	<0.002	0.012	0.007	0.003	0.003
	TiO_2	0.95	0.99	0.46	0.84	0.47	0.78	0.72
	MnO	0.24	0.24	0.05	0.12	0.04	0.10	0.47
	P_2O_5	0.24	0.20	0.15	0.09	0.02	0.19	0.18
	SrO	0.05	0.05	0.07	0.01	<0.01	0.03	0.03
	BaO	0.01	0.01	0.15	0.09	0.04	0.03	0.03
	LOI	0.68	0.41	0.59	2.68	1.65	0.67	0.86
	Total	101.27	101.03	99.79	99.86	100.89	100.09	99.76
Trace Element (ppm)	Ba	98.5	57.8	1380	874	330	284	247
	Ce	31.7	21.3	78.4	110	93.4	84.8	78
	Cr	160	50	10	100	60	30	20
	Cs	0.94	0.12	0.68	28.2	3.94	14.7	14.45
	Dy	4.19	3.66	4.55	5.77	3.41	6.08	8.33
	Er	2.64	2.26	2.79	3.51	1.74	3.43	6.53
	Eu	1.38	1.25	1.06	1.34	0.67	1.52	1.34
	Ga	20.5	20	16.1	29.1	22.7	22.6	21.8
	Gd	4.67	3.88	4.74	6.88	4.78	6.83	7.14
	Hf	2.3	1.8	5.8	6.6	5.4	6.6	6.1
	Ho	0.88	0.79	0.93	1.19	0.63	1.2	1.89
	La	18	9.2	42	55.2	46.2	41	37.8
	Lu	0.34	0.3	0.4	0.52	0.26	0.44	1.4
	Nb	4.5	3.3	9.5	21.1	9.3	14.1	13.9
	Nd	18.8	13	27.4	40.9	35.9	36.5	32.7
	Pr	4.52	2.89	8.15	11.85	10.25	9.63	8.88
	Rb	38.6	9.3	59.2	347	175	115.5	118
	Sm	4.31	3.22	4.83	7.37	5.87	6.99	6.59
	Sn	1	2	1	11	17	6	6
	Sr	430	403	585	43.1	16.4	300	222
	Ta	0.2	0.2	0.8	1.7	0.7	1.3	1.2
	Tb	0.69	0.59	0.74	1.01	0.65	1.01	1.2
	Th	1.38	1.39	12.95	23.5	12.75	15.75	13.9
	Tm	0.35	0.33	0.42	0.51	0.27	0.45	1.15
	U	0.83	0.97	2.16	6.7	2.24	4.71	4.82
	V	321	334	69	114	58	70	76
	W	1	2	15	7	16	16	15
	Y	24.2	21.5	27.8	35.6	16.6	34.8	63.9
	Yb	2.25	1.98	2.65	3.49	1.68	2.93	8.53
	Zr	79	63	207	232	198	229	207

doi:10.6342/NTU202202659

8.3 Field Structural Measurement Data

D_1		D_2		D_3		D_4		D_5		D_6	
Dip/Plunge	Dip Az./Trend	Dip	Dip Az.	Dip/Plunge	Dip Az./Trend	Dip/Plunge	Dip Az./Trend	Dip	Dip Az.	Dip	Dip Az.
HCT		TGF		TGF		TGF		NSH		TGF	
S_1		S_2		$S_{2/3}$		C-fabric		Dyke Contact		Dyke Contact	
05	005	50	342	54	274	88	335	55	348	88	108
25	331	33	317	52	276	84	354	41	347	82	296
16	338	33	313	51	272	45	005	69	335	ZS	
16	004	28	318	62	283	36	350	DC		Dyke Contact	
20	003	25	326	65	283	52	358	Dyke Contact		79	311
30	353	25	154	66	283	39	002	44	354	84	137
25	348	19	340	37	342	54	333	46	351	87	309
20	358	15	033	39	331	50	352	64	003	87	120
25	339	14	351	46	332	53	034	59	016	70	314
27	317	14	329	39	339	73	017	44	355	82	113
18	329	13	311	35	333	55	021	36	024	85	125
19	001	11	049	35	322	70	025	42	020	74	143
15	357	10	110	47	336	62	006	70	006	89	142
27	353	10	322	S_3		81	353	53	004	76	135
18	014	08	092	70	143	74	004	TP		82	132
26	358	08	302	83	133	67	011	Dyke Contact		77	299
34	314	07	341	82	137	68	011	64	346	89	137
38	349	07	133	72	336	82	017	60	336	89	319
34	348	07	031	69	325	80	025	72	177	90	310
32	354	06	339	66	313	$S_{2/3/4}$		74	005	80	313
41	352	06	055	64	338	68	014	69	148	TP	
38	339	05	021	65	138	64	030	66	334	Dyke Contact	
L_1		05	084	61	136	62	032	49	332	89	129
40	341	05	114	69	312	56	010	55	325	87	140
35	346	05	337	73	093	55	006	81	001	77	317
GS		05	011	64	321	55	061	54	197	79	299
S_1		03	047	59	098	45	033	61	181	69	309
42	348	02	047	60	156	39	009	56	180	72	321
37	004	02	330	56	153	30	042	45	340	85	123
36	340	40	337	52	138	38	356			84	313
15	311	38	247	55	145	47	001			79	144
17	321	34	279	63	133	25	010			CG	
25	329	32	018	44	141	20	000			Dyke Contact	
16	326	30	015	63	129	34	011			70	121
22	357	30	001	54	115	27	005			85	124
14	323	27	352	75	121	34	012			84	138
20	337	27	098	60	132	36	004			86	138
L_1		20	115	57	132	41	009			79	121
30	302	19	004	51	133	JMS				83	133
33	304	19	019	S-fabric		S-fabric				79	126
35	313	40	337	33	302	82	347			79	128
29	310	38	247	35	302	85	353			JG	
19	286	34	279	C-fabric		80	347			Dyke Contact	
29	308	32	018	62	095	C-fabric				89	309
NSH		30	015	70	090	80	348			90	135
S_1		30	001	74	096	81	174			86	132
42	140	27	352	70	101	85	355			87	132
45	147	27	098	70	117	80	160			75	310
30	168	20	115	76	101	80	163			72	137
25	177	19	004	73	103	74	330				
23	148	19	019	83	294	76	333				
20	175	43	005	80	292	74	344				
25	167	42	031	88	104	79	335				
40	128	35	325	75	287	80	334				
17	143	32	049	73	281	84	333				
20	128	27	026	70	103	80	332				
15	145	27	098	76	098	72	329				
24	138	20	073	79	304	75	336				
23	185	36	355	71	313	74	334				
27	180	32	096	62	304	80	334				
28	165	28	119	70	308	76	326				
34	159	26	051	76	305	L_4					
24	139	25	059	60	307	72	273				
22	176	24	299	60	313	78	277				
24	174	23	287	60	318	HJT					
30	160	23	002	74	309	C-fabric					
22	174	22	061	74	309	45	324				
20	109	21	301	79	315	49	325				
26	094	20	295	79	121	48	317				
35	118	20	046	68	125	45	318				
24	130	16	026	80	130	44	325				
35	118	15	291	80	312	47	325				
42	095	59	117	76	328	L_4					
50	125	56	348	68	334	42	330				
42	126	46	043	74	122	48	302				
50	116	45	025	72	320	48	294				
L_1		45	013	57	331	39	290				

doi:10.6342/NTU202202659

D_1		D_2		D_3		D_4		D_5		D_6	
Dip/Plunge	**Dip Az./Trend**	**Dip**	**Dip Az.**	**Dip/Plunge**	**Dip Az./Trend**	**Dip/Plunge**	**Dip Az./Trend**	**Dip**	**Dip Az.**	**Dip**	**Dip Az.**
24	176	40	332	86	127	45	303				
25	171	39	133	80	121	49	306				
26	171	38	338	70	322	45	293				
23	183	37	005	75	327	**CLS**					
21	175	34	037	66	323	C-fabric					
20	178	29	024	70	341	61	328				
23	191	28	040	68	344	50	346				
24	181	26	329	60	349	62	325				
25	182	25	121	69	341	62	345				
26	179	20	067	82	324	58	343				
20	185	20	064	82	322	64	331				
25	179	14	048	90	129	52	333				
03	199	23	126	90	126	50	314				
11	170	10	270	72	313	45	337				
02	201	14	153	68	318	45	337				
19	182	26	000	69	308	44	328				
02	213	**JMS**		69	302	45	341				
09	208	S_2		68	281	47	321				
DC		16	209	85	130	45	344				
S_1		16	290	79	304	49	331				
17	123	14	131	71	313	45	332				
21	147	06	317	62	304	L_4					
23	155	00	090	L_{3a}		65	21				
29	137	**THR**		26	289	37	322				
37	129	S_2		30	298	40	307				
32	126	10	214	35	286	45	347				
30	120	14	226	19	313	40	323				
25	150	06	036	L_{3b}		40	300				
39	111	07	039	15	064	37	313				
27	121	14	214	16	064	**THR**					
26	135	04	109	23	357	C-fabric					
41	106	20	204	22	011	49	183				
36	106	18	205	10	013	48	172				
30	123	**SS**		26	025	50	183				
30	116	S_2		21	027	50	194				
30	121	08	218	19	023	60	206				
35	110	09	240	17	027	**FGD**					
46	081	08	241	09	040	C-fabric					
23	125	09	192	09	046	59	156				
26	120	10	192	02	214	48	160				
28	112	05	187	02	218	49	154				
25	115	03	164	02	210	45	150				
34	114	L_2		01	223	45	320				
33	122	01	317	**JMS**		40	154				
24	154	00	316	S_3		75	168				
20	156	01	135	53	276	**HSH**					
28	157	03	142	54	279	C-fabric					
28	108	05	135	29	269	52	176				
24	138	05	315	30	270	56	175				
36	091	01	307	45	288	68	170				
40	126	**ZS**		55	274	62	156				
43	134	S_2		55	275	51	167				
54	120	22	255	47	297	41	161				
55	112	13	257	63	271	41	157				
34	124	16	305	46	296	30	169				
29	144	17	259	39	290	35	194				
42	116	33	242	46	301	36	177				
40	117	20	311	46	303	37	178				
41	129	16	230	30	295	30	194				
38	120	15	311	38	289	42	149				
43	114	20	289	36	301	54	178				
40	114	14	294	50	296	55	169				
43	118	13	092	C-fabric		56	177				
45	135	18	263	69	292	60	172				
39	137	15	262	50	279	55	165				
42	141	25	057	45	302	42	158				
35	134	18	318	51	284	45	178				
34	145	18	053	70	255	50	178				
L_1		13	162	64	256	58	144				
34	163	13	252	70	284	46	154				
29	164	19	200	82	268	56	157				
33	166	11	005	85	255	L_4					
30	165	20	139	L_{3a}		19	211				
34	158	12	264	70	284	33	212				
30	157	21	179	35	218	30	192				
30	157	20	192	32	216	34	212				
24	169	20	208	43	214	30	220				
32	169	20	257	54	247	51	212				
39	163	26	353	61	248	45	217				

doi:10.6342/NTU202202659

D_1		D_2		D_3		D_4		D_5		D_6	
Dip/Plunge	Dip Az./Trend	Dip	Dip Az.	Dip/Plunge	Dip Az./Trend	Dip/Plunge	Dip Az./Trend	Dip	Dip Az.	Dip	Dip Az.
40	157	07	010	64	255	36	214				
42	163	11	119	**NSH**		Fold axial plane					
FGD		**GYR**		C-fabric		55	164				
S_1		S_2		44	107	64	168				
39	135	15	164	54	111	46	174				
56	160	20	149	74	106	44	178				
40	154	15	216	46	100	Fold axis					
15	167	03	008	45	120	14	252				
39	146	18	010	50	115	14	252				
34	158	09	214	60	103	07	253				
35	141	L_2		60	116	12	256				
16	149	05	231	67	098	**GS**					
HJR		08	232	L_{3b}		C-fabric					
S_1		03	056	35	169	64	005				
56	300	03	064	34	172	68	015				
45	297	**FGD**		26	178	73	023				
31	277	S_2		**CG**		66	351				
56	283	05	010	C-fabric		50	349				
25	267	10	252	79	122	61	351				
25	272	19	197	74	127	56	346				
20	252	15	006	79	113	62	001				
17	279	15	183	44	107	50	345				
17	292	04	152	54	111	49	354				
06	287	06	217	74	106	55	352				
27	312	16	183	46	100	52	003				
15	288	L_2		45	120	55	002				
16	330	10	253	50	115	52	005				
26	258	07	252	60	103	53	008				
24	251	06	128	60	116	L_4					
L_1		06	319	67	098	43	297				
26	275	**HSH**		**TP**		51	316				
15	271	S_2		S_3		46	306				
KBG		16	212	64	125	46	317				
S_1		14	216	57	131	48	320				
25	237	10	214	60	118	40	310				
22	239	15	224	60	97	42	320				
31	231	**JG**		60	106	40	316				
24	249	$S_{2/3}$		45	141	37	314				
15	237	33	343	40	136	41	323				
25	237	37	331	40	129	44	319				
20	216	33	328	37	111	**TP**					
17	265	28	334	C-fabric		C-fabric					
18	235	31	342	65	105	53	034				
LJF		27	342	65	085	73	017				
S_1		20	010	72	104	55	021				
30	174	30	332	72	104	70	025				
11	203	26	317	75	095	62	006				
24	245	21	334	75	089	81	353				
18	220	26	332	62	104	74	004				
20	215	24	002	62	098	67	011				
12	155	18	003	66	098	68	011				
L_1		27	313	75	115	82	017				
15	209	24	311	79	105	80	025				
07	223	35	317	76	103	88	335				
SH		35	295	86	112	84	354				
S_1		L_2		89	109	45	005				
15	253	24	342	85	118	36	350				
34	258	25	347	86	117	52	358				
33	246	22	347	69	302	39	002				
30	227	05	343	74	105	54	333				
L_1		10	344	73	107	50	352				
17	213	**TP**		75	303	80	159				
24	221	$S_{2/4}$		69	316	79	157				
CG		29	045	70	320	70	155				
S_1		45	034	73	106	80	150				
42	221	31	039	90	287	79	153				
36	231	34	077	81	312	50	127				
30	214	30	076	80	121	66	135				
45	223	46	060	63	125	69	135				
40	234	45	090	74	124	70	146				
48	239	45	109	74	120	70	155				
35	229	55	039	64	125	60	158				
34	228	56	029	70	136	62	160				
36	216	70	033	69	128	70	160				
50	229	76	014	L_{3a}		77	178				
65	228	41	017	39	040	79	161				
39	244	50	045	45	019	80	167				
51	221	60	062	50	025	74	157				
45	215	24	147	31	082	70	160				

doi:10.6342/NTU202202659

D_1		D_2		D_3		D_4		D_5		D_6	
Dip/Plunge	Dip Az./Trend	Dip	Dip Az.	Dip/Plunge	Dip Az./Trend	Dip/Plunge	Dip Az./Trend	Dip	Dip Az.	Dip	Dip Az.
46	219	24	164	**JG**		59	161				
60	244	46	165	S_3		70	155				
52	220	50	119	55	274	76	148				
65	230	47	118	57	280	70	150				
59	238	**CG**		57	287	65	157				
62	241	S_2		66	289	69	165				
77	201	24	229	72	286	75	166				
70	235	30	220			62	354				
80	212	20	227			50	347				
50	230	21	224			49	339				
44	221	35	222			54	356				
59	220	20	215			45	355				
40	217	34	202			60	358				
80	238	20	257			55	356				
60	238	22	027			53	354				
65	240	09	269			42	346				
64	240	05	034			76	346				
64	233	40	054			44	332				
62	236	01	274			50	327				
65	228	**HB**				49	343				
61	220	S_2				66	319				
54	222	45	272			45	330				
63	233	32	256			64	006				
60	219	40	262			64	008				
56	221	20	296			64	354				
50	221	22	278			63	358				
59	219	25	273			63	001				
27	228	30	295			65	352				
45	210	32	265			67	351				
16	204	22	247			59	352				
20	180	24	277			80	356				
45	214	25	347			65	359				
30	200	20	262			67	358				
27	207					63	333				
25	202					63	357				
26	195					68	352				
40	231					66	168				
30	243					70	180				
24	227					70	180				
30	263					75	175				
44	228					76	177				
30	224					71	176				
43	239					80	163				
L_1						Fold axial plane					
35	218					65	358				
50	205					66	002				
34	221					79	171				
45	230					71	171				
25	228					60	166				
34	225					60	165				
30	229					84	179				
40	235					Fold axis					
41	229					40	077				
39	228					40	063				
41	232					43	054				
45	215					44	085				
35	222					44	104				
39	223					40	116				
59	218					37	090				
13	270					**HB**					
13	271					C-fabric					
15	269					70	166				
23	277					79	175				
23	260					84	174				
19	267					80	177				
25	263					68	175				
34	259					72	167				
						74	173				
						76	186				

doi:10.6342/NTU202202659

8.4 BSE images with Marked Positions of EPMA Analyses

8.4.1 18LYA01 Sillimanite Mica Schist

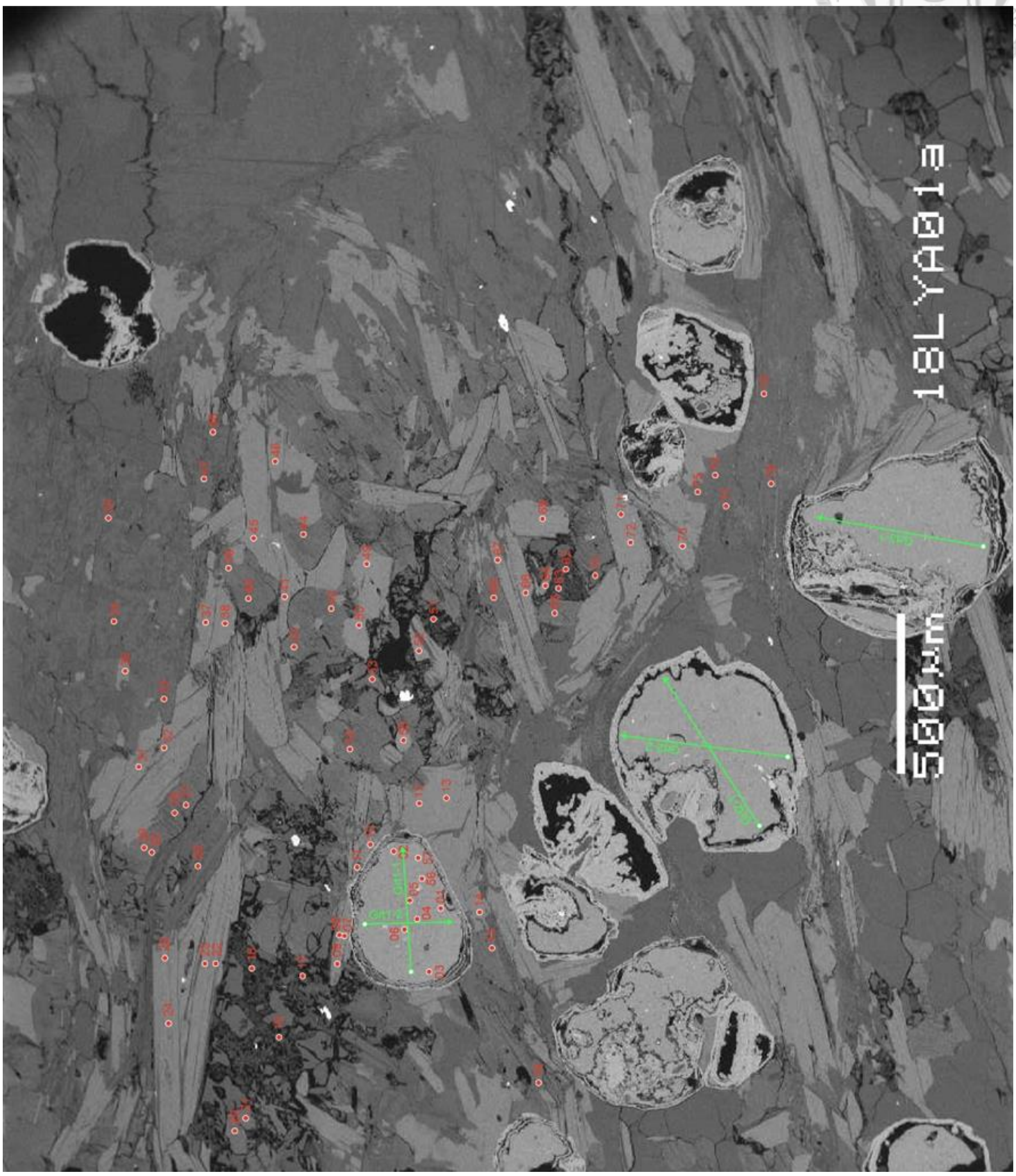

doi:10.6342/NTU202202659

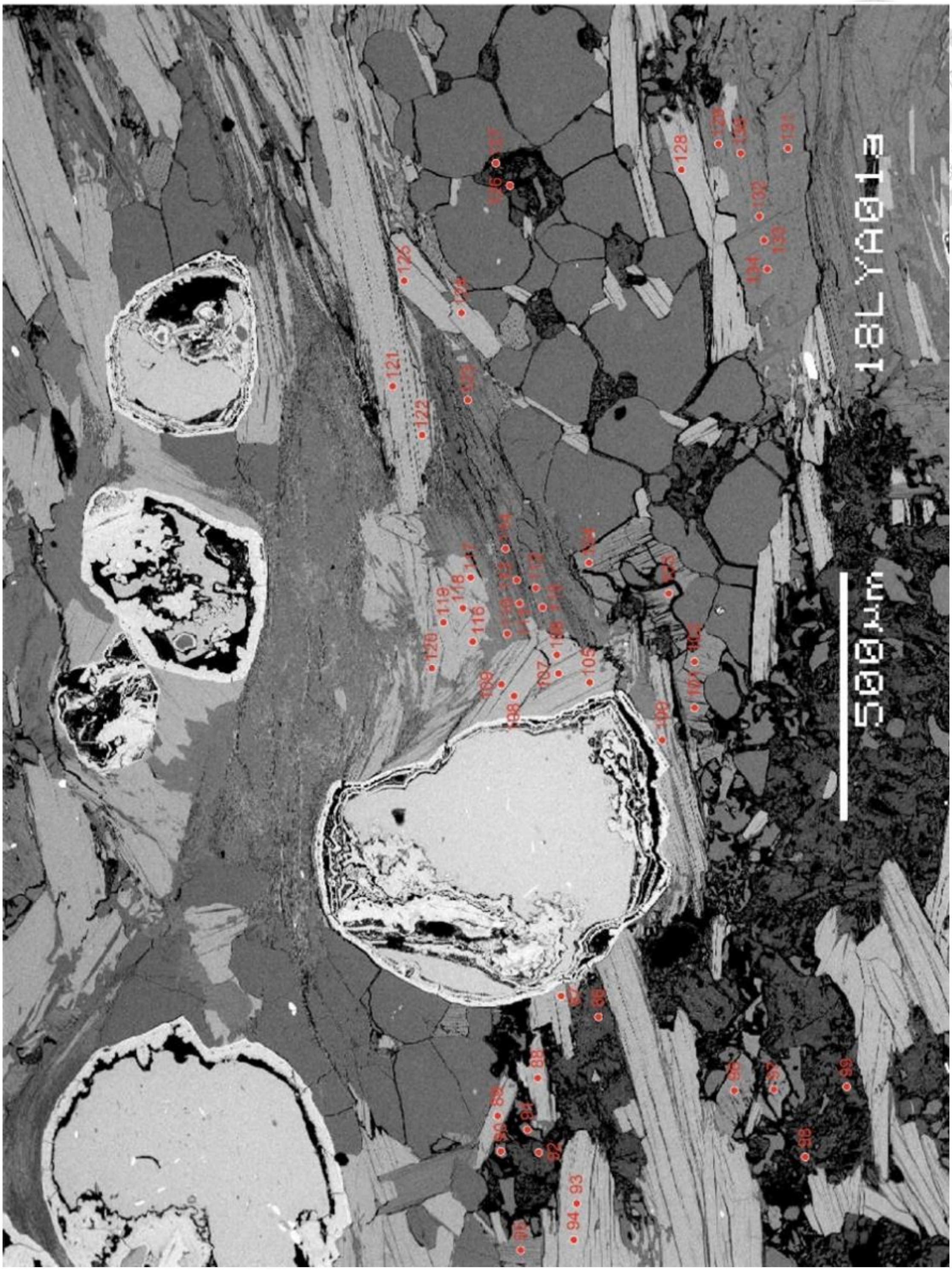

doi:10.6342/NTU202202659

8.4.2 181117A01 Sillimanite Mica Schist

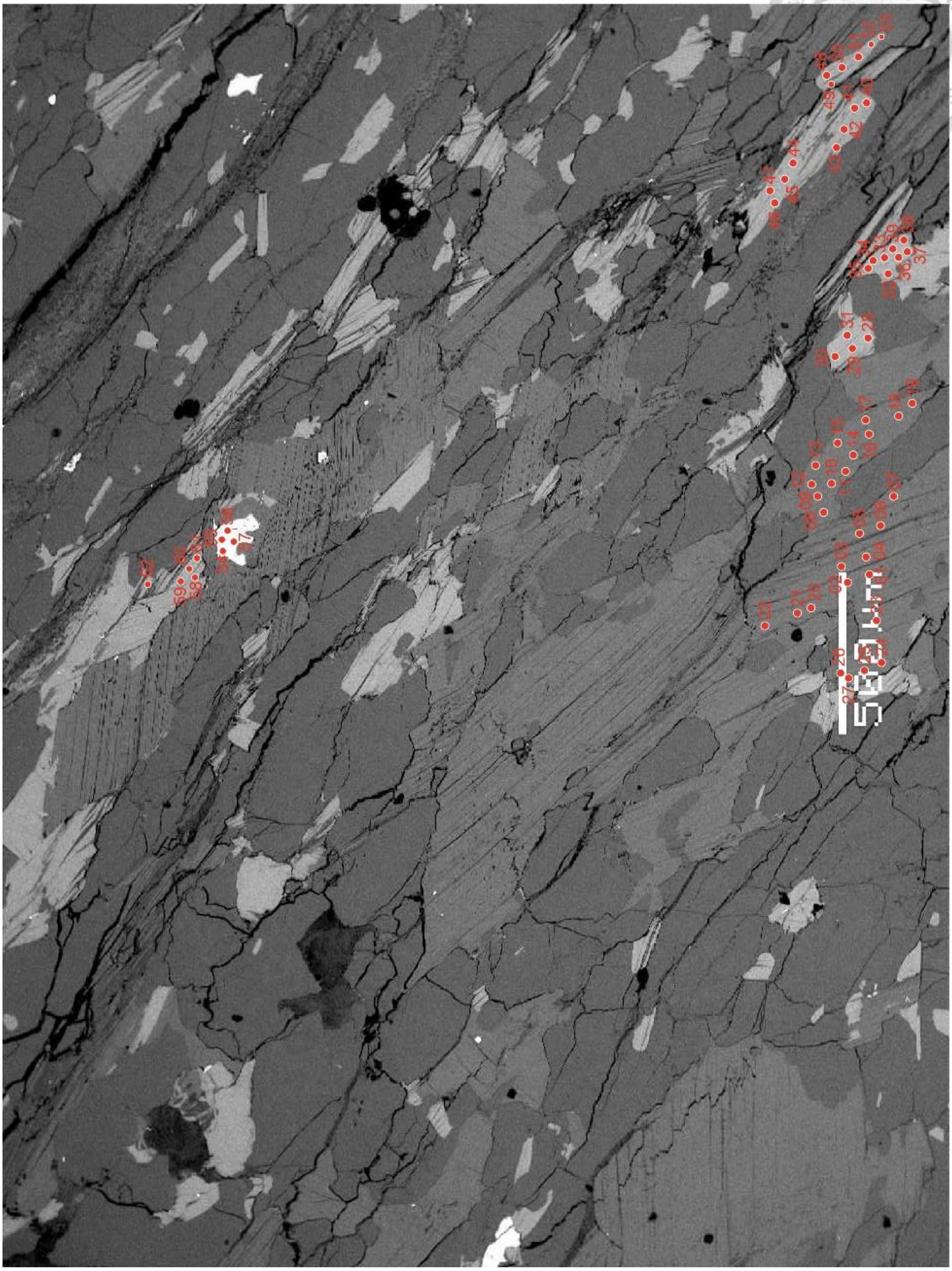

doi:10.6342/NTU202202659

8.4.3 18LYB03 Biotite Gneiss

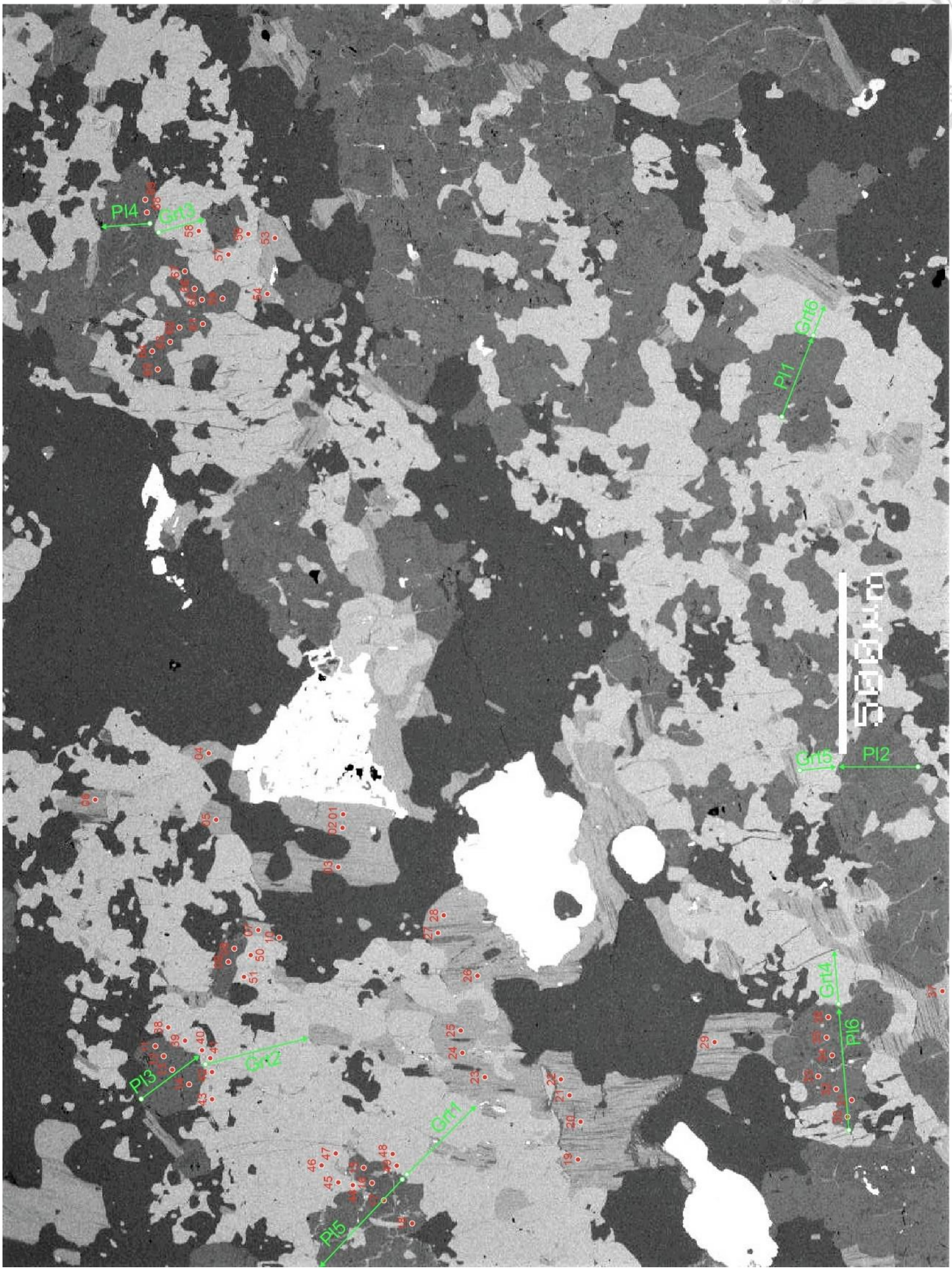

doi:10.6342/NTU202202659

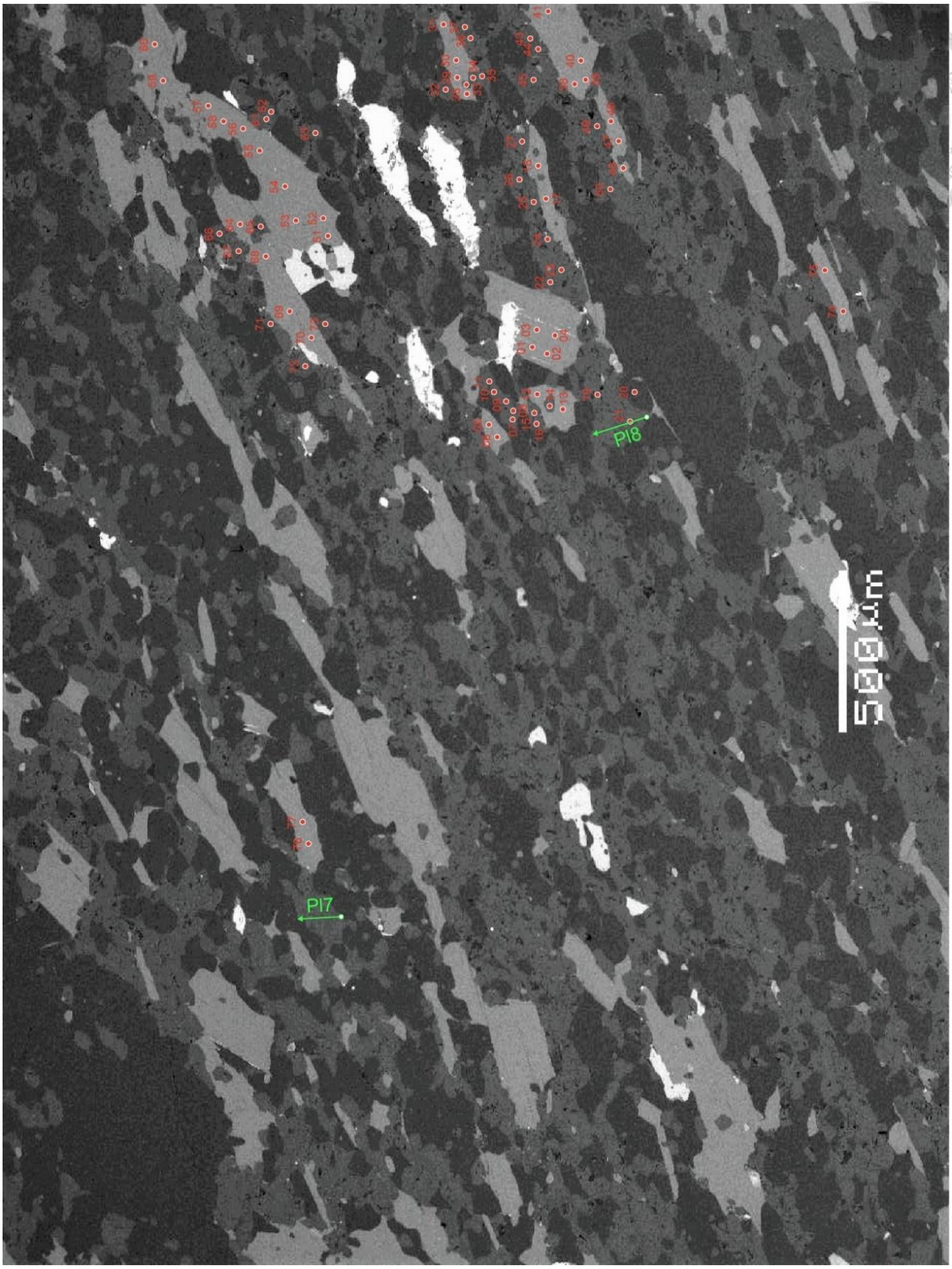

doi:10.6342/NTU202202659

8.4.4 18TP01 Amphibolite

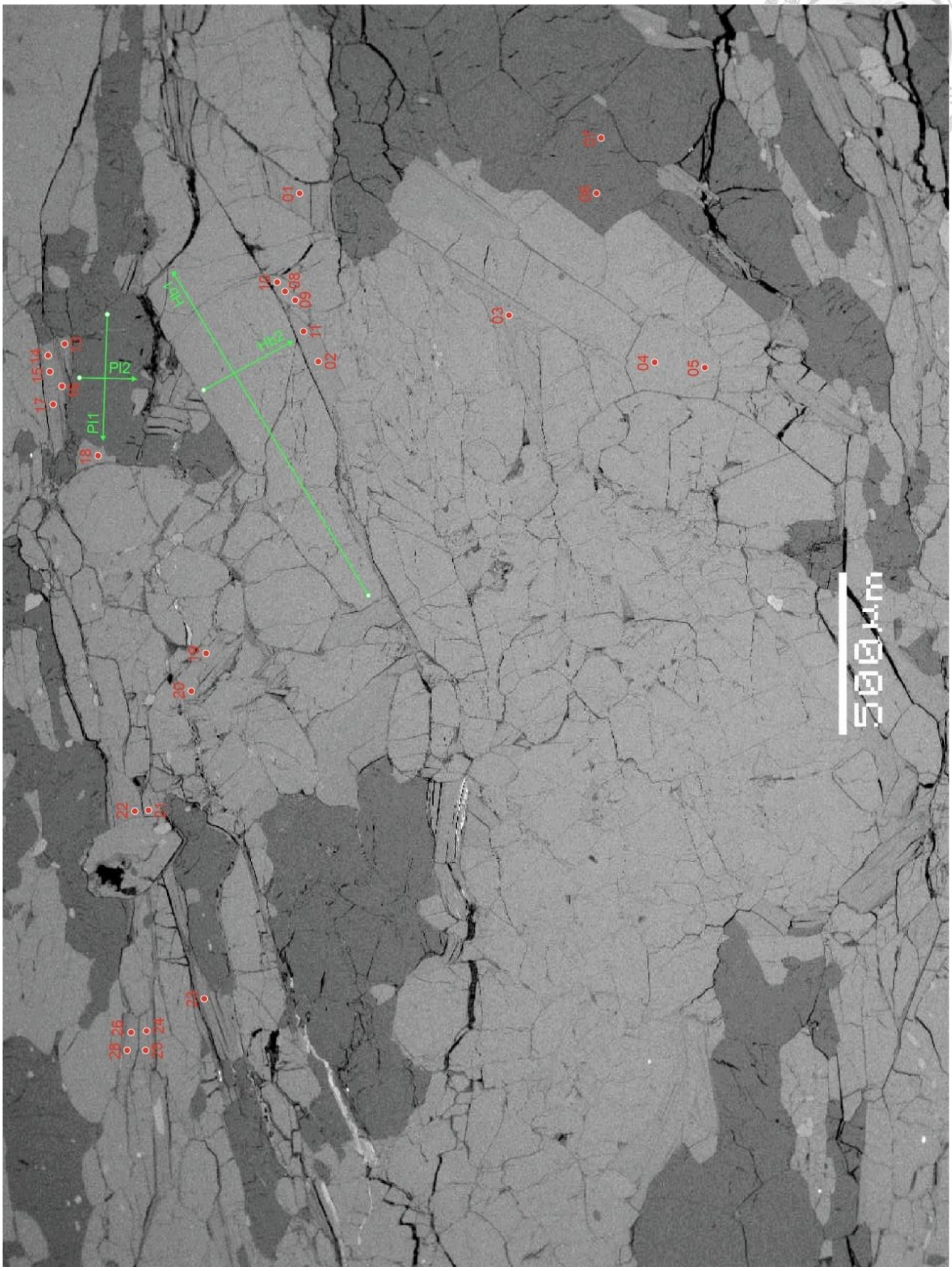

doi:10.6342/NTU202202659

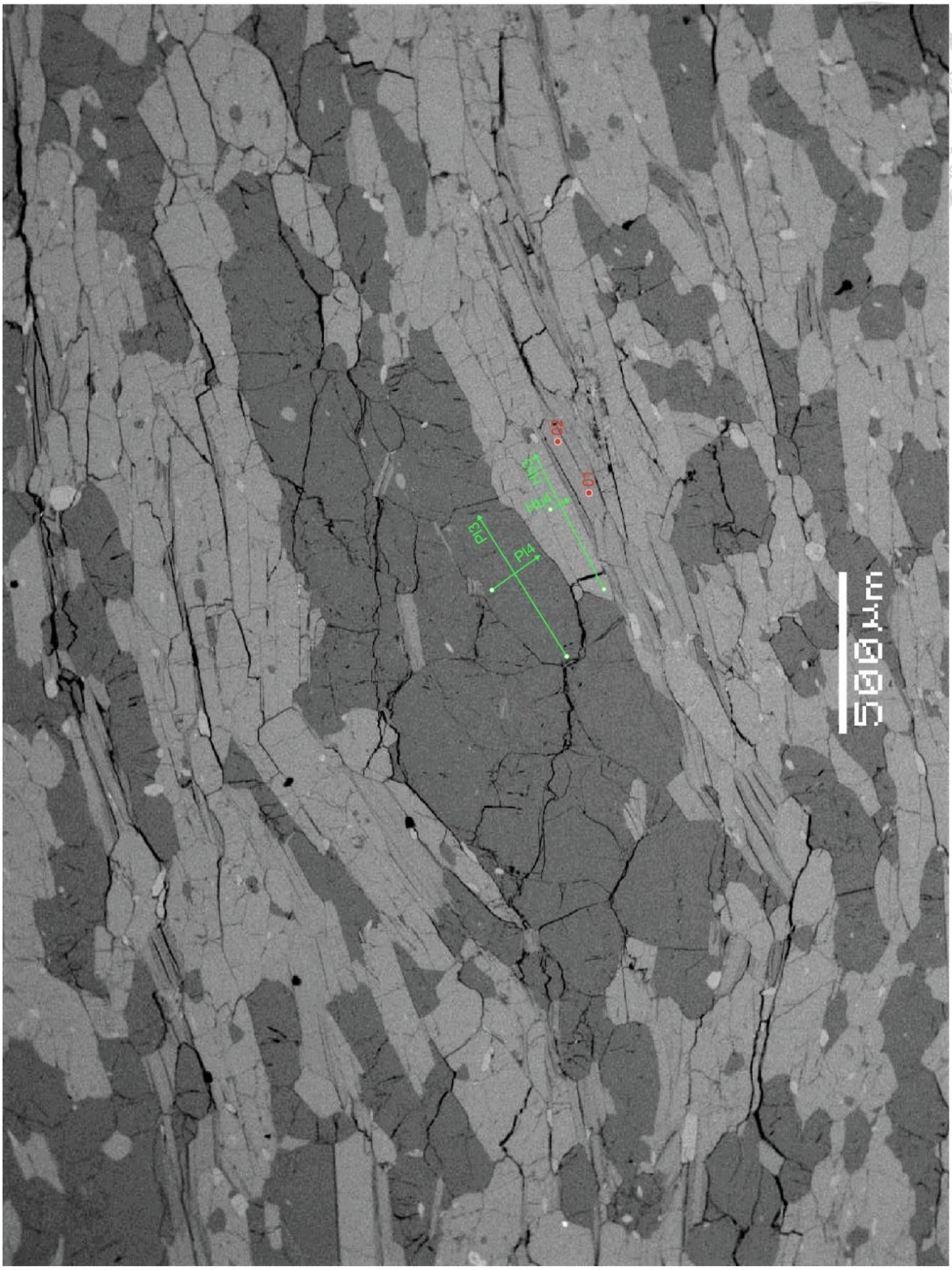

doi:10.6342/NTU202202659

8.4.5 18TP04 Amphibolite and Tonalitic gneiss

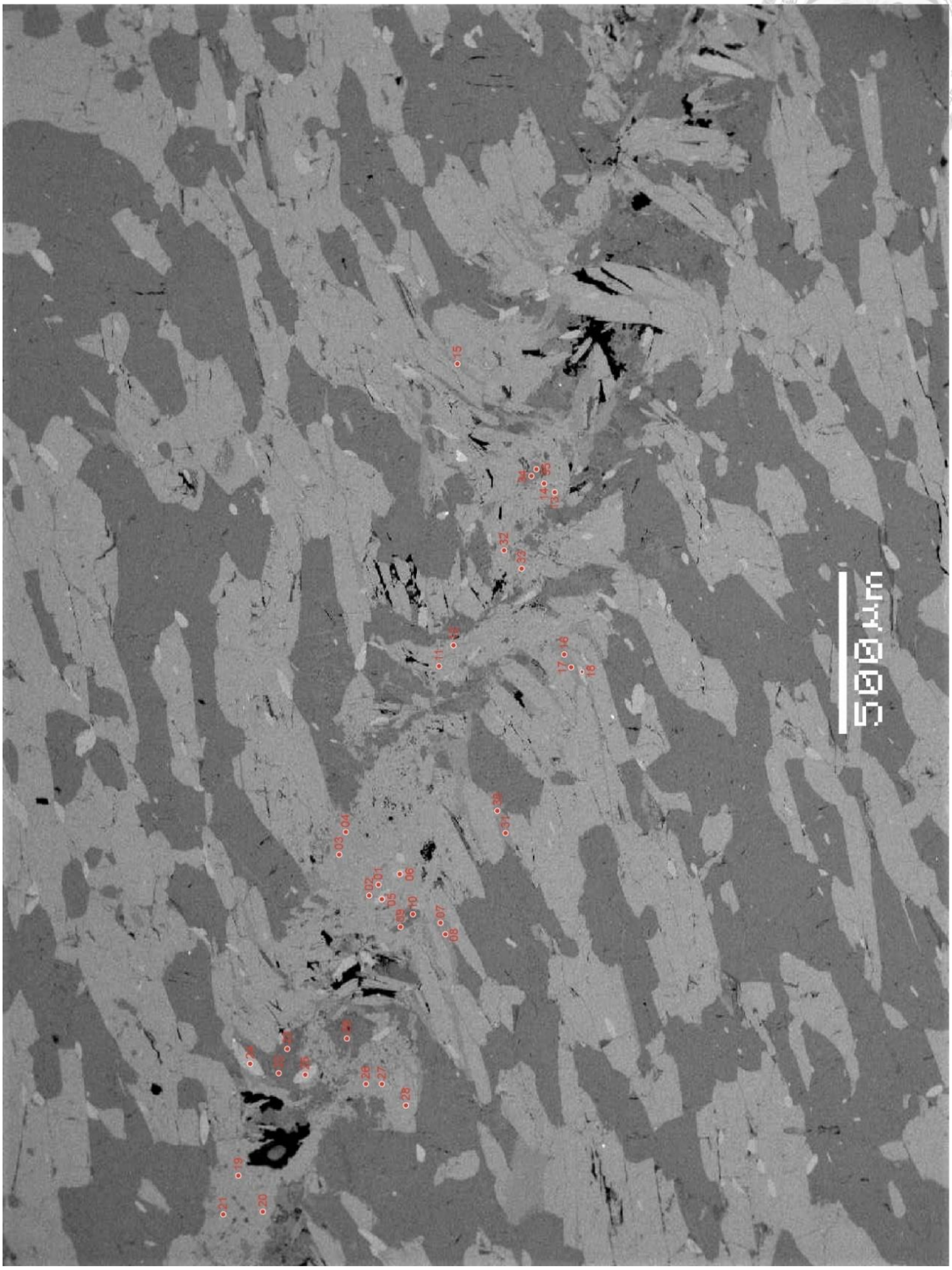

doi:10.6342/NTU202202659

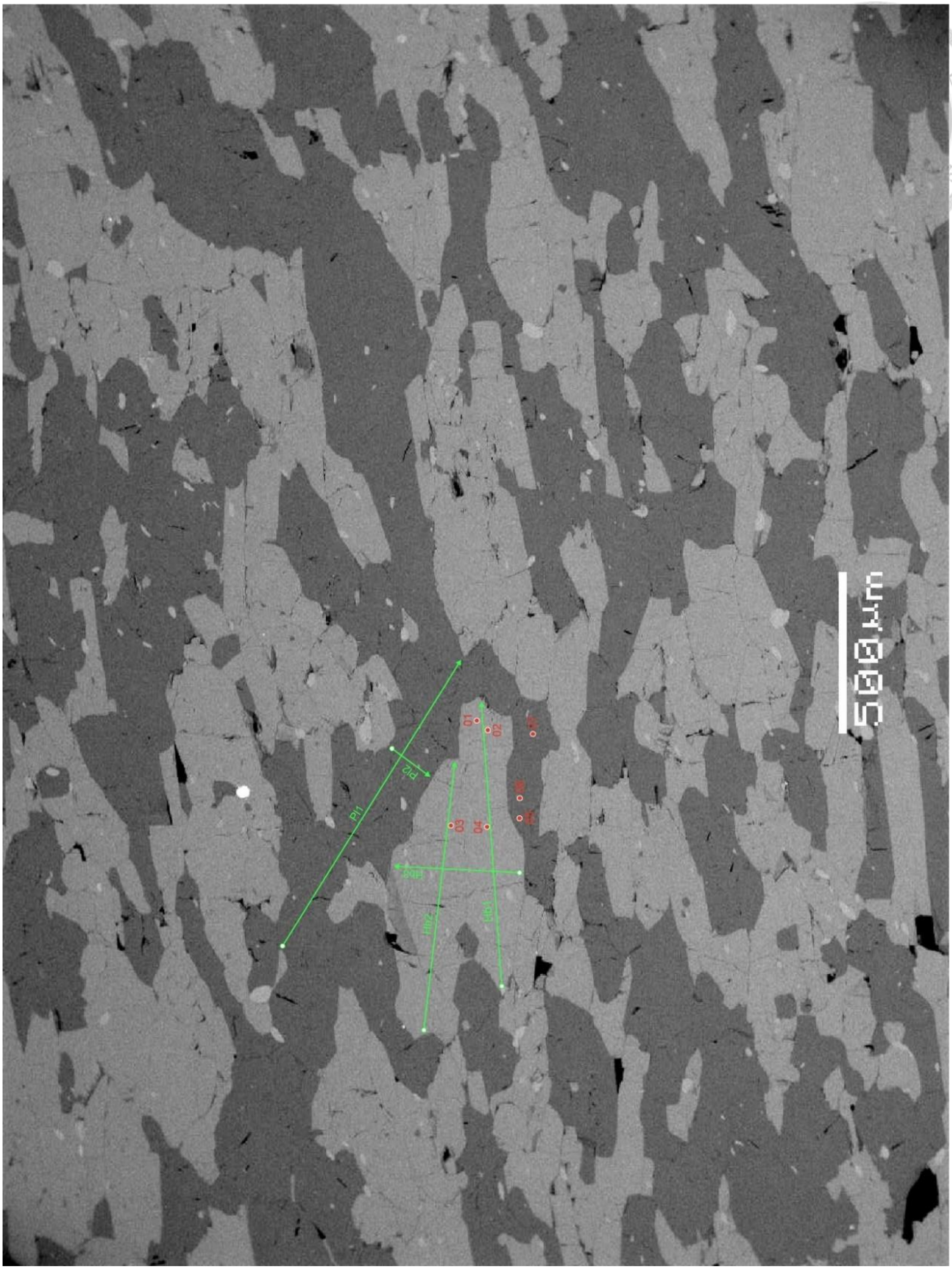

doi:10.6342/NTU202202659

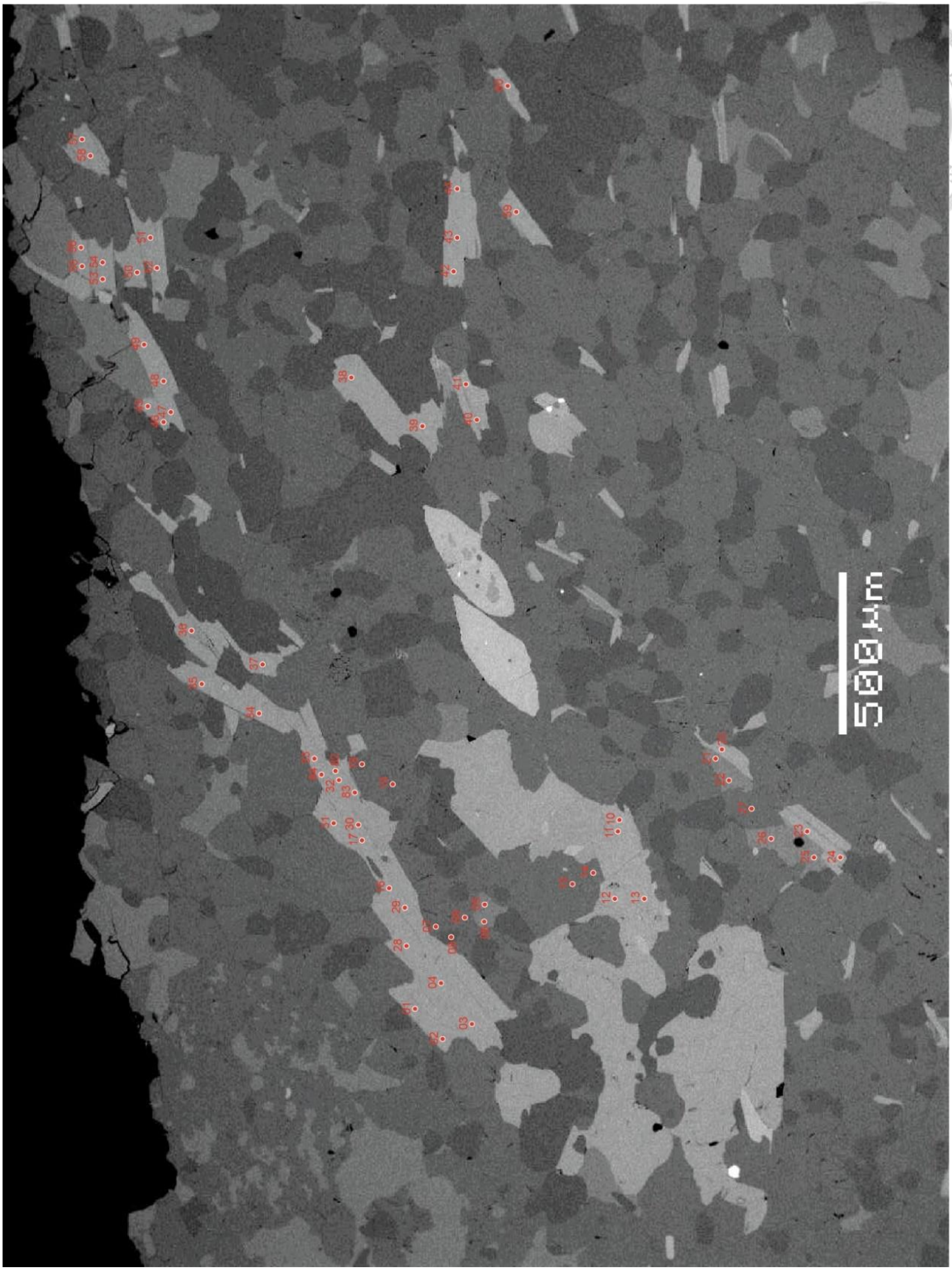

doi:10.6342/NTU202202659

8.5 Analytical Results of Mineral Chemistry

8.5.1 18LYA01 Sillimanite Mica Schist

Mineral	No.	SiO_2	TiO_2	Al_2O_3	FeO	Fe_2O_3	MnO	MgO	CaO	Na_2O	K_2O	Total	Si^{4+}	Ti^{4+}	Al^{3+}	Fe^{3+}	Mn^{2+}	Mg^{2+}	Ca^{2+}	Na^{+}	K^{+}	$T_{(total)}$	$M_{(total)}$	Ab	Or	An
Alkali Fsp.	A-20	64.38	0.00	19.22	0.14	0.15	0.00	0.00	0.01	1.39	14.31	99.44	2.97	0.00	1.04	0.01	0.00	0.00	0.00	0.12	0.84	4.02	0.97	12.84	87.13	0.03
	A-28	65.95	0.02	19.60	0.04	0.05	0.01	0.00	0.08	5.37	8.06	99.13	2.98	0.00	1.04	0.00	0.00	0.00	0.00	0.47	0.46	4.02	0.94	50.11	49.47	0.42
	A-30	64.46	0.00	19.33	0.16	0.18	0.06	0.00	0.00	1.04	14.69	99.73	2.97	0.00	1.05	0.01	0.00	0.00	0.00	0.09	0.86	4.02	0.95	9.67	90.33	0.00
	A-42	64.54	0.03	19.23	0.23	0.25	0.05	0.00	0.01	2.40	13.06	99.55	2.96	0.00	1.04	0.01	0.00	0.00	0.00	0.21	0.76	4.01	0.98	21.85	78.12	0.03
	A-54	64.28	0.04	19.22	0.06	0.07	0.00	0.00	0.00	1.46	14.60	99.65	2.96	0.00	1.04	0.00	0.00	0.00	0.00	0.13	0.86	4.01	0.99	13.19	86.81	0.00
	A-15	63.66	0.04	19.00	0.26	0.29	0.00	0.00	0.00	1.05	14.85	98.86	2.96	0.00	1.04	0.01	0.00	0.00	0.00	0.09	0.88	4.01	0.98	9.66	90.34	0.00
	A-21	64.12	0.14	18.81	0.04	0.05	0.00	0.00	0.00	1.41	14.13	98.66	2.98	0.00	1.03	0.00	0.00	0.00	0.00	0.13	0.84	4.02	0.97	13.20	86.79	0.02
	A-43	64.44	0.00	18.90	0.00	0.00	0.02	0.00	0.04	2.86	11.84	98.10	2.99	0.00	1.03	0.00	0.00	0.00	0.00	0.26	0.70	4.02	0.96	26.78	73.00	0.21
	A-53	63.29	0.04	18.28	0.03	0.03	0.00	0.00	0.00	1.00	14.93	97.57	2.99	0.00	1.02	0.00	0.00	0.00	0.00	0.09	0.90	4.01	0.99	9.25	90.75	0.00
	A-65	63.60	0.00	18.64	0.10	0.11	0.00	0.00	0.00	1.18	14.66	98.17	2.98	0.00	1.03	0.00	0.00	0.00	0.00	0.11	0.88	4.01	0.98	10.92	89.08	0.00
	A-97	63.92	0.00	18.93	0.02	0.03	0.01	0.00	0.02	1.16	14.76	98.83	2.97	0.00	1.04	0.00	0.00	0.00	0.00	0.10	0.88	4.01	0.98	10.68	89.20	0.11
	A-103	64.58	0.01	18.81	0.00	0.00	0.03	0.00	0.01	1.09	14.14	98.67	2.99	0.00	1.03	0.00	0.00	0.00	0.00	0.10	0.84	4.02	0.93	10.48	89.49	0.03
	A-16	62.71	0.06	18.47	0.12	0.13	0.01	0.00	0.02	0.72	14.50	96.58	2.98	0.00	1.03	0.00	0.00	0.00	0.00	0.07	0.88	4.02	0.95	6.99	92.93	0.08
	A-27	61.83	0.13	18.25	0.13	0.15	0.05	0.00	0.00	0.81	14.34	95.54	2.97	0.00	1.03	0.01	0.00	0.00	0.00	0.08	0.88	4.02	0.95	7.87	92.13	0.00
	A-29	59.20	0.06	18.28	0.32	0.36	0.00	0.03	0.04	0.72	13.99	92.63	2.94	0.00	1.07	0.01	0.00	0.00	0.00	0.07	0.89	4.02	0.96	7.20	92.59	0.21
	A-38	62.19	0.08	18.91	0.45	0.50	0.04	0.00	0.01	0.70	14.25	96.63	2.95	0.00	1.06	0.02	0.00	0.00	0.00	0.06	0.86	4.03	0.93	6.96	92.96	0.08
	A-39	61.19	0.00	18.59	0.18	0.20	0.00	0.07	0.01	0.93	13.98	94.95	2.96	0.00	1.06	0.01	0.00	0.01	0.00	0.09	0.86	4.02	0.96	9.17	90.77	0.06
	A-95	60.89	0.09	18.99	0.15	0.17	0.02	0.00	0.00	0.91	14.74	95.78	2.93	0.00	1.08	0.01	0.00	0.00	0.00	0.08	0.91	4.02	0.99	8.55	91.45	0.00
	A-96	58.39	0.00	17.78	0.00	0.00	0.09	0.00	0.01	0.66	13.99	90.91	2.96	0.00	1.06	0.00	0.00	0.00	0.00	0.06	0.90	4.02	0.97	6.64	93.32	0.03
	A-101	62.38	0.00	18.25	0.18	0.20	0.00	0.00	0.00	0.89	14.50	96.20	2.98	0.00	1.03	0.01	0.00	0.00	0.00	0.08	0.88	4.01	0.97	8.50	91.50	0.00
	A-102	62.79	0.13	18.67	0.03	0.03	0.02	0.00	0.00	1.06	13.86	96.56	2.98	0.00	1.04	0.00	0.00	0.00	0.00	0.10	0.84	4.03	0.94	10.38	89.60	0.02
	A-104	59.84	0.00	17.36	0.11	0.12	0.04	0.01	0.00	0.72	14.32	92.40	2.98	0.00	1.02	0.00	0.00	0.00	0.00	0.07	0.91	4.01	0.98	7.12	92.88	0.00
Plagioclase	A-90	64.62	0.07	22.67	0.10	0.11	0.02	0.00	2.62	9.70	0.29	100.09	2.84	0.00	1.17	0.00	0.00	0.00	0.12	0.83	0.02	4.02	0.97	85.53	1.71	12.76
	A-91	66.04	0.02	21.56	0.06	0.07	0.00	0.01	1.26	10.64	0.23	99.83	2.90	0.00	1.12	0.00	0.00	0.00	0.06	0.91	0.01	4.02	0.98	92.63	1.30	6.07
	A-70	68.43	0.03	20.44	0.09	0.10	0.00	0.00	0.32	11.67	0.17	101.15	2.96	0.00	1.04	0.00	0.00	0.00	0.01	0.98	0.01	4.01	1.00	97.60	0.92	1.48

doi:10.6342/NTU202202659

Mineral	No.	SiO_2	TiO_2	Al_2O_3	FeO	MnO	MgO	CaO	Na_2O	K_2O	Total	Si^{4+}	Ti^{4+}	Al^{3+}	Fe^{2+}	Mn^{2+}	Mg^{2+}	Ca^{2+}	Na^{+}	K^{+}	$Al_{(M)}$	$Al_{(T)}$	$I_{(total)}$	$M_{(total)}$	$T_{(total)}$	Mg/(Mg+Fe)	Ti-in-Bt thermometer (°C)
Biotite	7	34.79	2.90	20.50	21.52	0.21	6.30	0.08	0.22	8.96	95.47	5.32	0.33	3.70	2.75	0.03	1.44	0.01	0.07	1.75	1.02	2.68	1.83	5.57	8.00	0.34	655
	8	35.15	2.73	20.28	22.39	0.26	6.12	0.01	0.19	8.92	96.06	5.36	0.31	3.65	2.86	0.03	1.39	0.00	0.05	1.74	1.01	2.64	1.79	5.60	8.00	0.33	643
	9	35.17	2.59	20.27	21.50	0.18	6.26	0.00	0.22	9.13	95.32	5.39	0.30	3.66	2.76	0.02	1.43	0.00	0.06	1.78	1.05	2.61	1.85	5.56	8.00	0.34	636
	10	34.73	2.41	20.89	21.03	0.24	6.26	0.00	0.22	9.11	94.88	5.34	0.28	3.78	2.70	0.03	1.43	0.00	0.06	1.79	1.12	2.66	1.85	5.57	8.00	0.35	624
	11	34.80	2.56	20.59	20.89	0.19	6.19	0.00	0.23	8.88	94.31	5.37	0.30	3.74	2.70	0.02	1.42	0.00	0.07	1.75	1.11	2.63	1.82	5.55	8.00	0.35	635
	12	34.68	2.34	20.85	21.87	0.20	6.47	0.00	0.26	8.75	95.41	5.31	0.27	3.76	2.80	0.03	1.48	0.00	0.08	1.71	1.07	2.69	1.79	5.65	8.00	0.35	618
	13	34.53	2.56	20.60	21.58	0.18	6.38	0.03	0.21	8.91	94.97	5.31	0.30	3.74	2.78	0.02	1.46	0.00	0.06	1.75	1.05	2.69	1.82	5.61	8.00	0.35	635
	22	35.27	2.81	20.24	21.53	0.24	6.14	0.10	0.25	8.80	95.36	5.39	0.32	3.65	2.75	0.03	1.40	0.02	0.07	1.72	1.04	2.61	1.80	5.55	8.00	0.34	649
	23	35.00	2.84	19.93	22.35	0.31	6.08	0.03	0.18	9.07	95.78	5.37	0.33	3.60	2.87	0.04	1.39	0.00	0.05	1.77	0.97	2.63	1.83	5.59	8.00	0.33	650
	24	33.53	2.66	21.13	21.59	0.30	6.35	0.02	0.22	8.93	94.74	5.19	0.31	3.85	2.79	0.04	1.47	0.00	0.07	1.76	1.04	2.81	1.83	5.65	8.00	0.34	643
	25	34.95	2.58	20.62	20.92	0.22	6.23	0.00	0.23	9.00	94.75	5.37	0.30	3.73	2.69	0.03	1.43	0.00	0.07	1.76	1.11	2.63	1.83	5.55	8.00	0.35	636
	31	35.02	2.37	20.46	22.25	0.28	6.27	0.05	0.22	8.99	95.92	5.35	0.27	3.68	2.84	0.04	1.43	0.01	0.07	1.75	1.04	2.65	1.83	5.62	8.00	0.33	619
	37	34.94	2.25	20.94	20.70	0.22	6.43	0.02	0.21	9.14	94.84	5.36	0.26	3.79	2.66	0.03	1.47	0.00	0.06	1.79	1.15	2.64	1.85	5.56	8.00	0.36	613
	40	35.14	2.37	20.58	21.08	0.26	6.42	0.00	0.24	9.01	95.11	5.38	0.27	3.71	2.70	0.03	1.47	0.00	0.07	1.76	1.10	2.62	1.83	5.57	8.00	0.35	621
	44	34.66	1.94	20.90	21.78	0.22	6.19	0.00	0.24	8.98	94.91	5.34	0.22	3.80	2.81	0.03	1.42	0.00	0.07	1.77	1.14	2.66	1.84	5.62	8.00	0.34	581
	45	35.44	2.49	20.32	20.43	0.21	6.47	0.01	0.23	9.08	94.67	5.44	0.29	3.67	2.62	0.03	1.48	0.00	0.07	1.78	1.11	2.56	1.84	5.52	8.00	0.36	631
	46	34.53	1.98	20.57	21.78	0.32	6.09	0.00	0.23	9.17	94.68	5.35	0.23	3.75	2.82	0.04	1.41	0.00	0.07	1.81	1.10	2.65	1.88	5.60	8.00	0.33	587
	49	35.14	2.38	20.94	20.23	0.31	6.06	0.02	0.30	9.01	94.38	5.40	0.28	3.79	2.60	0.04	1.39	0.00	0.09	1.77	1.19	2.60	1.86	5.50	8.00	0.35	622
	52	34.84	2.40	20.98	20.39	0.24	6.34	0.05	0.19	9.06	94.47	5.36	0.28	3.80	2.62	0.03	1.45	0.01	0.06	1.78	1.16	2.64	1.84	5.54	8.00	0.36	625
	55	34.99	3.04	20.33	20.91	0.38	6.17	0.00	0.17	9.07	95.06	5.37	0.35	3.67	2.68	0.05	1.41	0.00	0.05	1.77	1.04	2.63	1.83	5.53	8.00	0.34	663
	64	34.47	2.56	20.55	22.06	0.26	6.30	0.07	0.20	8.26	94.74	5.31	0.30	3.73	2.84	0.03	1.45	0.01	0.06	1.62	1.05	2.69	1.70	5.67	8.00	0.34	635
	67	35.08	2.49	20.97	21.93	0.21	5.89	0.00	0.24	8.91	95.72	5.35	0.29	3.77	2.80	0.03	1.34	0.00	0.07	1.73	1.12	2.65	1.81	5.57	8.00	0.32	627
	69	34.56	2.41	21.05	21.83	0.26	5.93	0.00	0.15	9.23	95.41	5.31	0.28	3.81	2.80	0.03	1.36	0.00	0.04	1.81	1.11	2.69	1.85	5.59	8.00	0.33	622
	71	35.09	2.96	20.33	21.04	0.32	6.34	0.00	0.27	8.86	95.21	5.37	0.34	3.66	2.69	0.04	1.45	0.00	0.08	1.73	1.03	2.63	1.81	5.55	8.00	0.35	659
	72	35.17	2.73	20.58	22.30	0.28	6.35	0.05	0.32	8.93	96.71	5.33	0.31	3.67	2.82	0.04	1.43	0.01	0.09	1.73	1.00	2.67	1.83	5.61	8.00	0.34	642
	73	34.50	3.03	20.37	21.85	0.21	6.46	0.00	0.22	9.18	95.83	5.28	0.35	3.67	2.80	0.03	1.47	0.00	0.06	1.79	0.96	2.72	1.86	5.60	8.00	0.35	662
	89	35.40	2.55	20.90	21.73	0.28	6.09	0.03	0.27	8.98	96.23	5.37	0.29	3.73	2.76	0.04	1.38	0.00	0.08	1.74	1.10	2.63	1.82	5.56	8.00	0.33	631
	93	34.65	2.64	19.51	21.08	0.34	6.46	0.01	0.22	9.12	94.03	5.39	0.31	3.58	2.74	0.04	1.50	0.00	0.07	1.81	0.97	2.61	1.88	5.57	8.00	0.35	643
	94	34.67	2.72	20.55	22.27	0.27	6.09	0.00	0.22	9.20	95.97	5.31	0.31	3.71	2.85	0.03	1.39	0.00	0.07	1.79	1.01	2.69	1.86	5.60	8.00	0.33	643
	100	34.64	2.93	20.35	20.95	0.17	6.29	0.00	0.27	8.78	94.38	5.35	0.34	3.70	2.70	0.02	1.45	0.00	0.08	1.73	1.05	2.65	1.81	5.56	8.00	0.35	659
	105	35.40	3.01	20.17	21.54	0.23	6.40	0.00	0.16	9.21	96.11	5.38	0.34	3.61	2.74	0.03	1.45	0.00	0.05	1.78	0.99	2.62	1.83	5.55	8.00	0.35	660
	106	34.58	3.20	20.06	21.95	0.27	6.53	0.00	0.19	9.18	95.95	5.29	0.37	3.62	2.81	0.03	1.49	0.00	0.05	1.79	0.91	2.71	1.85	5.61	8.00	0.35	671
	107	34.64	3.08	20.33	22.29	0.17	6.40	0.04	0.22	8.74	95.91	5.29	0.35	3.66	2.85	0.02	1.46	0.01	0.07	1.70	0.95	2.71	1.78	5.63	8.00	0.34	664
	108	34.83	2.61	20.38	23.08	0.30	6.36	0.00	0.21	9.11	96.88	5.30	0.30	3.65	2.94	0.04	1.44	0.00	0.06	1.77	0.95	2.70	1.83	5.66	8.00	0.33	635
	116	34.94	3.31	20.32	22.52	0.25	6.30	0.00	0.18	9.28	97.09	5.29	0.38	3.63	2.85	0.03	1.42	0.00	0.05	1.79	0.92	2.71	1.84	5.60	8.00	0.33	673
	117	35.09	3.23	20.91	20.96	0.21	6.17	0.05	0.14	8.91	95.67	5.33	0.37	3.74	2.66	0.03	1.40	0.01	0.04	1.73	1.08	2.67	1.78	5.53	8.00	0.34	671
	118	34.48	3.17	20.22	21.70	0.25	5.92	0.03	0.15	9.12	95.03	5.32	0.37	3.68	2.80	0.03	1.36	0.01	0.05	1.80	0.99	2.68	1.85	5.55	8.00	0.33	669
	120	34.87	3.03	20.54	22.16	0.20	6.22	0.01	0.19	9.14	96.37	5.30	0.35	3.68	2.82	0.03	1.41	0.00	0.06	1.77	0.99	2.70	1.83	5.59	8.00	0.33	660
	121	35.08	2.81	20.57	21.18	0.28	6.18	0.00	0.18	8.61	94.88	5.38	0.32	3.72	2.71	0.04	1.41	0.00	0.05	1.68	1.09	2.62	1.73	5.58	8.00	0.34	650
	122	35.44	2.42	21.10	22.53	0.31	6.32	0.00	0.24	8.91	97.26	5.33	0.27	3.74	2.83	0.04	1.42	0.00	0.07	1.71	1.07	2.67	1.78	5.64	8.00	0.33	620
	124	35.03	2.20	20.86	21.85	0.31	6.25	0.00	0.22	8.90	95.61	5.35	0.25	3.76	2.79	0.04	1.42	0.00	0.07	1.73	1.11	2.65	1.80	5.62	8.00	0.34	605
	125	34.91	2.35	19.91	21.69	0.36	6.24	0.00	0.22	9.00	94.66	5.40	0.27	3.63	2.81	0.05	1.44	0.00	0.07	1.77	1.03	2.60	1.84	5.59	8.00	0.34	620
	128	34.92	2.82	20.65	21.99	0.24	6.09	0.03	0.28	8.79	95.80	5.33	0.32	3.71	2.81	0.03	1.38	0.00	0.08	1.71	1.04	2.67	1.80	5.59	8.00	0.33	649

doi:10.6342/NTU202202659

Mineral	No.	SiO_2	TiO_2	Al_2O_3	FeO	MnO	MgO	CaO	Na_2O	K_2O	Total	Si^{4+}	Ti^{4+}	Al^{3+}	Fe^{2+}	Mn^{2+}	Mg^{2+}	Ca^{2+}	Na^{+}	K^{+}	$Al_{(M)}$	$Al_{(T)}$	$I_{(total)}$	$M_{(total)}$	$T_{(total)}$
Muscovite	A-32	45.28	0.32	36.66	1.22	0.04	0.37	0.00	0.73	9.83	94.46	6.06	0.03	5.78	0.14	0.00	0.07	0.00	0.19	1.68	3.84	1.94	1.87	4.09	8.00
	A-35	47.00	0.32	35.55	0.94	0.01	0.36	0.00	0.57	9.49	94.25	6.26	0.03	5.58	0.10	0.00	0.07	0.00	0.15	1.61	3.83	1.74	1.76	4.04	8.00
	A-47	45.83	0.48	36.77	1.02	0.00	0.46	0.03	0.72	9.90	95.21	6.07	0.05	5.74	0.11	0.00	0.09	0.00	0.19	1.67	3.82	1.93	1.86	4.07	8.00
	A-48	45.60	0.56	36.33	1.03	0.07	0.47	0.00	0.62	10.18	94.85	6.08	0.06	5.71	0.11	0.01	0.09	0.00	0.16	1.73	3.79	1.92	1.89	4.06	8.00
	A-74	45.57	0.88	36.79	1.33	0.02	0.42	0.00	0.62	9.75	95.37	6.04	0.09	5.74	0.15	0.00	0.08	0.00	0.16	1.65	3.78	1.96	1.81	4.10	8.00
	A-110	45.58	0.50	36.59	1.12	0.02	0.37	0.00	0.71	9.94	94.81	6.07	0.05	5.75	0.12	0.00	0.07	0.00	0.18	1.69	3.82	1.93	1.87	4.07	8.00
	A-111	45.35	0.64	36.48	0.83	0.08	0.38	0.00	0.62	10.09	94.46	6.06	0.06	5.75	0.09	0.01	0.08	0.00	0.16	1.72	3.81	1.94	1.88	4.06	8.00
	A-112	45.68	0.68	36.30	1.12	0.03	0.48	0.00	0.67	9.90	94.86	6.08	0.07	5.70	0.13	0.00	0.10	0.00	0.17	1.68	3.78	1.92	1.85	4.07	8.00
	A-123	46.34	0.41	37.02	0.90	0.00	0.40	0.04	0.66	9.85	95.62	6.10	0.04	5.75	0.10	0.00	0.08	0.01	0.17	1.65	3.85	1.90	1.83	4.07	8.00
	A-129	45.55	0.92	36.39	0.94	0.03	0.38	0.01	0.70	9.51	94.42	6.08	0.09	5.72	0.10	0.00	0.07	0.00	0.18	1.62	3.80	1.92	1.80	4.07	8.00
	A-130	46.35	1.15	36.25	0.97	0.01	0.41	0.01	0.63	10.01	95.80	6.11	0.11	5.63	0.11	0.00	0.08	0.00	0.16	1.68	3.74	1.89	1.85	4.04	8.00
	A-131	46.21	0.82	37.26	0.96	0.00	0.35	0.00	0.62	9.91	96.13	6.06	0.08	5.76	0.11	0.00	0.07	0.00	0.16	1.66	3.82	1.94	1.81	4.07	8.00
	A-132	46.09	0.51	37.50	1.06	0.01	0.45	0.03	0.74	9.97	96.36	6.04	0.05	5.79	0.12	0.00	0.09	0.00	0.19	1.67	3.83	1.96	1.86	4.08	8.00
	A-133	46.02	0.85	37.11	1.08	0.05	0.36	0.02	0.66	9.97	96.12	6.05	0.08	5.75	0.12	0.01	0.07	0.00	0.17	1.67	3.79	1.95	1.84	4.07	8.00
	A-134	46.41	1.08	36.96	1.09	0.05	0.46	0.00	0.69	9.75	96.48	6.07	0.11	5.69	0.12	0.01	0.09	0.00	0.18	1.63	3.76	1.93	1.80	4.08	8.00

doi:10.6342/NTU202202659

Mineral	No.	SiO_2	TiO_2	Al_2O_3	FeO	MnO	MgO	CaO	Na_2O	K_2O	Total	Si^{4+}	Ti^{4+}	Al^{3+}	Fe^{2+}	Fe^{3+}	Mn^{2+}	Mg^{2+}	Ca^{2+}	Na^{+}	K^{+}	Al_Z	Al_Y	$X_{(total)}$	$Y_{(total)}$	$Z_{(total)}$	Alm	Py	Sp	Gro
Garnet1-1	1	37.76	0.00	21.80	30.49	8.00	1.91	1.22	0.00	0.00	101.17	3.02	0.00	2.06	2.04	0.00	0.54	0.23	0.10	0.00	0.00	0.00	2.06	2.92	2.06	3.02	0.70	0.08	0.19	0.04
	4	37.88	0.00	21.81	30.77	6.67	2.05	1.48	0.00	0.00	100.66	3.04	0.00	2.06	2.07	0.00	0.45	0.25	0.13	0.00	0.00	0.00	2.06	2.89	2.06	3.04	0.71	0.08	0.16	0.04
	5	37.83	0.00	21.84	32.10	6.30	2.24	1.44	0.03	0.00	101.78	3.01	0.00	2.05	2.13	0.00	0.42	0.26	0.12	0.00	0.00	0.00	2.05	2.94	2.05	3.01	0.72	0.09	0.14	0.04
	8	37.53	0.02	21.45	33.62	5.57	2.33	1.21	0.00	0.00	101.73	2.99	0.00	2.01	2.24	0.00	0.38	0.28	0.10	0.00	0.00	0.01	2.00	3.00	2.00	3.00	0.75	0.09	0.13	0.03
	11	37.72	0.01	21.86	32.27	5.08	2.31	1.60	0.01	0.00	100.86	3.02	0.00	2.06	2.16	0.00	0.34	0.28	0.14	0.00	0.00	0.00	2.06	2.92	2.06	3.02	0.74	0.09	0.12	0.05
	12	37.56	0.02	21.73	33.41	4.96	2.22	1.26	0.04	0.00	101.20	3.00	0.00	2.05	2.23	0.00	0.34	0.26	0.11	0.01	0.00	0.00	2.05	2.94	2.05	3.00	0.76	0.09	0.11	0.04
	13	37.81	0.00	21.88	32.97	5.03	2.39	1.37	0.01	0.00	101.46	3.01	0.00	2.05	2.20	0.00	0.34	0.28	0.12	0.00	0.00	0.00	2.05	2.93	2.05	3.01	0.75	0.10	0.12	0.04
	16	38.02	0.00	21.46	33.42	5.01	2.24	1.57	0.00	0.00	101.73	3.03	0.00	2.01	2.22	0.00	0.34	0.27	0.13	0.00	0.00	0.00	2.01	2.96	2.01	3.03	0.75	0.09	0.11	0.05
	17	37.74	0.00	21.90	33.14	4.98	2.34	1.50	0.01	0.00	101.62	3.00	0.00	2.05	2.20	0.00	0.34	0.28	0.13	0.00	0.00	0.00	2.05	2.94	2.05	3.00	0.75	0.09	0.11	0.04
	21	36.06	0.00	21.97	32.94	4.71	2.32	1.61	0.00	0.00	99.62	2.92	0.00	2.10	2.23	0.03	0.32	0.28	0.14	0.00	0.00	0.08	2.02	2.98	2.05	3.00	0.75	0.09	0.11	0.05
	23	38.04	0.00	21.92	32.92	5.04	2.28	1.54	0.00	0.00	101.74	3.02	0.00	2.05	2.19	0.00	0.34	0.27	0.13	0.00	0.00	0.00	2.05	2.93	2.05	3.02	0.75	0.09	0.12	0.04
	25	37.83	0.12	21.73	33.28	5.03	2.33	1.42	0.03	0.00	101.77	3.01	0.01	2.04	2.21	0.00	0.34	0.28	0.12	0.00	0.00	0.00	2.04	2.95	2.04	3.01	0.75	0.09	0.11	0.04
	27	37.03	0.01	22.30	33.50	4.94	2.26	1.43	0.00	0.00	101.47	2.95	0.00	2.09	2.23	0.00	0.33	0.27	0.12	0.00	0.00	0.05	2.04	2.96	2.04	3.00	0.76	0.09	0.11	0.04
	29	38.16	0.00	22.06	32.97	4.98	2.09	1.57	0.04	0.00	101.86	3.03	0.00	2.06	2.19	0.00	0.33	0.25	0.13	0.01	0.00	0.00	2.06	2.90	2.06	3.03	0.75	0.09	0.12	0.05
	31	38.20	0.06	21.98	33.17	4.69	2.42	1.43	0.02	0.00	101.97	3.02	0.00	2.05	2.20	0.00	0.31	0.29	0.12	0.00	0.00	0.00	2.05	2.92	2.05	3.02	0.75	0.10	0.11	0.04
	32	36.69	0.06	20.98	33.80	5.17	2.35	1.24	0.00	0.00	100.28	2.97	0.00	2.00	2.29	0.03	0.35	0.28	0.11	0.00	0.00	0.03	1.97	3.03	2.00	3.00	0.75	0.09	0.12	0.04
	33	37.48	0.04	21.95	33.39	5.01	2.30	1.55	0.03	0.00	101.74	2.98	0.00	2.06	2.22	0.00	0.34	0.27	0.13	0.01	0.00	0.02	2.03	2.96	2.03	3.00	0.75	0.09	0.11	0.04
	35	37.66	0.03	21.28	33.56	5.25	2.27	1.64	0.03	0.00	101.74	3.00	0.00	2.00	2.23	0.00	0.35	0.27	0.14	0.01	0.00	0.00	2.00	3.00	2.00	3.00	0.75	0.09	0.12	0.05
	36	37.73	0.00	21.76	32.46	5.47	2.28	1.53	0.02	0.00	101.26	3.01	0.00	2.05	2.17	0.00	0.37	0.27	0.13	0.00	0.00	0.00	2.05	2.94	2.05	3.01	0.74	0.09	0.13	0.04
	37	37.40	0.04	21.49	32.05	5.52	2.26	1.45	0.00	0.00	100.22	3.02	0.00	2.04	2.16	0.00	0.38	0.27	0.13	0.00	0.00	0.00	2.04	2.94	2.04	3.02	0.74	0.09	0.13	0.04
	38	36.99	0.05	21.89	31.83	6.09	2.32	1.41	0.03	0.01	100.60	2.97	0.00	2.07	2.14	0.00	0.41	0.28	0.12	0.00	0.00	0.03	2.04	2.95	2.04	3.00	0.72	0.09	0.14	0.04
	39	37.20	0.00	21.87	31.61	6.59	2.28	1.22	0.01	0.00	100.78	2.98	0.00	2.07	2.12	0.00	0.45	0.27	0.10	0.00	0.00	0.02	2.05	2.95	2.05	3.00	0.72	0.09	0.15	0.04
	42	36.86	0.04	21.29	32.08	6.55	2.19	1.04	0.04	0.01	100.10	2.98	0.00	2.03	2.17	0.00	0.45	0.26	0.09	0.01	0.00	0.02	2.01	2.97	2.01	3.00	0.73	0.09	0.15	0.03
Garnet1-2	2	36.78	0.00	21.79	32.91	6.22	2.24	1.51	0.00	0.02	101.46	2.94	0.00	2.05	2.20	0.04	0.42	0.27	0.13	0.00	0.00	0.06	1.99	3.01	2.03	3.00	0.73	0.09	0.14	0.04
	4	36.58	0.07	21.80	32.06	5.62	2.20	1.88	0.00	0.00	100.20	2.95	0.00	2.07	2.16	0.01	0.38	0.26	0.16	0.00	0.00	0.05	2.02	2.97	2.03	3.00	0.73	0.09	0.13	0.05
	5	38.00	0.08	21.76	32.88	5.30	2.32	1.65	0.00	0.00	101.98	3.01	0.00	2.03	2.18	0.00	0.36	0.27	0.14	0.00	0.00	0.00	2.03	2.95	2.03	3.01	0.74	0.09	0.12	0.05
	6	38.25	0.00	22.09	32.37	5.07	2.12	1.55	0.00	0.00	101.46	3.05	0.00	2.07	2.16	0.00	0.34	0.25	0.13	0.00	0.00	0.00	2.07	2.88	2.07	3.05	0.75	0.09	0.12	0.05
	7	36.92	0.00	21.86	33.33	5.10	2.32	1.54	0.00	0.00	101.07	2.95	0.00	2.06	2.23	0.02	0.35	0.28	0.13	0.00	0.00	0.05	2.02	2.98	2.03	3.00	0.75	0.09	0.12	0.04
	9	38.15	0.02	21.97	33.44	4.63	2.28	1.45	0.00	0.00	101.94	3.02	0.00	2.05	2.22	0.00	0.31	0.27	0.12	0.00	0.00	0.00	2.05	2.92	2.05	3.02	0.76	0.09	0.11	0.04
	10	37.61	0.07	21.57	33.23	4.92	2.37	1.33	0.02	0.00	101.13	3.01	0.00	2.03	2.22	0.00	0.33	0.28	0.11	0.00	0.00	0.00	2.03	2.95	2.03	3.01	0.75	0.10	0.11	0.04
	11	38.25	0.09	21.70	32.87	5.03	2.12	1.42	0.01	0.00	101.48	3.05	0.01	2.04	2.19	0.00	0.34	0.25	0.12	0.00	0.00	0.00	2.04	2.90	2.04	3.05	0.75	0.09	0.12	0.04
	14	37.67	0.06	21.68	33.95	4.87	2.32	1.37	0.03	0.00	101.94	2.99	0.00	2.03	2.25	0.00	0.33	0.28	0.12	0.01	0.00	0.01	2.02	2.97	2.02	3.00	0.76	0.09	0.11	0.04
	15	37.82	0.09	22.12	32.72	4.46	2.17	1.42	0.00	0.00	100.80	3.03	0.01	2.09	2.19	0.00	0.30	0.26	0.12	0.00	0.00	0.00	2.09	2.88	2.09	3.03	0.76	0.09	0.11	0.04
	16	37.01	0.04	21.24	32.41	5.07	2.24	1.36	0.04	0.00	99.41	3.01	0.00	2.04	2.20	0.00	0.35	0.27	0.12	0.01	0.00	0.00	2.04	2.94	2.04	3.01	0.75	0.09	0.12	0.04
	19	37.81	0.00	21.82	32.86	5.01	2.13	1.45	0.00	0.00	101.08	3.03	0.00	2.06	2.20	0.00	0.34	0.25	0.12	0.00	0.00	0.00	2.06	2.92	2.06	3.03	0.75	0.09	0.12	0.04
	21	38.22	0.02	21.91	31.39	5.01	2.33	1.28	0.00	0.00	100.15	3.08	0.00	2.08	2.11	0.00	0.34	0.28	0.11	0.00	0.00	0.00	2.08	2.84	2.08	3.08	0.74	0.10	0.12	0.04
	22	37.82	0.04	21.83	32.81	5.25	2.38	1.17	0.02	0.00	101.31	3.02	0.00	2.05	2.19	0.00	0.35	0.28	0.10	0.00	0.00	0.00	2.05	2.93	2.05	3.02	0.75	0.10	0.12	0.03
	23	36.88	0.00	21.79	32.51	5.84	2.32	1.30	0.00	0.00	100.64	2.96	0.00	2.06	2.19	0.00	0.40	0.28	0.11	0.00	0.00	0.04	2.03	2.97	2.03	3.00	0.74	0.09	0.13	0.04
	24	37.18	0.01	22.05	32.30	5.84	2.20	1.29	0.00	0.00	100.88	2.98	0.00	2.08	2.17	0.00	0.40	0.26	0.11	0.00	0.00	0.02	2.06	2.94	2.06	3.00	0.74	0.09	0.14	0.04
	25	37.77	0.00	21.57	31.69	6.29	2.24	1.17	0.00	0.00	100.73	3.03	0.00	2.04	2.13	0.00	0.43	0.27	0.10	0.00	0.00	0.00	2.04	2.93	2.04	3.03	0.73	0.09	0.15	0.03
	27	37.92	0.00	21.92	31.70	6.95	2.16	0.69	0.02	0.01	101.35	3.03	0.00	2.06	2.12	0.00	0.47	0.26	0.06	0.00	0.00	0.00	2.06	2.90	2.06	3.03	0.73	0.09	0.16	0.02
	29	37.63	0.00	21.99	30.98	7.57	2.17	0.55	0.06	0.00	100.96	3.02	0.00	2.08	2.08	0.00	0.51	0.26	0.05	0.01	0.00	0.00	2.08	2.90	2.08	3.02	0.72	0.09	0.18	0.02

doi:10.6342/NTU202202659

Mineral	No.	SiO_2	TiO_2	Al_2O_3	FeO	MnO	MgO	CaO	Na_2O	K_2O	Total	Si^{4+}	Ti^{4+}	Al^{3+}	Fe^{2+}	Fe^{3+}	Mn^{2+}	Mg^{2+}	Ca^{2+}	Na^{+}	K^{+}	Al_Z	Al_Y	$X_{(total)}$	$Y_{(total)}$	$Z_{(total)}$	Alm	Py	Sp	Gro
Garnet2-1	1	37.83	0.00	21.64	32.47	6.13	2.07	1.48	0.00	0.00	101.60	3.02	0.00	2.03	2.16	0.00	0.41	0.25	0.13	0.00	0.00	0.00	2.03	2.95	2.03	3.02	0.73	0.08	0.14	0.04
	2	37.73	0.00	21.74	32.39	5.49	2.15	1.56	0.00	0.00	101.06	3.02	0.00	2.05	2.17	0.00	0.37	0.26	0.13	0.00	0.00	0.00	2.05	2.93	2.05	3.02	0.74	0.09	0.13	0.05
	3	38.18	0.07	21.92	32.41	5.49	2.20	1.65	0.02	0.00	101.94	3.03	0.00	2.05	2.15	0.00	0.37	0.26	0.14	0.00	0.00	0.00	2.05	2.92	2.05	3.03	0.74	0.09	0.13	0.05
	4	37.76	0.00	22.00	32.53	5.57	2.35	1.43	0.00	0.00	101.64	3.00	0.00	2.06	2.16	0.00	0.38	0.28	0.12	0.00	0.00	0.00	2.06	2.94	2.06	3.00	0.74	0.09	0.13	0.04
	5	38.15	0.08	21.75	32.93	5.35	1.73	1.51	0.05	0.00	101.55	3.05	0.00	2.05	2.20	0.00	0.36	0.21	0.13	0.00	0.00	0.00	2.05	2.90	2.05	3.05	0.76	0.07	0.12	0.04
	6	38.22	0.00	21.86	33.18	4.74	2.39	1.53	0.00	0.00	101.92	3.03	0.00	2.04	2.20	0.00	0.32	0.28	0.13	0.00	0.00	0.00	2.04	2.93	2.04	3.03	0.75	0.10	0.11	0.04
	7	37.82	0.00	21.79	31.19	5.33	2.24	1.27	0.02	0.00	99.66	3.06	0.00	2.08	2.11	0.00	0.37	0.27	0.11	0.00	0.00	0.00	2.08	2.86	2.08	3.06	0.74	0.09	0.13	0.04
	8	38.33	0.04	21.75	32.47	5.09	2.25	1.52	0.04	0.00	101.49	3.05	0.00	2.04	2.16	0.00	0.34	0.27	0.13	0.00	0.00	0.00	2.04	2.90	2.04	3.05	0.75	0.09	0.12	0.04
	14	38.19	0.15	21.73	32.94	5.36	2.23	1.31	0.04	0.00	101.95	3.03	0.01	2.03	2.19	0.00	0.36	0.26	0.11	0.00	0.00	0.00	2.03	2.92	2.03	3.03	0.75	0.09	0.12	0.04
	15	37.87	0.00	21.92	32.28	5.24	2.17	1.53	0.00	0.00	101.01	3.03	0.00	2.07	2.16	0.00	0.35	0.26	0.13	0.00	0.00	0.00	2.07	2.90	2.07	3.03	0.74	0.09	0.12	0.05
	16	37.54	0.00	21.93	32.99	5.30	2.16	1.36	0.01	0.00	101.27	3.00	0.00	2.06	2.20	0.00	0.36	0.26	0.12	0.00	0.00	0.00	2.06	2.94	2.06	3.00	0.75	0.09	0.12	0.04
	19	37.62	0.00	21.60	32.66	5.16	2.14	1.50	0.04	0.00	100.71	3.02	0.00	2.05	2.19	0.00	0.35	0.26	0.13	0.00	0.00	0.00	2.05	2.93	2.05	3.02	0.75	0.09	0.12	0.04
	20	37.77	0.00	21.85	33.69	4.77	2.13	1.23	0.00	0.00	101.44	3.01	0.00	2.06	2.25	0.00	0.32	0.25	0.11	0.00	0.00	0.00	2.06	2.93	2.06	3.01	0.77	0.09	0.11	0.04
	21	37.20	0.11	22.23	33.68	5.25	2.23	1.13	0.00	0.00	101.82	2.96	0.01	2.08	2.24	0.00	0.35	0.26	0.10	0.00	0.00	0.04	2.04	2.95	2.08	3.00	0.76	0.09	0.12	0.03
	22	37.14	0.01	22.12	33.41	5.22	2.29	1.39	0.03	0.00	101.60	2.96	0.00	2.07	2.22	0.01	0.35	0.27	0.12	0.00	0.00	0.04	2.03	2.97	2.08	3.00	0.75	0.09	0.12	0.04
	23	37.84	0.00	22.37	32.79	5.02	2.33	1.44	0.01	0.00	101.81	3.00	0.00	2.09	2.17	0.00	0.34	0.28	0.12	0.00	0.00	0.00	2.09	2.91	2.09	3.00	0.75	0.09	0.12	0.04
	24	37.81	0.09	21.58	32.41	5.28	2.29	1.37	0.03	0.00	100.86	3.03	0.01	2.04	2.17	0.00	0.36	0.27	0.12	0.00	0.00	0.00	2.04	2.92	2.04	3.03	0.74	0.09	0.12	0.04
	26	37.78	0.03	22.04	32.92	5.30	2.27	1.36	0.02	0.00	101.71	3.00	0.00	2.06	2.19	0.00	0.36	0.27	0.12	0.00	0.00	0.00	2.06	2.93	2.06	3.00	0.75	0.09	0.12	0.04
	29	38.26	0.00	21.73	32.76	5.24	2.31	1.52	0.03	0.02	101.87	3.04	0.00	2.03	2.17	0.00	0.35	0.27	0.13	0.00	0.00	0.00	2.03	2.93	2.03	3.04	0.74	0.09	0.12	0.04
	30	36.62	0.00	22.09	33.06	5.27	2.26	1.38	0.00	0.00	100.68	2.94	0.00	2.09	2.22	0.01	0.36	0.27	0.12	0.00	0.00	0.06	2.03	2.97	2.10	3.00	0.75	0.09	0.12	0.04
	31	37.74	0.08	21.82	32.57	4.94	2.23	1.40	0.00	0.00	100.79	3.03	0.00	2.06	2.18	0.00	0.34	0.27	0.12	0.00	0.00	0.00	2.06	2.91	2.06	3.03	0.75	0.09	0.12	0.04
	33	38.22	0.00	21.43	32.84	5.28	2.31	1.50	0.03	0.00	101.61	3.04	0.00	2.01	2.19	0.00	0.36	0.27	0.13	0.00	0.00	0.00	2.01	2.94	2.01	3.04	0.74	0.09	0.12	0.04
	35	38.00	0.00	21.91	32.17	5.29	2.24	1.29	0.04	0.00	100.92	3.04	0.00	2.07	2.15	0.00	0.36	0.27	0.11	0.00	0.00	0.00	2.07	2.89	2.07	3.04	0.75	0.09	0.12	0.04
	39	38.15	0.01	21.80	32.52	5.76	2.30	1.39	0.02	0.00	101.97	3.03	0.00	2.04	2.16	0.00	0.39	0.27	0.12	0.00	0.00	0.00	2.04	2.93	2.04	3.03	0.73	0.09	0.13	0.04
	40	37.58	0.00	21.98	32.61	5.66	2.27	1.38	0.05	0.00	101.52	2.99	0.00	2.06	2.17	0.00	0.38	0.27	0.12	0.00	0.00	0.01	2.06	2.94	2.06	3.00	0.74	0.09	0.13	0.04
	41	35.59	0.00	21.95	32.80	5.85	2.21	1.34	0.00	0.00	99.73	2.89	0.00	2.10	2.23	0.06	0.40	0.27	0.12	0.00	0.00	0.11	1.99	3.01	2.16	3.00	0.74	0.09	0.13	0.04
	42	38.34	0.08	21.96	32.23	5.95	2.14	1.08	0.00	0.00	101.76	3.05	0.00	2.06	2.14	0.00	0.40	0.25	0.09	0.00	0.00	0.00	2.06	2.89	2.06	3.05	0.74	0.09	0.14	0.03
	45	37.75	0.05	22.07	31.87	6.59	2.04	1.22	0.00	0.00	101.58	3.01	0.00	2.07	2.12	0.00	0.44	0.24	0.10	0.00	0.00	0.00	2.07	2.91	2.07	3.01	0.73	0.08	0.15	0.04
	46	37.61	0.00	22.20	31.63	6.97	1.98	1.24	0.00	0.00	101.63	3.00	0.00	2.08	2.11	0.00	0.47	0.24	0.11	0.00	0.00	0.00	2.08	2.92	2.08	3.00	0.72	0.08	0.16	0.04
Garnet2-2	4	37.42	0.00	21.83	31.54	5.59	2.25	1.55	0.00	0.00	100.17	3.02	0.00	2.07	2.13	0.00	0.38	0.27	0.13	0.00	0.00	0.00	2.07	2.91	2.07	3.02	0.73	0.09	0.13	0.05
	6	38.15	0.00	22.18	32.38	5.53	2.20	1.48	0.00	0.00	101.93	3.02	0.00	2.07	2.15	0.00	0.37	0.26	0.13	0.00	0.00	0.00	2.07	2.90	2.07	3.02	0.74	0.09	0.13	0.04
	8	37.57	0.00	22.15	32.81	5.34	2.12	1.38	0.00	0.00	101.36	3.00	0.00	2.08	2.19	0.00	0.36	0.25	0.12	0.00	0.00	0.00	2.08	2.92	2.08	3.00	0.75	0.09	0.12	0.04
	10	37.69	0.10	22.02	33.13	5.56	2.23	1.16	0.00	0.00	101.88	2.99	0.01	2.06	2.20	0.00	0.37	0.26	0.10	0.00	0.00	0.01	2.06	2.94	2.06	3.00	0.75	0.09	0.13	0.03
	12	38.46	0.00	21.84	30.86	5.76	2.30	1.44	0.00	0.00	100.66	3.08	0.00	2.06	2.07	0.00	0.39	0.27	0.12	0.00	0.00	0.00	2.06	2.86	2.06	3.08	0.72	0.10	0.14	0.04
	13	37.87	0.05	21.99	32.20	5.71	2.33	1.30	0.00	0.00	101.45	3.02	0.00	2.06	2.14	0.00	0.39	0.28	0.11	0.00	0.00	0.00	2.06	2.92	2.06	3.02	0.74	0.09	0.13	0.04
	16	37.58	0.08	21.92	32.27	5.38	2.23	1.37	0.00	0.02	100.84	3.01	0.00	2.07	2.16	0.00	0.36	0.27	0.12	0.00	0.00	0.00	2.07	2.91	2.07	3.01	0.74	0.09	0.13	0.04
	19	38.11	0.02	21.98	32.02	5.61	2.22	1.42	0.00	0.00	101.39	3.04	0.00	2.06	2.13	0.00	0.38	0.26	0.12	0.00	0.00	0.00	2.06	2.90	2.06	3.04	0.74	0.09	0.13	0.04
	25	37.96	0.00	22.12	32.92	5.32	2.26	1.38	0.00	0.00	101.94	3.01	0.00	2.07	2.18	0.00	0.36	0.27	0.12	0.00	0.00	0.00	2.07	2.92	2.07	3.01	0.75	0.09	0.12	0.04
	26	37.44	0.00	22.04	32.35	5.32	2.15	1.44	0.01	0.00	100.75	3.00	0.00	2.08	2.17	0.00	0.36	0.26	0.12	0.00	0.00	0.00	2.08	2.91	2.08	3.00	0.75	0.09	0.12	0.04
	28	37.62	0.03	21.81	32.33	4.81	2.25	1.43	0.00	0.00	100.29	3.03	0.00	2.07	2.18	0.00	0.33	0.27	0.12	0.00	0.00	0.00	2.07	2.90	2.07	3.03	0.75	0.09	0.11	0.04
	29	37.35	0.02	22.12	32.67	5.34	2.26	1.53	0.01	0.00	101.31	2.98	0.00	2.08	2.18	0.00	0.36	0.27	0.13	0.00	0.00	0.02	2.06	2.94	2.08	3.00	0.74	0.09	0.12	0.04
	36	38.31	0.02	21.96	32.42	5.28	2.39	1.24	0.00	0.00	101.61	3.04	0.00	2.06	2.15	0.00	0.36	0.28	0.11	0.00	0.00	0.00	2.06	2.90	2.06	3.04	0.74	0.10	0.12	0.04
	40	36.30	0.00	22.20	33.98	5.27	2.19	1.53	0.01	0.00	101.47	2.90	0.00	2.09	2.27	0.06	0.36	0.26	0.13	0.00	0.00	0.10	1.98	3.02	2.15	3.00	0.75	0.09	0.12	0.04
	41	37.78	0.06	22.07	33.14	5.15	2.28	1.41	0.00	0.00	101.88	3.00	0.00	2.06	2.20	0.00	0.35	0.27	0.12	0.00	0.00	0.00	2.06	2.93	2.06	3.00	0.75	0.09	0.12	0.04
	43	37.92	0.00	22.06	32.79	5.26	2.33	1.45	0.01	0.00	101.82	3.01	0.00	2.06	2.18	0.00	0.35	0.28	0.12	0.00	0.00	0.00	2.06	2.93	2.06	3.01	0.74	0.09	0.12	0.04
	47	37.94	0.11	22.08	32.54	5.34	2.32	1.49	0.01	0.00	101.83	3.01	0.01	2.06	2.16	0.00	0.36	0.27	0.13	0.00	0.00	0.00	2.06	2.92	2.06	3.01	0.74	0.09	0.12	0.04
	48	37.94	0.07	21.91	31.68	5.20	2.23	1.61	0.01	0.00	100.64	3.04	0.00	2.07	2.12	0.00	0.35	0.27	0.14	0.00	0.00	0.00	2.07	2.88	2.07	3.04	0.74	0.09	0.12	0.05
	49	37.93	0.13	21.76	31.81	5.74	2.23	1.32	0.01	0.00	100.92	3.04	0.01	2.05	2.13	0.00	0.39	0.27	0.11	0.00	0.00	0.00	2.05	2.90	2.05	3.04	0.73	0.09	0.13	0.04
	51	37.32	0.05	21.82	32.25	6.18	2.14	1.24	0.03	0.00	101.03	2.99	0.00	2.06	2.16	0.00	0.42	0.26	0.11	0.00	0.00	0.01	2.05	2.94	2.06	3.00	0.73	0.09	0.14	0.04

doi:10.6342/NTU202202659

Mineral	No.	SiO_2	TiO_2	Al_2O_3	FeO	MnO	MgO	CaO	Na_2O	K_2O	Total	Si^{4+}	Ti^{4+}	Al^{3+}	Fe^{2+}	Fe^{3+}	Mn^{2+}	Mg^{2+}	Ca^{2+}	Na^{+}	K^{+}	Al_Z	Al_Y	$X_{(total)}$	$Y_{(total)}$	$Z_{(total)}$	Alm	Py	Sp	Gro
Garnet3-1	2	37.07	0.00	22.08	31.66	6.89	2.14	0.92	0.00	0.00	100.77	2.98	0.00	2.09	2.13	0.00	0.47	0.26	0.08	0.00	0.00	0.02	2.07	2.93	2.07	3.00	0.73	0.09	0.16	0.03
	3	37.82	0.00	21.89	31.40	6.59	2.09	1.02	0.00	0.00	100.80	3.04	0.00	2.07	2.11	0.00	0.45	0.25	0.09	0.00	0.00	0.00	2.07	2.89	2.07	3.04	0.73	0.09	0.15	0.03
	5	38.05	0.00	21.63	32.68	6.02	2.29	1.31	0.01	0.00	102.00	3.02	0.00	2.02	2.17	0.00	0.40	0.27	0.11	0.00	0.00	0.00	2.02	2.96	2.02	3.02	0.73	0.09	0.14	0.04
	7	37.35	0.00	21.77	30.61	6.91	2.21	0.87	0.00	0.00	99.71	3.03	0.00	2.08	2.08	0.00	0.47	0.27	0.08	0.00	0.00	0.00	2.08	2.89	2.08	3.03	0.72	0.09	0.16	0.03
	9	37.74	0.00	21.80	32.48	5.96	2.24	1.02	0.02	0.00	101.27	3.02	0.00	2.05	2.17	0.00	0.40	0.27	0.09	0.00	0.00	0.00	2.05	2.93	2.05	3.02	0.74	0.09	0.14	0.03
	10	37.81	0.12	22.25	32.01	5.93	2.38	1.04	0.00	0.00	101.54	3.01	0.01	2.09	2.13	0.00	0.40	0.28	0.09	0.00	0.00	0.00	2.09	2.90	2.09	3.01	0.73	0.10	0.14	0.03
	11	38.49	0.02	21.65	32.60	5.93	2.19	1.08	0.00	0.00	101.95	3.06	0.00	2.03	2.17	0.00	0.40	0.26	0.09	0.00	0.00	0.00	2.03	2.91	2.03	3.06	0.74	0.09	0.14	0.03
	14	37.99	0.00	22.05	31.57	5.71	2.26	1.13	0.00	0.00	100.71	3.05	0.00	2.08	2.12	0.00	0.39	0.27	0.10	0.00	0.00	0.00	2.08	2.87	2.08	3.05	0.74	0.09	0.14	0.03
	18	38.12	0.00	21.91	32.33	6.02	2.25	1.28	0.00	0.00	101.90	3.03	0.00	2.05	2.15	0.00	0.40	0.27	0.11	0.00	0.00	0.00	2.05	2.93	2.05	3.03	0.73	0.09	0.14	0.04
	19	38.28	0.30	22.00	32.10	5.77	2.07	1.33	0.02	0.00	101.86	3.04	0.02	2.06	2.13	0.00	0.39	0.25	0.11	0.00	0.00	0.00	2.06	2.88	2.06	3.04	0.74	0.09	0.13	0.04
	20	38.11	0.00	21.72	31.91	5.75	2.22	1.41	0.00	0.02	101.13	3.05	0.00	2.05	2.13	0.00	0.39	0.26	0.12	0.00	0.00	0.00	2.05	2.91	2.05	3.05	0.73	0.09	0.13	0.04
	21	37.63	0.03	22.09	32.91	5.67	2.11	1.53	0.00	0.00	101.97	2.99	0.00	2.07	2.18	0.00	0.38	0.25	0.13	0.00	0.00	0.01	2.05	2.94	2.05	3.00	0.74	0.08	0.13	0.04
	23	38.26	0.08	21.85	30.58	5.81	1.99	1.58	0.00	0.00	100.16	3.08	0.01	2.08	2.06	0.00	0.40	0.24	0.14	0.00	0.00	0.00	2.08	2.83	2.08	3.08	0.73	0.08	0.14	0.05
	24	38.14	0.16	21.89	31.92	5.63	2.06	1.69	0.00	0.00	101.48	3.04	0.01	2.06	2.13	0.00	0.38	0.24	0.14	0.00	0.00	0.00	2.06	2.90	2.06	3.04	0.73	0.08	0.13	0.05
	25	38.32	0.00	21.93	30.94	5.78	2.17	1.72	0.03	0.00	100.89	3.06	0.00	2.07	2.07	0.00	0.39	0.26	0.15	0.00	0.00	0.00	2.07	2.87	2.07	3.06	0.72	0.09	0.14	0.05
	27	36.55	2.81	21.48	30.69	5.34	2.09	1.65	0.02	0.00	100.64	2.95	0.17	2.04	2.07	0.00	0.37	0.25	0.14	0.00	0.00	0.05	1.99	2.83	1.99	3.00	0.73	0.09	0.13	0.05
	30	38.20	0.05	21.93	31.63	5.76	2.19	1.59	0.03	0.00	101.37	3.04	0.00	2.06	2.11	0.00	0.39	0.26	0.14	0.00	0.00	0.00	2.06	2.89	2.06	3.04	0.73	0.09	0.13	0.05
	31	37.90	0.01	21.99	32.73	5.42	1.77	1.56	0.00	0.00	101.37	3.03	0.00	2.07	2.19	0.00	0.37	0.21	0.13	0.00	0.00	0.00	2.07	2.90	2.07	3.03	0.75	0.07	0.13	0.05
	33	37.94	0.12	22.09	32.09	5.62	2.15	1.71	0.00	0.00	101.71	3.01	0.01	2.07	2.13	0.00	0.38	0.25	0.15	0.00	0.00	0.00	2.07	2.91	2.07	3.01	0.73	0.09	0.13	0.05
	35	38.23	0.06	21.78	31.57	5.39	2.07	1.65	0.05	0.00	100.78	3.06	0.00	2.06	2.12	0.00	0.37	0.25	0.14	0.01	0.00	0.00	2.06	2.87	2.06	3.06	0.74	0.09	0.13	0.05
	37	37.79	0.03	22.08	32.51	5.69	2.05	1.60	0.00	0.00	101.75	3.00	0.00	2.07	2.16	0.00	0.38	0.24	0.14	0.00	0.00	0.00	2.07	2.92	2.07	3.00	0.74	0.08	0.13	0.05
	38	37.33	0.00	22.12	32.34	5.47	1.99	1.85	0.07	0.01	101.18	2.98	0.00	2.08	2.16	0.00	0.37	0.24	0.16	0.01	0.00	0.02	2.06	2.93	2.06	3.00	0.74	0.08	0.13	0.05
	39	37.75	0.02	22.02	32.20	5.39	2.04	1.65	0.05	0.00	101.10	3.02	0.00	2.07	2.15	0.00	0.36	0.24	0.14	0.01	0.00	0.00	2.07	2.90	2.07	3.02	0.74	0.08	0.13	0.05
	42	38.11	0.00	21.41	32.55	4.93	2.25	1.63	0.01	0.00	100.88	3.05	0.00	2.02	2.18	0.00	0.33	0.27	0.14	0.00	0.00	0.00	2.02	2.92	2.02	3.05	0.75	0.09	0.11	0.05
	43	37.80	0.00	21.95	32.32	5.46	2.00	1.42	0.03	0.00	100.99	3.03	0.00	2.07	2.16	0.00	0.37	0.24	0.12	0.00	0.00	0.00	2.07	2.90	2.07	3.03	0.75	0.08	0.13	0.04
	46	38.35	0.11	21.89	32.64	5.19	2.14	1.49	0.00	0.00	101.81	3.05	0.01	2.05	2.17	0.00	0.35	0.25	0.13	0.00	0.00	0.00	2.05	2.90	2.05	3.05	0.75	0.09	0.12	0.04
	47	37.50	0.07	22.00	33.08	5.07	2.25	1.49	0.00	0.00	101.47	2.99	0.00	2.07	2.20	0.00	0.34	0.27	0.13	0.00	0.00	0.01	2.05	2.94	2.05	3.00	0.75	0.09	0.12	0.04
	49	38.46	0.00	21.57	32.85	5.13	2.31	1.64	0.03	0.00	101.97	3.05	0.00	2.01	2.18	0.00	0.34	0.27	0.14	0.00	0.00	0.00	2.01	2.93	2.01	3.05	0.74	0.09	0.12	0.05
	51	38.23	0.00	22.07	32.92	4.78	2.22	1.63	0.01	0.00	101.85	3.03	0.00	2.06	2.18	0.00	0.32	0.26	0.14	0.00	0.00	0.00	2.06	2.90	2.06	3.03	0.75	0.09	0.11	0.05
	53	37.96	0.00	20.88	32.90	5.29	2.31	1.52	0.00	0.00	100.87	3.05	0.00	1.98	2.21	0.00	0.36	0.28	0.13	0.00	0.00	0.00	1.98	2.98	1.98	3.05	0.74	0.09	0.12	0.04
	54	37.70	0.06	22.35	32.17	5.64	2.11	1.46	0.05	0.00	101.53	3.00	0.00	2.10	2.14	0.00	0.38	0.25	0.12	0.01	0.00	0.00	2.10	2.89	2.10	3.00	0.74	0.09	0.13	0.04

doi:10.6342/NTU202202659

8.5.2 181117A01 Sillimanite Mica Schist

Mineral	No.	SiO_2	TiO_2	Al_2O_3	Cr_2O_3	FeO	MnO	MgO	CaO	Na_2O	K_2O	Total	Si^{4+}	Ti^{4+}	Al^{3+}	Fe^{2+}	Mn^{2+}	Mg^{2+}	Ca^{2+}	Na^{+}	K^{+}	$Al_{(M)}$	$Al_{(T)}$	$I_{(total)}$	$M_{(total)}$	$T_{(total)}$	X_{Mg}	Ti-in-Bt thermometer (°C)
Biotite	28	33.97	3.14	18.77	0.04	24.08	0.42	4.75	0.02	0.28	8.97	94.44	5.36	0.37	3.49	3.18	0.06	1.12	0.00	0.08	1.81	0.85	2.64	1.89	5.57	8.00	0.26	667
	29	35.89	2.77	18.18	0.03	24.13	0.36	5.29	0.01	0.32	9.23	96.20	5.53	0.32	3.30	3.11	0.05	1.22	0.00	0.09	1.82	0.84	2.47	1.91	5.53	8.00	0.28	643
	30	34.80	2.73	18.57	0.00	24.29	0.46	5.06	0.00	0.25	9.35	95.51	5.43	0.32	3.41	3.17	0.06	1.18	0.00	0.08	1.86	0.84	2.57	1.94	5.57	8.00	0.27	643
	31	34.72	2.56	17.84	0.02	25.13	0.42	4.89	0.00	0.23	9.05	94.87	5.47	0.30	3.32	3.31	0.06	1.15	0.00	0.07	1.82	0.79	2.53	1.89	5.61	8.00	0.26	632
	32	34.26	2.71	18.15	0.03	24.20	0.39	5.09	0.00	0.21	9.43	94.46	5.42	0.32	3.38	3.20	0.05	1.20	0.00	0.06	1.90	0.80	2.58	1.97	5.58	8.00	0.27	644
	33	34.87	2.71	18.56	0.00	24.34	0.44	5.19	0.00	0.26	9.24	95.61	5.43	0.32	3.41	3.17	0.06	1.20	0.00	0.08	1.84	0.84	2.57	1.92	5.59	8.00	0.28	641
	34	34.21	2.72	18.60	0.03	24.27	0.42	5.05	0.00	0.20	9.21	94.71	5.39	0.32	3.45	3.20	0.06	1.19	0.00	0.06	1.85	0.84	2.61	1.91	5.60	8.00	0.27	643
	35	34.48	2.33	18.99	0.04	24.26	0.40	5.23	0.01	0.24	9.34	95.32	5.39	0.27	3.50	3.17	0.05	1.22	0.00	0.07	1.86	0.89	2.61	1.94	5.61	8.00	0.28	615
	36	34.21	2.66	18.36	0.05	24.24	0.35	5.39	0.00	0.31	9.25	94.82	5.39	0.32	3.41	3.19	0.05	1.27	0.00	0.09	1.86	0.79	2.61	1.95	5.61	8.00	0.28	640
	37	34.53	2.47	18.25	0.00	23.95	0.40	5.23	0.02	0.23	9.33	94.41	5.45	0.29	3.39	3.16	0.05	1.23	0.00	0.07	1.88	0.84	2.55	1.95	5.58	8.00	0.28	628
	38	34.72	1.90	18.03	0.01	24.34	0.38	5.96	0.04	0.28	9.17	94.83	5.46	0.22	3.34	3.20	0.05	1.40	0.01	0.09	1.84	0.80	2.54	1.93	5.67	8.00	0.30	578
	39	34.42	2.40	18.31	0.01	25.10	0.42	5.40	0.00	0.28	9.20	95.53	5.40	0.28	3.38	3.29	0.06	1.26	0.00	0.08	1.84	0.78	2.60	1.92	5.67	8.00	0.28	621
	40	35.50	3.13	19.42	0.04	22.29	0.41	4.32	0.04	0.27	9.26	94.67	5.51	0.37	3.55	2.89	0.05	1.00	0.01	0.08	1.83	1.06	2.49	1.92	5.38	8.00	0.26	663
	42	35.47	2.95	18.96	0.04	23.58	0.41	4.88	0.02	0.30	9.17	95.77	5.48	0.34	3.45	3.05	0.05	1.12	0.00	0.09	1.81	0.93	2.52	1.90	5.49	8.00	0.27	653
	43	34.54	2.28	18.14	0.01	24.81	0.41	5.54	0.00	0.27	9.13	95.12	5.43	0.27	3.36	3.26	0.05	1.30	0.00	0.08	1.83	0.79	2.57	1.91	5.67	8.00	0.28	612
	44	34.78	2.68	18.58	0.00	23.85	0.43	4.96	0.00	0.31	9.05	94.64	5.46	0.32	3.44	3.13	0.06	1.16	0.00	0.10	1.81	0.89	2.54	1.91	5.56	8.00	0.27	640
	45	34.59	2.66	18.74	0.02	24.42	0.41	4.96	0.02	0.41	9.23	95.44	5.40	0.31	3.45	3.19	0.05	1.16	0.00	0.12	1.84	0.86	2.60	1.97	5.57	8.00	0.27	637
	46	34.82	2.59	18.29	0.02	24.34	0.43	5.13	0.06	0.37	9.13	95.17	5.45	0.30	3.37	3.19	0.06	1.20	0.01	0.11	1.82	0.83	2.55	1.95	5.57	8.00	0.27	634
	47	34.74	2.19	18.69	0.02	23.86	0.38	5.43	0.00	0.36	9.28	94.95	5.44	0.26	3.45	3.13	0.05	1.27	0.00	0.11	1.85	0.89	2.56	1.96	5.59	8.00	0.29	604
	48	34.84	2.58	18.42	0.05	23.96	0.37	4.95	0.00	0.26	9.33	94.76	5.47	0.30	3.41	3.15	0.05	1.16	0.00	0.08	1.87	0.88	2.53	1.95	5.54	8.00	0.27	634
	49	34.13	2.56	18.22	0.04	24.72	0.45	4.96	0.00	0.29	9.18	94.53	5.41	0.30	3.40	3.27	0.06	1.17	0.00	0.09	1.85	0.80	2.59	1.94	5.61	8.00	0.26	633
	50	35.03	2.47	18.59	0.00	24.38	0.41	4.96	0.01	0.29	9.43	95.57	5.46	0.29	3.42	3.18	0.05	1.15	0.00	0.09	1.87	0.88	2.54	1.96	5.56	8.00	0.27	625
	52	35.00	2.66	17.88	0.01	23.89	0.37	5.14	0.00	0.22	9.31	94.50	5.51	0.32	3.32	3.15	0.05	1.21	0.00	0.07	1.87	0.83	2.49	1.94	5.55	8.00	0.28	640
	53	35.15	2.54	18.26	0.00	24.20	0.37	5.30	0.00	0.26	9.17	95.24	5.49	0.30	3.36	3.16	0.05	1.23	0.00	0.08	1.83	0.84	2.51	1.90	5.58	8.00	0.28	630
	58	34.98	2.67	18.19	0.05	24.08	0.39	5.42	0.00	0.26	9.27	95.31	5.46	0.31	3.35	3.14	0.05	1.26	0.00	0.08	1.85	0.81	2.54	1.93	5.58	8.00	0.29	640
	59	35.60	2.68	17.89	0.06	24.26	0.38	5.54	0.00	0.26	8.93	95.61	5.53	0.31	3.27	3.15	0.05	1.28	0.00	0.08	1.77	0.80	2.47	1.85	5.59	8.00	0.29	640
	61	35.45	3.09	18.10	0.02	23.52	0.37	5.13	0.00	0.31	9.31	95.31	5.51	0.36	3.32	3.06	0.05	1.19	0.00	0.09	1.85	0.83	2.49	1.94	5.49	8.00	0.28	663
	62	35.25	1.75	18.53	0.03	23.83	0.35	5.60	0.00	0.31	9.13	94.78	5.52	0.21	3.42	3.12	0.05	1.31	0.00	0.09	1.82	0.93	2.48	1.92	5.61	8.00	0.30	558
	95	34.54	2.57	17.57	0.04	25.17	0.39	5.35	0.00	0.28	9.05	94.95	5.45	0.30	3.27	3.32	0.05	1.26	0.00	0.08	1.82	0.72	2.55	1.91	5.65	8.00	0.27	634
	96	34.56	2.27	17.73	0.02	25.36	0.41	5.53	0.00	0.21	9.02	95.11	5.44	0.27	3.29	3.34	0.05	1.30	0.00	0.06	1.81	0.74	2.56	1.87	5.70	8.00	0.28	611
	97	34.96	2.03	17.83	0.00	24.39	0.40	5.66	0.00	0.25	9.19	94.71	5.50	0.24	3.31	3.21	0.05	1.33	0.00	0.08	1.85	0.81	2.50	1.92	5.64	8.00	0.29	591
	98	34.86	2.53	18.15	0.01	24.07	0.41	5.28	0.03	0.32	9.35	95.00	5.47	0.30	3.35	3.16	0.05	1.24	0.00	0.10	1.87	0.82	2.53	1.97	5.57	8.00	0.28	631
	99	35.51	2.46	19.65	0.05	23.31	0.37	5.03	0.01	0.28	8.41	95.07	5.48	0.29	3.58	3.01	0.05	1.16	0.00	0.08	1.66	1.06	2.52	1.74	5.56	8.00	0.28	623
	100	34.87	2.55	17.89	0.05	24.36	0.40	5.46	0.01	0.28	8.81	94.68	5.48	0.30	3.31	3.20	0.05	1.28	0.00	0.08	1.77	0.79	2.52	1.85	5.63	8.00	0.29	633
	101	34.99	2.41	17.87	0.01	24.90	0.41	5.66	0.00	0.22	9.21	95.69	5.46	0.28	3.29	3.25	0.05	1.32	0.00	0.07	1.83	0.75	2.54	1.90	5.66	8.00	0.29	622
	102	34.47	2.62	18.50	0.04	24.34	0.35	5.22	0.01	0.22	9.20	94.97	5.41	0.31	3.42	3.20	0.05	1.22	0.00	0.07	1.84	0.83	2.59	1.91	5.61	8.00	0.28	636
	103	35.24	2.57	19.14	0.01	23.88	0.38	5.15	0.00	0.31	9.25	95.93	5.45	0.30	3.49	3.09	0.05	1.19	0.00	0.09	1.82	0.93	2.55	1.92	5.55	8.00	0.28	630
	104	35.29	2.69	18.80	0.04	24.05	0.39	5.20	0.00	0.22	9.07	95.75	5.46	0.31	3.43	3.11	0.05	1.20	0.00	0.07	1.79	0.89	2.54	1.86	5.57	8.00	0.28	639
	105	34.70	2.51	18.30	0.02	24.76	0.40	5.23	0.00	0.26	9.36	95.54	5.43	0.30	3.37	3.24	0.05	1.22	0.00	0.08	1.87	0.80	2.57	1.95	5.61	8.00	0.27	628
	106	35.25	2.28	18.81	0.02	24.03	0.39	5.29	0.00	0.37	9.32	95.75	5.47	0.27	3.44	3.12	0.05	1.22	0.00	0.11	1.84	0.91	2.53	1.95	5.57	8.00	0.28	609
	107	34.73	2.61	18.71	0.07	24.33	0.39	5.18	0.00	0.33	9.42	95.77	5.41	0.31	3.43	3.17	0.05	1.20	0.00	0.10	1.87	0.84	2.59	1.97	5.57	8.00	0.28	635
	108	35.26	2.46	18.53	0.06	24.54	0.42	5.37	0.00	0.30	9.33	96.26	5.46	0.29	3.38	3.18	0.06	1.24	0.00	0.09	1.84	0.84	2.54	1.93	5.59	8.00	0.28	623
	109	34.92	2.46	18.86	0.04	23.52	0.34	5.41	0.04	0.31	9.11	94.99	5.45	0.29	3.47	3.07	0.04	1.26	0.01	0.09	1.81	0.91	2.55	1.91	5.57	8.00	0.29	625
	110	35.13	2.31	19.06	0.01	22.63	0.38	5.65	0.00	0.30	9.29	94.75	5.47	0.27	3.50	2.95	0.05	1.31	0.00	0.09	1.85	0.96	2.53	1.94	5.54	8.00	0.31	615
	111	34.70	2.29	18.25	0.02	25.20	0.40	5.53	0.00	0.25	9.17	95.81	5.42	0.27	3.36	3.29	0.05	1.29	0.00	0.08	1.83	0.78	2.58	1.90	5.68	8.00	0.28	612
	112	35.11	2.55	18.13	0.02	24.43	0.36	5.54	0.00	0.21	9.18	95.53	5.47	0.30	3.33	3.18	0.05	1.29	0.00	0.06	1.82	0.80	2.53	1.89	5.62	8.00	0.29	631
	113	35.41	2.65	19.41	0.03	23.30	0.41	5.01	0.04	0.30	9.20	95.75	5.46	0.31	3.53	3.00	0.05	1.15	0.01	0.09	1.81	0.99	2.54	1.90	5.51	8.00	0.28	636
	114	35.67	2.64	19.09	0.03	22.93	0.37	5.34	0.00	0.34	9.29	95.70	5.49	0.31	3.47	2.95	0.05	1.23	0.00	0.10	1.83	0.96	2.51	1.93	5.50	8.00	0.29	636
	115	34.90	2.66	18.69	0.05	22.77	0.34	5.70	0.00	0.31	9.41	94.83	5.44	0.31	3.44	2.97	0.04	1.32	0.00	0.09	1.87	0.88	2.56	1.97	5.53	8.00	0.31	640
	116	34.62	2.26	19.13	0.05	23.55	0.39	5.54	0.00	0.28	9.49	95.29	5.40	0.27	3.52	3.07	0.05	1.29	0.00	0.08	1.89	0.91	2.60	1.97	5.59	8.00	0.30	610
	117	35.29	2.78	18.76	0.05	22.71	0.37	5.39	0.00	0.29	9.38	95.01	5.48	0.33	3.44	2.95	0.05	1.25	0.00	0.09	1.86	0.92	2.52	1.95	5.49	8.00	0.30	647

doi:10.6342/NTU202202659

Mineral	No.	SiO_2	TiO_2	Al_2O_3	Cr_2O_3	FeO	MnO	MgO	CaO	Na_2O	K_2O	Total	Si^{4+}	Ti^{4+}	Al^{3+}	Fe^{2+}	Mn^{2+}	Mg^{2+}	Ca^{2+}	Na^{+}	K^{+}	$Al_{(M)}$	$Al_{(T)}$	$I_{(total)}$	$M_{(total)}$	$T_{(total)}$
Muscvoite	1	46.56	0.97	34.72	0.02	1.87	0.07	0.67	0.07	0.66	9.41	95.01	6.20	0.10	5.45	0.21	0.01	0.13	0.01	0.17	1.60	3.64	1.80	1.78	4.09	8.00
	2	45.55	0.86	34.47	0.01	1.88	0.00	0.65	0.06	0.70	9.91	94.08	6.15	0.09	5.49	0.21	0.00	0.13	0.01	0.18	1.71	3.64	1.85	1.90	4.07	8.00
	3	46.24	0.82	34.98	0.05	1.78	0.01	0.68	0.06	0.66	9.28	94.56	6.18	0.08	5.51	0.20	0.00	0.13	0.01	0.17	1.58	3.68	1.82	1.76	4.10	8.00
	4	45.81	0.88	34.20	0.04	1.84	0.01	0.67	0.05	0.69	9.84	94.02	6.18	0.09	5.44	0.21	0.00	0.13	0.01	0.18	1.69	3.62	1.82	1.88	4.06	8.00
	5	46.94	0.85	34.87	0.00	1.73	0.01	0.67	0.04	0.77	9.34	95.21	6.22	0.08	5.45	0.19	0.00	0.13	0.01	0.20	1.58	3.67	1.78	1.78	4.08	8.00
	7	46.18	0.97	34.88	0.00	1.78	0.05	0.70	0.06	0.76	9.29	94.66	6.17	0.10	5.49	0.20	0.01	0.14	0.01	0.20	1.58	3.65	1.83	1.79	4.09	8.00
	8	46.34	0.74	34.42	0.01	1.63	0.00	0.68	0.05	0.73	9.88	94.48	6.21	0.07	5.44	0.18	0.00	0.13	0.01	0.19	1.69	3.65	1.79	1.89	4.04	8.00
	9	46.16	0.53	35.01	0.00	1.66	0.00	0.63	0.03	0.73	9.30	94.04	6.19	0.05	5.53	0.19	0.00	0.13	0.00	0.19	1.59	3.73	1.81	1.78	4.09	8.00
	11	46.72	0.79	34.73	0.02	1.62	0.01	0.63	0.04	0.74	9.06	94.35	6.23	0.08	5.46	0.18	0.00	0.12	0.01	0.19	1.54	3.70	1.77	1.74	4.08	8.00
	13	46.61	0.87	35.03	0.01	1.72	0.00	0.61	0.03	0.69	9.30	94.86	6.20	0.09	5.49	0.19	0.00	0.12	0.00	0.18	1.58	3.69	1.80	1.76	4.09	8.00
	15	46.61	0.91	34.93	0.02	1.62	0.03	0.56	0.02	0.68	9.44	94.81	6.20	0.09	5.48	0.18	0.00	0.11	0.00	0.17	1.60	3.68	1.80	1.78	4.07	8.00
	16	46.06	0.93	34.56	0.00	1.63	0.00	0.56	0.01	0.74	9.94	94.45	6.18	0.09	5.47	0.18	0.00	0.11	0.00	0.19	1.70	3.65	1.82	1.90	4.04	8.00
	17	46.61	1.00	34.97	0.01	1.60	0.03	0.62	0.02	0.67	9.12	94.65	6.20	0.10	5.48	0.18	0.00	0.12	0.00	0.17	1.55	3.69	1.80	1.72	4.09	8.00
	18	46.02	0.98	33.31	0.01	1.61	0.05	0.65	0.02	0.65	9.72	93.01	6.26	0.10	5.34	0.18	0.01	0.13	0.00	0.17	1.69	3.61	1.74	1.86	4.03	8.00
	19	46.83	0.97	34.89	0.01	1.60	0.00	0.60	0.02	0.74	9.22	94.87	6.22	0.10	5.46	0.18	0.00	0.12	0.00	0.19	1.56	3.68	1.78	1.76	4.07	8.00
	21	46.05	0.58	35.23	0.04	1.69	0.00	0.62	0.06	0.67	9.35	94.27	6.17	0.06	5.56	0.19	0.00	0.12	0.01	0.17	1.60	3.73	1.83	1.78	4.10	8.00
	23	45.65	0.99	34.57	0.04	1.87	0.04	0.70	0.05	0.71	9.33	93.95	6.15	0.10	5.49	0.21	0.00	0.14	0.01	0.19	1.60	3.64	1.85	1.80	4.10	8.00
	24	46.11	1.03	34.19	0.05	1.91	0.02	0.74	0.05	0.69	9.81	94.60	6.19	0.10	5.41	0.21	0.00	0.15	0.01	0.18	1.68	3.59	1.81	1.87	4.06	8.00
	25	46.23	0.89	35.19	0.01	1.83	0.02	0.67	0.04	0.69	9.32	94.88	6.16	0.09	5.52	0.20	0.00	0.13	0.01	0.18	1.58	3.68	1.84	1.77	4.11	8.00
	26	45.65	0.71	34.11	0.03	1.67	0.01	0.66	0.04	0.71	9.80	93.38	6.20	0.07	5.46	0.19	0.00	0.13	0.01	0.19	1.70	3.65	1.80	1.89	4.05	8.00
	27	47.00	0.90	34.46	0.00	1.67	0.02	0.72	0.04	0.73	8.98	94.52	6.26	0.09	5.41	0.19	0.00	0.14	0.01	0.19	1.53	3.66	1.74	1.72	4.09	8.00
Muscvoite	63	46.12	0.79	35.15	0.00	1.50	0.06	0.56	0.00	0.72	9.89	94.79	6.16	0.08	5.53	0.17	0.01	0.11	0.00	0.19	1.68	3.69	1.84	1.87	4.06	8.00
Line1	64	46.14	0.75	34.25	0.03	1.91	0.00	0.71	0.01	0.81	10.20	94.79	6.19	0.08	5.42	0.21	0.00	0.14	0.00	0.21	1.75	3.61	1.81	1.96	4.04	8.00
	65	46.85	0.83	35.13	0.03	1.74	0.05	0.66	0.00	0.70	9.55	95.52	6.20	0.08	5.48	0.19	0.01	0.13	0.00	0.18	1.61	3.67	1.80	1.79	4.08	8.00
	69	46.00	0.81	34.08	0.04	1.67	0.00	0.63	0.00	0.66	9.63	93.52	6.22	0.08	5.43	0.19	0.00	0.13	0.00	0.17	1.66	3.66	1.78	1.83	4.05	8.00
	70	46.28	0.90	34.14	0.00	1.68	0.04	0.68	0.00	0.64	10.30	94.65	6.21	0.09	5.40	0.19	0.00	0.14	0.00	0.17	1.76	3.61	1.79	1.93	4.03	8.00
	71	46.26	0.89	34.59	0.00	1.69	0.01	0.66	0.00	0.60	8.91	93.62	6.22	0.09	5.48	0.19	0.00	0.13	0.00	0.16	1.53	3.70	1.78	1.68	4.11	8.00
	73	46.44	0.81	34.70	0.00	1.51	0.00	0.60	0.00	0.72	9.57	94.35	6.21	0.08	5.47	0.17	0.00	0.12	0.00	0.19	1.63	3.69	1.79	1.82	4.06	8.00
	74	45.90	0.78	34.61	0.00	1.48	0.01	0.55	0.01	0.71	10.43	94.48	6.17	0.08	5.49	0.17	0.00	0.11	0.00	0.19	1.79	3.66	1.83	1.98	4.02	8.00
	76	45.41	0.74	34.38	0.03	1.76	0.02	0.67	0.00	0.61	9.99	93.60	6.16	0.08	5.50	0.20	0.00	0.13	0.00	0.16	1.73	3.66	1.84	1.89	4.07	8.00
	77	46.02	0.78	34.56	0.00	1.77	0.03	0.68	0.00	0.64	10.03	94.49	6.18	0.08	5.47	0.20	0.00	0.14	0.00	0.17	1.72	3.65	1.82	1.88	4.06	8.00
	80	46.45	0.76	34.42	0.02	1.56	0.05	0.57	0.03	0.73	10.25	94.84	6.22	0.08	5.43	0.17	0.01	0.11	0.00	0.19	1.75	3.65	1.78	1.94	4.02	8.00
	81	46.21	0.73	35.52	0.01	1.44	0.03	0.59	0.01	0.77	9.77	95.08	6.15	0.07	5.57	0.16	0.00	0.12	0.00	0.20	1.66	3.71	1.85	1.86	4.07	8.00
	82	45.76	0.73	34.05	0.00	1.75	0.01	0.68	0.00	0.60	10.14	93.72	6.20	0.07	5.44	0.20	0.00	0.14	0.00	0.16	1.75	3.64	1.80	1.91	4.05	8.00
Muscvoite2	83	45.51	0.81	35.93	0.00	1.59	0.03	0.57	0.00	0.72	9.39	94.54	6.08	0.08	5.66	0.18	0.00	0.11	0.00	0.19	1.60	3.74	1.92	1.79	4.11	8.00
Line2	88	45.77	0.82	34.20	0.02	1.42	0.00	0.57	0.00	0.72	9.93	93.45	6.20	0.08	5.46	0.16	0.00	0.11	0.00	0.19	1.72	3.67	1.80	1.91	4.03	8.00
	90	45.85	0.95	34.41	0.03	1.51	0.02	0.60	0.00	0.72	10.10	94.19	6.18	0.10	5.46	0.17	0.00	0.12	0.00	0.19	1.74	3.64	1.82	1.92	4.03	8.00
	92	46.05	0.95	34.37	0.03	1.53	0.01	0.63	0.00	0.75	10.07	94.40	6.19	0.10	5.44	0.17	0.00	0.13	0.00	0.20	1.73	3.63	1.81	1.92	4.03	8.00
	93	46.58	0.94	35.29	0.01	1.69	0.02	0.71	0.00	0.75	9.73	95.70	6.16	0.09	5.50	0.19	0.00	0.14	0.00	0.19	1.64	3.66	1.84	1.83	4.08	8.00

doi:10.6342/NTU202202659

8.5.3 18LYB03 Biotite Gneiss

Mineral	No.	SiO_2	TiO_2	Al_2O_3	Cr_2O_3	FeO	Fe_2O_3	MnO	MgO	CaO	Na_2O	K_2O	Total	Si^{4+}	Ti^{4+}	Al^{3+}	Fe^{3+}	Mn^{2+}	Mg^{2+}	Ca^{2+}	Na^{+}	K^{+}	$T_{(total)}$	$M_{(total)}$	Ab	Or	An
Plagioclase in boudin	8	53.10	0.02	29.24	0.00	0.19	0.21	0.03	0.00	12.46	4.20	0.12	99.35	2.42	0.00	1.57	0.01	0.00	0.00	0.61	0.37	0.01	3.99	0.99	37.62	0.71	61.67
	9	53.74	0.00	29.17	0.00	0.16	0.18	0.05	0.00	12.09	4.58	0.16	99.95	2.43	0.00	1.56	0.01	0.00	0.00	0.59	0.40	0.01	3.99	1.00	40.29	0.93	58.78
	10	53.17	0.02	30.05	0.01	0.22	0.24	0.08	0.00	12.70	4.19	0.13	100.57	2.40	0.00	1.60	0.01	0.00	0.00	0.61	0.37	0.01	3.99	0.99	37.10	0.76	62.14
	11	48.27	0.04	32.53	0.01	0.15	0.17	0.02	0.00	16.14	2.08	0.04	99.28	2.22	0.00	1.77	0.01	0.00	0.00	0.80	0.19	0.00	3.99	0.98	18.87	0.24	80.90
	12	46.98	0.00	33.64	0.00	0.20	0.22	0.01	0.01	17.20	1.47	0.02	99.54	2.17	0.00	1.83	0.01	0.00	0.00	0.85	0.13	0.00	3.99	0.98	13.38	0.12	86.50
	13	47.26	0.00	33.05	0.00	0.19	0.21	0.03	0.02	16.92	1.79	0.01	99.25	2.18	0.00	1.80	0.01	0.00	0.00	0.84	0.16	0.00	3.98	1.00	16.06	0.06	83.88
	15	52.66	0.08	29.71	0.00	0.42	0.47	0.05	0.00	12.61	4.29	0.12	99.95	2.39	0.00	1.59	0.02	0.00	0.00	0.61	0.38	0.01	3.98	1.00	37.84	0.70	61.46
	16	55.73	0.04	27.82	0.00	0.20	0.22	0.00	0.00	10.45	5.53	0.13	99.89	2.51	0.00	1.48	0.01	0.00	0.00	0.50	0.48	0.01	3.99	0.99	48.55	0.75	50.70
	17	55.07	0.00	28.46	0.00	0.20	0.22	0.02	0.01	10.96	5.18	0.14	100.02	2.48	0.00	1.51	0.01	0.00	0.00	0.53	0.45	0.01	3.99	0.99	45.72	0.81	53.46
	30	47.27	0.00	33.21	0.00	0.24	0.27	0.05	0.00	17.23	1.80	0.06	99.86	2.18	0.00	1.80	0.01	0.00	0.00	0.85	0.16	0.00	3.98	1.01	15.84	0.35	83.81
	31	46.40	0.02	33.88	0.00	0.20	0.22	0.01	0.00	17.40	1.54	0.03	99.47	2.14	0.00	1.84	0.01	0.00	0.00	0.86	0.14	0.00	3.99	1.00	13.78	0.18	86.04
	33	47.90	0.00	32.93	0.00	0.24	0.27	0.03	0.00	16.70	1.94	0.06	99.79	2.20	0.00	1.78	0.01	0.00	0.00	0.82	0.17	0.00	3.98	1.00	17.31	0.35	82.34
	35	47.27	0.00	33.65	0.00	0.17	0.19	0.02	0.00	17.29	1.62	0.04	100.05	2.17	0.00	1.82	0.01	0.00	0.00	0.85	0.14	0.00	3.99	1.00	14.46	0.23	85.30
	65	52.50	0.01	30.27	0.00	0.24	0.27	0.04	0.00	13.08	3.96	0.15	100.24	2.38	0.00	1.61	0.01	0.00	0.00	0.63	0.35	0.01	3.99	0.99	35.09	0.87	64.04
	66	49.28	0.01	32.35	0.00	0.30	0.33	0.08	0.00	15.55	2.55	0.07	100.18	2.25	0.00	1.74	0.01	0.00	0.00	0.76	0.23	0.00	3.99	0.99	22.79	0.41	76.80
	67	51.75	0.00	30.29	0.02	0.24	0.27	0.04	0.00	13.41	3.76	0.09	99.60	2.36	0.00	1.63	0.01	0.00	0.00	0.65	0.33	0.01	3.99	0.99	33.48	0.53	65.99
	69	54.43	0.02	28.58	0.00	0.18	0.20	0.02	0.00	11.19	4.85	0.13	99.40	2.47	0.00	1.53	0.01	0.00	0.00	0.54	0.43	0.01	4.00	0.98	43.62	0.77	55.61
	70	54.90	0.00	28.55	0.00	0.25	0.28	0.04	0.02	11.07	4.87	0.19	99.88	2.48	0.00	1.52	0.01	0.00	0.00	0.53	0.43	0.01	3.99	0.97	43.83	1.12	55.05
	72	53.37	0.00	29.25	0.00	0.28	0.31	0.09	0.00	12.31	4.36	0.13	99.78	2.42	0.00	1.56	0.01	0.00	0.00	0.60	0.38	0.01	3.98	0.99	38.76	0.76	60.48
	73	47.31	0.00	33.65	0.00	0.30	0.33	0.07	0.00	17.16	1.69	0.05	100.22	2.17	0.00	1.82	0.01	0.00	0.00	0.84	0.15	0.00	3.98	1.00	15.08	0.29	84.62
	74	51.56	0.00	30.62	0.02	0.23	0.26	0.00	0.00	13.56	3.72	0.11	99.82	2.35	0.00	1.64	0.01	0.00	0.00	0.66	0.33	0.01	3.99	1.00	32.96	0.64	66.40
Plagioclase in boudin Pl1	163	47.21	0.01	33.31	0.00	0.35	0.39	0.06	0.03	16.95	1.76	0.04	99.70	2.17	0.00	1.81	0.01	0.00	0.00	0.84	0.16	0.00	3.98	1.00	15.78	0.24	83.98
	164	47.26	0.00	33.82	0.00	0.25	0.28	0.03	0.00	17.30	1.69	0.02	100.36	2.16	0.00	1.82	0.01	0.00	0.00	0.85	0.15	0.00	3.99	1.00	15.00	0.12	84.88
	165	48.27	0.03	33.28	0.00	0.16	0.18	0.05	0.00	16.46	1.94	0.03	100.22	2.20	0.00	1.79	0.01	0.00	0.00	0.81	0.17	0.00	4.00	0.98	17.55	0.18	82.27
	166	47.73	0.00	33.34	0.00	0.21	0.23	0.02	0.00	16.64	1.99	0.02	99.94	2.19	0.00	1.80	0.01	0.00	0.00	0.82	0.18	0.00	3.99	1.00	17.77	0.12	82.11
	167	47.43	0.01	33.42	0.01	0.14	0.16	0.03	0.00	16.74	1.98	0.05	99.80	2.18	0.00	1.81	0.01	0.00	0.00	0.82	0.18	0.00	3.99	1.00	17.58	0.29	82.13
	168	47.16	0.00	33.58	0.00	0.18	0.20	0.00	0.00	17.22	1.69	0.04	99.86	2.17	0.00	1.82	0.01	0.00	0.00	0.85	0.15	0.00	3.99	1.00	15.05	0.23	84.72
	169	47.61	0.03	33.59	0.01	0.15	0.17	0.01	0.00	16.94	1.79	0.02	100.15	2.18	0.00	1.81	0.01	0.00	0.00	0.83	0.16	0.00	3.99	0.99	16.03	0.12	83.85
	171	46.98	0.00	33.71	0.01	0.16	0.18	0.01	0.00	17.20	1.73	0.05	99.84	2.16	0.00	1.83	0.01	0.00	0.00	0.85	0.15	0.00	3.99	1.00	15.35	0.29	84.35
	172	48.03	0.01	32.71	0.00	0.24	0.27	0.00	0.03	15.98	2.23	0.04	99.27	2.21	0.00	1.78	0.01	0.00	0.00	0.79	0.20	0.00	3.99	0.99	20.11	0.24	79.65
	173	47.71	0.00	33.45	0.01	0.16	0.18	0.01	0.00	16.80	1.83	0.03	99.99	2.19	0.00	1.81	0.01	0.00	0.00	0.82	0.16	0.00	3.99	0.99	16.44	0.18	83.39
	174	48.05	0.00	33.10	0.00	0.18	0.20	0.03	0.00	16.50	2.00	0.07	99.92	2.20	0.00	1.79	0.01	0.00	0.00	0.81	0.18	0.00	3.99	0.99	17.91	0.41	81.67
	175	45.77	0.00	34.15	0.00	0.23	0.26	0.03	0.01	17.89	1.33	0.02	99.43	2.12	0.00	1.86	0.01	0.00	0.00	0.89	0.12	0.00	3.98	1.01	11.84	0.12	88.04
	176	47.12	0.00	33.54	0.01	0.19	0.21	0.04	0.00	16.94	1.78	0.05	99.66	2.17	0.00	1.82	0.01	0.00	0.00	0.84	0.16	0.00	3.99	1.00	15.93	0.29	83.78
	177	47.33	0.02	32.99	0.00	0.17	0.19	0.01	0.02	16.60	1.90	0.02	99.06	2.19	0.00	1.80	0.01	0.00	0.00	0.82	0.17	0.00	3.99	0.99	17.14	0.12	82.74
	179	47.23	0.00	33.79	0.01	0.22	0.24	0.02	0.00	16.98	1.69	0.03	99.95	2.17	0.00	1.83	0.01	0.00	0.00	0.83	0.15	0.00	3.99	0.99	15.23	0.18	84.59
	184	48.98	0.01	32.32	0.01	0.33	0.37	0.08	0.00	15.62	2.46	0.09	99.90	2.24	0.00	1.74	0.01	0.00	0.00	0.77	0.22	0.01	3.99	0.99	22.06	0.53	77.41

doi:10.6342/NTU202202659

Mineral	No.	SiO_2	TiO_2	Al_2O_3	Cr_2O_3	FeO	Fe_2O_3	MnO	MgO	CaO	Na_2O	K_2O	Total	Si^{4+}	Ti^{4+}	Al^{3+}	Fe^{3+}	Mn^{2+}	Mg^{2+}	Ca^{2+}	Na^{+}	K^{+}	$T_{(total)}$	$M_{(total)}$	Ab	Or	An
Plagioclase	186	46.58	0.00	33.43	0.00	0.29	0.32	0.05	0.00	17.37	1.56	0.05	99.34	2.16	0.00	1.82	0.01	0.00	0.00	0.86	0.14	0.00	3.98	1.00	13.94	0.29	85.77
in boudin	187	48.01	0.00	33.11	0.00	0.28	0.31	0.03	0.00	16.11	2.06	0.04	99.63	2.20	0.00	1.79	0.01	0.00	0.00	0.79	0.18	0.00	4.00	0.98	18.75	0.24	81.01
Pl2	188	47.25	0.01	33.54	0.00	0.23	0.26	0.05	0.00	17.11	1.64	0.04	99.88	2.17	0.00	1.82	0.01	0.00	0.00	0.84	0.15	0.00	3.99	0.99	14.75	0.24	85.02
	189	46.70	0.00	33.55	0.00	0.23	0.26	0.05	0.00	17.09	1.71	0.01	99.33	2.16	0.00	1.83	0.01	0.00	0.00	0.85	0.15	0.00	3.99	1.00	15.32	0.06	84.62
	190	46.89	0.00	33.54	0.00	0.15	0.17	0.03	0.01	17.60	1.45	0.03	99.70	2.16	0.00	1.82	0.01	0.00	0.00	0.87	0.13	0.00	3.98	1.00	12.95	0.18	86.87
	191	47.09	0.00	33.80	0.00	0.17	0.19	0.00	0.00	17.30	1.59	0.05	99.99	2.16	0.00	1.83	0.01	0.00	0.00	0.85	0.14	0.00	3.99	1.00	14.22	0.29	85.49
	192	47.05	0.02	33.71	0.00	0.10	0.11	0.02	0.00	17.41	1.51	0.03	99.84	2.16	0.00	1.83	0.00	0.00	0.00	0.86	0.13	0.00	3.99	0.99	13.54	0.18	86.28
	193	46.80	0.00	33.56	0.00	0.16	0.18	0.03	0.00	17.22	1.60	0.04	99.40	2.16	0.00	1.83	0.01	0.00	0.00	0.85	0.14	0.00	3.99	1.00	14.36	0.24	85.40
	194	48.30	0.03	32.28	0.00	0.16	0.18	0.00	0.00	15.82	2.45	0.05	99.09	2.23	0.00	1.76	0.01	0.00	0.00	0.78	0.22	0.00	3.99	1.00	21.83	0.29	77.88
	195	48.20	0.01	33.29	0.00	0.15	0.17	0.00	0.00	16.55	2.06	0.08	100.35	2.20	0.00	1.79	0.01	0.00	0.00	0.81	0.18	0.00	3.99	1.00	18.30	0.47	81.23
	196	47.17	0.00	33.39	0.00	0.38	0.42	0.02	0.01	15.55	1.48	1.05	99.04	2.19	0.00	1.82	0.01	0.00	0.00	0.77	0.13	0.06	4.01	0.97	13.75	6.42	79.83
Plagioclase	205	46.78	0.00	33.51	0.00	0.19	0.21	0.02	0.00	17.20	1.54	0.02	99.25	2.16	0.00	1.83	0.01	0.00	0.00	0.85	0.14	0.00	3.99	0.99	13.93	0.12	85.95
in boudin	206	46.71	0.00	33.53	0.04	0.17	0.19	0.04	0.00	17.11	1.61	0.04	99.24	2.16	0.00	1.83	0.01	0.00	0.00	0.85	0.14	0.00	3.99	0.99	14.52	0.24	85.25
Pl3	209	46.90	0.01	34.00	0.00	0.17	0.19	0.03	0.00	17.59	1.50	0.02	100.22	2.15	0.00	1.84	0.01	0.00	0.00	0.86	0.13	0.00	3.99	1.00	13.35	0.12	86.53
	211	47.99	0.00	33.27	0.00	0.12	0.13	0.03	0.00	16.64	1.96	0.05	100.05	2.20	0.00	1.80	0.00	0.00	0.00	0.82	0.17	0.00	3.99	0.99	17.52	0.29	82.19
	212	48.65	0.01	32.26	0.01	0.12	0.13	0.02	0.00	16.04	2.40	0.08	99.59	2.24	0.00	1.75	0.00	0.00	0.00	0.79	0.21	0.00	3.98	1.01	21.21	0.47	78.33
	213	47.55	0.00	33.33	0.00	0.22	0.24	0.02	0.00	16.72	1.86	0.04	99.74	2.19	0.00	1.81	0.01	0.00	0.00	0.82	0.17	0.00	3.99	0.99	16.72	0.24	83.05
	215	47.96	0.01	33.27	0.03	0.14	0.16	0.04	0.01	16.50	1.92	0.06	99.95	2.20	0.00	1.80	0.01	0.00	0.00	0.81	0.17	0.00	3.99	0.98	17.33	0.36	82.31
	216	47.82	0.00	33.08	0.00	0.14	0.16	0.01	0.00	16.76	1.77	0.07	99.64	2.20	0.00	1.79	0.01	0.00	0.00	0.83	0.16	0.00	3.99	0.99	15.98	0.42	83.61
	217	47.87	0.00	33.12	0.02	0.18	0.20	0.01	0.00	16.61	1.98	0.02	99.82	2.20	0.00	1.79	0.01	0.00	0.00	0.82	0.18	0.00	3.99	0.99	17.72	0.12	82.16
	218	46.61	0.00	33.31	0.00	0.20	0.22	0.04	0.00	17.52	1.47	0.01	99.16	2.16	0.00	1.82	0.01	0.00	0.00	0.87	0.13	0.00	3.98	1.00	13.17	0.06	86.77
	219	47.17	0.02	33.74	0.00	0.19	0.21	0.03	0.00	17.37	1.56	0.05	100.13	2.16	0.00	1.82	0.01	0.00	0.00	0.85	0.14	0.00	3.99	1.00	13.94	0.29	85.77
Plagioclase	220	47.52	0.01	33.32	0.01	0.19	0.21	0.03	0.00	16.61	1.93	0.03	99.64	2.19	0.00	1.81	0.01	0.00	0.00	0.82	0.17	0.00	3.99	0.99	17.34	0.18	82.48
in boudin	221	47.65	0.00	33.06	0.00	0.15	0.17	0.03	0.00	16.21	2.21	0.05	99.35	2.20	0.00	1.80	0.01	0.00	0.00	0.80	0.20	0.00	3.99	1.00	19.73	0.29	79.98
Pl4	222	49.75	0.02	31.04	0.01	0.16	0.18	0.03	0.00	15.17	2.80	0.06	99.02	2.29	0.00	1.69	0.01	0.00	0.00	0.75	0.25	0.00	3.98	1.00	24.95	0.35	74.70
	224	48.89	0.02	32.58	0.00	0.21	0.23	0.03	0.01	16.01	2.39	0.08	100.21	2.23	0.00	1.75	0.01	0.00	0.00	0.78	0.21	0.00	3.99	1.00	21.17	0.47	78.36
	225	51.97	0.00	30.10	0.00	0.19	0.21	0.03	0.01	13.26	3.94	0.10	99.61	2.37	0.00	1.62	0.01	0.00	0.00	0.65	0.35	0.01	3.99	1.00	34.76	0.58	64.65
	226	51.59	0.00	30.25	0.00	0.18	0.20	0.01	0.00	13.45	3.74	0.05	99.26	2.36	0.00	1.63	0.01	0.00	0.00	0.66	0.33	0.00	3.99	0.99	33.38	0.29	66.33
	227	52.10	0.00	30.76	0.01	0.20	0.22	0.02	0.00	13.49	3.66	0.05	100.29	2.36	0.00	1.64	0.01	0.00	0.00	0.65	0.32	0.00	4.00	0.98	32.83	0.30	66.87
	228	51.00	0.01	31.38	0.00	0.16	0.18	0.04	0.01	14.28	3.24	0.04	100.16	2.32	0.00	1.68	0.01	0.00	0.00	0.69	0.29	0.00	3.99	0.98	29.04	0.24	70.73
	229	48.40	0.01	32.80	0.00	0.27	0.30	0.03	0.00	16.29	2.14	0.03	99.97	2.22	0.00	1.77	0.01	0.00	0.00	0.80	0.19	0.00	3.99	0.99	19.17	0.18	80.65

doi:10.6342/NTU202202659

Mineral	No.	SiO_2	TiO_2	Al_2O_3	Cr_2O_3	FeO	Fe_2O_3	MnO	MgO	CaO	Na_2O	K_2O	Total	Si^{4+}	Ti^{4+}	Al^{3+}	Fe^{3+}	Mn^{2+}	Mg^{2+}	Ca^{2+}	Na^{+}	K^{+}	$T_{(total)}$	$M_{(total)}$	Ab	Or	An
Plagioclase	230	55.09	0.00	28.45	0.00	0.25	0.28	0.04	0.00	10.99	4.99	0.17	99.97	2.48	0.00	1.51	0.01	0.00	0.00	0.53	0.44	0.01	3.99	0.98	44.65	1.00	54.35
in boudin	231	55.67	0.01	28.11	0.00	0.29	0.32	0.02	0.00	10.76	5.22	0.23	100.30	2.50	0.00	1.49	0.01	0.00	0.00	0.52	0.45	0.01	3.99	0.99	46.12	1.34	52.54
Pl5	232	55.35	0.01	28.25	0.02	0.33	0.37	0.02	0.00	10.75	5.19	0.20	100.11	2.49	0.00	1.50	0.01	0.00	0.00	0.52	0.45	0.01	3.99	0.98	46.08	1.17	52.75
	233	54.74	0.00	28.23	0.00	0.19	0.21	0.04	0.00	11.10	5.04	0.20	99.55	2.48	0.00	1.51	0.01	0.00	0.00	0.54	0.44	0.01	3.99	0.99	44.58	1.16	54.26
	234	55.19	0.00	28.10	0.00	0.22	0.24	0.00	0.01	11.07	5.11	0.22	99.94	2.49	0.00	1.49	0.01	0.00	0.00	0.54	0.45	0.01	3.98	0.99	44.93	1.27	53.79
	235	54.72	0.00	27.99	0.00	0.16	0.18	0.00	0.00	10.96	5.26	0.19	99.28	2.49	0.00	1.50	0.01	0.00	0.00	0.53	0.46	0.01	3.98	1.01	45.97	1.09	52.93
	236	55.00	0.01	27.81	0.00	0.19	0.21	0.03	0.00	10.60	5.18	0.20	99.03	2.50	0.00	1.49	0.01	0.00	0.00	0.52	0.46	0.01	3.99	0.98	46.38	1.18	52.44
	237	55.20	0.01	27.86	0.00	0.24	0.27	0.03	0.00	10.83	5.13	0.15	99.44	2.50	0.00	1.49	0.01	0.00	0.00	0.53	0.45	0.01	3.99	0.98	45.75	0.88	53.37
	238	48.51	0.00	32.00	0.00	0.14	0.16	0.01	0.00	15.97	2.41	0.06	99.09	2.24	0.00	1.74	0.01	0.00	0.00	0.79	0.22	0.00	3.98	1.01	21.38	0.35	78.27
	239	50.46	0.00	31.13	0.00	0.22	0.24	0.00	0.00	14.25	3.24	0.07	99.36	2.31	0.00	1.68	0.01	0.00	0.00	0.70	0.29	0.00	3.99	0.99	29.03	0.41	70.56
	240	48.30	0.02	32.32	0.00	0.20	0.22	0.00	0.00	16.10	2.27	0.05	99.26	2.23	0.00	1.76	0.01	0.00	0.00	0.80	0.20	0.00	3.98	1.00	20.27	0.29	79.44
	242	49.93	0.00	31.54	0.02	0.17	0.19	0.03	0.00	14.92	2.96	0.04	99.61	2.29	0.00	1.70	0.01	0.00	0.00	0.73	0.26	0.00	3.99	1.00	26.36	0.23	73.41
	243	49.86	0.01	31.50	0.00	0.24	0.27	0.01	0.00	14.81	2.91	0.07	99.43	2.29	0.00	1.70	0.01	0.00	0.00	0.73	0.26	0.00	3.99	0.99	26.12	0.41	73.46
	244	51.62	0.00	30.68	0.03	0.25	0.28	0.00	0.00	13.80	3.56	0.09	100.03	2.34	0.00	1.64	0.01	0.00	0.00	0.67	0.31	0.01	3.99	0.99	31.66	0.53	67.82
	245	47.44	0.00	32.93	0.00	0.33	0.37	0.03	0.00	16.98	1.81	0.04	99.55	2.19	0.00	1.79	0.01	0.00	0.00	0.84	0.16	0.00	3.98	1.00	16.13	0.23	83.63
	246	50.10	0.00	31.20	0.01	0.25	0.28	0.07	0.01	14.82	2.92	0.06	99.43	2.30	0.00	1.69	0.01	0.00	0.00	0.73	0.26	0.00	3.98	0.99	26.19	0.35	73.46
	247	49.39	0.01	32.19	0.00	0.21	0.23	0.02	0.02	15.46	2.67	0.09	100.05	2.26	0.00	1.73	0.01	0.00	0.00	0.76	0.24	0.01	3.99	1.00	23.69	0.53	75.79
	248	49.36	0.00	32.29	0.00	0.30	0.33	0.05	0.00	15.29	2.58	0.06	99.92	2.25	0.00	1.74	0.01	0.00	0.00	0.75	0.23	0.00	3.99	0.98	23.31	0.36	76.33
	249	51.77	0.00	30.32	0.00	0.25	0.28	0.04	0.00	13.34	3.87	0.07	99.66	2.36	0.00	1.63	0.01	0.00	0.00	0.65	0.34	0.00	3.99	1.00	34.28	0.41	65.31
	251	49.19	0.01	32.13	0.01	0.28	0.31	0.02	0.00	15.40	2.56	0.05	99.64	2.25	0.00	1.74	0.01	0.00	0.00	0.76	0.23	0.00	3.99	0.99	23.06	0.30	76.65
	252	48.61	0.01	32.44	0.00	0.35	0.39	0.03	0.00	15.89	2.37	0.05	99.74	2.23	0.00	1.75	0.01	0.00	0.00	0.78	0.21	0.00	3.98	0.99	21.19	0.29	78.51
	253	48.68	0.00	32.37	0.00	0.24	0.27	0.03	0.00	15.61	2.39	0.08	99.40	2.24	0.00	1.75	0.01	0.00	0.00	0.77	0.21	0.00	3.99	0.99	21.59	0.48	77.93
	254	51.28	0.00	31.10	0.00	0.21	0.23	0.01	0.00	14.09	3.31	0.06	100.06	2.33	0.00	1.66	0.01	0.00	0.00	0.69	0.29	0.00	3.99	0.98	29.72	0.35	69.92
	255	47.72	0.01	33.16	0.00	0.24	0.27	0.04	0.00	16.79	1.93	0.01	99.89	2.19	0.00	1.79	0.01	0.00	0.00	0.83	0.17	0.00	3.98	1.00	17.21	0.06	82.73
	256	48.90	0.00	32.40	0.00	0.20	0.22	0.02	0.00	15.68	2.64	0.05	99.89	2.24	0.00	1.75	0.01	0.00	0.00	0.77	0.23	0.00	3.99	1.01	23.29	0.29	76.42
	257	49.11	0.02	31.86	0.00	0.19	0.21	0.02	0.00	15.40	2.54	0.04	99.18	2.26	0.00	1.73	0.01	0.00	0.00	0.76	0.23	0.00	3.99	0.99	22.93	0.24	76.83
	258	46.90	0.00	33.42	0.00	0.30	0.33	0.07	0.00	17.12	1.57	0.04	99.41	2.17	0.00	1.82	0.01	0.00	0.00	0.85	0.14	0.00	3.99	0.99	14.20	0.24	85.56
Plagioclase	259	47.69	0.00	33.04	0.00	0.15	0.17	0.03	0.00	16.64	2.03	0.05	99.63	2.19	0.00	1.79	0.01	0.00	0.00	0.82	0.18	0.00	3.99	1.00	18.03	0.29	81.68
in boudin	262	47.42	0.00	33.16	0.00	0.18	0.20	0.01	0.00	16.87	1.75	0.03	99.41	2.19	0.00	1.80	0.01	0.00	0.00	0.83	0.16	0.00	3.99	0.99	15.78	0.18	84.05
Pl6	263	46.66	0.00	33.28	0.00	0.20	0.22	0.07	0.01	17.28	1.55	0.03	99.07	2.16	0.00	1.82	0.01	0.00	0.00	0.86	0.14	0.00	3.98	1.00	13.94	0.18	85.88
	264	48.14	0.00	32.64	0.00	0.17	0.19	0.02	0.00	16.10	2.08	0.03	99.17	2.22	0.00	1.77	0.01	0.00	0.00	0.80	0.19	0.00	3.99	0.98	18.91	0.18	80.91
	265	49.72	0.00	31.83	0.00	0.16	0.18	0.02	0.01	15.05	3.08	0.02	99.88	2.27	0.00	1.71	0.01	0.00	0.00	0.74	0.27	0.00	3.99	1.01	26.99	0.12	72.89
	266	48.55	0.00	32.62	0.00	0.10	0.11	0.00	0.00	15.82	2.40	0.04	99.54	2.23	0.00	1.77	0.00	0.00	0.00	0.78	0.21	0.00	4.00	0.99	21.49	0.24	78.28
	267	48.98	0.00	32.31	0.01	0.19	0.21	0.01	0.00	15.35	2.54	0.08	99.46	2.25	0.00	1.75	0.01	0.00	0.00	0.75	0.23	0.00	4.00	0.99	22.93	0.48	76.59
	268	46.34	0.00	34.03	0.00	0.17	0.19	0.00	0.00	17.59	1.16	0.02	99.31	2.14	0.00	1.85	0.01	0.00	0.00	0.87	0.10	0.00	4.00	0.98	10.65	0.12	89.23
	269	46.84	0.00	33.87	0.01	0.19	0.21	0.02	0.00	17.55	1.55	0.04	100.08	2.15	0.00	1.83	0.01	0.00	0.00	0.86	0.14	0.00	3.99	1.00	13.75	0.23	86.02
	270	47.09	0.01	33.68	0.00	0.27	0.30	0.00	0.00	17.34	1.56	0.03	99.97	2.16	0.00	1.82	0.01	0.00	0.00	0.85	0.14	0.00	3.99	0.99	13.98	0.18	85.85
	271	46.93	0.03	33.55	0.00	0.27	0.30	0.01	0.01	17.36	1.61	0.04	99.81	2.16	0.00	1.82	0.01	0.00	0.00	0.86	0.14	0.00	3.98	1.00	14.34	0.23	85.43
	278	46.61	0.01	33.48	0.00	0.25	0.28	0.06	0.01	17.07	1.49	0.29	99.27	2.16	0.00	1.83	0.01	0.00	0.00	0.85	0.13	0.02	3.99	1.00	13.41	1.72	84.88
	279	46.27	0.00	33.85	0.00	0.19	0.21	0.02	0.00	17.39	1.43	0.10	99.24	2.14	0.00	1.85	0.01	0.00	0.00	0.86	0.13	0.01	3.99	1.00	12.88	0.59	86.53

doi:10.6342/NTU202202659

Mineral	No.	SiO_2	TiO_2	Al_2O_3	Cr_2O_3	FeO	Fe_2O_3	MnO	MgO	CaO	Na_2O	K_2O	Total	Si^{4+}	Ti^{4+}	Al^{3+}	Fe^{3+}	Mn^{2+}	Mg^{2+}	Ca^{2+}	Na^{+}	K^{+}	$T_{(total)}$	$M_{(total)}$	Ab	Or	An
Plagioclase	294	47.85	0.00	33.16	0.00	0.18	0.20	0.04	0.00	16.63	1.82	0.04	99.71	2.20	0.00	1.80	0.01	0.00	0.00	0.82	0.16	0.00	3.99	0.98	16.47	0.21	83.32
in host	295	48.73	0.00	32.60	0.01	0.15	0.17	0.01	0.01	15.93	2.37	0.01	99.81	2.23	0.00	1.76	0.01	0.00	0.00	0.78	0.21	0.00	3.99	0.99	21.16	0.06	78.78
	296	51.98	0.00	30.10	0.00	0.15	0.16	0.01	0.00	13.17	3.94	0.11	99.46	2.37	0.00	1.62	0.01	0.00	0.00	0.64	0.35	0.01	3.99	1.00	34.92	0.62	64.46
	297	47.78	0.00	33.00	0.00	0.14	0.16	0.00	0.00	16.66	1.96	0.01	99.55	2.20	0.00	1.79	0.01	0.00	0.00	0.82	0.17	0.00	3.99	1.00	17.51	0.04	82.45
	301	46.69	0.05	33.54	0.00	0.53	0.59	0.00	0.00	17.21	1.67	0.08	99.78	2.15	0.00	1.82	0.02	0.00	0.00	0.85	0.15	0.00	3.97	1.00	14.90	0.46	84.64
	302	46.73	0.02	33.51	0.01	0.45	0.50	0.03	0.00	16.95	1.79	0.08	99.55	2.16	0.00	1.82	0.02	0.00	0.00	0.84	0.16	0.00	3.98	1.00	15.97	0.44	83.59
	303	46.85	0.02	33.16	0.00	0.36	0.39	0.00	0.00	16.90	1.81	0.04	99.15	2.17	0.00	1.81	0.01	0.00	0.00	0.84	0.16	0.00	3.98	1.00	16.22	0.25	83.54
	306	47.26	0.01	33.05	0.00	0.13	0.14	0.03	0.00	16.45	2.03	0.05	99.00	2.19	0.00	1.80	0.01	0.00	0.00	0.82	0.18	0.00	3.99	1.00	18.17	0.28	81.55
	308	47.63	0.01	33.40	0.00	0.07	0.08	0.01	0.01	16.56	1.81	0.03	99.53	2.19	0.00	1.81	0.00	0.00	0.00	0.82	0.16	0.00	4.00	0.98	16.47	0.20	83.34
	310	47.19	0.01	33.09	0.00	0.16	0.18	0.00	0.00	16.67	1.92	0.03	99.07	2.18	0.00	1.81	0.01	0.00	0.00	0.83	0.17	0.00	3.99	1.00	17.20	0.20	82.60
	311	48.61	0.02	32.26	0.03	0.23	0.25	0.01	0.00	15.37	2.56	0.07	99.17	2.24	0.00	1.75	0.01	0.00	0.00	0.76	0.23	0.00	3.99	0.99	23.08	0.43	76.49
	313	47.14	0.03	33.25	0.00	0.14	0.15	0.00	0.00	16.89	1.71	0.04	99.20	2.18	0.00	1.81	0.01	0.00	0.00	0.84	0.15	0.00	3.99	0.99	15.42	0.23	84.35
	321	47.46	0.02	33.50	0.00	0.55	0.61	0.03	0.00	16.63	1.76	0.10	100.05	2.18	0.00	1.81	0.02	0.00	0.00	0.82	0.16	0.01	3.99	0.98	15.97	0.60	83.43
	322	47.69	0.00	33.04	0.00	0.24	0.27	0.00	0.00	16.63	1.94	0.08	99.61	2.19	0.00	1.79	0.01	0.00	0.00	0.82	0.17	0.00	3.99	1.00	17.32	0.44	82.24
	323	47.30	0.04	33.28	0.00	0.28	0.31	0.03	0.00	16.67	1.84	0.05	99.48	2.18	0.00	1.81	0.01	0.00	0.00	0.82	0.16	0.00	3.99	0.99	16.57	0.32	83.11
	324	52.14	0.00	30.25	0.01	0.25	0.27	0.01	0.00	12.97	3.99	0.09	99.70	2.37	0.00	1.62	0.01	0.00	0.00	0.63	0.35	0.00	3.99	0.99	35.58	0.50	63.91
	331	52.09	0.00	29.82	0.03	0.19	0.21	0.00	0.00	13.22	3.93	0.11	99.39	2.38	0.00	1.60	0.01	0.00	0.00	0.65	0.35	0.01	3.98	1.00	34.74	0.66	64.60
	336	48.93	0.01	32.32	0.00	0.19	0.21	0.01	0.00	15.75	2.40	0.06	99.67	2.24	0.00	1.75	0.01	0.00	0.00	0.77	0.21	0.00	3.99	0.99	21.56	0.34	78.10
	337	49.87	0.00	31.41	0.00	0.09	0.10	0.00	0.00	14.92	2.87	0.06	99.22	2.29	0.00	1.70	0.00	0.00	0.00	0.73	0.26	0.00	3.99	0.99	25.75	0.32	73.93
	348	46.92	0.00	33.22	0.04	0.17	0.19	0.01	0.00	17.14	1.71	0.05	99.25	2.17	0.00	1.81	0.01	0.00	0.00	0.85	0.15	0.00	3.98	1.01	15.27	0.30	84.43
	349	47.15	0.00	33.52	0.01	0.16	0.18	0.01	0.00	16.99	1.68	0.02	99.54	2.17	0.00	1.82	0.01	0.00	0.00	0.84	0.15	0.00	3.99	0.99	15.13	0.11	84.76
	350	48.21	0.00	33.38	0.01	0.11	0.12	0.01	0.00	16.50	1.84	0.03	100.08	2.20	0.00	1.80	0.00	0.00	0.00	0.81	0.16	0.00	4.00	0.97	16.72	0.20	83.08
	352	48.01	0.00	32.40	0.00	0.36	0.40	0.00	0.00	16.54	2.00	0.06	99.36	2.21	0.00	1.76	0.01	0.00	0.00	0.82	0.18	0.00	3.98	1.00	17.87	0.32	81.81
	354	51.37	0.00	31.17	0.01	0.20	0.22	0.00	0.00	14.03	3.47	0.09	100.35	2.33	0.00	1.66	0.01	0.00	0.00	0.68	0.31	0.01	3.99	0.99	30.77	0.52	68.71
	359	47.50	0.05	33.25	0.02	0.22	0.24	0.00	0.00	16.66	1.89	0.02	99.60	2.19	0.00	1.80	0.01	0.00	0.00	0.82	0.17	0.00	3.99	0.99	16.99	0.12	82.89
	360	52.65	0.02	30.12	0.00	0.12	0.13	0.02	0.00	12.86	3.91	0.12	99.83	2.39	0.00	1.61	0.00	0.00	0.00	0.62	0.34	0.01	4.00	0.98	35.25	0.73	64.02
Plagioclase	363	52.24	0.00	29.97	0.00	0.08	0.09	0.02	0.00	12.93	3.94	0.12	99.31	2.38	0.00	1.61	0.00	0.00	0.00	0.63	0.35	0.01	4.00	0.99	35.25	0.73	64.02
in host	365	52.15	0.00	30.25	0.01	0.12	0.13	0.00	0.00	12.89	3.99	0.11	99.51	2.37	0.00	1.62	0.00	0.00	0.00	0.63	0.35	0.01	4.00	0.99	35.67	0.63	63.70
Pl7	367	53.50	0.00	29.39	0.00	0.09	0.10	0.00	0.00	12.26	4.30	0.11	99.65	2.43	0.00	1.57	0.00	0.00	0.00	0.60	0.38	0.01	4.00	0.98	38.58	0.67	60.75
	369	49.31	0.01	32.14	0.00	0.11	0.12	0.02	0.01	15.20	2.77	0.05	99.60	2.26	0.00	1.74	0.00	0.00	0.00	0.75	0.25	0.00	3.99	0.99	24.72	0.28	75.01
	370	47.25	0.01	33.38	0.00	0.10	0.11	0.01	0.00	17.10	1.77	0.04	99.66	2.18	0.00	1.81	0.00	0.00	0.00	0.84	0.16	0.00	3.99	1.00	15.72	0.25	84.03
	371	47.68	0.00	33.23	0.00	0.10	0.11	0.00	0.00	16.71	1.88	0.06	99.66	2.19	0.00	1.80	0.00	0.00	0.00	0.82	0.17	0.00	3.99	0.99	16.85	0.32	82.83
	372	46.56	0.00	33.50	0.00	0.14	0.16	0.02	0.00	17.48	1.50	0.03	99.22	2.16	0.00	1.83	0.01	0.00	0.00	0.87	0.13	0.00	3.99	1.00	13.40	0.19	86.40
Plagioclase	373	54.18	0.00	28.71	0.00	0.05	0.06	0.02	0.00	11.59	4.69	0.08	99.32	2.46	0.00	1.54	0.00	0.00	0.00	0.56	0.41	0.00	4.00	0.98	42.10	0.44	57.46
in host	376	47.60	0.00	33.36	0.00	0.09	0.10	0.00	0.00	16.30	1.87	0.05	99.27	2.19	0.00	1.81	0.00	0.00	0.00	0.80	0.17	0.00	4.01	0.98	17.16	0.31	82.53
Pl8	378	49.16	0.00	32.25	0.01	0.10	0.11	0.00	0.00	15.54	2.48	0.05	99.58	2.25	0.00	1.74	0.00	0.00	0.00	0.76	0.22	0.00	3.99	0.99	22.36	0.28	77.36
	379	48.42	0.02	32.88	0.00	0.08	0.09	0.05	0.00	16.10	2.16	0.05	99.78	2.22	0.00	1.78	0.00	0.00	0.00	0.79	0.19	0.00	4.00	0.99	19.49	0.31	80.20
	380	48.45	0.00	32.67	0.00	0.06	0.07	0.02	0.00	16.13	2.25	0.04	99.61	2.22	0.00	1.77	0.00	0.00	0.00	0.79	0.20	0.00	3.99	1.00	20.07	0.26	79.67
	383	47.47	0.03	32.97	0.01	0.10	0.11	0.01	0.00	16.91	1.84	0.03	99.36	2.19	0.00	1.79	0.00	0.00	0.00	0.84	0.16	0.00	3.98	1.00	16.41	0.19	83.40
	384	49.23	0.00	31.90	0.00	0.08	0.08	0.00	0.00	15.35	2.72	0.05	99.33	2.26	0.00	1.73	0.00	0.00	0.00	0.76	0.24	0.00	3.99	1.00	24.20	0.32	75.48

doi:10.6342/NTU202202659

Mineral	No.	SiO_2	TiO_2	Al_2O_3	Cr_2O_3	FeO	MnO	MgO	CaO	Na_2O	K_2O	Total	Si^{4+}	Ti^{4+}	Al^{3+}	Fe^{2+}	Mn^{2+}	Mg^{2+}	Ca^{2+}	Na^{+}	K^{+}	$Al_{(M)}$	$Al_{(T)}$	$I_{(total)}$	$M_{(total)}$	$T_{(total)}$	X_{Mg}	Ti-in-Bt thermometer (°C)
Biotite	1	33.53	2.13	17.16	0.00	26.55	0.53	5.09	0.01	0.04	8.15	93.19	5.42	0.26	3.27	3.59	0.07	1.23	0.00	0.01	1.68	0.69	2.58	1.70	5.84	8.00	0.25	603
boudin	2	34.85	2.49	17.14	0.00	25.86	0.56	5.54	0.00	0.03	9.05	95.51	5.48	0.29	3.18	3.40	0.07	1.30	0.00	0.01	1.82	0.66	2.52	1.82	5.72	8.00	0.28	628
	4	33.67	2.18	17.17	0.06	26.56	0.47	5.99	0.04	0.03	8.07	94.25	5.37	0.26	3.23	3.55	0.06	1.43	0.01	0.01	1.64	0.61	2.63	1.66	5.90	8.00	0.29	607
	5	34.79	2.21	17.96	0.00	24.18	0.55	5.77	0.01	0.06	8.43	93.95	5.49	0.26	3.34	3.19	0.07	1.36	0.00	0.02	1.70	0.83	2.51	1.72	5.72	8.00	0.30	609
	7	34.34	1.91	17.74	0.00	27.09	0.58	5.26	0.03	0.04	8.61	95.59	5.42	0.23	3.30	3.57	0.08	1.24	0.00	0.01	1.73	0.72	2.58	1.75	5.83	8.00	0.26	575
	21	35.27	2.57	17.03	0.00	24.85	0.47	4.99	0.01	0.04	9.23	94.46	5.58	0.31	3.17	3.29	0.06	1.18	0.00	0.01	1.86	0.75	2.42	1.88	5.59	8.00	0.26	634
	27	34.93	2.54	17.61	0.00	24.48	0.54	5.66	0.04	0.08	9.42	95.30	5.48	0.30	3.25	3.21	0.07	1.32	0.01	0.03	1.88	0.73	2.52	1.92	5.63	8.00	0.29	632
	28	34.72	2.25	17.73	0.05	25.54	0.51	5.70	0.06	0.03	9.16	95.75	5.44	0.26	3.27	3.35	0.07	1.33	0.01	0.01	1.83	0.71	2.56	1.85	5.72	8.00	0.28	609
	29	34.88	2.89	17.53	0.00	24.59	0.51	5.58	0.03	0.06	9.51	95.57	5.46	0.34	3.23	3.22	0.07	1.30	0.01	0.02	1.90	0.69	2.54	1.92	5.62	8.00	0.29	653
Biotite	58	35.32	3.01	17.43	0.00	25.03	0.48	5.32	0.00	0.04	9.08	95.71	5.51	0.35	3.20	3.26	0.06	1.24	0.00	0.01	1.81	0.71	2.49	1.82	5.63	8.00	0.27	659
host	315	34.73	4.02	16.09	0.04	26.21	0.51	5.25	0.00	0.03	9.20	96.08	5.45	0.48	2.98	3.44	0.07	1.23	0.00	0.01	1.84	0.43	2.55	1.85	5.65	8.00	0.26	703
	316	34.88	4.13	16.20	0.00	25.69	0.53	4.85	0.03	0.05	9.56	95.92	5.48	0.49	3.00	3.38	0.07	1.14	0.00	0.02	1.92	0.48	2.52	1.94	5.56	8.00	0.25	706
	317	34.94	4.01	16.02	0.00	25.72	0.47	4.92	0.00	0.07	9.64	95.78	5.50	0.47	2.97	3.39	0.06	1.15	0.00	0.02	1.94	0.48	2.50	1.96	5.56	8.00	0.25	702
	318	34.25	3.76	16.46	0.00	25.02	0.52	5.15	0.05	0.07	9.46	94.74	5.44	0.45	3.08	3.32	0.07	1.22	0.01	0.02	1.92	0.52	2.56	1.95	5.59	8.00	0.27	695
	325	34.69	3.71	16.34	0.00	25.42	0.55	5.32	0.02	0.06	9.49	95.59	5.47	0.44	3.03	3.35	0.07	1.25	0.00	0.02	1.91	0.50	2.53	1.93	5.61	8.00	0.27	692
	326	33.99	3.86	16.17	0.03	24.96	0.46	5.03	1.15	0.07	9.19	94.92	5.41	0.46	3.03	3.32	0.06	1.19	0.20	0.02	1.86	0.44	2.59	2.08	5.47	8.00	0.26	699
	327	34.53	4.28	16.52	0.02	24.88	0.48	5.26	0.00	0.06	9.64	95.68	5.43	0.51	3.06	3.27	0.06	1.23	0.00	0.02	1.93	0.49	2.57	1.95	5.56	8.00	0.27	712
	328	34.54	4.31	16.50	0.01	25.13	0.46	5.11	0.01	0.06	9.44	95.57	5.43	0.51	3.06	3.31	0.06	1.20	0.00	0.02	1.89	0.49	2.57	1.92	5.57	8.00	0.27	713
	333	35.20	3.90	16.20	0.04	23.89	0.55	5.19	0.11	0.03	9.36	94.46	5.56	0.46	3.02	3.16	0.07	1.22	0.02	0.01	1.89	0.58	2.44	1.91	5.49	8.00	0.28	700
	334	35.08	4.02	16.25	0.02	24.37	0.52	5.34	0.02	0.05	9.49	95.17	5.52	0.48	3.01	3.21	0.07	1.25	0.00	0.02	1.90	0.53	2.48	1.92	5.53	8.00	0.28	704
	335	34.81	3.83	16.42	0.00	24.55	0.47	5.14	0.03	0.08	9.70	95.03	5.50	0.45	3.06	3.24	0.06	1.21	0.00	0.02	1.95	0.55	2.50	1.98	5.53	8.00	0.27	697
	338	35.04	3.04	16.71	0.01	25.06	0.42	5.52	0.01	0.02	9.63	95.46	5.51	0.36	3.10	3.30	0.06	1.29	0.00	0.00	1.93	0.61	2.49	1.94	5.61	8.00	0.28	662
	339	34.00	3.30	16.74	0.00	25.62	0.43	5.58	0.01	0.03	9.47	95.17	5.39	0.39	3.13	3.40	0.06	1.32	0.00	0.01	1.92	0.52	2.61	1.93	5.69	8.00	0.28	676
	340	34.83	3.26	16.91	0.00	25.82	0.43	5.46	0.00	0.09	9.58	96.39	5.44	0.38	3.12	3.38	0.06	1.27	0.00	0.03	1.91	0.56	2.56	1.94	5.65	8.00	0.27	672
	341	34.94	3.50	16.53	0.00	25.26	0.46	5.45	0.00	0.04	9.58	95.76	5.49	0.41	3.06	3.32	0.06	1.27	0.00	0.01	1.92	0.54	2.51	1.93	5.61	8.00	0.28	683
	342	34.53	3.48	16.38	0.03	25.82	0.46	5.59	0.00	0.06	9.42	95.76	5.44	0.41	3.04	3.40	0.06	1.31	0.00	0.02	1.89	0.48	2.56	1.91	5.67	8.00	0.28	683
	343	34.79	3.46	16.20	0.00	24.84	0.47	5.59	0.01	0.04	9.62	95.02	5.50	0.41	3.02	3.28	0.06	1.32	0.00	0.01	1.94	0.52	2.50	1.96	5.60	8.00	0.29	683
	344	34.99	3.71	17.10	0.01	24.48	0.48	5.23	0.01	0.06	9.51	95.57	5.47	0.44	3.15	3.20	0.06	1.22	0.00	0.02	1.90	0.63	2.53	1.92	5.55	8.00	0.28	691
	345	35.08	3.67	16.39	0.04	24.47	0.46	5.24	0.01	0.08	9.42	94.86	5.53	0.43	3.05	3.23	0.06	1.23	0.00	0.02	1.89	0.58	2.47	1.92	5.54	8.00	0.28	691
	346	34.70	3.67	15.95	0.00	24.63	0.46	5.39	0.00	0.03	9.24	94.07	5.53	0.44	3.00	3.28	0.06	1.28	0.00	0.01	1.88	0.53	2.47	1.89	5.59	8.00	0.28	693
	347	34.56	3.75	16.22	0.00	25.45	0.49	5.30	0.02	0.04	9.61	95.44	5.46	0.45	3.02	3.36	0.06	1.25	0.00	0.01	1.94	0.48	2.54	1.95	5.60	8.00	0.27	694
	355	34.72	3.22	16.18	0.00	25.65	0.42	5.72	0.01	0.04	9.18	95.14	5.49	0.38	3.02	3.39	0.06	1.35	0.00	0.01	1.85	0.51	2.51	1.87	5.68	8.00	0.28	672
	356	34.48	3.20	16.38	0.04	25.87	0.42	5.67	0.06	0.04	9.30	95.45	5.45	0.38	3.05	3.42	0.06	1.34	0.01	0.01	1.88	0.50	2.55	1.90	5.69	8.00	0.28	671
	357	34.13	2.65	16.24	0.04	25.38	0.32	5.68	0.04	0.05	9.33	93.85	5.48	0.32	3.07	3.41	0.04	1.36	0.01	0.01	1.91	0.55	2.52	1.93	5.69	8.00	0.29	643
	361	34.22	3.75	16.07	0.06	25.42	0.55	5.28	0.04	0.07	9.52	94.98	5.44	0.45	3.01	3.38	0.07	1.25	0.01	0.02	1.93	0.45	2.56	1.96	5.61	8.00	0.27	695
	362	35.39	3.61	16.20	0.02	24.22	0.45	5.04	0.39	0.11	8.80	94.24	5.59	0.43	3.02	3.20	0.06	1.19	0.07	0.03	1.78	0.61	2.41	1.88	5.49	8.00	0.27	689
	385	34.77	3.75	16.11	0.01	25.97	0.54	5.08	0.00	0.02	9.50	95.75	5.48	0.44	2.99	3.43	0.07	1.19	0.00	0.00	1.91	0.48	2.52	1.92	5.61	8.00	0.26	693
	386	34.70	3.87	16.01	0.00	26.27	0.53	5.04	0.01	0.05	9.42	95.88	5.47	0.46	2.98	3.46	0.07	1.18	0.00	0.01	1.89	0.45	2.53	1.91	5.63	8.00	0.25	698

doi:10.6342/NTU202202659

Mineral	No.	SiO_2	TiO_2	Al_2O_3	Cr_2O_3	FeO	MnO	MgO	CaO	Na_2O	K_2O	Total	Si^{4+}	Ti^{4+}	Al^{3+}	Fe^{2+}	Mn^{2+}	Mg^{2+}	Ca^{2+}	Na^{+}	K^{+}	$Al_{(M)}$	$Al_{(T)}$	$I_{(total)}$	$M_{(total)}$	$T_{(total)}$
Muscvoite	36	47.49	0.00	33.03	0.00	2.43	0.06	0.37	0.08	0.03	10.90	94.39	6.41	0.00	5.25	0.27	0.01	0.07	0.01	0.01	1.88	3.66	1.59	1.90	4.01	8.00
	197	47.71	0.00	32.97	0.00	2.76	0.07	0.59	0.03	0.05	11.10	95.27	6.40	0.00	5.21	0.31	0.01	0.12	0.00	0.01	1.90	3.60	1.60	1.92	4.04	8.00
	198	45.76	0.00	33.75	0.00	2.11	0.03	0.23	0.02	0.02	11.18	93.11	6.27	0.00	5.45	0.24	0.00	0.05	0.00	0.01	1.95	3.73	1.73	1.96	4.02	8.00
	199	46.66	0.00	34.58	0.01	2.05	0.06	0.08	0.02	0.04	10.81	94.30	6.29	0.00	5.49	0.23	0.01	0.02	0.00	0.01	1.86	3.78	1.71	1.87	4.03	8.00
	200	46.27	0.01	34.52	0.00	1.92	0.06	0.17	0.02	0.04	11.01	94.02	6.26	0.00	5.51	0.22	0.01	0.03	0.00	0.01	1.90	3.77	1.74	1.91	4.03	8.00
	201	47.23	0.02	34.11	0.00	2.38	0.07	0.23	0.01	0.05	10.71	94.81	6.33	0.00	5.39	0.27	0.01	0.05	0.00	0.01	1.83	3.72	1.67	1.85	4.05	8.00
	203	47.60	0.00	32.82	0.01	2.24	0.09	0.36	0.03	0.01	10.66	93.82	6.44	0.00	5.23	0.25	0.01	0.07	0.00	0.00	1.84	3.68	1.56	1.85	4.01	8.00
	272	46.60	0.00	33.21	0.00	2.30	0.08	0.08	0.10	0.04	10.87	93.27	6.36	0.00	5.34	0.26	0.01	0.02	0.01	0.01	1.89	3.71	1.64	1.92	4.00	8.00
	275	47.30	0.02	34.93	0.02	1.84	0.03	0.29	0.07	0.04	10.54	95.08	6.30	0.00	5.48	0.20	0.00	0.06	0.01	0.01	1.79	3.78	1.70	1.81	4.05	8.00
	277	47.39	0.00	34.65	0.03	1.74	0.08	0.14	0.10	0.00	10.88	95.01	6.32	0.00	5.45	0.19	0.01	0.03	0.01	0.00	1.85	3.77	1.68	1.87	4.01	8.00
	280	47.35	0.00	32.80	0.01	2.31	0.05	0.42	1.68	0.23	9.90	94.74	6.37	0.00	5.20	0.26	0.01	0.08	0.24	0.06	1.70	3.56	1.63	2.00	3.91	8.00
	281	47.48	0.01	33.88	0.00	2.28	0.04	0.24	0.03	0.02	10.72	94.69	6.37	0.00	5.35	0.26	0.00	0.05	0.00	0.01	1.83	3.72	1.63	1.84	4.03	8.00
	284	47.87	0.01	32.14	0.00	3.38	0.06	0.57	0.03	0.00	10.89	94.94	6.45	0.00	5.10	0.38	0.01	0.11	0.00	0.00	1.87	3.55	1.55	1.88	4.06	8.00
	285	48.33	0.00	33.14	0.00	2.79	0.11	0.37	0.34	0.06	10.82	95.95	6.42	0.00	5.19	0.31	0.01	0.07	0.05	0.02	1.83	3.61	1.58	1.90	4.01	8.00
	286	49.13	0.03	31.13	0.00	2.97	0.10	0.60	0.03	0.01	11.12	95.12	6.59	0.00	4.92	0.33	0.01	0.12	0.00	0.00	1.90	3.52	1.41	1.91	3.98	8.00

doi:10.6342/NTU202202659

Mineral	No.	SiO_2	TiO_2	Al_2O_3	Cr_2O_3	FeO	MnO	MgO	CaO	Na_2O	K_2O	Total	Si^{4+}	Ti^{4+}	Al^{3+}	Fe^{2+}	Fe^{3+}	Mn^{2+}	Mg^{2+}	Ca^{2+}	Na^{+}	K^{+}	Al_Z	Al_Y	$X_{(total)}$	$Y_{(total)}$	$Z_{(total)}$	Alm	Py	Sp	Gro
Garnet1	75	37.66	0.02	20.77	0.02	26.12	9.81	1.11	5.03	0.00	0.00	100.53	3.03	0.00	1.97	1.76	0.00	0.67	0.13	0.43	0.00	0.00	0.00	1.97	2.99	1.97	3.03	0.59	0.04	0.22	0.14
	76	37.86	0.01	20.92	0.00	26.83	9.53	1.17	4.89	0.01	0.00	101.22	3.03	0.00	1.97	1.79	0.00	0.65	0.14	0.42	0.00	0.00	0.00	1.97	3.00	1.97	3.03	0.60	0.05	0.22	0.14
	77	37.87	0.03	20.84	0.00	25.90	8.91	1.14	6.20	0.00	0.00	100.88	3.03	0.00	1.96	1.73	0.00	0.60	0.14	0.53	0.00	0.00	0.00	1.96	3.00	1.96	3.03	0.58	0.05	0.20	0.18
	78	37.89	0.01	20.91	0.01	26.10	8.79	1.12	6.37	0.01	0.00	101.20	3.02	0.00	1.96	1.74	0.00	0.59	0.13	0.54	0.00	0.00	0.00	1.96	3.01	1.96	3.02	0.58	0.04	0.20	0.18
	79	37.41	0.13	20.74	0.00	25.33	8.70	1.08	6.88	0.00	0.00	100.26	3.01	0.01	1.97	1.70	0.00	0.59	0.13	0.59	0.00	0.00	0.00	1.97	3.02	1.97	3.01	0.56	0.04	0.20	0.20
	80	37.88	0.01	20.90	0.00	26.01	8.69	1.15	6.75	0.00	0.00	101.38	3.01	0.00	1.96	1.72	0.01	0.59	0.14	0.58	0.00	0.00	0.00	1.96	3.02	1.97	3.01	0.57	0.05	0.19	0.19
	81	37.78	0.01	20.72	0.02	25.82	8.72	1.13	6.66	0.01	0.00	100.87	3.02	0.00	1.95	1.73	0.00	0.59	0.13	0.57	0.00	0.00	0.00	1.95	3.02	1.95	3.02	0.57	0.04	0.20	0.19
	82	37.92	0.08	20.56	0.00	25.20	8.63	1.08	7.39	0.00	0.00	100.85	3.03	0.00	1.94	1.69	0.00	0.58	0.13	0.63	0.00	0.00	0.00	1.94	3.03	1.94	3.03	0.56	0.04	0.19	0.21
	83	38.00	0.01	20.41	0.00	24.80	8.80	1.05	6.71	0.00	0.00	99.78	3.07	0.00	1.94	1.68	0.00	0.60	0.13	0.58	0.00	0.00	0.00	1.94	2.99	1.94	3.07	0.56	0.04	0.20	0.19
	84	38.16	0.00	20.74	0.00	25.10	9.81	1.07	6.01	0.05	0.00	100.94	3.05	0.00	1.95	1.68	0.00	0.66	0.13	0.51	0.01	0.00	0.00	1.95	2.99	1.95	3.05	0.56	0.04	0.22	0.17
	85	38.00	0.05	20.65	0.00	24.98	10.22	0.95	6.06	0.00	0.00	100.90	3.05	0.00	1.95	1.67	0.00	0.69	0.11	0.52	0.00	0.00	0.00	1.95	3.00	1.95	3.05	0.56	0.04	0.23	0.17
	86	37.89	0.03	21.20	0.00	25.90	10.28	1.14	5.00	0.00	0.00	101.44	3.02	0.00	1.99	1.73	0.00	0.69	0.14	0.43	0.00	0.00	0.00	1.99	2.98	1.99	3.02	0.58	0.05	0.23	0.14
	87	37.87	0.01	20.93	0.00	25.86	10.21	1.12	5.11	0.00	0.00	101.11	3.03	0.00	1.97	1.73	0.00	0.69	0.13	0.44	0.00	0.00	0.00	1.97	2.99	1.97	3.03	0.58	0.04	0.23	0.15
	88	37.90	0.03	21.16	0.00	26.28	10.42	1.09	5.08	0.00	0.00	101.96	3.01	0.00	1.98	1.75	0.00	0.70	0.13	0.43	0.00	0.00	0.00	1.98	3.01	1.98	3.01	0.58	0.04	0.23	0.14
	89	37.76	0.00	21.08	0.00	25.76	10.17	1.07	5.06	0.00	0.00	100.90	3.03	0.00	1.99	1.73	0.00	0.69	0.13	0.43	0.00	0.00	0.00	1.99	2.98	1.99	3.03	0.58	0.04	0.23	0.15
	90	37.75	0.01	20.89	0.00	25.59	10.99	0.98	5.09	0.00	0.00	101.28	3.02	0.00	1.97	1.72	0.00	0.74	0.12	0.44	0.00	0.00	0.00	1.97	3.02	1.97	3.02	0.57	0.04	0.25	0.14
	91	37.95	0.00	20.90	0.00	25.90	10.99	1.00	5.03	0.00	0.00	101.78	3.02	0.00	1.96	1.73	0.00	0.74	0.12	0.43	0.00	0.00	0.00	1.96	3.01	1.96	3.02	0.57	0.04	0.25	0.14
	92	37.89	0.01	20.92	0.02	25.87	10.68	1.03	5.29	0.01	0.00	101.71	3.02	0.00	1.96	1.72	0.00	0.72	0.12	0.45	0.00	0.00	0.00	1.96	3.02	1.96	3.02	0.57	0.04	0.24	0.15
	93	37.69	0.00	20.81	0.00	25.10	10.66	0.98	5.41	0.00	0.00	100.65	3.03	0.00	1.97	1.69	0.00	0.73	0.12	0.47	0.00	0.00	0.00	1.97	3.00	1.97	3.03	0.56	0.04	0.24	0.16
	94	37.75	0.02	20.86	0.00	25.77	10.10	1.05	5.45	0.00	0.00	101.00	3.02	0.00	1.97	1.73	0.00	0.69	0.13	0.47	0.00	0.00	0.00	1.97	3.01	1.97	3.02	0.57	0.04	0.23	0.16
	95	37.89	0.01	20.85	0.02	26.07	9.60	1.05	5.53	0.00	0.00	101.01	3.03	0.00	1.97	1.75	0.00	0.65	0.13	0.47	0.00	0.00	0.00	1.97	3.00	1.97	3.03	0.58	0.04	0.22	0.16
	96	37.79	0.02	20.78	0.00	26.24	9.80	1.07	5.19	0.02	0.00	100.90	3.03	0.00	1.96	1.76	0.00	0.67	0.13	0.45	0.00	0.00	0.00	1.96	3.00	1.96	3.03	0.59	0.04	0.22	0.15
	97	37.80	0.01	20.76	0.00	25.97	10.13	1.12	5.09	0.00	0.00	100.87	3.03	0.00	1.96	1.74	0.00	0.69	0.13	0.44	0.00	0.00	0.00	1.96	3.00	1.96	3.03	0.58	0.04	0.23	0.15
	98	37.69	0.00	20.84	0.00	25.76	10.59	1.04	5.01	0.00	0.00	100.93	3.02	0.00	1.97	1.74	0.00	0.72	0.12	0.43	0.00	0.00	0.00	1.97	3.01	1.97	3.02	0.58	0.04	0.24	0.14
	99	37.39	0.02	20.64	0.00	25.24	10.72	1.02	5.05	0.00	0.00	100.06	3.03	0.00	1.97	1.71	0.00	0.73	0.12	0.44	0.00	0.00	0.00	1.97	3.00	1.97	3.03	0.57	0.04	0.24	0.15

doi:10.6342/NTU202202659

Mineral	No.	SiO_2	TiO_2	Al_2O_3	Cr_2O_3	FeO	MnO	MgO	CaO	Na_2O	K_2O	Total	Si^{4+}	Ti^{4+}	Al^{3+}	Fe^{2+}	Fe^{3+}	Mn^{2+}	Mg^{2+}	Ca^{2+}	Na^{+}	K^{+}	Al_Z	Al_Y	$X_{(total)}$	$Y_{(total)}$	$Z_{(total)}$	Alm	Py	Sp	Gro
Garnet2	100	37.94	0.01	21.04	0.00	25.44	10.42	1.07	5.19	0.00	0.00	101.11	3.04	0.00	1.98	1.70	0.00	0.71	0.13	0.44	0.00	0.00	0.00	1.98	2.98	1.98	3.04	0.57	0.04	0.24	0.15
	101	38.22	0.01	20.92	0.00	24.95	9.85	0.95	6.43	0.00	0.00	101.34	3.05	0.00	1.96	1.66	0.00	0.66	0.11	0.55	0.00	0.00	0.00	1.96	2.99	1.96	3.05	0.56	0.04	0.22	0.18
	102	38.05	0.02	20.85	0.01	24.96	9.59	0.99	6.63	0.00	0.00	101.11	3.04	0.00	1.96	1.67	0.00	0.65	0.12	0.57	0.00	0.00	0.00	1.96	3.00	1.96	3.04	0.56	0.04	0.22	0.19
	103	37.88	0.02	20.65	0.00	24.84	10.42	0.99	4.97	0.00	0.00	99.78	3.07	0.00	1.97	1.68	0.00	0.72	0.12	0.43	0.00	0.00	0.00	1.97	2.95	1.97	3.07	0.57	0.04	0.24	0.15
	104	37.89	0.01	20.68	0.00	25.32	10.55	1.01	4.92	0.00	0.00	100.38	3.06	0.00	1.97	1.71	0.00	0.72	0.12	0.43	0.00	0.00	0.00	1.97	2.98	1.97	3.06	0.57	0.04	0.24	0.14
	105	37.76	0.06	20.73	0.00	24.85	10.04	0.98	6.23	0.02	0.00	100.67	3.03	0.00	1.96	1.67	0.00	0.68	0.12	0.54	0.00	0.00	0.00	1.96	3.00	1.96	3.03	0.56	0.04	0.23	0.18
	106	37.71	0.02	20.76	0.00	25.70	10.51	0.99	5.33	0.00	0.00	101.03	3.02	0.00	1.96	1.72	0.00	0.71	0.12	0.46	0.00	0.00	0.00	1.96	3.01	1.96	3.02	0.57	0.04	0.24	0.15
	107	37.70	0.03	20.83	0.00	25.54	10.11	1.01	5.69	0.00	0.00	100.90	3.02	0.00	1.97	1.71	0.00	0.69	0.12	0.49	0.00	0.00	0.00	1.97	3.01	1.97	3.02	0.57	0.04	0.23	0.16
	108	37.76	0.00	21.06	0.01	25.89	10.04	1.03	5.80	0.00	0.00	101.59	3.01	0.00	1.98	1.72	0.01	0.68	0.12	0.49	0.00	0.00	0.00	1.98	3.01	1.98	3.01	0.57	0.04	0.22	0.16
	109	37.77	0.01	20.84	0.00	25.74	10.52	0.95	5.26	0.00	0.00	101.09	3.03	0.00	1.97	1.73	0.00	0.71	0.11	0.45	0.00	0.00	0.00	1.97	3.00	1.97	3.03	0.57	0.04	0.24	0.15
	110	37.83	0.00	20.72	0.03	25.80	10.44	0.93	5.38	0.00	0.00	101.12	3.03	0.00	1.96	1.73	0.00	0.71	0.11	0.46	0.00	0.00	0.00	1.96	3.01	1.96	3.03	0.57	0.04	0.24	0.15
	111	38.01	0.04	20.74	0.00	25.46	10.20	0.94	5.14	0.00	0.00	100.53	3.06	0.00	1.97	1.72	0.00	0.70	0.11	0.44	0.00	0.00	0.00	1.97	2.97	1.97	3.06	0.58	0.04	0.23	0.15
	112	38.20	0.04	20.76	0.00	25.34	9.18	0.97	5.91	0.00	0.00	100.40	3.07	0.00	1.97	1.70	0.00	0.63	0.12	0.51	0.00	0.00	0.00	1.97	2.96	1.97	3.07	0.58	0.04	0.21	0.17
	113	37.95	0.01	20.98	0.02	25.01	9.56	1.00	6.25	0.02	0.00	100.80	3.04	0.00	1.98	1.67	0.00	0.65	0.12	0.54	0.00	0.00	0.00	1.98	2.98	1.98	3.04	0.56	0.04	0.22	0.18
	114	38.39	0.05	20.81	0.02	25.00	9.31	0.97	6.95	0.00	0.00	101.48	3.05	0.00	1.95	1.66	0.00	0.63	0.11	0.59	0.00	0.00	0.00	1.95	3.00	1.95	3.05	0.55	0.04	0.21	0.20
	115	37.97	0.04	20.84	0.00	25.38	9.54	0.98	6.46	0.02	0.00	101.24	3.03	0.00	1.96	1.69	0.00	0.64	0.12	0.55	0.00	0.00	0.00	1.96	3.01	1.96	3.03	0.56	0.04	0.21	0.18
	116	37.82	0.00	20.94	0.00	25.29	8.90	1.03	7.03	0.00	0.00	101.01	3.02	0.00	1.97	1.69	0.00	0.60	0.12	0.60	0.00	0.00	0.00	1.97	3.01	1.97	3.02	0.56	0.04	0.20	0.20
	117	38.22	0.03	20.73	0.04	25.29	8.71	1.07	7.03	0.01	0.00	101.12	3.05	0.00	1.95	1.69	0.00	0.59	0.13	0.60	0.00	0.00	0.00	1.95	3.00	1.95	3.05	0.56	0.04	0.20	0.20
	118	38.24	0.01	19.96	0.03	25.48	9.11	1.05	6.33	0.00	0.00	100.21	3.08	0.00	1.90	1.72	0.00	0.62	0.13	0.55	0.00	0.00	0.00	1.90	3.01	1.90	3.08	0.57	0.04	0.21	0.18
	119	37.72	0.03	20.83	0.02	25.39	9.49	1.06	5.96	0.00	0.00	100.50	3.03	0.00	1.97	1.71	0.00	0.65	0.13	0.51	0.00	0.00	0.00	1.97	2.99	1.97	3.03	0.57	0.04	0.22	0.17
	120	37.98	0.00	20.67	0.00	25.97	9.79	1.10	5.85	0.01	0.00	101.36	3.03	0.00	1.94	1.73	0.00	0.66	0.13	0.50	0.00	0.00	0.00	1.94	3.03	1.94	3.03	0.57	0.04	0.22	0.17
	121	37.87	0.00	20.75	0.00	25.41	9.91	1.01	5.92	0.01	0.00	100.88	3.03	0.00	1.96	1.70	0.00	0.67	0.12	0.51	0.00	0.00	0.00	1.96	3.00	1.96	3.03	0.57	0.04	0.22	0.17
	122	37.99	0.02	20.66	0.00	25.51	9.80	1.04	5.84	0.00	0.00	100.85	3.05	0.00	1.95	1.71	0.00	0.67	0.12	0.50	0.00	0.00	0.00	1.95	3.00	1.95	3.05	0.57	0.04	0.22	0.17
	123	38.04	0.01	20.80	0.00	25.27	9.29	1.00	5.99	0.02	0.00	100.42	3.06	0.00	1.97	1.70	0.00	0.63	0.12	0.52	0.00	0.00	0.00	1.97	2.97	1.97	3.06	0.57	0.04	0.21	0.17
Garnet3	124	38.15	0.00	20.96	0.00	25.39	9.96	0.96	5.38	0.02	0.00	100.80	3.06	0.00	1.98	1.70	0.00	0.68	0.11	0.46	0.00	0.00	0.00	1.98	2.96	1.98	3.06	0.58	0.04	0.23	0.16
	125	37.32	0.03	20.95	0.00	25.21	9.60	0.98	6.05	0.00	0.00	100.12	3.01	0.00	1.99	1.70	0.00	0.66	0.12	0.52	0.00	0.00	0.00	1.99	3.00	1.99	3.01	0.57	0.04	0.22	0.17
	126	37.19	0.03	20.27	0.00	25.65	9.35	1.09	5.96	0.02	0.00	99.55	3.02	0.00	1.94	1.73	0.01	0.64	0.13	0.52	0.00	0.00	0.00	1.94	3.03	1.95	3.02	0.57	0.04	0.21	0.17
	127	37.84	0.03	20.60	0.00	25.85	9.45	1.12	5.64	0.00	0.00	100.53	3.04	0.00	1.95	1.74	0.00	0.64	0.13	0.49	0.00	0.00	0.00	1.95	3.00	1.95	3.04	0.58	0.04	0.21	0.16
	129	37.41	0.00	20.82	0.02	25.64	9.22	1.15	5.98	0.00	0.00	100.23	3.01	0.00	1.98	1.73	0.00	0.63	0.14	0.52	0.00	0.00	0.00	1.98	3.01	1.98	3.01	0.57	0.05	0.21	0.17
	130	37.65	0.06	20.60	0.00	26.11	9.06	1.08	6.23	0.00	0.00	100.77	3.02	0.00	1.95	1.75	0.00	0.62	0.13	0.54	0.00	0.00	0.00	1.95	3.03	1.95	3.02	0.58	0.04	0.20	0.18
	131	38.06	0.03	20.76	0.00	25.47	9.16	1.11	6.36	0.00	0.00	100.93	3.04	0.00	1.96	1.70	0.00	0.62	0.13	0.54	0.00	0.00	0.00	1.96	3.00	1.96	3.04	0.57	0.04	0.21	0.18
	132	37.48	0.03	20.80	0.02	25.56	9.26	1.06	6.41	0.00	0.00	100.60	3.01	0.00	1.97	1.71	0.01	0.63	0.13	0.55	0.00	0.00	0.00	1.97	3.02	1.97	3.01	0.57	0.04	0.21	0.18
	133	38.10	0.06	20.88	0.00	25.14	9.14	1.02	6.37	0.00	0.00	100.71	3.05	0.00	1.97	1.68	0.00	0.62	0.12	0.55	0.00	0.00	0.00	1.97	2.97	1.97	3.05	0.57	0.04	0.21	0.18

doi:10.6342/NTU202202659

Mineral	No.	SiO_2	TiO_2	Al_2O_3	Cr_2O_3	FeO	MnO	MgO	CaO	Na_2O	K_2O	Total	Si^{4+}	Ti^{4+}	Al^{3+}	Fe^{2+}	Fe^{3+}	Mn^{2+}	Mg^{2+}	Ca^{2+}	Na^{+}	K^{+}	Al_Z	Al_Y	$X_{(total)}$	$Y_{(total)}$	$Z_{(total)}$	Alm	Py	Sp	Gro
Garnet4	134	37.70	0.02	20.83	0.00	26.20	9.60	1.09	5.14	0.03	0.00	100.60	3.03	0.00	1.97	1.76	0.00	0.65	0.13	0.44	0.00	0.00	0.00	1.97	2.99	1.97	3.03	0.59	0.04	0.22	0.15
	135	37.82	0.03	20.88	0.00	26.39	9.33	1.13	5.37	0.00	0.00	100.96	3.03	0.00	1.97	1.77	0.00	0.63	0.13	0.46	0.00	0.00	0.00	1.97	3.00	1.97	3.03	0.59	0.05	0.21	0.15
	136	37.87	0.00	20.68	0.03	26.43	9.46	1.14	5.45	0.00	0.00	101.05	3.03	0.00	1.95	1.77	0.00	0.64	0.14	0.47	0.00	0.00	0.00	1.95	3.01	1.95	3.03	0.59	0.05	0.21	0.16
	137	37.47	0.00	20.64	0.03	24.81	9.73	1.16	5.33	0.01	0.00	99.17	3.05	0.00	1.98	1.69	0.00	0.67	0.14	0.46	0.00	0.00	0.00	1.98	2.97	1.98	3.05	0.57	0.05	0.23	0.16
	138	37.83	0.03	20.49	0.00	25.49	9.49	1.10	5.75	0.01	0.00	100.19	3.05	0.00	1.95	1.72	0.00	0.65	0.13	0.50	0.00	0.00	0.00	1.95	3.00	1.95	3.05	0.57	0.04	0.22	0.17
	139	37.87	0.02	20.68	0.00	25.81	9.52	1.11	5.61	0.01	0.00	100.63	3.04	0.00	1.96	1.73	0.00	0.65	0.13	0.48	0.00	0.00	0.00	1.96	3.00	1.96	3.04	0.58	0.04	0.22	0.16
	140	36.97	0.04	20.96	0.02	26.11	9.77	1.11	5.48	0.00	0.00	100.45	2.98	0.00	1.99	1.73	0.03	0.67	0.13	0.47	0.00	0.00	0.02	1.97	3.00	2.01	2.98	0.58	0.04	0.22	0.16
	141	37.71	0.04	20.64	0.02	25.83	9.34	1.08	6.06	0.00	0.00	100.71	3.03	0.00	1.95	1.73	0.00	0.63	0.13	0.52	0.00	0.00	0.00	1.95	3.02	1.95	3.03	0.57	0.04	0.21	0.17
	142	36.69	0.03	20.65	0.00	25.59	9.39	1.11	6.14	0.00	0.00	99.59	2.98	0.00	1.97	1.70	0.04	0.65	0.13	0.53	0.00	0.00	0.02	1.95	3.01	2.01	2.98	0.56	0.04	0.21	0.18
	143	37.79	0.03	20.76	0.01	24.05	9.17	1.10	6.35	0.00	0.00	99.25	3.07	0.00	1.98	1.63	0.00	0.63	0.13	0.55	0.00	0.00	0.00	1.98	2.95	1.98	3.07	0.55	0.05	0.21	0.19
	144	37.41	0.05	20.90	0.01	23.93	9.04	1.08	6.74	0.05	0.00	99.19	3.03	0.00	2.00	1.62	0.00	0.62	0.13	0.59	0.01	0.00	0.00	2.00	2.96	2.00	3.03	0.55	0.04	0.21	0.20
	145	38.09	0.00	20.62	0.01	24.78	9.43	1.04	6.25	0.01	0.00	100.23	3.07	0.00	1.96	1.67	0.00	0.64	0.12	0.54	0.00	0.00	0.00	1.96	2.98	1.96	3.07	0.56	0.04	0.22	0.18
	146	37.89	0.03	20.84	0.00	24.75	10.41	0.93	5.64	0.00	0.00	100.48	3.05	0.00	1.98	1.67	0.00	0.71	0.11	0.49	0.00	0.00	0.00	1.98	2.97	1.98	3.05	0.56	0.04	0.24	0.16
Garnet5	147	37.11	0.04	20.99	0.00	24.79	10.72	0.89	5.55	0.00	0.00	100.09	3.00	0.00	2.00	1.68	0.00	0.73	0.11	0.48	0.00	0.00	0.00	2.00	3.00	2.00	3.00	0.56	0.04	0.24	0.16
	148	38.18	0.01	20.82	0.00	24.85	10.58	0.90	6.00	0.02	0.00	101.36	3.05	0.00	1.96	1.66	0.00	0.71	0.11	0.51	0.00	0.00	0.00	1.96	2.99	1.96	3.05	0.55	0.04	0.24	0.17
	149	37.72	0.02	20.83	0.00	25.15	10.43	0.96	5.59	0.01	0.00	100.72	3.03	0.00	1.97	1.69	0.00	0.71	0.11	0.48	0.00	0.00	0.00	1.97	3.00	1.97	3.03	0.56	0.04	0.24	0.16
	150	36.03	0.05	20.93	0.00	25.24	10.34	0.99	5.67	0.00	0.00	99.26	2.94	0.00	2.01	1.67	0.05	0.71	0.12	0.50	0.00	0.00	0.06	1.95	2.99	2.07	2.94	0.56	0.04	0.24	0.17
	151	37.82	0.05	20.67	0.01	25.34	10.21	0.92	5.94	0.00	0.00	100.97	3.03	0.00	1.95	1.70	0.00	0.69	0.11	0.51	0.00	0.00	0.00	1.95	3.01	1.95	3.03	0.56	0.04	0.23	0.17
	152	37.65	0.02	20.77	0.01	25.54	9.84	0.95	6.07	0.00	0.00	100.84	3.02	0.00	1.96	1.71	0.00	0.67	0.11	0.52	0.00	0.00	0.00	1.96	3.02	1.96	3.02	0.57	0.04	0.22	0.17
	153	37.61	0.05	20.99	0.01	24.95	9.23	1.03	6.42	0.00	0.00	100.30	3.02	0.00	1.99	1.68	0.00	0.63	0.12	0.55	0.00	0.00	0.00	1.99	2.98	1.99	3.02	0.56	0.04	0.21	0.19
	154	37.62	0.03	20.96	0.00	25.02	8.91	0.96	6.80	0.02	0.00	100.31	3.02	0.00	1.98	1.68	0.00	0.61	0.11	0.59	0.00	0.00	0.00	1.98	2.99	1.98	3.02	0.56	0.04	0.20	0.20
	155	37.31	0.01	20.82	0.00	24.92	9.58	0.98	6.77	0.01	0.00	100.39	3.00	0.00	1.97	1.66	0.01	0.65	0.12	0.58	0.00	0.00	0.00	1.97	3.01	1.99	3.00	0.55	0.04	0.22	0.19
Garnet6	156	36.90	0.05	20.63	0.00	25.85	9.54	1.05	6.07	0.00	0.00	100.10	2.98	0.00	1.96	1.71	0.03	0.65	0.13	0.53	0.00	0.00	0.02	1.95	3.02	2.00	2.98	0.57	0.04	0.22	0.17
	157	37.43	0.05	20.41	0.01	26.04	9.58	1.11	5.92	0.00	0.00	100.55	3.01	0.00	1.94	1.74	0.02	0.65	0.13	0.51	0.00	0.00	0.00	1.94	3.03	1.95	3.01	0.57	0.04	0.22	0.17
	158	36.74	0.05	20.64	0.00	26.32	9.61	1.13	5.39	0.01	0.00	99.88	2.98	0.00	1.97	1.75	0.03	0.66	0.14	0.47	0.00	0.00	0.02	1.95	3.01	2.01	2.98	0.58	0.05	0.22	0.16
	159	37.85	0.01	20.98	0.00	25.58	9.44	0.91	5.81	0.00	0.00	100.58	3.04	0.00	1.99	1.72	-0.04	0.64	0.11	0.50	0.00	0.00	0.00	1.99	2.97	1.99	3.04	0.58	0.04	0.22	0.17
	160	37.69	0.02	20.97	0.00	26.08	9.38	0.89	6.07	0.01	0.00	101.11	3.01	0.00	1.98	1.74	0.00	0.64	0.11	0.52	0.00	0.00	0.00	1.98	3.01	1.98	3.01	0.58	0.04	0.21	0.17
	161	38.17	0.00	21.03	0.00	25.52	9.93	1.03	6.11	0.07	0.00	101.86	3.03	0.00	1.96	1.69	-0.01	0.67	0.12	0.52	0.01	0.00	0.00	1.96	3.00	1.96	3.03	0.56	0.04	0.22	0.17
	162	38.21	0.01	20.84	0.00	25.82	10.32	1.04	5.33	0.00	0.00	101.56	3.05	0.00	1.96	1.72	-0.02	0.70	0.12	0.46	0.00	0.00	0.00	1.96	3.00	1.96	3.05	0.57	0.04	0.23	0.15

doi:10.6342/NTU202202659

Mineral	No.	SiO_2	TiO_2	Al_2O_3	Cr_2O_3	FeO	Fe_2O_3	MnO	MgO	CaO	Na_2O	K_2O	Total	Si^{4+}	Ti^{4+}	Al^{3+}	Fe^{3+}	Mn^{2+}	Mg^{2+}	Ca^{2+}	Na^{+}	K^{+}	$T_{(total)}$	$M_{(total)}$	Ab	Or	An
Plagioclase	79	58.81	0.00	26.51	0.00	0.13	0.14	0.00	0.00	8.53	6.40	0.17	100.55	2.61	0.00	1.39	0.00	0.00	0.00	0.41	0.55	0.01	4.00	0.97	0.57	0.01	0.42
Pl1	80	58.39	0.01	26.49	0.00	0.13	0.14	0.00	0.00	8.60	6.34	0.26	100.21	2.61	0.00	1.39	0.00	0.00	0.00	0.41	0.55	0.01	4.00	0.97	0.56	0.02	0.42
	81	58.07	0.01	26.50	0.00	0.10	0.11	0.02	0.00	8.62	6.39	0.19	99.89	2.60	0.00	1.40	0.00	0.00	0.00	0.41	0.55	0.01	4.00	0.98	0.57	0.01	0.42
	82	57.95	0.00	26.56	0.00	0.16	0.18	0.00	0.00	8.59	6.23	0.23	99.72	2.60	0.00	1.40	0.01	0.00	0.00	0.41	0.54	0.01	4.00	0.97	0.56	0.01	0.43
	83	58.29	0.02	26.46	0.02	0.13	0.15	0.00	0.00	8.57	6.36	0.25	100.11	2.60	0.00	1.39	0.00	0.00	0.00	0.41	0.55	0.01	4.00	0.98	0.56	0.01	0.42
	84	58.42	0.01	26.68	0.01	0.07	0.08	0.03	0.00	8.58	6.26	0.23	100.28	2.60	0.00	1.40	0.00	0.00	0.00	0.41	0.54	0.01	4.00	0.96	0.56	0.01	0.42
	85	58.14	0.01	26.50	0.00	0.14	0.15	0.02	0.00	8.60	6.35	0.28	100.03	2.60	0.00	1.40	0.01	0.00	0.00	0.41	0.55	0.02	4.00	0.98	0.56	0.02	0.42
	86	57.86	0.00	26.26	0.00	0.11	0.12	0.00	0.02	8.58	6.34	0.23	99.39	2.60	0.00	1.39	0.00	0.00	0.00	0.41	0.55	0.01	4.00	0.98	0.56	0.01	0.42
	87	56.54	0.00	26.35	0.02	0.11	0.13	0.03	0.01	8.63	6.33	0.25	98.27	2.58	0.00	1.42	0.00	0.00	0.00	0.42	0.56	0.01	3.99	1.00	0.56	0.01	0.42
	88	56.56	0.00	26.64	0.00	0.08	0.09	0.00	0.02	8.41	6.25	0.24	98.19	2.58	0.00	1.43	0.00	0.00	0.00	0.41	0.55	0.01	4.01	0.98	0.57	0.01	0.42
	89	57.01	0.00	26.11	0.00	0.09	0.10	0.00	0.00	8.44	6.21	0.25	98.11	2.60	0.00	1.40	0.00	0.00	0.00	0.41	0.55	0.01	4.00	0.98	0.56	0.01	0.42
	90	58.00	0.03	26.64	0.00	0.08	0.09	0.05	0.00	8.66	6.15	0.24	99.85	2.60	0.00	1.41	0.00	0.00	0.00	0.42	0.53	0.01	4.00	0.96	0.55	0.01	0.43
	91	58.11	0.00	26.49	0.02	0.09	0.10	0.00	0.00	8.60	6.23	0.26	99.79	2.60	0.00	1.40	0.00	0.00	0.00	0.41	0.54	0.01	4.00	0.97	0.56	0.02	0.43
	92	58.41	0.00	26.68	0.00	0.11	0.12	0.00	0.02	8.71	6.31	0.26	100.49	2.60	0.00	1.40	0.00	0.00	0.00	0.42	0.54	0.01	4.00	0.97	0.56	0.02	0.43
	93	58.00	0.01	26.51	0.00	0.08	0.09	0.00	0.02	8.60	6.27	0.25	99.74	2.60	0.00	1.40	0.00	0.00	0.00	0.41	0.54	0.01	4.00	0.97	0.56	0.01	0.43
	94	58.07	0.00	26.66	0.00	0.13	0.14	0.00	0.00	8.57	6.28	0.26	99.97	2.60	0.00	1.41	0.00	0.00	0.00	0.41	0.54	0.01	4.00	0.97	0.56	0.02	0.42
	95	58.44	0.00	26.45	0.02	0.10	0.11	0.00	0.01	8.51	6.21	0.23	99.95	2.61	0.00	1.39	0.00	0.00	0.00	0.41	0.54	0.01	4.00	0.96	0.56	0.01	0.43
	96	57.72	0.02	26.61	0.01	0.11	0.13	0.02	0.00	8.55	6.34	0.25	99.63	2.59	0.00	1.41	0.00	0.00	0.00	0.41	0.55	0.01	4.00	0.98	0.56	0.01	0.42
	97	58.15	0.01	26.53	0.00	0.07	0.08	0.00	0.00	8.66	6.23	0.22	99.87	2.60	0.00	1.40	0.00	0.00	0.00	0.42	0.54	0.01	4.00	0.97	0.56	0.01	0.43
	98	57.98	0.00	26.71	0.00	0.13	0.14	0.00	0.00	8.58	6.18	0.22	99.78	2.60	0.00	1.41	0.00	0.00	0.00	0.41	0.54	0.01	4.01	0.96	0.56	0.01	0.43
Plagioclase	99	58.38	0.01	26.69	0.00	0.19	0.21	0.00	0.00	8.50	6.28	0.22	100.27	2.60	0.00	1.40	0.01	0.00	0.00	0.41	0.54	0.01	4.00	0.96	0.56	0.01	0.42
Pl2	100	58.26	0.01	26.47	0.00	0.15	0.17	0.00	0.00	8.59	6.25	0.23	99.95	2.61	0.00	1.39	0.01	0.00	0.00	0.41	0.54	0.01	4.00	0.97	0.56	0.01	0.43
	101	58.33	0.03	26.44	0.00	0.08	0.08	0.02	0.00	8.65	6.36	0.22	100.13	2.61	0.00	1.39	0.00	0.00	0.00	0.41	0.55	0.01	4.00	0.98	0.56	0.01	0.42
	102	57.98	0.00	26.40	0.00	0.11	0.13	0.00	0.00	8.72	6.30	0.27	99.79	2.60	0.00	1.40	0.00	0.00	0.00	0.42	0.55	0.02	4.00	0.98	0.56	0.02	0.43
	103	58.03	0.00	26.47	0.00	0.10	0.11	0.00	0.01	8.60	6.30	0.25	99.75	2.60	0.00	1.40	0.00	0.00	0.00	0.41	0.55	0.01	4.00	0.97	0.56	0.01	0.42
	104	57.78	0.00	26.45	0.00	0.10	0.11	0.00	0.00	8.67	6.19	0.28	99.46	2.60	0.00	1.40	0.00	0.00	0.00	0.42	0.54	0.02	4.00	0.97	0.55	0.02	0.43
	105	57.62	0.00	26.46	0.00	0.14	0.16	0.00	0.01	8.73	6.27	0.24	99.47	2.59	0.00	1.40	0.01	0.00	0.00	0.42	0.55	0.01	4.00	0.98	0.56	0.01	0.43
	106	56.96	0.02	26.36	0.00	0.16	0.18	0.00	0.00	8.70	6.23	0.22	98.65	2.59	0.00	1.41	0.01	0.00	0.00	0.42	0.55	0.01	4.00	0.98	0.56	0.01	0.43
	107	57.60	0.01	26.15	0.00	0.16	0.17	0.02	0.00	8.66	6.35	0.21	99.16	2.60	0.00	1.39	0.01	0.00	0.00	0.42	0.56	0.01	3.99	0.99	0.56	0.01	0.42

doi:10.6342/NTU202202659

Mineral	No.	SiO_2	TiO_2	Al_2O_3	Cr_2O_3	FeO	Fe_2O_3	MnO	MgO	CaO	Na_2O	K_2O	Total	Si^{4+}	Ti^{4+}	Al^{3+}	Fe^{3+}	Mn^{2+}	Mg^{2+}	Ca^{2+}	Na^{+}	K^{+}	$T_{(total)}$	$M_{(total)}$	Ab	Or	An
Plagioclase	210	57.20	0.02	26.41	0.00	0.07	0.08	0.00	0.00	8.63	6.05	0.22	98.61	2.59	0.00	1.41	0.00	0.00	0.00	0.42	0.53	0.01	4.00	0.96	0.55	0.01	0.43
Pl3	211	58.26	0.01	25.95	0.00	0.06	0.07	0.00	0.00	8.26	6.21	0.24	99.00	2.63	0.00	1.38	0.00	0.00	0.00	0.40	0.54	0.01	4.00	0.96	0.57	0.01	0.42
	212	57.42	0.00	26.21	0.00	0.09	0.10	0.00	0.00	8.47	6.10	0.24	98.52	2.60	0.00	1.40	0.00	0.00	0.00	0.41	0.54	0.01	4.00	0.96	0.56	0.01	0.43
	213	57.23	0.03	26.03	0.03	0.08	0.09	0.00	0.00	8.46	6.11	0.27	98.22	2.60	0.00	1.40	0.00	0.00	0.00	0.41	0.54	0.02	4.00	0.97	0.56	0.02	0.43
	214	56.99	0.01	26.23	0.00	0.10	0.11	0.02	0.01	8.59	5.92	0.27	98.11	2.60	0.00	1.41	0.00	0.00	0.00	0.42	0.52	0.02	4.00	0.96	0.55	0.02	0.44
	215	56.65	0.00	26.50	0.00	0.05	0.05	0.03	0.00	8.79	5.90	0.23	98.15	2.58	0.00	1.42	0.00	0.00	0.00	0.43	0.52	0.01	4.01	0.96	0.54	0.01	0.45
	216	56.57	0.02	26.54	0.00	0.07	0.07	0.00	0.00	8.75	5.89	0.27	98.11	2.58	0.00	1.43	0.00	0.00	0.00	0.43	0.52	0.02	4.01	0.96	0.54	0.02	0.44
	217	57.39	0.01	26.03	0.01	0.07	0.08	0.00	0.00	8.62	6.06	0.27	98.44	2.61	0.00	1.39	0.00	0.00	0.00	0.42	0.53	0.02	4.00	0.97	0.55	0.02	0.43
	218	57.50	0.01	26.27	0.00	0.08	0.09	0.01	0.00	8.45	6.04	0.25	98.61	2.60	0.00	1.40	0.00	0.00	0.00	0.41	0.53	0.01	4.01	0.95	0.56	0.01	0.43
	219	57.67	0.00	26.06	0.00	0.06	0.06	0.00	0.00	8.35	6.06	0.26	98.45	2.61	0.00	1.39	0.00	0.00	0.00	0.41	0.53	0.02	4.01	0.95	0.56	0.02	0.43
	220	57.64	0.01	26.04	0.01	0.09	0.10	0.01	0.00	8.52	6.09	0.23	98.64	2.61	0.00	1.39	0.00	0.00	0.00	0.41	0.53	0.01	4.00	0.96	0.56	0.01	0.43
	221	56.91	0.00	26.13	0.01	0.11	0.12	0.01	0.00	8.57	5.97	0.25	97.96	2.60	0.00	1.41	0.00	0.00	0.00	0.42	0.53	0.01	4.00	0.96	0.55	0.02	0.44
	222	57.81	0.00	25.95	0.00	0.10	0.11	0.00	0.01	8.17	6.16	0.27	98.48	2.62	0.00	1.39	0.00	0.00	0.00	0.40	0.54	0.02	4.01	0.95	0.57	0.02	0.42
	223	56.77	0.01	26.43	0.00	0.08	0.09	0.00	0.00	8.82	5.93	0.25	98.28	2.58	0.00	1.42	0.00	0.00	0.00	0.43	0.52	0.01	4.00	0.97	0.54	0.02	0.44
	224	57.24	0.00	26.62	0.00	0.11	0.12	0.00	0.00	9.02	5.74	0.25	98.98	2.59	0.00	1.42	0.00	0.00	0.00	0.44	0.50	0.01	4.00	0.95	0.53	0.02	0.46
	225	58.07	0.01	26.08	0.00	0.11	0.12	0.00	0.00	8.41	6.05	0.28	99.01	2.62	0.00	1.39	0.00	0.00	0.00	0.41	0.53	0.02	4.00	0.95	0.56	0.02	0.43
	226	57.42	0.01	26.56	0.01	0.09	0.10	0.01	0.00	8.60	5.79	0.23	98.70	2.60	0.00	1.42	0.00	0.00	0.00	0.42	0.51	0.01	4.01	0.94	0.54	0.01	0.44
	227	57.55	0.00	26.54	0.00	0.06	0.06	0.00	0.00	8.74	5.77	0.25	98.90	2.60	0.00	1.41	0.00	0.00	0.00	0.42	0.51	0.01	4.01	0.94	0.54	0.02	0.45
	228	57.31	0.03	26.43	0.00	0.06	0.06	0.00	0.01	8.62	5.96	0.24	98.65	2.60	0.00	1.41	0.00	0.00	0.00	0.42	0.52	0.01	4.01	0.96	0.55	0.01	0.44
	229	57.93	0.00	25.98	0.00	0.08	0.09	0.02	0.00	8.35	6.11	0.21	98.69	2.62	0.00	1.38	0.00	0.00	0.00	0.40	0.54	0.01	4.00	0.95	0.56	0.01	0.42
	230	56.66	0.00	25.98	0.02	0.08	0.09	0.02	0.00	8.42	5.98	0.26	97.42	2.60	0.00	1.40	0.00	0.00	0.00	0.41	0.53	0.02	4.00	0.96	0.55	0.02	0.43
	231	56.34	0.00	26.31	0.00	0.09	0.10	0.01	0.02	8.43	6.11	0.27	97.58	2.58	0.00	1.42	0.00	0.00	0.00	0.41	0.54	0.02	4.01	0.97	0.56	0.02	0.43
	232	57.88	0.03	26.42	0.01	0.10	0.11	0.01	0.01	8.16	6.00	0.25	98.86	2.61	0.00	1.40	0.00	0.00	0.00	0.39	0.53	0.01	4.01	0.93	0.56	0.02	0.42
	233	57.84	0.00	26.21	0.00	0.10	0.11	0.00	0.00	8.14	5.98	0.26	98.52	2.62	0.00	1.40	0.00	0.00	0.00	0.39	0.52	0.01	4.01	0.93	0.56	0.02	0.42
	234	58.02	0.00	26.07	0.00	0.07	0.08	0.00	0.00	8.48	6.15	0.28	99.07	2.62	0.00	1.39	0.00	0.00	0.00	0.41	0.54	0.02	4.00	0.96	0.56	0.02	0.43
	235	57.63	0.00	25.94	0.02	0.09	0.10	0.00	0.00	8.41	6.07	0.26	98.41	2.61	0.00	1.39	0.00	0.00	0.00	0.41	0.53	0.01	4.00	0.96	0.56	0.02	0.43
Plagioclase	189	57.51	0.00	26.32	0.00	0.09	0.09	0.01	0.00	8.23	6.27	0.23	98.65	2.60	0.00	1.40	0.00	0.00	0.00	0.40	0.55	0.01	4.01	0.96	0.57	0.01	0.41
Pl4	190	54.37	0.00	26.32	0.00	0.09	0.10	0.02	0.00	8.41	6.09	0.21	95.52	2.55	0.00	1.46	0.00	0.00	0.00	0.42	0.55	0.01	4.01	0.99	0.56	0.01	0.43
	191	57.14	0.00	26.38	0.02	0.13	0.14	0.01	0.00	8.59	6.16	0.22	98.65	2.59	0.00	1.41	0.00	0.00	0.00	0.42	0.54	0.01	4.00	0.97	0.56	0.01	0.43
	192	56.80	0.00	26.31	0.00	0.06	0.07	0.00	0.00	8.55	6.11	0.25	98.08	2.59	0.00	1.41	0.00	0.00	0.00	0.42	0.54	0.01	4.00	0.97	0.56	0.01	0.43
	193	57.47	0.00	26.31	0.00	0.09	0.10	0.01	0.00	8.57	6.13	0.24	98.83	2.60	0.00	1.40	0.00	0.00	0.00	0.42	0.54	0.01	4.00	0.97	0.56	0.01	0.43
	194	56.69	0.01	26.43	0.01	0.09	0.10	0.00	0.00	8.70	6.16	0.29	98.37	2.58	0.00	1.42	0.00	0.00	0.00	0.42	0.54	0.02	4.00	0.98	0.55	0.02	0.43
	195	56.80	0.00	26.53	0.00	0.13	0.15	0.02	0.00	8.76	6.13	0.25	98.62	2.58	0.00	1.42	0.01	0.00	0.00	0.43	0.54	0.01	4.00	0.98	0.55	0.01	0.43
	196	54.24	0.00	26.42	0.00	0.10	0.11	0.00	0.01	8.82	6.02	0.28	95.88	2.54	0.00	1.46	0.00	0.00	0.00	0.44	0.55	0.02	4.00	1.01	0.54	0.02	0.44
	197	56.72	0.02	26.46	0.00	0.09	0.10	0.00	0.00	8.66	6.08	0.28	98.31	2.58	0.00	1.42	0.00	0.00	0.00	0.42	0.54	0.02	4.00	0.98	0.55	0.02	0.43
	198	56.43	0.01	26.56	0.00	0.12	0.14	0.00	0.00	8.90	5.99	0.24	98.25	2.57	0.00	1.43	0.00	0.00	0.00	0.43	0.53	0.01	4.00	0.98	0.54	0.01	0.44
	199	57.07	0.02	26.70	0.02	0.08	0.08	0.00	0.00	9.04	5.87	0.24	99.04	2.58	0.00	1.42	0.00	0.00	0.00	0.44	0.51	0.01	4.00	0.97	0.53	0.01	0.45
	200	58.01	0.00	26.37	0.00	0.12	0.13	0.01	0.00	8.50	6.14	0.27	99.42	2.61	0.00	1.40	0.00	0.00	0.00	0.41	0.54	0.02	4.00	0.96	0.56	0.02	0.43
	201	57.91	0.01	26.04	0.00	0.09	0.10	0.00	0.00	8.44	6.22	0.27	98.97	2.61	0.00	1.39	0.00	0.00	0.00	0.41	0.54	0.02	4.00	0.97	0.56	0.02	0.42
	202	57.63	0.00	26.07	0.00	0.08	0.09	0.00	0.00	8.41	6.30	0.29	98.78	2.61	0.00	1.39	0.00	0.00	0.00	0.41	0.55	0.02	4.00	0.98	0.57	0.02	0.42
	203	57.65	0.00	26.16	0.00	0.10	0.12	0.01	0.00	8.31	6.31	0.29	98.82	2.61	0.00	1.39	0.00	0.00	0.00	0.40	0.55	0.02	4.00	0.97	0.57	0.02	0.41
	204	55.56	0.00	26.17	0.00	0.10	0.11	0.00	0.00	8.34	6.31	0.30	96.79	2.57	0.00	1.43	0.00	0.00	0.00	0.41	0.57	0.02	4.00	1.00	0.57	0.02	0.41
	205	58.18	0.00	25.92	0.00	0.11	0.12	0.02	0.00	8.29	6.21	0.26	98.98	2.62	0.00	1.38	0.00	0.00	0.00	0.40	0.54	0.02	4.00	0.96	0.57	0.02	0.42
	206	58.12	0.01	26.00	0.01	0.12	0.13	0.00	0.00	8.21	6.31	0.28	99.06	2.62	0.00	1.38	0.00	0.00	0.00	0.40	0.55	0.02	4.00	0.96	0.57	0.02	0.41
	207	58.20	0.00	26.01	0.01	0.10	0.11	0.00	0.00	8.25	6.32	0.30	99.18	2.62	0.00	1.38	0.00	0.00	0.00	0.40	0.55	0.02	4.00	0.97	0.57	0.02	0.41

doi:10.6342/NTU202202659

Mineral	No.	SiO_2	TiO_2	Al_2O_3	Cr_2O_3	FeO	MnO	MgO	CaO	Na_2O	K_2O	Total	Si^{4+}	Ti^{4+}	Al^{3+}	Fe^{2+}	Mn^{2+}	Mg^{2+}	Ca^{2+}	Na^{+}	K^{+}	$Al_{(M)}$	$Al_{(T)}$	$I_{(total)}$	$M_{(total)}$	$T_{(total)}$	X_{Mg}	Ti-in-Bt thermometer (°C)
Biotite	1	37.36	2.42	15.42	0.08	17.59	0.26	11.65	0.11	0.08	8.76	93.72	5.72	0.28	2.78	2.25	0.03	2.66	0.02	0.02	1.71	0.50	2.28	1.75	5.72	8.00	0.54	659
	239	37.87	2.20	15.26	0.09	17.22	0.25	11.60	0.30	0.09	8.70	93.58	5.79	0.25	2.75	2.20	0.03	2.64	0.05	0.03	1.70	0.53	2.21	1.77	5.66	8.00	0.55	644
	240	37.58	2.00	15.40	0.04	16.91	0.21	11.34	0.21	0.16	8.62	92.48	5.80	0.23	2.80	2.18	0.03	2.61	0.03	0.05	1.70	0.60	2.20	1.78	5.65	8.00	0.54	629
	241	37.71	2.03	15.49	0.01	16.80	0.20	12.01	0.14	0.11	8.58	93.09	5.77	0.23	2.79	2.15	0.03	2.74	0.02	0.03	1.67	0.57	2.23	1.73	5.72	8.00	0.56	634
	242	38.10	2.04	15.49	0.04	17.00	0.22	12.23	0.11	0.06	8.84	94.12	5.78	0.23	2.77	2.16	0.03	2.76	0.02	0.02	1.71	0.54	2.22	1.74	5.72	8.00	0.56	634
	243	37.70	2.07	15.42	0.02	16.93	0.23	11.89	0.12	0.13	8.45	92.93	5.78	0.24	2.79	2.17	0.03	2.72	0.02	0.04	1.65	0.57	2.22	1.71	5.72	8.00	0.56	637
	245	38.52	2.04	15.96	0.04	16.05	0.26	12.05	0.11	0.10	8.54	93.66	5.82	0.23	2.84	2.03	0.03	2.71	0.02	0.03	1.65	0.66	2.18	1.69	5.67	8.00	0.57	636
	246	37.48	2.41	15.29	0.06	17.95	0.23	11.94	0.16	0.12	8.72	94.36	5.70	0.28	2.74	2.28	0.03	2.71	0.03	0.04	1.69	0.45	2.30	1.75	5.75	8.00	0.54	658
	247	37.68	2.17	15.83	0.13	17.38	0.28	11.63	0.11	0.07	9.25	94.51	5.72	0.25	2.83	2.21	0.04	2.63	0.02	0.02	1.79	0.55	2.28	1.83	5.67	8.00	0.54	640
	2	38.14	2.32	14.87	0.07	16.92	0.29	12.25	0.24	0.13	8.58	93.79	5.80	0.27	2.67	2.15	0.04	2.78	0.04	0.04	1.66	0.47	2.20	1.74	5.70	8.00	0.56	657
	248	36.07	2.09	14.98	0.14	18.25	0.27	11.44	0.17	0.10	8.77	92.29	5.65	0.25	2.77	2.39	0.04	2.67	0.03	0.03	1.75	0.42	2.35	1.81	5.77	8.00	0.53	635
	250	36.82	1.91	15.60	0.08	16.16	0.25	11.80	0.15	0.07	9.00	91.83	5.73	0.22	2.86	2.10	0.03	2.74	0.02	0.02	1.79	0.59	2.27	1.83	5.68	8.00	0.57	628
	252	38.37	1.64	16.25	0.06	15.43	0.20	11.41	0.21	0.10	8.45	92.13	5.87	0.19	2.93	1.97	0.03	2.60	0.03	0.03	1.65	0.80	2.13	1.71	5.59	8.00	0.57	598
	254	37.88	2.02	15.40	0.02	16.70	0.28	11.99	0.13	0.08	8.65	93.14	5.79	0.23	2.78	2.14	0.04	2.73	0.02	0.02	1.69	0.57	2.21	1.73	5.71	8.00	0.56	634
	255	37.72	2.13	15.29	0.05	15.68	0.24	12.06	0.17	0.07	8.48	91.90	5.81	0.25	2.78	2.02	0.03	2.77	0.03	0.02	1.67	0.59	2.19	1.72	5.67	8.00	0.58	649
	256	37.22	1.94	15.07	0.04	16.82	0.26	12.06	0.13	0.10	8.87	92.51	5.76	0.23	2.75	2.18	0.03	2.78	0.02	0.03	1.75	0.51	2.24	1.80	5.72	8.00	0.56	628
	3	37.51	2.22	15.14	0.11	17.34	0.26	11.62	0.09	0.09	9.37	93.75	5.75	0.26	2.74	2.22	0.03	2.66	0.01	0.03	1.83	0.49	2.25	1.88	5.66	8.00	0.54	645
	209	37.32	2.13	14.57	0.01	17.65	0.23	11.96	0.17	0.14	8.01	92.20	5.79	0.25	2.66	2.29	0.03	2.77	0.03	0.04	1.58	0.45	2.21	1.66	5.79	8.00	0.55	641

doi:10.6342/NTU202202659

8.5.4 18TP01 Amphibolite

Mineral	No.	SiO_2	TiO_2	Al_2O_3	Cr_2O_3	FeO	MnO	MgO	CaO	Na_2O	K_2O	Total	T		C							B					A			T_{total}	C_{total}	B_{total}	A_{total}
													Si^{4+}	Al^{3+}	Al^{3+}	Ti^{4+}	Fe^{3+}	Cr^{3+}	Mn^{2+}	Mg^{2+}	Fe^{2+}	Mn^{2+}	Mg^{2+}	Fe^{2+}	Ca^{2+}	Na^{+}	Ca^{2+}	Na^{+}	K^{+}				
Hornblende	8	45.51	0.53	9.89	0.09	16.29	0.37	11.19	11.91	1.08	0.96	97.82	6.71	1.30	0.42	0.06	0.44	0.01	0.03	2.44	1.56	0.01	0.00	0.02	1.89	0.08	0.00	0.23	0.18	8.00	4.98	1.99	0.41
Hb1	9	45.04	0.70	10.50	0.09	16.29	0.35	10.99	11.92	1.18	1.08	98.13	6.64	1.36	0.46	0.08	0.43	0.01	0.03	2.40	1.57	0.01	0.01	0.01	1.89	0.08	0.00	0.26	0.20	8.00	4.99	1.99	0.46
	10	44.53	0.76	10.64	0.05	16.24	0.35	10.91	11.91	1.20	1.07	97.65	6.60	1.41	0.45	0.09	0.45	0.01	0.03	2.40	1.56	0.01	0.01	0.01	1.89	0.07	0.00	0.27	0.20	8.01	4.98	2.00	0.48
	11	44.78	0.74	10.49	0.15	16.31	0.38	10.86	11.85	1.22	1.07	97.83	6.62	1.38	0.45	0.09	0.44	0.02	0.04	2.38	1.58	0.01	0.00	0.01	1.88	0.09	0.00	0.26	0.20	8.00	4.98	1.99	0.47
	12	44.68	0.73	10.31	0.12	16.02	0.36	10.96	11.79	1.16	1.08	97.21	6.63	1.37	0.43	0.09	0.44	0.01	0.03	2.41	1.55	0.01	0.00	0.01	1.88	0.09	0.00	0.24	0.21	8.00	4.97	2.00	0.45
	13	44.54	0.80	10.05	0.15	16.30	0.34	10.81	11.85	1.15	1.11	97.09	6.64	1.37	0.40	0.10	0.43	0.02	0.03	2.39	1.61	0.01	0.00	0.01	1.89	0.09	0.00	0.24	0.21	8.00	4.97	2.00	0.46
	14	44.69	0.73	10.22	0.13	16.26	0.40	10.91	11.92	1.20	1.15	97.59	6.63	1.37	0.41	0.09	0.45	0.01	0.04	2.40	1.58	0.01	0.00	0.01	1.90	0.09	0.00	0.26	0.22	8.00	4.98	2.01	0.47
	15	44.64	0.69	10.20	0.07	16.29	0.34	10.94	11.87	1.27	1.10	97.41	6.63	1.38	0.41	0.08	0.45	0.01	0.03	2.41	1.58	0.01	0.00	0.01	1.89	0.10	0.00	0.27	0.21	8.00	4.97	2.00	0.48
	16	44.64	0.71	10.35	0.08	15.74	0.37	10.93	11.91	1.12	1.09	96.94	6.64	1.37	0.44	0.09	0.43	0.01	0.04	2.42	1.55	0.01	0.00	0.00	1.90	0.10	0.00	0.22	0.21	8.01	4.97	2.01	0.43
	17	44.29	0.70	10.27	0.07	16.13	0.36	11.02	11.94	1.12	1.10	97.00	6.60	1.41	0.39	0.09	0.47	0.01	0.03	2.44	1.54	0.01	0.00	0.01	1.91	0.07	0.00	0.26	0.21	8.01	4.97	2.00	0.47
	18	44.96	0.71	10.61	0.08	16.30	0.38	10.80	11.94	1.15	1.12	98.05	6.63	1.37	0.48	0.08	0.43	0.01	0.04	2.37	1.58	0.01	0.00	0.01	1.89	0.09	0.00	0.24	0.21	8.00	4.99	1.99	0.45
	19	44.88	0.78	10.62	0.05	16.44	0.38	11.01	12.01	1.13	1.10	98.38	6.61	1.39	0.45	0.09	0.45	0.01	0.04	2.40	1.55	0.01	0.02	0.01	1.90	0.05	0.00	0.27	0.21	8.00	4.99	1.99	0.48
	20	44.28	0.73	10.41	0.07	16.45	0.38	10.92	11.83	1.12	1.06	97.24	6.59	1.42	0.40	0.10	0.49	0.01	0.04	2.40	1.54	0.01	0.02	0.02	1.89	0.06	0.00	0.27	0.20	8.01	4.97	1.99	0.47
	21	43.87	0.63	10.49	0.08	16.21	0.37	11.05	11.74	1.16	1.10	96.68	6.56	1.46	0.39	0.09	0.50	0.01	0.03	2.44	1.50	0.01	0.02	0.02	1.88	0.06	0.00	0.28	0.21	8.01	4.96	2.00	0.49
	22	44.84	0.66	10.48	0.08	16.30	0.36	10.98	12.02	1.11	1.10	97.93	6.62	1.38	0.44	0.08	0.44	0.01	0.04	2.41	1.57	0.01	0.00	0.01	1.91	0.07	0.00	0.25	0.21	8.00	4.98	2.00	0.46
	23	44.85	0.65	10.33	0.08	16.31	0.39	10.95	12.07	1.12	1.08	97.82	6.63	1.37	0.43	0.08	0.45	0.01	0.04	2.41	1.57	0.01	0.00	0.01	1.92	0.07	0.00	0.25	0.20	8.00	4.98	2.00	0.46
	24	44.39	0.64	10.15	0.11	16.09	0.35	10.93	11.96	1.09	1.06	96.75	6.62	1.39	0.40	0.08	0.44	0.01	0.03	2.42	1.57	0.01	0.00	0.01	1.91	0.08	0.00	0.24	0.20	8.01	4.97	2.01	0.44
	25	44.38	0.75	10.52	0.13	16.12	0.33	10.71	11.89	1.12	1.15	97.08	6.61	1.39	0.45	0.09	0.42	0.02	0.03	2.37	1.60	0.01	0.00	0.01	1.90	0.09	0.00	0.23	0.22	8.00	4.98	2.00	0.45
	26	45.41	0.58	9.32	0.20	16.14	0.41	11.12	11.63	0.92	0.79	96.51	6.76	1.26	0.38	0.08	0.46	0.02	0.04	2.44	1.55	0.01	0.00	0.03	1.86	0.09	0.00	0.18	0.15	8.01	4.96	1.99	0.33
	27	44.07	0.78	10.97	0.08	16.79	0.37	10.56	11.73	1.20	1.23	97.78	6.55	1.46	0.46	0.09	0.47	0.01	0.04	2.32	1.59	0.01	0.03	0.02	1.87	0.07	0.00	0.27	0.24	8.00	4.98	1.99	0.51
	28	44.49	0.65	10.60	0.10	16.25	0.35	10.77	12.12	0.93	1.08	97.33	6.61	1.40	0.46	0.08	0.43	0.01	0.03	2.38	1.59	0.01	0.00	0.01	1.93	0.05	0.00	0.22	0.21	8.01	4.98	2.00	0.43
	29	44.40	0.76	10.28	0.11	16.34	0.42	10.78	11.94	1.19	1.20	97.43	6.60	1.40	0.40	0.09	0.46	0.01	0.04	2.38	1.58	0.01	0.00	0.01	1.90	0.09	0.00	0.26	0.23	8.00	4.98	2.01	0.49
	30	44.08	0.76	10.84	0.08	16.38	0.39	10.72	11.95	1.22	1.19	97.61	6.55	1.46	0.44	0.09	0.46	0.01	0.04	2.37	1.57	0.01	0.00	0.01	1.90	0.07	0.00	0.28	0.23	8.01	4.98	2.00	0.51
	31	44.13	0.74	10.88	0.30	16.31	0.31	10.57	11.91	1.24	1.19	97.59	6.56	1.44	0.47	0.08	0.40	0.03	0.03	2.33	1.64	0.01	0.00	0.01	1.90	0.09	0.00	0.27	0.23	8.00	4.99	2.00	0.50
	32	44.14	0.65	10.86	0.10	15.85	0.39	10.60	11.95	1.20	1.18	96.92	6.58	1.43	0.48	0.08	0.43	0.01	0.04	2.36	1.58	0.01	0.00	0.00	1.91	0.11	0.00	0.24	0.23	8.01	4.97	2.03	0.46
	33	44.02	0.71	10.95	0.08	15.86	0.35	10.70	12.00	1.27	1.18	97.11	6.56	1.45	0.47	0.09	0.42	0.01	0.04	2.37	1.57	0.01	0.00	0.00	1.92	0.10	0.00	0.27	0.23	8.01	4.97	2.02	0.49
	34	44.67	0.72	10.91	0.10	15.81	0.34	10.78	11.82	1.25	1.12	97.52	6.61	1.39	0.51	0.08	0.40	0.01	0.03	2.38	1.56	0.01	0.00	0.00	1.88	0.11	0.00	0.24	0.21	8.00	4.98	2.00	0.46
	35	44.63	0.67	10.92	0.06	16.02	0.37	10.78	11.87	1.25	1.14	97.70	6.60	1.40	0.50	0.08	0.43	0.01	0.04	2.37	1.56	0.01	0.00	0.00	1.88	0.10	0.00	0.25	0.22	8.00	4.98	2.00	0.47
	36	44.34	0.67	11.01	0.07	15.94	0.38	10.70	11.76	1.20	1.12	97.19	6.59	1.42	0.51	0.08	0.44	0.01	0.04	2.36	1.54	0.01	0.00	0.01	1.87	0.10	0.00	0.24	0.21	8.01	4.98	1.99	0.45
	37	47.86	0.36	6.90	0.08	15.58	0.35	11.74	11.32	0.74	0.56	95.50	7.10	0.91	0.29	0.05	0.41	0.01	0.03	2.58	1.57	0.02	0.00	0.02	1.81	0.18	0.00	0.03	0.11	8.01	4.94	2.03	0.14
	38	44.53	0.66	10.83	0.08	16.35	0.37	10.83	11.62	1.22	1.19	97.66	6.60	1.41	0.48	0.08	0.46	0.01	0.04	2.37	1.54	0.01	0.02	0.02	1.85	0.09	0.00	0.25	0.23	8.00	4.98	1.99	0.48
	39	44.33	0.68	10.77	0.10	16.29	0.35	10.78	11.58	1.24	1.12	97.23	6.59	1.42	0.47	0.09	0.46	0.01	0.03	2.37	1.55	0.01	0.02	0.02	1.85	0.10	0.00	0.26	0.21	8.01	4.98	1.99	0.47
	40	44.06	0.71	10.90	0.05	16.38	0.37	10.96	11.72	1.25	1.13	97.51	6.54	1.47	0.44	0.09	0.49	0.01	0.03	2.41	1.51	0.01	0.03	0.02	1.87	0.06	0.00	0.30	0.22	8.01	4.98	1.99	0.51

Mineral	No.	SiO_2	TiO_2	Al_2O_3	Cr_2O_3	FeO	MnO	MgO	CaO	Na_2O	K_2O	Total	T		C							B					A						
													Si^{4+}	Al^{3+}	Al^{3+}	Ti^{4+}	Fe^{3+}	Cr^{3+}	Mn^{2+}	Mg^{2+}	Fe^{2+}	Mn^{2+}	Mg^{2+}	Fe^{2+}	Ca^{2+}	Na^{+}	Ca^{2+}	Na^{+}	K^{+}	T_{total}	C_{total}	B_{total}	A_{total}
Hornblende	41	44.46	0.72	10.75	0.09	16.13	0.35	10.88	11.76	1.25	1.12	97.51	6.59	1.41	0.47	0.09	0.44	0.01	0.03	2.39	1.55	0.01	0.01	0.01	1.87	0.09	0.00	0.27	0.21	8.00	4.98	1.99	0.48
Hb1	42	44.28	0.70	10.90	0.10	16.01	0.35	10.84	11.85	1.17	1.14	97.34	6.58	1.43	0.48	0.09	0.44	0.01	0.03	2.39	1.54	0.01	0.01	0.01	1.89	0.08	0.00	0.26	0.22	8.01	4.98	1.99	0.47
	43	44.52	0.72	10.78	0.10	15.94	0.35	10.90	11.97	1.25	1.15	97.67	6.59	1.41	0.47	0.08	0.42	0.01	0.03	2.40	1.56	0.01	0.00	0.00	1.90	0.09	0.00	0.27	0.22	8.00	4.98	2.00	0.48
	44	44.22	0.69	11.01	0.10	16.38	0.36	10.92	11.83	1.22	1.20	97.93	6.55	1.46	0.46	0.08	0.47	0.01	0.03	2.39	1.54	0.01	0.03	0.02	1.88	0.06	0.00	0.29	0.23	8.00	4.99	1.99	0.52
	45	44.41	0.73	10.81	0.06	16.21	0.35	10.87	11.85	1.22	1.18	97.69	6.58	1.42	0.46	0.09	0.45	0.01	0.03	2.39	1.55	0.01	0.01	0.01	1.88	0.08	0.00	0.27	0.22	8.00	4.98	2.00	0.49
	46	44.53	0.76	10.95	0.07	16.28	0.35	10.85	11.87	1.24	1.14	98.04	6.58	1.42	0.48	0.09	0.44	0.01	0.03	2.38	1.56	0.01	0.01	0.01	1.88	0.08	0.00	0.28	0.22	8.00	4.99	1.99	0.49
	47	44.35	0.69	10.98	0.07	16.20	0.35	10.83	11.71	1.20	1.15	97.53	6.57	1.43	0.49	0.08	0.45	0.01	0.03	2.38	1.53	0.01	0.02	0.01	1.86	0.08	0.00	0.26	0.22	8.01	4.98	1.99	0.48
	48	44.72	0.74	11.01	0.03	16.23	0.32	10.82	11.62	1.21	1.21	97.90	6.61	1.40	0.52	0.08	0.43	0.00	0.03	2.37	1.55	0.01	0.03	0.01	1.84	0.10	0.00	0.24	0.23	8.00	4.99	1.99	0.47
	49	45.21	0.75	10.92	0.05	16.60	0.34	11.03	11.85	1.25	1.21	99.22	6.61	1.38	0.50	0.08	0.44	0.01	0.03	2.39	1.56	0.01	0.04	0.02	1.86	0.07	0.00	0.28	0.23	7.99	5.00	1.99	0.51
	50	44.26	0.71	10.77	0.06	16.02	0.34	10.91	11.90	1.25	1.21	97.43	6.57	1.43	0.45	0.08	0.44	0.01	0.03	2.41	1.55	0.01	0.00	0.00	1.90	0.09	0.00	0.27	0.23	8.00	4.98	2.00	0.50
	51	44.59	0.72	11.05	0.06	16.24	0.28	10.91	11.89	1.24	1.24	98.23	6.58	1.42	0.50	0.08	0.42	0.01	0.03	2.39	1.57	0.01	0.02	0.01	1.88	0.08	0.00	0.28	0.23	8.00	4.99	2.00	0.51
	52	44.08	0.76	10.93	0.05	16.21	0.40	10.91	11.70	1.25	1.20	97.48	6.55	1.46	0.45	0.10	0.49	0.01	0.04	2.40	1.50	0.01	0.02	0.02	1.86	0.08	0.00	0.28	0.23	8.01	4.98	1.99	0.51
	53	44.66	0.74	10.92	0.05	16.14	0.34	10.82	11.67	1.22	1.15	97.68	6.61	1.40	0.51	0.09	0.43	0.01	0.03	2.37	1.54	0.01	0.02	0.01	1.85	0.10	0.00	0.25	0.22	8.00	4.98	1.99	0.47
	54	44.53	0.72	10.98	0.04	16.02	0.34	10.82	12.03	1.26	1.16	97.88	6.58	1.42	0.49	0.08	0.41	0.01	0.03	2.38	1.57	0.01	0.00	0.00	1.91	0.09	0.00	0.27	0.22	8.00	4.98	2.01	0.49
	55	44.72	0.79	10.92	0.06	16.08	0.36	10.89	11.98	1.21	1.13	98.14	6.59	1.41	0.49	0.09	0.42	0.01	0.04	2.39	1.55	0.01	0.01	0.00	1.90	0.08	0.00	0.27	0.21	8.00	4.99	2.00	0.48
	56	44.63	0.73	10.84	0.02	16.10	0.34	10.85	11.83	1.28	1.08	97.68	6.60	1.40	0.49	0.09	0.43	0.00	0.03	2.39	1.55	0.01	0.01	0.00	1.88	0.10	0.00	0.27	0.21	8.00	4.98	2.00	0.47
	57	44.31	0.75	11.00	0.04	16.35	0.34	10.79	11.84	1.23	1.12	97.75	6.56	1.44	0.48	0.09	0.45	0.00	0.03	2.37	1.56	0.01	0.02	0.01	1.88	0.07	0.00	0.28	0.21	8.01	4.98	1.99	0.49
	58	44.53	0.76	10.86	0.04	16.28	0.34	10.91	11.90	1.24	1.05	97.91	6.58	1.42	0.47	0.09	0.44	0.01	0.03	2.39	1.55	0.01	0.02	0.01	1.89	0.07	0.00	0.29	0.20	8.01	4.98	2.00	0.49
	59	44.62	0.74	10.83	0.02	16.35	0.35	10.81	11.77	1.19	1.06	97.74	6.60	1.41	0.48	0.09	0.45	0.00	0.03	2.37	1.55	0.01	0.02	0.01	1.87	0.08	0.00	0.26	0.20	8.01	4.98	1.99	0.46
	60	44.02	0.74	10.77	0.03	15.83	0.35	10.78	11.95	1.16	1.07	96.68	6.57	1.44	0.45	0.10	0.44	0.00	0.03	2.40	1.55	0.01	0.00	0.00	1.91	0.08	0.00	0.25	0.21	8.01	4.97	2.01	0.46
	61	44.49	0.72	10.79	0.04	15.88	0.35	10.70	11.86	1.21	1.07	97.08	6.61	1.40	0.49	0.09	0.42	0.00	0.03	2.37	1.57	0.01	0.00	0.00	1.89	0.11	0.00	0.24	0.20	8.01	4.97	2.01	0.44
	62	44.38	0.71	10.93	0.02	16.18	0.39	10.67	11.84	1.19	1.07	97.37	6.59	1.42	0.49	0.09	0.45	0.00	0.04	2.36	1.55	0.01	0.00	0.00	1.89	0.09	0.00	0.25	0.20	8.01	4.98	1.99	0.46
	63	44.14	0.71	10.88	0.00	16.31	0.34	10.65	12.01	1.18	1.07	97.30	6.56	1.45	0.46	0.09	0.45	0.00	0.03	2.36	1.58	0.01	0.00	0.00	1.92	0.07	0.00	0.27	0.20	8.01	4.98	2.00	0.47
Hornblende	64	44.62	0.70	10.31	0.00	16.22	0.35	10.74	11.91	1.12	1.02	96.98	6.64	1.37	0.44	0.09	0.44	0.00	0.03	2.38	1.59	0.01	0.00	0.00	1.90	0.09	0.00	0.23	0.19	8.01	4.97	2.00	0.43
Hb2	65	44.72	0.74	10.09	0.00	15.96	0.41	10.73	11.91	1.11	0.99	96.66	6.66	1.35	0.43	0.09	0.44	0.00	0.04	2.38	1.57	0.01	0.00	0.00	1.91	0.11	0.00	0.21	0.19	8.01	4.96	2.03	0.40
	66	44.09	0.70	10.89	0.16	16.20	0.31	10.85	11.81	1.19	1.04	97.23	6.56	1.45	0.46	0.09	0.44	0.02	0.03	2.39	1.56	0.01	0.02	0.02	1.88	0.06	0.00	0.28	0.20	8.01	4.98	1.99	0.48
	67	44.33	0.77	10.96	0.11	16.03	0.32	10.77	11.82	1.26	1.03	97.38	6.58	1.43	0.49	0.09	0.42	0.01	0.03	2.37	1.56	0.01	0.01	0.01	1.88	0.09	0.00	0.27	0.20	8.01	4.98	1.99	0.47
	68	44.41	0.76	10.85	0.01	15.94	0.32	10.78	11.88	1.20	1.03	97.18	6.59	1.41	0.49	0.09	0.42	0.00	0.03	2.38	1.56	0.01	0.00	0.00	1.89	0.09	0.00	0.26	0.20	8.01	4.97	2.00	0.45
	69	44.36	0.71	10.89	0.10	16.12	0.32	10.84	11.86	1.23	1.03	97.45	6.58	1.43	0.47	0.09	0.43	0.01	0.03	2.39	1.56	0.01	0.01	0.01	1.89	0.08	0.00	0.28	0.20	8.01	4.98	1.99	0.47
	70	44.16	0.72	10.78	0.11	16.25	0.39	10.87	11.76	1.19	1.09	97.31	6.56	1.44	0.44	0.09	0.47	0.01	0.04	2.39	1.53	0.01	0.02	0.02	1.88	0.07	0.00	0.27	0.21	8.01	4.98	1.99	0.48
	71	44.45	0.69	10.87	0.10	16.26	0.36	10.86	11.71	1.27	1.00	97.56	6.58	1.42	0.47	0.09	0.46	0.01	0.03	2.38	1.54	0.01	0.02	0.02	1.86	0.08	0.00	0.28	0.19	8.01	4.98	1.99	0.47
	72	44.28	0.73	10.69	0.08	16.12	0.33	10.66	11.95	1.19	1.02	97.05	6.59	1.42	0.46	0.09	0.42	0.01	0.03	2.37	1.60	0.01	0.00	0.00	1.91	0.09	0.00	0.26	0.20	8.01	4.97	2.01	0.45
	73	44.19	0.69	10.73	0.11	16.36	0.36	10.71	11.80	1.25	1.07	97.26	6.57	1.43	0.45	0.09	0.46	0.01	0.04	2.36	1.57	0.01	0.01	0.01	1.88	0.08	0.00	0.28	0.20	8.01	4.98	2.00	0.48
	74	43.95	0.70	10.48	0.09	16.10	0.37	10.94	11.75	1.28	1.04	96.69	6.57	1.45	0.40	0.10	0.48	0.01	0.04	2.42	1.53	0.01	0.01	0.01	1.88	0.08	0.00	0.29	0.20	8.01	4.97	2.00	0.49
	75	44.28	0.71	10.87	0.14	16.08	0.35	10.84	11.70	1.24	1.08	97.28	6.58	1.43	0.47	0.09	0.45	0.02	0.03	2.38	1.54	0.01	0.01	0.02	1.86	0.09	0.00	0.27	0.21	8.01	4.98	1.99	0.47
	76	43.97	0.74	10.85	0.18	16.12	0.30	10.75	11.84	1.19	1.13	97.07	6.56	1.45	0.46	0.09	0.42	0.02	0.03	2.38	1.58	0.01	0.01	0.01	1.89	0.07	0.00	0.27	0.22	8.01	4.98	2.00	0.49
	77	44.33	0.73	10.84	0.21	16.17	0.33	10.92	11.91	1.20	1.05	97.69	6.57	1.44	0.46	0.09	0.43	0.02	0.03	2.39	1.56	0.01	0.01	0.02	1.89	0.06	0.00	0.28	0.20	8.01	4.99	1.99	0.49
	78	44.22	0.71	10.86	0.23	16.16	0.36	10.92	11.81	1.20	1.05	97.52	6.56	1.44	0.46	0.09	0.44	0.03	0.03	2.39	1.54	0.01	0.02	0.02	1.88	0.06	0.00	0.28	0.20	8.01	4.98	1.99	0.49

doi:10.6342/NTU202202659

Mineral	No.	SiO_2	TiO_2	Al_2O_3	Cr_2O_3	FeO	MnO	MgO	CaO	Na_2O	K_2O	Total	T		C							B					A			T_{total}	C_{total}	B_{total}	A_{total}
													Si^{4+}	Al^{3+}	Al^{3+}	Ti^{4+}	Fe^{3+}	Cr^{3+}	Mn^{2+}	Mg^{2+}	Fe^{2+}	Mn^{2+}	Mg^{2+}	Fe^{2+}	Ca^{2+}	Na^{+}	Ca^{2+}	Na^{+}	K^{+}				
Hornblende	108	44.13	0.65	10.30	0.00	16.51	0.41	10.44	11.84	1.13	0.96	96.37	6.61	1.41	0.41	0.09	0.48	0.00	0.04	2.33	1.60	0.01	0.00	0.00	1.90	0.09	0.00	0.23	0.19	8.02	4.96	2.01	0.42
Hb3	109	43.96	0.64	10.26	0.01	16.25	0.38	10.53	11.78	1.12	0.93	95.85	6.61	1.41	0.41	0.09	0.48	0.00	0.04	2.36	1.58	0.01	0.00	0.00	1.90	0.10	0.00	0.23	0.18	8.02	4.95	2.01	0.41
	110	44.02	0.73	10.48	0.05	16.59	0.34	10.57	11.75	1.16	1.04	96.72	6.58	1.43	0.42	0.10	0.47	0.01	0.03	2.35	1.60	0.01	0.01	0.01	1.89	0.08	0.00	0.26	0.20	8.01	4.96	2.00	0.46
	111	43.23	0.74	10.79	0.04	16.71	0.39	10.50	11.79	1.17	1.08	96.42	6.50	1.52	0.39	0.11	0.52	0.00	0.04	2.34	1.57	0.01	0.02	0.02	1.90	0.05	0.00	0.29	0.21	8.02	4.96	2.00	0.50
	112	43.60	0.74	10.73	0.03	16.51	0.33	10.36	11.77	1.20	1.07	96.33	6.55	1.46	0.43	0.10	0.46	0.00	0.03	2.32	1.61	0.01	0.00	0.00	1.90	0.09	0.00	0.26	0.21	8.01	4.96	2.00	0.47
	113	43.26	0.73	10.82	0.06	16.72	0.34	10.28	11.82	1.15	1.09	96.26	6.52	1.50	0.42	0.10	0.48	0.01	0.03	2.30	1.62	0.01	0.01	0.01	1.91	0.07	0.00	0.27	0.21	8.02	4.96	2.00	0.48
	114	43.15	0.74	10.83	0.03	16.87	0.40	10.39	11.80	1.19	1.09	96.50	6.49	1.53	0.39	0.11	0.52	0.00	0.04	2.32	1.58	0.01	0.02	0.01	1.90	0.05	0.00	0.29	0.21	8.02	4.96	2.00	0.51
	115	43.50	0.74	10.76	0.03	17.06	0.39	10.31	11.78	1.17	1.08	96.83	6.52	1.49	0.41	0.10	0.51	0.00	0.04	2.29	1.61	0.01	0.02	0.01	1.89	0.06	0.00	0.28	0.21	8.02	4.97	2.00	0.49
	116	43.29	0.72	10.74	0.03	16.55	0.38	10.43	11.70	1.16	1.07	96.07	6.52	1.50	0.41	0.10	0.50	0.00	0.04	2.33	1.57	0.01	0.01	0.01	1.89	0.07	0.00	0.27	0.21	8.02	4.96	2.00	0.47
	117	43.77	0.70	10.76	0.04	16.95	0.41	10.41	11.67	1.18	1.06	96.93	6.55	1.47	0.43	0.10	0.51	0.00	0.04	2.30	1.58	0.01	0.02	0.02	1.87	0.07	0.00	0.27	0.20	8.02	4.97	1.99	0.48
	118	43.34	0.67	10.27	0.01	16.56	0.36	10.48	11.84	1.14	1.06	95.73	6.55	1.47	0.36	0.10	0.50	0.00	0.03	2.36	1.60	0.01	0.00	0.00	1.92	0.07	0.00	0.26	0.21	8.02	4.95	2.01	0.47
	119	43.54	0.75	10.15	0.00	16.63	0.37	10.53	11.78	1.14	0.98	95.87	6.57	1.45	0.35	0.11	0.51	0.00	0.04	2.36	1.59	0.01	0.00	0.01	1.90	0.07	0.00	0.26	0.19	8.02	4.95	2.00	0.45
	120	43.77	0.73	10.62	0.03	16.72	0.37	10.44	11.59	1.11	1.00	96.37	6.57	1.45	0.43	0.10	0.50	0.00	0.04	2.32	1.58	0.01	0.02	0.02	1.87	0.07	0.00	0.25	0.19	8.02	4.96	1.99	0.44
	121	43.62	0.77	10.74	0.04	16.82	0.38	10.40	11.62	1.10	1.04	96.51	6.55	1.47	0.43	0.11	0.51	0.00	0.04	2.31	1.58	0.01	0.03	0.02	1.87	0.06	0.00	0.26	0.20	8.02	4.96	1.99	0.46
	122	44.01	0.77	10.88	0.01	16.62	0.38	10.26	11.68	1.16	1.12	96.89	6.58	1.43	0.48	0.10	0.46	0.00	0.04	2.28	1.61	0.01	0.01	0.00	1.87	0.10	0.00	0.24	0.21	8.01	4.97	1.99	0.45
	123	43.83	0.79	10.76	0.06	16.87	0.42	10.29	11.67	1.06	1.04	96.79	6.56	1.45	0.45	0.11	0.50	0.01	0.04	2.28	1.59	0.01	0.02	0.02	1.87	0.07	0.00	0.24	0.20	8.01	4.97	1.99	0.44
	124	43.79	0.75	10.67	0.04	16.46	0.36	10.37	11.95	1.02	1.08	96.46	6.57	1.45	0.44	0.10	0.45	0.00	0.03	2.32	1.62	0.01	0.00	0.00	1.92	0.07	0.00	0.23	0.21	8.01	4.96	2.00	0.44
	125	44.06	0.74	10.34	0.03	16.40	0.36	10.55	11.93	1.09	0.98	96.50	6.60	1.42	0.41	0.10	0.46	0.00	0.03	2.35	1.60	0.01	0.00	0.00	1.92	0.07	0.00	0.24	0.19	8.01	4.96	2.01	0.43
	126	44.32	0.70	10.09	0.02	16.08	0.38	10.78	11.83	1.02	0.97	96.18	6.64	1.38	0.40	0.10	0.46	0.00	0.04	2.40	1.56	0.01	0.00	0.01	1.90	0.08	0.00	0.21	0.19	8.02	4.96	2.00	0.40
	127	44.34	0.70	10.23	0.03	16.33	0.39	10.66	11.89	0.98	0.95	96.50	6.63	1.39	0.41	0.10	0.47	0.00	0.04	2.37	1.58	0.01	0.00	0.01	1.91	0.07	0.00	0.22	0.18	8.02	4.96	2.00	0.40
	128	43.61	0.68	10.50	0.01	16.60	0.35	10.22	11.86	1.06	1.01	95.88	6.57	1.45	0.42	0.10	0.47	0.00	0.03	2.30	1.64	0.01	0.00	0.00	1.92	0.08	0.00	0.23	0.20	8.02	4.95	2.01	0.42
	129	44.12	0.63	10.10	0.00	16.56	0.40	10.64	11.89	1.01	0.91	96.24	6.61	1.41	0.38	0.09	0.50	0.00	0.04	2.37	1.58	0.01	0.00	0.01	1.91	0.06	0.00	0.23	0.18	8.02	4.95	2.00	0.41
	130	44.03	0.72	10.59	0.02	16.55	0.39	10.24	11.70	1.10	0.99	96.33	6.60	1.41	0.46	0.10	0.47	0.00	0.04	2.29	1.61	0.01	0.00	0.00	1.88	0.10	0.00	0.22	0.19	8.02	4.96	2.00	0.41
	131	44.04	0.65	10.42	0.03	16.62	0.36	10.37	11.78	0.93	0.90	96.10	6.61	1.41	0.44	0.10	0.47	0.00	0.03	2.31	1.61	0.01	0.01	0.01	1.90	0.07	0.00	0.21	0.18	8.02	4.96	1.99	0.38
	132	44.14	0.60	10.28	0.00	16.40	0.37	10.38	11.62	0.89	0.95	95.63	6.64	1.38	0.44	0.09	0.47	0.00	0.03	2.32	1.59	0.01	0.00	0.01	1.88	0.09	0.00	0.17	0.19	8.02	4.95	1.99	0.35
Hornblende	133	44.07	0.70	10.40	0.00	16.70	0.38	10.47	11.54	1.03	0.98	96.26	6.61	1.41	0.43	0.10	0.50	0.00	0.03	2.32	1.57	0.01	0.02	0.02	1.86	0.08	0.00	0.22	0.19	8.02	4.96	1.99	0.41
Hb4	134	43.86	0.80	10.66	0.04	16.62	0.40	10.35	11.88	1.08	1.07	96.77	6.57	1.45	0.43	0.11	0.47	0.01	0.04	2.30	1.61	0.01	0.00	0.01	1.91	0.07	0.00	0.24	0.21	8.01	4.97	2.00	0.45
	135	43.78	0.75	10.75	0.04	16.54	0.38	10.45	11.87	1.06	1.05	96.66	6.56	1.46	0.44	0.10	0.47	0.00	0.04	2.32	1.59	0.01	0.01	0.01	1.91	0.06	0.00	0.25	0.20	8.01	4.97	2.00	0.45
	136	43.50	0.74	10.99	0.02	16.68	0.34	10.25	11.74	1.12	1.09	96.47	6.53	1.48	0.46	0.10	0.47	0.00	0.03	2.29	1.61	0.01	0.01	0.01	1.89	0.08	0.00	0.25	0.21	8.02	4.97	2.00	0.46
	137	43.75	0.75	10.78	0.00	16.75	0.39	10.32	11.87	1.07	1.07	96.75	6.55	1.46	0.44	0.10	0.48	0.00	0.04	2.30	1.61	0.01	0.01	0.01	1.91	0.06	0.00	0.25	0.21	8.01	4.97	2.00	0.45
	138	43.65	0.75	10.58	0.06	16.34	0.37	10.59	11.54	1.05	1.04	95.98	6.57	1.45	0.42	0.11	0.49	0.01	0.03	2.35	1.54	0.01	0.02	0.02	1.86	0.07	0.00	0.23	0.20	8.02	4.96	1.99	0.43
	139	42.77	0.79	10.42	0.00	16.62	0.39	10.57	11.55	1.07	1.03	95.22	6.50	1.53	0.33	0.12	0.56	0.00	0.04	2.37	1.52	0.01	0.03	0.03	1.88	0.05	0.00	0.27	0.20	8.03	4.94	2.00	0.47

doi:10.6342/NTU202202659

8.5.5 18TP04 Amphibolite and Tonalitic Gneiss

Mineral	No.	SiO_2	TiO_2	Al_2O_3	Cr_2O_3	FeO	Fe_2O_3	MnO	MgO	CaO	Na_2O	K_2O	Total	Si^{4+}	Ti^{4+}	Al^{3+}	Fe^{3+}	Mn^{2+}	Mg^{2+}	Ca^{2+}	Na^{+}	K^{+}	$T_{(total)}$	$M_{(total)}$	Ab	Or	An
Amphibolite	110	58.88	0.03	25.75	0.00	0.12	0.13	0.00	0.02	7.79	6.84	0.23	99.65	2.64	0.00	1.36	0.00	0.00	0.00	0.37	0.59	0.01	4.00	0.98	0.61	0.01	0.38
Plagioclase	111	58.88	0.01	25.78	0.01	0.14	0.16	0.00	0.00	7.90	6.91	0.29	99.92	2.63	0.00	1.36	0.01	0.00	0.00	0.38	0.60	0.02	3.99	0.99	0.60	0.02	0.38
Pl1	112	59.29	0.03	25.90	0.01	0.10	0.11	0.00	0.00	7.87	6.86	0.29	100.33	2.64	0.00	1.36	0.00	0.00	0.00	0.38	0.59	0.02	4.00	0.98	0.60	0.02	0.38
	113	59.28	0.00	25.67	0.01	0.13	0.15	0.00	0.00	7.92	6.78	0.25	100.04	2.64	0.00	1.35	0.00	0.00	0.00	0.38	0.59	0.01	3.99	0.98	0.60	0.01	0.39
	114	58.88	0.01	25.65	0.03	0.12	0.13	0.02	0.01	7.90	6.79	0.30	99.69	2.64	0.00	1.35	0.00	0.00	0.00	0.38	0.59	0.02	3.99	0.99	0.60	0.02	0.38
	115	58.87	0.00	25.57	0.00	0.11	0.12	0.02	0.01	7.90	6.75	0.23	99.45	2.64	0.00	1.35	0.00	0.00	0.00	0.38	0.59	0.01	3.99	0.98	0.60	0.01	0.39
	116	59.16	0.00	26.06	0.01	0.11	0.13	0.03	0.00	7.93	6.84	0.14	100.28	2.63	0.00	1.37	0.00	0.00	0.00	0.38	0.59	0.01	4.00	0.98	0.60	0.01	0.39
	117	59.79	0.00	25.49	0.00	0.09	0.10	0.00	0.00	7.89	6.90	0.24	100.40	2.66	0.00	1.33	0.00	0.00	0.00	0.38	0.59	0.01	3.99	0.98	0.60	0.01	0.38
	118	59.24	0.00	25.83	0.00	0.11	0.13	0.00	0.00	7.92	6.78	0.24	100.12	2.64	0.00	1.36	0.00	0.00	0.00	0.38	0.59	0.01	4.00	0.98	0.60	0.01	0.39
	119	58.97	0.00	25.78	0.00	0.09	0.10	0.03	0.00	7.92	6.79	0.26	99.84	2.64	0.00	1.36	0.00	0.00	0.00	0.38	0.59	0.01	4.00	0.98	0.60	0.02	0.39
	120	59.39	0.00	25.77	0.00	0.12	0.13	0.00	0.01	7.85	6.75	0.25	100.14	2.65	0.00	1.35	0.00	0.00	0.00	0.37	0.58	0.01	4.00	0.97	0.60	0.01	0.39
	121	58.95	0.00	25.73	0.00	0.11	0.12	0.00	0.00	7.83	7.02	0.25	99.88	2.64	0.00	1.36	0.00	0.00	0.00	0.38	0.61	0.01	3.99	1.00	0.61	0.01	0.38
	122	58.90	0.00	25.78	0.00	0.15	0.17	0.01	0.00	7.92	6.76	0.24	99.75	2.64	0.00	1.36	0.01	0.00	0.00	0.38	0.59	0.01	4.00	0.98	0.60	0.01	0.39
	123	58.81	0.01	25.67	0.00	0.10	0.11	0.00	0.00	7.86	6.81	0.27	99.53	2.64	0.00	1.36	0.00	0.00	0.00	0.38	0.59	0.02	4.00	0.99	0.60	0.02	0.38
	124	58.84	0.01	25.53	0.00	0.11	0.12	0.00	0.00	7.61	6.93	0.27	99.29	2.64	0.00	1.35	0.00	0.00	0.00	0.37	0.60	0.02	4.00	0.99	0.61	0.02	0.37
	125	58.53	0.00	25.87	0.00	0.12	0.13	0.00	0.00	7.70	6.95	0.23	99.39	2.63	0.00	1.37	0.00	0.00	0.00	0.37	0.61	0.01	4.00	0.99	0.61	0.01	0.37
	126	59.44	0.00	25.84	0.00	0.05	0.06	0.00	0.00	7.83	6.81	0.18	100.15	2.65	0.00	1.36	0.00	0.00	0.00	0.37	0.59	0.01	4.00	0.97	0.61	0.01	0.38
	127	59.47	0.00	25.97	0.01	0.10	0.11	0.00	0.00	7.84	6.87	0.16	100.42	2.64	0.00	1.36	0.00	0.00	0.00	0.37	0.59	0.01	4.00	0.97	0.61	0.01	0.38
	128	59.20	0.01	25.83	0.01	0.09	0.10	0.01	0.00	7.88	6.82	0.19	100.04	2.64	0.00	1.36	0.00	0.00	0.00	0.38	0.59	0.01	4.00	0.98	0.60	0.01	0.39
	129	59.39	0.01	25.77	0.00	0.10	0.11	0.01	0.00	7.93	6.83	0.22	100.25	2.64	0.00	1.35	0.00	0.00	0.00	0.38	0.59	0.01	4.00	0.98	0.60	0.01	0.39
	130	59.29	0.01	25.83	0.04	0.08	0.08	0.01	0.00	7.58	6.86	0.19	99.88	2.65	0.00	1.36	0.00	0.00	0.00	0.36	0.59	0.01	4.00	0.97	0.61	0.01	0.37
	131	59.17	0.02	25.74	0.01	0.11	0.12	0.00	0.00	7.72	6.80	0.22	99.78	2.64	0.00	1.36	0.00	0.00	0.00	0.37	0.59	0.01	4.00	0.97	0.61	0.01	0.38
	132	59.05	0.04	25.86	0.00	0.12	0.13	0.00	0.00	7.94	6.74	0.21	99.95	2.64	0.00	1.36	0.00	0.00	0.00	0.38	0.58	0.01	4.00	0.97	0.60	0.01	0.39
	133	59.28	0.00	25.88	0.00	0.07	0.08	0.01	0.00	8.10	6.61	0.24	100.18	2.64	0.00	1.36	0.00	0.00	0.00	0.39	0.57	0.01	4.00	0.97	0.59	0.01	0.40
	134	58.51	0.00	26.22	0.00	0.09	0.10	0.00	0.01	8.34	6.53	0.23	99.93	2.62	0.00	1.38	0.00	0.00	0.00	0.40	0.57	0.01	4.00	0.98	0.58	0.01	0.41
	135	58.27	0.00	26.60	0.00	0.14	0.15	0.00	0.01	8.79	6.35	0.19	100.34	2.60	0.00	1.40	0.01	0.00	0.00	0.42	0.55	0.01	4.00	0.98	0.56	0.01	0.43
	136	57.14	0.00	26.98	0.01	0.09	0.10	0.00	0.00	9.16	6.14	0.18	99.70	2.57	0.00	1.43	0.00	0.00	0.00	0.44	0.54	0.01	4.00	0.99	0.54	0.01	0.45
	137	57.80	0.00	26.86	0.00	0.09	0.10	0.00	0.00	8.93	6.14	0.23	100.05	2.59	0.00	1.42	0.00	0.00	0.00	0.43	0.53	0.01	4.00	0.97	0.55	0.01	0.44
	138	59.49	0.02	25.70	0.00	0.08	0.09	0.04	0.00	7.76	6.84	0.22	100.15	2.65	0.00	1.35	0.00	0.00	0.00	0.37	0.59	0.01	4.00	0.97	0.61	0.01	0.38
	139	59.06	0.03	25.79	0.00	0.09	0.10	0.00	0.00	7.73	6.87	0.23	99.81	2.64	0.00	1.36	0.00	0.00	0.00	0.37	0.60	0.01	4.00	0.98	0.61	0.01	0.38
	140	59.20	0.00	25.90	0.00	0.11	0.12	0.00	0.00	8.04	6.81	0.23	100.29	2.64	0.00	1.36	0.00	0.00	0.00	0.38	0.59	0.01	3.99	0.98	0.60	0.01	0.39
	141	58.53	0.00	26.26	0.01	0.12	0.13	0.01	0.00	8.15	6.73	0.20	100.01	2.62	0.00	1.38	0.00	0.00	0.00	0.39	0.58	0.01	4.00	0.98	0.59	0.01	0.40
	142	59.03	0.01	26.02	0.00	0.08	0.09	0.00	0.00	7.90	6.73	0.25	100.02	2.63	0.00	1.37	0.00	0.00	0.00	0.38	0.58	0.01	4.00	0.97	0.60	0.01	0.39
	143	58.86	0.00	26.00	0.01	0.08	0.09	0.01	0.01	8.00	6.75	0.23	99.93	2.63	0.00	1.37	0.00	0.00	0.00	0.38	0.58	0.01	4.00	0.98	0.60	0.01	0.39
	144	59.13	0.00	25.70	0.00	0.12	0.13	0.02	0.00	7.86	6.85	0.28	99.95	2.64	0.00	1.35	0.00	0.00	0.00	0.38	0.59	0.02	3.99	0.99	0.60	0.02	0.38
	145	58.63	0.01	25.59	0.00	0.12	0.13	0.04	0.00	7.72	6.88	0.26	99.24	2.64	0.00	1.36	0.00	0.00	0.00	0.37	0.60	0.01	4.00	0.99	0.61	0.02	0.38
	146	58.80	0.00	25.21	0.01	0.10	0.12	0.00	0.00	7.52	6.78	0.25	98.68	2.66	0.00	1.34	0.00	0.00	0.00	0.36	0.59	0.01	4.00	0.97	0.61	0.01	0.37
	147	59.16	0.00	25.47	0.00	0.13	0.15	0.01	0.00	7.69	6.80	0.22	99.48	2.65	0.00	1.35	0.00	0.00	0.00	0.37	0.59	0.01	4.00	0.97	0.61	0.01	0.38
	148	59.42	0.01	25.87	0.02	0.10	0.11	0.00	0.00	7.68	6.67	0.22	99.98	2.65	0.00	1.36	0.00	0.00	0.00	0.37	0.58	0.01	4.01	0.95	0.60	0.01	0.38
	149	58.77	0.00	25.74	0.03	0.11	0.12	0.00	0.00	7.75	6.82	0.24	99.46	2.64	0.00	1.36	0.00	0.00	0.00	0.37	0.59	0.01	4.00	0.98	0.61	0.01	0.38
	150	57.35	0.00	26.92	0.00	0.09	0.10	0.00	0.00	9.05	6.12	0.19	99.73	2.58	0.00	1.42	0.00	0.00	0.00	0.44	0.53	0.01	4.00	0.98	0.54	0.01	0.44

doi:10.6342/NTU202202659

Mineral	No.	SiO_2	TiO_2	Al_2O_3	Cr_2O_3	FeO	Fe_2O_3	MnO	MgO	CaO	Na_2O	K_2O	Total	Si^{4+}	Ti^{4+}	Al^{3+}	Fe^{3+}	Mn^{2+}	Mg^{2+}	Ca^{2+}	Na^{+}	K^{+}	$T_{(total)}$	$M_{(total)}$	Ab	Or	An
	151	58.10	0.01	26.38	0.00	0.10	0.11	0.00	0.00	8.76	6.41	0.19	99.96	2.60	0.00	1.39	0.00	0.00	0.00	0.42	0.56	0.01	3.99	0.99	0.56	0.01	0.43
	152	59.06	0.02	25.96	0.01	0.07	0.08	0.00	0.00	7.99	6.80	0.21	100.12	2.63	0.00	1.36	0.00	0.00	0.00	0.38	0.59	0.01	4.00	0.98	0.60	0.01	0.39
	153	59.29	0.01	25.81	0.01	0.13	0.14	0.00	0.01	7.86	6.73	0.24	100.08	2.64	0.00	1.36	0.00	0.00	0.00	0.38	0.58	0.01	4.00	0.97	0.60	0.01	0.39
	154	58.85	0.04	25.83	0.00	0.09	0.10	0.02	0.00	7.79	6.77	0.20	99.59	2.64	0.00	1.36	0.00	0.00	0.00	0.37	0.59	0.01	4.00	0.97	0.60	0.01	0.38
	155	59.14	0.00	25.83	0.00	0.12	0.13	0.01	0.00	7.76	6.79	0.25	99.89	2.64	0.00	1.36	0.00	0.00	0.00	0.37	0.59	0.01	4.00	0.97	0.60	0.01	0.38
	156	58.90	0.03	25.72	0.02	0.11	0.12	0.00	0.01	7.94	6.81	0.25	99.77	2.64	0.00	1.36	0.00	0.00	0.00	0.38	0.59	0.01	3.99	0.99	0.60	0.01	0.39
	157	59.57	0.00	25.40	0.00	0.09	0.10	0.04	0.00	7.96	6.90	0.25	100.22	2.65	0.00	1.33	0.00	0.00	0.00	0.38	0.60	0.01	3.99	0.99	0.60	0.01	0.38
	158	59.40	0.02	24.99	0.00	0.12	0.13	0.00	0.00	7.69	6.95	0.25	99.41	2.67	0.00	1.32	0.00	0.00	0.00	0.37	0.60	0.01	3.99	0.99	0.61	0.01	0.37
	159	58.48	0.00	25.75	0.00	0.15	0.16	0.00	0.00	7.85	6.94	0.25	99.42	2.63	0.00	1.36	0.01	0.00	0.00	0.38	0.61	0.01	3.99	1.00	0.61	0.01	0.38
	160	59.29	0.01	25.88	0.00	0.17	0.19	0.01	0.00	7.82	6.88	0.23	100.30	2.64	0.00	1.36	0.01	0.00	0.00	0.37	0.59	0.01	4.00	0.98	0.61	0.01	0.38
Amphibolite	161	59.00	0.00	25.76	0.00	0.16	0.18	0.00	0.00	7.75	6.79	0.25	99.72	2.64	0.00	1.36	0.01	0.00	0.00	0.37	0.59	0.01	4.00	0.97	0.60	0.01	0.38
Plagioclase	162	59.42	0.00	25.78	0.00	0.16	0.18	0.00	0.00	7.77	6.84	0.28	100.25	2.64	0.00	1.35	0.01	0.00	0.00	0.37	0.59	0.02	4.00	0.98	0.60	0.02	0.38
Pl2	163	59.13	0.00	25.68	0.00	0.13	0.15	0.00	0.00	7.76	6.77	0.27	99.74	2.64	0.00	1.35	0.00	0.00	0.00	0.37	0.59	0.02	4.00	0.97	0.60	0.02	0.38
	164	58.44	0.01	26.68	0.02	0.09	0.09	0.02	0.00	8.73	6.30	0.24	100.51	2.60	0.00	1.40	0.00	0.00	0.00	0.42	0.54	0.01	4.00	0.97	0.56	0.01	0.43
	165	59.10	0.02	25.85	0.02	0.15	0.17	0.01	0.00	7.94	6.77	0.23	100.10	2.64	0.00	1.36	0.01	0.00	0.00	0.38	0.59	0.01	3.99	0.98	0.60	0.01	0.39
	166	59.28	0.03	25.29	0.00	0.14	0.16	0.01	0.00	7.76	6.84	0.25	99.58	2.66	0.00	1.33	0.01	0.00	0.00	0.37	0.59	0.01	3.99	0.98	0.61	0.01	0.38
	167	59.02	0.00	25.32	0.00	0.14	0.16	0.00	0.01	7.83	6.87	0.24	99.43	2.65	0.00	1.34	0.01	0.00	0.00	0.38	0.60	0.01	3.99	0.99	0.60	0.01	0.38
Tonalitic gneiss	308	58.44	0.00	25.18	0.00	0.18	0.20	0.00	0.01	7.44	7.02	0.19	98.45	2.65	0.00	1.34	0.01	0.00	0.00	0.36	0.62	0.01	3.99	0.99	0.62	0.01	0.37
Plagioclase	309	57.94	0.00	25.94	0.01	0.11	0.12	0.00	0.00	7.96	6.83	0.14	98.92	2.62	0.00	1.38	0.00	0.00	0.00	0.39	0.60	0.01	4.00	0.99	0.60	0.01	0.39
Pl3	310	58.30	0.00	25.73	0.00	0.17	0.19	0.00	0.00	7.81	6.58	0.21	98.80	2.63	0.00	1.37	0.01	0.00	0.00	0.38	0.58	0.01	4.00	0.97	0.60	0.01	0.39
	311	58.52	0.01	26.05	0.02	0.22	0.25	0.00	0.00	8.20	6.54	0.20	99.75	2.62	0.00	1.37	0.01	0.00	0.00	0.39	0.57	0.01	4.00	0.97	0.58	0.01	0.40
	312	58.45	0.00	25.86	0.00	0.16	0.18	0.00	0.00	8.18	6.53	0.23	99.40	2.63	0.00	1.37	0.01	0.00	0.00	0.39	0.57	0.01	4.00	0.98	0.58	0.01	0.40
	313	58.30	0.00	25.77	0.00	0.17	0.19	0.00	0.00	8.12	6.49	0.20	99.05	2.63	0.00	1.37	0.01	0.00	0.00	0.39	0.57	0.01	4.00	0.97	0.58	0.01	0.40
	314	58.23	0.00	25.61	0.00	0.18	0.20	0.00	0.00	8.07	6.53	0.26	98.88	2.63	0.00	1.36	0.01	0.00	0.00	0.39	0.57	0.01	3.99	0.98	0.59	0.02	0.40
	315	59.34	0.00	25.86	0.01	0.17	0.19	0.01	0.00	7.65	6.75	0.20	99.98	2.65	0.00	1.36	0.01	0.00	0.00	0.37	0.58	0.01	4.00	0.96	0.61	0.01	0.38
	316	58.66	0.01	25.84	0.00	0.20	0.22	0.00	0.00	7.82	6.50	0.20	99.23	2.64	0.00	1.37	0.01	0.00	0.00	0.38	0.57	0.01	4.00	0.95	0.59	0.01	0.39
	317	58.11	0.02	26.00	0.01	0.15	0.16	0.00	0.00	8.06	6.57	0.22	99.13	2.62	0.00	1.38	0.01	0.00	0.00	0.39	0.57	0.01	4.00	0.98	0.59	0.01	0.40
	318	58.18	0.00	25.80	0.00	0.14	0.15	0.00	0.00	7.75	6.77	0.21	98.84	2.63	0.00	1.37	0.01	0.00	0.00	0.37	0.59	0.01	4.00	0.98	0.61	0.01	0.38
	319	58.26	0.00	26.13	0.04	0.15	0.16	0.00	0.00	8.34	6.62	0.19	99.72	2.61	0.00	1.38	0.01	0.00	0.00	0.40	0.58	0.01	3.99	0.99	0.58	0.01	0.41
	320	58.50	0.00	25.69	0.00	0.13	0.14	0.01	0.00	8.23	6.64	0.19	99.39	2.63	0.00	1.36	0.00	0.00	0.00	0.40	0.58	0.01	3.99	0.99	0.59	0.01	0.40
	321	58.71	0.00	25.87	0.00	0.10	0.11	0.00	0.00	8.11	6.43	0.20	99.42	2.63	0.00	1.37	0.00	0.00	0.00	0.39	0.56	0.01	4.00	0.96	0.58	0.01	0.41
	322	59.20	0.00	25.39	0.00	0.16	0.18	0.00	0.00	7.44	6.94	0.22	99.34	2.66	0.00	1.34	0.01	0.00	0.00	0.36	0.60	0.01	4.00	0.97	0.62	0.01	0.37
	323	59.01	0.00	25.57	0.00	0.15	0.17	0.00	0.00	7.51	6.72	0.20	99.16	2.65	0.00	1.35	0.01	0.00	0.00	0.36	0.58	0.01	4.00	0.96	0.61	0.01	0.38
	324	58.96	0.01	25.90	0.00	0.13	0.14	0.00	0.00	7.83	6.62	0.21	99.65	2.64	0.00	1.37	0.00	0.00	0.00	0.38	0.57	0.01	4.00	0.96	0.60	0.01	0.39
	325	58.70	0.02	25.59	0.00	0.11	0.12	0.00	0.00	7.87	6.77	0.21	99.26	2.64	0.00	1.36	0.00	0.00	0.00	0.38	0.59	0.01	4.00	0.98	0.60	0.01	0.39
	326	58.87	0.00	25.39	0.00	0.10	0.11	0.01	0.00	7.66	6.77	0.18	98.97	2.65	0.00	1.35	0.00	0.00	0.00	0.37	0.59	0.01	4.00	0.97	0.61	0.01	0.38
	327	58.74	0.00	25.47	0.02	0.11	0.12	0.00	0.00	7.81	6.76	0.26	99.17	2.64	0.00	1.35	0.00	0.00	0.00	0.38	0.59	0.02	3.99	0.98	0.60	0.02	0.38
	328	59.02	0.01	24.97	0.00	0.19	0.21	0.00	0.00	7.52	6.88	0.21	98.80	2.66	0.00	1.33	0.01	0.00	0.00	0.36	0.60	0.01	3.99	0.98	0.62	0.01	0.37
	329	58.20	0.02	25.95	0.00	0.17	0.19	0.01	0.01	8.19	6.41	0.22	99.17	2.62	0.00	1.38	0.01	0.00	0.00	0.40	0.56	0.01	4.00	0.97	0.58	0.01	0.41
	330	58.85	0.01	26.00	0.00	0.21	0.23	0.00	0.00	8.15	6.45	0.22	99.88	2.63	0.00	1.37	0.01	0.00	0.00	0.39	0.56	0.01	4.00	0.96	0.58	0.01	0.41
	331	58.50	0.01	25.99	0.03	0.23	0.25	0.01	0.00	8.04	6.61	0.21	99.61	2.62	0.00	1.37	0.01	0.00	0.00	0.39	0.57	0.01	4.00	0.97	0.59	0.01	0.40
Tonalitic gneiss	332	58.93	0.00	25.34	0.00	0.14	0.16	0.00	0.00	7.37	6.86	0.23	98.87	2.66	0.00	1.35	0.01	0.00	0.00	0.36	0.60	0.01	4.00	0.97	0.62	0.01	0.37
Plagioclase	333	59.15	0.00	24.90	0.00	0.11	0.12	0.03	0.00	6.70	7.37	0.24	98.50	2.67	0.00	1.33	0.00	0.00	0.00	0.32	0.65	0.01	4.00	0.98	0.66	0.01	0.33
Pl4	334	56.84	0.02	25.44	0.00	0.10	0.11	0.00	0.01	7.75	6.66	0.25	97.06	2.62	0.00	1.38	0.00	0.00	0.00	0.38	0.59	0.01	4.00	0.99	0.60	0.01	0.39
	335	58.84	0.00	25.75	0.00	0.10	0.11	0.01	0.00	7.91	6.60	0.24	99.46	2.64	0.00	1.36	0.00	0.00	0.00	0.38	0.57	0.01	4.00	0.97	0.59	0.01	0.39
	336	58.42	0.00	25.45	0.00	0.12	0.13	0.00	0.01	7.90	6.80	0.22	98.92	2.64	0.00	1.35	0.00	0.00	0.00	0.38	0.60	0.01	3.99	0.99	0.60	0.01	0.39
	337	58.64	0.00	25.72	0.00	0.14	0.15	0.00	0.01	8.12	6.43	0.27	99.33	2.63	0.00	1.36	0.01	0.00	0.00	0.39	0.56	0.02	4.00	0.97	0.58	0.02	0.40
	338	58.10	0.00	25.37	0.00	0.23	0.26	0.00	0.00	7.72	6.83	0.25	98.50	2.64	0.00	1.36	0.01	0.00	0.00	0.37	0.60	0.01	3.99	0.99	0.61	0.01	0.38

doi:10.6342/NTU202202659

Mineral	No.	SiO_2	TiO_2	Al_2O_3	Cr_2O_3	FeO	Fe_2O_3	MnO	MgO	CaO	Na_2O	K_2O	Total	Si^{4+}	Ti^{4+}	Al^{3+}	Fe^{3+}	Mn^{2+}	Mg^{2+}	Ca^{2+}	Na^{+}	K^{+}	$T_{(total)}$	$M_{(total)}$	Ab	Or	An
Tonalitic gneiss	411	59.48	0.00	25.11	0.00	0.06	0.06	0.00	0.01	7.32	6.95	0.26	99.17	2.67	0.00	1.33	0.00	0.00	0.00	0.35	0.60	0.01	4.00	0.97	0.62	0.02	0.36
Plagioclase	412	58.66	0.00	24.33	0.01	0.08	0.09	0.01	0.00	7.23	7.15	0.28	97.74	2.68	0.00	1.31	0.00	0.00	0.00	0.35	0.63	0.02	3.99	1.00	0.63	0.02	0.35
Pl5	413	58.93	0.01	25.53	0.01	0.13	0.14	0.00	0.00	7.56	6.97	0.31	99.44	2.65	0.00	1.35	0.00	0.00	0.00	0.36	0.61	0.02	4.00	0.99	0.61	0.02	0.37
	414	58.40	0.00	25.45	0.00	0.10	0.11	0.00	0.00	7.52	6.89	0.32	98.66	2.64	0.00	1.36	0.00	0.00	0.00	0.36	0.60	0.02	4.00	0.99	0.61	0.02	0.37
	415	58.64	0.00	25.40	0.00	0.12	0.13	0.00	0.00	7.31	6.72	0.31	98.49	2.65	0.00	1.35	0.00	0.00	0.00	0.35	0.59	0.02	4.01	0.96	0.61	0.02	0.37
	416	59.11	0.02	25.40	0.00	0.08	0.09	0.02	0.00	7.34	6.81	0.31	99.08	2.66	0.00	1.35	0.00	0.00	0.00	0.35	0.59	0.02	4.00	0.96	0.62	0.02	0.37
	417	59.05	0.00	25.34	0.00	0.07	0.07	0.00	0.02	7.53	6.79	0.31	99.10	2.66	0.00	1.34	0.00	0.00	0.00	0.36	0.59	0.02	4.00	0.97	0.61	0.02	0.37
	418	58.15	0.00	25.35	0.00	0.10	0.11	0.00	0.00	7.56	6.82	0.33	98.31	2.64	0.00	1.36	0.00	0.00	0.00	0.37	0.60	0.02	4.00	0.99	0.61	0.02	0.37
	419	59.05	0.00	25.43	0.00	0.09	0.10	0.01	0.00	7.55	6.88	0.34	99.35	2.65	0.00	1.35	0.00	0.00	0.00	0.36	0.60	0.02	4.00	0.98	0.61	0.02	0.37
	420	58.76	0.00	25.68	0.00	0.09	0.10	0.00	0.00	7.57	6.72	0.31	99.14	2.64	0.00	1.36	0.00	0.00	0.00	0.36	0.59	0.02	4.00	0.97	0.60	0.02	0.38
	421	58.36	0.00	25.41	0.00	0.06	0.07	0.01	0.00	7.60	6.89	0.31	98.63	2.64	0.00	1.36	0.00	0.00	0.00	0.37	0.60	0.02	4.00	0.99	0.61	0.02	0.37
	422	58.14	0.03	25.42	0.00	0.11	0.12	0.01	0.00	7.57	6.88	0.33	98.50	2.64	0.00	1.36	0.00	0.00	0.00	0.37	0.61	0.02	4.00	0.99	0.61	0.02	0.37
	423	59.63	0.00	25.30	0.00	0.07	0.08	0.00	0.00	7.34	6.91	0.28	99.52	2.67	0.00	1.33	0.00	0.00	0.00	0.35	0.60	0.02	4.00	0.97	0.62	0.02	0.36
Tonalitic gneiss	424	59.26	0.01	25.46	0.00	0.10	0.11	0.01	0.01	7.45	6.78	0.26	99.33	2.66	0.00	1.35	0.00	0.00	0.00	0.36	0.59	0.01	4.00	0.96	0.61	0.02	0.37
Plagioclase	425	59.26	0.00	25.20	0.00	0.08	0.09	0.00	0.01	7.62	6.83	0.30	99.28	2.66	0.00	1.33	0.00	0.00	0.00	0.37	0.59	0.02	3.99	0.98	0.61	0.02	0.37
Pl6	426	58.26	0.00	25.29	0.00	0.10	0.11	0.00	0.01	7.62	6.72	0.33	98.31	2.64	0.00	1.35	0.00	0.00	0.00	0.37	0.59	0.02	4.00	0.98	0.60	0.02	0.38
	427	58.97	0.01	25.28	0.03	0.13	0.14	0.00	0.00	7.50	6.86	0.32	99.09	2.65	0.00	1.34	0.00	0.00	0.00	0.36	0.60	0.02	4.00	0.98	0.61	0.02	0.37
	428	58.78	0.01	25.27	0.00	0.06	0.07	0.02	0.00	7.53	6.83	0.33	98.84	2.65	0.00	1.34	0.00	0.00	0.00	0.36	0.60	0.02	4.00	0.98	0.61	0.02	0.37
	429	58.80	0.01	25.39	0.00	0.08	0.09	0.00	0.00	7.56	6.82	0.30	98.95	2.65	0.00	1.35	0.00	0.00	0.00	0.36	0.60	0.02	4.00	0.98	0.61	0.02	0.37
	430	58.80	0.01	25.24	0.00	0.11	0.12	0.01	0.00	7.56	6.75	0.30	98.79	2.65	0.00	1.34	0.00	0.00	0.00	0.37	0.59	0.02	4.00	0.97	0.61	0.02	0.38
	431	58.88	0.02	25.40	0.00	0.08	0.08	0.01	0.01	7.63	6.90	0.31	99.21	2.65	0.00	1.35	0.00	0.00	0.00	0.37	0.60	0.02	4.00	0.99	0.61	0.02	0.37
	432	59.18	0.00	25.48	0.00	0.13	0.14	0.01	0.00	7.39	7.02	0.28	99.49	2.65	0.00	1.35	0.00	0.00	0.00	0.35	0.61	0.02	4.00	0.98	0.62	0.02	0.36
	433	59.02	0.00	25.28	0.00	0.11	0.12	0.00	0.00	7.27	6.98	0.26	98.90	2.66	0.00	1.34	0.00	0.00	0.00	0.35	0.61	0.01	4.00	0.97	0.63	0.02	0.36
	434	58.09	0.01	25.02	0.01	0.07	0.08	0.02	0.00	8.05	6.60	0.16	98.03	2.65	0.00	1.34	0.00	0.00	0.00	0.39	0.58	0.01	3.99	0.98	0.59	0.01	0.40
	435	58.61	0.01	25.95	0.00	0.07	0.08	0.05	0.00	8.09	6.65	0.21	99.64	2.63	0.00	1.37	0.00	0.00	0.00	0.39	0.58	0.01	4.00	0.98	0.59	0.01	0.40
	436	59.45	0.00	25.38	0.00	0.08	0.09	0.01	0.00	7.50	6.89	0.28	99.60	2.66	0.00	1.34	0.00	0.00	0.00	0.36	0.60	0.02	4.00	0.97	0.61	0.02	0.37
	437	59.45	0.00	25.38	0.00	0.14	0.16	0.02	0.00	7.53	6.87	0.29	99.68	2.66	0.00	1.34	0.01	0.00	0.00	0.36	0.60	0.02	4.00	0.97	0.61	0.02	0.37
	438	59.43	0.03	25.23	0.00	0.07	0.08	0.01	0.00	7.46	6.89	0.27	99.38	2.66	0.00	1.33	0.00	0.00	0.00	0.36	0.60	0.02	4.00	0.97	0.62	0.02	0.37
	439	59.41	0.01	25.54	0.00	0.11	0.12	0.00	0.01	7.43	6.89	0.29	99.68	2.66	0.00	1.35	0.00	0.00	0.00	0.36	0.60	0.02	4.00	0.97	0.62	0.02	0.37
	440	59.50	0.00	25.35	0.00	0.10	0.11	0.00	0.00	7.46	6.87	0.26	99.53	2.66	0.00	1.34	0.00	0.00	0.00	0.36	0.60	0.01	4.00	0.97	0.62	0.02	0.37
	441	59.00	0.00	25.68	0.00	0.12	0.14	0.00	0.00	7.69	6.68	0.27	99.45	2.65	0.00	1.36	0.00	0.00	0.00	0.37	0.58	0.02	4.00	0.97	0.60	0.02	0.38
	442	59.30	0.05	25.45	0.00	0.08	0.09	0.00	0.00	7.72	6.90	0.25	99.74	2.65	0.00	1.34	0.00	0.00	0.00	0.37	0.60	0.01	3.99	0.98	0.61	0.01	0.38
Tonalitic gneiss	339	64.30	0.01	18.41	0.01	0.09	0.09	0.00	0.00	0.00	0.40	15.89	99.11	2.99	0.00	1.01	0.00	0.00	0.00	0.00	0.04	0.94	4.00	0.98	0.04	0.96	0.00
K-feldspar	340	64.08	0.04	18.30	0.01	0.05	0.06	0.00	0.00	0.02	0.73	15.11	98.34	3.00	0.00	1.01	0.00	0.00	0.00	0.00	0.07	0.90	4.01	0.97	0.07	0.93	0.00
Kfs1	341	63.96	0.05	18.42	0.00	0.04	0.04	0.00	0.00	0.03	0.72	15.22	98.44	2.99	0.00	1.02	0.00	0.00	0.00	0.00	0.07	0.91	4.01	0.97	0.07	0.93	0.00
	342	64.23	0.06	18.26	0.00	0.03	0.04	0.00	0.00	0.02	0.65	15.12	98.36	3.00	0.00	1.01	0.00	0.00	0.00	0.00	0.06	0.90	4.01	0.96	0.06	0.94	0.00
	343	63.88	0.08	18.25	0.00	0.05	0.05	0.00	0.00	0.01	0.45	15.51	98.22	3.00	0.00	1.01	0.00	0.00	0.00	0.00	0.04	0.93	4.01	0.97	0.04	0.96	0.00
	344	63.53	0.07	18.25	0.00	0.00	0.00	0.00	0.00	0.00	0.65	15.23	97.73	2.99	0.00	1.01	0.00	0.00	0.00	0.00	0.06	0.92	4.01	0.97	0.06	0.94	0.00
	345	63.48	0.06	18.28	0.01	0.08	0.09	0.01	0.00	0.00	0.79	15.23	97.95	2.99	0.00	1.01	0.00	0.00	0.00	0.00	0.07	0.91	4.00	0.99	0.07	0.93	0.00
	346	63.80	0.05	18.27	0.00	0.03	0.03	0.00	0.00	0.03	0.81	15.02	97.99	3.00	0.00	1.01	0.00	0.00	0.00	0.00	0.07	0.90	4.01	0.97	0.08	0.92	0.00
	347	64.10	0.05	18.27	0.00	0.06	0.07	0.00	0.00	0.01	0.88	14.95	98.32	3.00	0.00	1.01	0.00	0.00	0.00	0.00	0.08	0.89	4.00	0.97	0.08	0.92	0.00
	348	63.92	0.04	18.23	0.00	0.09	0.10	0.00	0.00	0.04	0.81	15.09	98.22	3.00	0.00	1.01	0.00	0.00	0.00	0.00	0.07	0.90	4.00	0.98	0.08	0.92	0.00
	349	64.19	0.03	18.38	0.00	0.06	0.07	0.01	0.00	0.00	0.75	15.24	98.66	3.00	0.00	1.01	0.00	0.00	0.00	0.00	0.07	0.91	4.01	0.97	0.07	0.93	0.00
	350	62.24	0.05	18.29	0.00	0.10	0.11	0.00	0.00	0.07	0.77	15.29	96.81	2.97	0.00	1.03	0.00	0.00	0.00	0.00	0.07	0.93	4.00	1.01	0.07	0.93	0.00
	351	64.32	0.02	18.42	0.02	0.08	0.08	0.03	0.00	0.00	0.72	15.34	98.95	2.99	0.00	1.01	0.00	0.00	0.00	0.00	0.07	0.91	4.00	0.98	0.07	0.93	0.00
	352	63.19	0.04	18.44	0.00	0.09	0.10	0.04	0.00	0.02	0.63	15.48	97.92	2.98	0.00	1.02	0.00	0.00	0.00	0.00	0.06	0.93	4.00	0.99	0.06	0.94	0.00
	353	63.38	0.06	18.33	0.00	0.06	0.07	0.00	0.00	0.01	0.39	15.64	97.86	2.99	0.00	1.02	0.00	0.00	0.00	0.00	0.04	0.94	4.01	0.98	0.04	0.96	0.00
	354	63.40	0.07	18.35	0.00	0.15	0.16	0.02	0.00	0.01	0.62	15.34	97.94	2.98	0.00	1.02	0.01	0.00	0.00	0.00	0.06	0.92	4.00	0.98	0.06	0.94	0.00
	355	64.18	0.07	18.42	0.00	0.17	0.19	0.00	0.00	0.02	0.58	15.47	98.91	2.99	0.00	1.01	0.01	0.00	0.00	0.00	0.05	0.92	4.00	0.97	0.05	0.95	0.00

doi:10.6342/NTU202202659

Mineral	No.	SiO_2	TiO_2	Al_2O_3	Cr_2O_3	FeO	Fe_2O_3	MnO	MgO	CaO	Na_2O	K_2O	Total	Si^{4+}	Ti^{4+}	Al^{3+}	Fe^{3+}	Mn^{2+}	Mg^{2+}	Ca^{2+}	Na^{+}	K^{+}	$T_{(total)}$	$M_{(total)}$	Ab	Or	An
Tonalitic gneiss	356	59.67	0.06	18.35	0.00	0.21	0.24	0.00	0.00	0.03	0.69	15.21	94.22	2.94	0.00	1.06	0.01	0.00	0.00	0.00	0.07	0.95	4.00	1.02	0.06	0.93	0.00
K-feldspar	357	64.42	0.03	18.36	0.00	0.07	0.07	0.00	0.00	0.03	0.85	15.07	98.84	3.00	0.00	1.01	0.00	0.00	0.00	0.00	0.08	0.89	4.00	0.97	0.08	0.92	0.00
Kfs2	358	63.00	0.04	18.24	0.00	0.05	0.05	0.00	0.00	0.06	0.89	15.22	97.49	2.98	0.00	1.02	0.00	0.00	0.00	0.00	0.08	0.92	4.00	1.00	0.08	0.92	0.00
	359	63.59	0.05	18.45	0.00	0.06	0.07	0.03	0.00	0.01	0.84	15.06	98.08	2.99	0.00	1.02	0.00	0.00	0.00	0.00	0.08	0.90	4.01	0.98	0.08	0.92	0.00
	360	63.79	0.06	18.31	0.01	0.01	0.01	0.00	0.00	0.04	0.77	15.11	98.10	2.99	0.00	1.01	0.00	0.00	0.00	0.00	0.07	0.90	4.01	0.98	0.07	0.93	0.00
	361	64.09	0.06	18.36	0.00	0.04	0.04	0.00	0.00	0.02	0.64	15.08	98.28	3.00	0.00	1.01	0.00	0.00	0.00	0.00	0.06	0.90	4.01	0.96	0.06	0.94	0.00
Tonalitic gneiss	443	63.93	0.05	18.22	0.00	0.08	0.08	0.01	0.00	0.00	0.52	15.47	98.27	3.00	0.00	1.01	0.00	0.00	0.00	0.00	0.05	0.93	4.00	0.97	0.05	0.95	0.00
K-feldspar	444	63.48	0.04	18.24	0.00	0.10	0.11	0.01	0.00	0.01	0.80	15.21	97.89	2.99	0.00	1.01	0.00	0.00	0.00	0.00	0.07	0.91	4.00	0.99	0.07	0.93	0.00
Kfs3	445	64.17	0.03	18.24	0.00	0.06	0.06	0.02	0.00	0.02	0.89	15.07	98.51	3.00	0.00	1.00	0.00	0.00	0.00	0.00	0.08	0.90	4.00	0.98	0.08	0.92	0.00
	446	63.98	0.02	18.09	0.00	0.07	0.08	0.01	0.00	0.03	0.85	14.99	98.05	3.00	0.00	1.00	0.00	0.00	0.00	0.00	0.08	0.90	4.00	0.98	0.08	0.92	0.00
	447	63.67	0.08	18.23	0.00	0.05	0.06	0.00	0.00	0.01	0.74	15.02	97.81	3.00	0.00	1.01	0.00	0.00	0.00	0.00	0.07	0.90	4.01	0.97	0.07	0.93	0.00
	448	63.94	0.05	18.23	0.00	0.03	0.03	0.02	0.00	0.02	0.96	14.88	98.11	3.00	0.00	1.01	0.00	0.00	0.00	0.00	0.09	0.89	4.00	0.98	0.09	0.91	0.00
	449	63.57	0.06	18.32	0.01	0.06	0.06	0.00	0.00	0.01	0.89	15.07	97.99	2.99	0.00	1.01	0.00	0.00	0.00	0.00	0.08	0.90	4.00	0.99	0.08	0.92	0.00
	450	63.30	0.09	18.22	0.00	0.03	0.03	0.00	0.00	0.03	0.91	15.07	97.64	2.99	0.00	1.01	0.00	0.00	0.00	0.00	0.08	0.91	4.00	0.99	0.08	0.91	0.00
	451	63.27	0.05	18.37	0.01	0.04	0.05	0.01	0.00	0.05	0.89	14.20	96.89	2.99	0.00	1.02	0.00	0.00	0.00	0.00	0.08	0.86	4.02	0.94	0.09	0.91	0.00
	452	64.14	0.05	18.32	0.00	0.04	0.04	0.01	0.00	0.03	0.83	15.08	98.48	3.00	0.00	1.01	0.00	0.00	0.00	0.00	0.07	0.90	4.00	0.97	0.08	0.92	0.00
	453	63.55	0.03	18.34	0.03	0.09	0.10	0.00	0.00	0.02	0.83	15.13	98.01	2.99	0.00	1.02	0.00	0.00	0.00	0.00	0.08	0.91	4.00	0.98	0.08	0.92	0.00
	454	63.50	0.04	18.11	0.00	0.02	0.03	0.03	0.00	0.04	0.71	15.04	97.50	3.00	0.00	1.01	0.00	0.00	0.00	0.00	0.06	0.91	4.01	0.97	0.07	0.93	0.00
	455	62.93	0.05	18.05	0.00	0.03	0.03	0.01	0.00	0.00	0.65	15.40	97.12	2.99	0.00	1.01	0.00	0.00	0.00	0.00	0.06	0.93	4.00	0.99	0.06	0.94	0.00
	456	62.82	0.06	18.01	0.01	0.05	0.05	0.00	0.00	0.01	0.73	15.13	96.81	2.99	0.00	1.01	0.00	0.00	0.00	0.00	0.07	0.92	4.00	0.99	0.07	0.93	0.00
	457	63.79	0.05	17.95	0.00	0.04	0.05	0.01	0.00	0.02	0.80	15.33	97.98	3.00	0.00	1.00	0.00	0.00	0.00	0.00	0.07	0.92	4.00	0.99	0.07	0.93	0.00
	458	63.54	0.06	17.81	0.00	0.04	0.04	0.00	0.00	0.02	0.99	15.05	97.50	3.00	0.00	0.99	0.00	0.00	0.00	0.00	0.09	0.91	3.99	1.00	0.09	0.91	0.00
	459	63.85	0.03	18.36	0.00	0.00	0.00	0.00	0.00	0.01	0.82	15.03	98.10	2.99	0.00	1.01	0.00	0.00	0.00	0.00	0.07	0.90	4.01	0.97	0.08	0.92	0.00
	460	63.61	0.09	18.14	0.00	0.01	0.01	0.01	0.00	0.02	0.93	15.06	97.86	2.99	0.00	1.01	0.00	0.00	0.00	0.00	0.08	0.90	4.00	0.99	0.09	0.91	0.00
	461	63.78	0.05	18.08	0.00	0.03	0.03	0.01	0.00	0.03	0.89	14.83	97.70	3.00	0.00	1.00	0.00	0.00	0.00	0.00	0.08	0.89	4.00	0.97	0.08	0.92	0.00
	462	63.66	0.02	17.98	0.00	0.02	0.02	0.00	0.00	0.01	0.81	14.80	97.29	3.01	0.00	1.00	0.00	0.00	0.00	0.00	0.07	0.89	4.01	0.97	0.08	0.92	0.00
	463	63.40	0.04	18.25	0.00	0.02	0.02	0.03	0.00	0.02	0.52	15.51	97.78	2.99	0.00	1.01	0.00	0.00	0.00	0.00	0.05	0.93	4.01	0.98	0.05	0.95	0.00
	464	63.08	0.06	18.17	0.00	0.02	0.02	0.00	0.00	0.02	0.65	15.28	97.28	2.99	0.00	1.01	0.00	0.00	0.00	0.00	0.06	0.92	4.00	0.99	0.06	0.94	0.00
	465	63.80	0.07	18.14	0.01	0.04	0.04	0.00	0.00	0.01	0.76	15.20	98.04	3.00	0.00	1.00	0.00	0.00	0.00	0.00	0.07	0.91	4.00	0.98	0.07	0.93	0.00
	466	63.95	0.06	18.14	0.00	0.02	0.02	0.00	0.00	0.03	0.76	15.05	98.01	3.00	0.00	1.00	0.00	0.00	0.00	0.00	0.07	0.90	4.01	0.97	0.07	0.93	0.00
	467	63.50	0.05	18.26	0.00	0.03	0.03	0.00	0.00	0.01	0.74	15.09	97.68	2.99	0.00	1.01	0.00	0.00	0.00	0.00	0.07	0.91	4.01	0.98	0.07	0.93	0.00
	468	63.75	0.07	18.24	0.00	0.00	0.00	0.00	0.00	0.00	0.75	15.33	98.14	2.99	0.00	1.01	0.00	0.00	0.00	0.00	0.07	0.92	4.00	0.99	0.07	0.93	0.00
	469	63.35	0.08	18.16	0.00	0.01	0.01	0.02	0.00	0.02	0.72	15.15	97.49	2.99	0.00	1.01	0.00	0.00	0.00	0.00	0.07	0.91	4.00	0.98	0.07	0.93	0.00
	470	63.19	0.07	18.33	0.00	0.05	0.05	0.00	0.00	0.00	0.64	15.27	97.54	2.99	0.00	1.02	0.00	0.00	0.00	0.00	0.06	0.92	4.01	0.98	0.06	0.94	0.00
Tonalitic gneiss	471	62.85	0.08	18.07	0.00	0.02	0.02	0.00	0.00	0.03	0.45	15.24	96.74	2.99	0.00	1.01	0.00	0.00	0.00	0.00	0.04	0.93	4.01	0.97	0.04	0.96	0.00
K-feldspar	472	64.00	0.06	18.10	0.01	0.06	0.07	0.00	0.00	0.03	0.57	15.52	98.35	3.00	0.00	1.00	0.00	0.00	0.00	0.00	0.05	0.93	4.00	0.98	0.05	0.95	0.00
Kfs4	473	63.88	0.04	18.29	0.01	0.05	0.06	0.00	0.00	0.02	0.71	15.30	98.31	2.99	0.00	1.01	0.00	0.00	0.00	0.00	0.06	0.91	4.00	0.98	0.07	0.93	0.00
	474	62.71	0.05	18.16	0.00	0.02	0.02	0.00	0.00	0.03	0.75	15.22	96.94	2.98	0.00	1.02	0.00	0.00	0.00	0.00	0.07	0.92	4.00	0.99	0.07	0.93	0.00
	475	62.90	0.06	17.90	0.02	0.07	0.08	0.02	0.00	0.00	0.75	14.94	96.65	3.00	0.00	1.01	0.00	0.00	0.00	0.00	0.07	0.91	4.00	0.98	0.07	0.93	0.00
	476	62.67	0.04	17.42	0.02	0.03	0.03	0.00	0.00	0.03	0.91	14.67	95.78	3.01	0.00	0.99	0.00	0.00	0.00	0.00	0.08	0.90	4.00	0.99	0.09	0.91	0.00
	477	63.69	0.09	18.22	0.00	0.04	0.04	0.00	0.00	0.03	0.95	14.82	97.83	2.99	0.00	1.01	0.00	0.00	0.00	0.00	0.09	0.89	4.00	0.98	0.09	0.91	0.00
	478	61.25	0.05	18.17	0.00	0.06	0.06	0.00	0.00	0.01	0.88	14.97	95.38	2.97	0.00	1.04	0.00	0.00	0.00	0.00	0.08	0.92	4.00	1.01	0.08	0.92	0.00
	479	63.29	0.07	18.19	0.00	0.02	0.02	0.00	0.00	0.00	0.93	14.97	97.47	2.99	0.00	1.01	0.00	0.00	0.00	0.00	0.08	0.90	4.00	0.99	0.09	0.91	0.00
	480	63.43	0.07	18.26	0.01	0.02	0.02	0.00	0.00	0.01	0.85	15.11	97.76	2.99	0.00	1.01	0.00	0.00	0.00	0.00	0.08	0.91	4.00	0.99	0.08	0.92	0.00
	481	64.03	0.05	18.28	0.00	0.05	0.05	0.00	0.00	0.03	0.89	15.11	98.43	3.00	0.00	1.01	0.00	0.00	0.00	0.00	0.08	0.90	4.00	0.98	0.08	0.92	0.00
	482	64.03	0.03	18.27	0.00	0.04	0.05	0.00	0.00	0.02	0.85	15.25	98.49	3.00	0.00	1.01	0.00	0.00	0.00	0.00	0.08	0.91	4.00	0.99	0.08	0.92	0.00
	483	63.50	0.03	18.24	0.00	0.01	0.01	0.00	0.00	0.00	0.78	15.25	97.80	2.99	0.00	1.01	0.00	0.00	0.00	0.00	0.07	0.92	4.00	0.99	0.07	0.93	0.00

doi:10.6342/NTU202202659

Mineral	No.	SiO_2	TiO_2	Al_2O_3	Cr_2O_3	FeO	MnO	MgO	CaO	Na_2O	K_2O	Total	T		C							B					A			$T_{(total)}$	$C_{(total)}$	$B_{(total)}$	$A_{(total)}$
													Si^{4+}	Al^{3+}	Al^{3+}	Ti^{4+}	Fe^{3+}	Cr^{3+}	Mn^{2+}	Mg^{2+}	Fe^{2+}	Mn^{2+}	Fe^{2+}	Mg^{2+}	Ca^{2+}	Na^{+}	Ca^{2+}	Na^{+}	K^{+}				
Amphibolite	8	43.64	0.74	10.78	0.01	17.59	0.40	9.99	11.78	1.27	1.24	97.41	6.53	1.48	0.42	0.09	0.51	0.00	0.04	2.22	1.68	0.01	0.01	0.00	1.89	0.08	0.00	0.28	0.24	8.01	4.97	2.00	0.52
Hb1	9	43.72	0.76	10.60	0.00	17.57	0.42	9.93	11.91	1.25	1.25	97.39	6.55	1.46	0.41	0.10	0.50	0.00	0.04	2.22	1.70	0.01	0.00	0.00	1.91	0.09	0.00	0.27	0.24	8.01	4.97	2.01	0.51
	10	43.23	0.74	11.08	0.00	17.58	0.41	9.49	11.97	1.26	1.23	96.99	6.50	1.51	0.46	0.10	0.48	0.00	0.04	2.13	1.75	0.01	0.00	0.00	1.93	0.10	0.00	0.27	0.24	8.01	4.96	2.04	0.51
	11	43.45	0.75	10.96	0.01	17.74	0.37	9.39	11.89	1.21	1.27	97.04	6.53	1.47	0.47	0.09	0.47	0.00	0.04	2.11	1.78	0.01	0.00	0.00	1.92	0.11	0.00	0.25	0.24	8.01	4.96	2.03	0.49
	12	43.91	0.76	10.88	0.00	17.92	0.33	9.92	11.89	1.15	1.27	98.02	6.54	1.46	0.45	0.09	0.48	0.00	0.03	2.20	1.73	0.01	0.02	0.01	1.90	0.06	0.00	0.27	0.24	8.00	4.98	2.00	0.51
	13	43.57	0.76	11.00	0.00	17.80	0.38	9.88	11.84	1.26	1.24	97.74	6.51	1.50	0.44	0.10	0.50	0.00	0.04	2.20	1.70	0.01	0.02	0.00	1.90	0.07	0.00	0.30	0.24	8.01	4.98	2.00	0.53
	14	43.36	0.70	11.12	0.01	17.71	0.37	9.78	11.98	1.20	1.24	97.47	6.50	1.51	0.45	0.09	0.49	0.00	0.04	2.18	1.72	0.01	0.01	0.00	1.92	0.06	0.00	0.28	0.24	8.01	4.98	2.00	0.52
	15	43.40	0.72	10.94	0.00	17.87	0.38	9.96	11.88	1.28	1.20	97.63	6.49	1.52	0.41	0.10	0.52	0.00	0.04	2.22	1.69	0.01	0.02	0.01	1.91	0.06	0.00	0.31	0.23	8.01	4.98	2.00	0.54
	16	43.49	0.78	10.97	0.00	17.37	0.43	10.01	11.93	1.19	1.22	97.39	6.51	1.50	0.43	0.10	0.51	0.00	0.04	2.23	1.66	0.01	0.01	0.00	1.91	0.06	0.00	0.28	0.23	8.01	4.98	2.00	0.51
	17	44.02	0.75	10.99	0.00	18.01	0.42	10.02	11.87	1.19	1.21	98.48	6.53	1.47	0.45	0.09	0.52	0.00	0.04	2.20	1.68	0.01	0.03	0.01	1.89	0.05	0.00	0.29	0.23	8.01	4.99	2.00	0.52
	18	43.33	0.73	10.91	0.00	17.82	0.36	10.01	11.81	1.17	1.26	97.41	6.50	1.51	0.41	0.10	0.52	0.00	0.04	2.23	1.68	0.01	0.03	0.01	1.90	0.05	0.00	0.29	0.24	8.01	4.97	2.00	0.53
	19	41.51	0.79	10.97	0.02	17.83	0.40	9.99	11.88	1.17	1.21	95.76	6.35	1.68	0.29	0.13	0.61	0.00	0.04	2.26	1.63	0.01	0.04	0.02	1.94	0.00	0.01	0.35	0.24	8.03	4.95	2.02	0.59
	20	43.43	0.70	11.09	0.00	17.85	0.38	10.02	11.81	1.18	1.28	97.73	6.49	1.52	0.44	0.09	0.52	0.00	0.04	2.22	1.67	0.01	0.03	0.01	1.89	0.05	0.00	0.29	0.24	8.01	4.98	2.00	0.54
	21	43.01	0.68	11.05	0.00	17.93	0.35	9.85	11.86	1.17	1.29	97.18	6.47	1.54	0.42	0.09	0.52	0.00	0.03	2.20	1.71	0.01	0.03	0.01	1.91	0.05	0.00	0.29	0.25	8.01	4.97	2.00	0.54
	22	43.62	0.81	11.10	0.01	17.79	0.36	9.82	11.75	1.18	1.25	97.69	6.52	1.49	0.47	0.10	0.49	0.00	0.04	2.18	1.70	0.01	0.03	0.01	1.88	0.07	0.00	0.27	0.24	8.01	4.98	2.00	0.51
	23	43.18	0.79	11.15	0.01	17.73	0.38	9.96	11.65	1.24	1.24	97.32	6.48	1.54	0.44	0.10	0.53	0.00	0.04	2.21	1.65	0.01	0.04	0.02	1.87	0.06	0.00	0.30	0.24	8.01	4.98	2.00	0.54
	24	43.37	0.73	10.97	0.01	17.75	0.42	9.84	11.85	1.24	1.31	97.48	6.50	1.51	0.43	0.09	0.52	0.00	0.04	2.20	1.70	0.01	0.01	0.00	1.90	0.07	0.00	0.28	0.25	8.01	4.98	2.00	0.54
	25	43.41	0.71	10.91	0.00	17.72	0.39	9.92	11.74	1.22	1.30	97.31	6.51	1.50	0.43	0.09	0.52	0.00	0.04	2.21	1.69	0.01	0.02	0.01	1.89	0.08	0.00	0.28	0.25	8.01	4.97	2.00	0.53
	26	42.44	0.74	11.25	0.00	17.69	0.38	9.84	11.93	1.15	1.27	96.68	6.42	1.60	0.40	0.11	0.54	0.00	0.04	2.21	1.67	0.01	0.03	0.01	1.93	0.03	0.00	0.31	0.25	8.02	4.97	2.00	0.55
	27	43.26	0.77	11.15	0.00	17.75	0.39	9.88	11.86	1.20	1.30	97.56	6.48	1.53	0.44	0.10	0.52	0.00	0.04	2.20	1.69	0.01	0.02	0.01	1.90	0.06	0.00	0.29	0.25	8.01	4.98	2.00	0.54
	28	43.44	0.80	11.24	0.00	17.52	0.39	9.85	11.78	1.22	1.29	97.53	6.50	1.51	0.47	0.10	0.50	0.00	0.04	2.19	1.68	0.01	0.02	0.00	1.89	0.08	0.00	0.28	0.25	8.01	4.98	2.00	0.52
	29	43.36	0.78	11.24	0.00	17.85	0.39	9.87	11.81	1.26	1.29	97.85	6.48	1.53	0.45	0.10	0.52	0.00	0.04	2.19	1.69	0.01	0.03	0.01	1.89	0.06	0.00	0.30	0.25	8.01	4.98	2.00	0.55
	30	43.30	0.74	11.25	0.00	17.79	0.40	9.89	11.75	1.18	1.17	97.46	6.48	1.53	0.45	0.10	0.53	0.00	0.04	2.19	1.66	0.01	0.04	0.01	1.89	0.05	0.00	0.29	0.23	8.01	4.98	2.00	0.52
	31	43.28	0.76	11.14	0.00	17.96	0.37	9.81	11.79	1.23	1.22	97.57	6.48	1.53	0.44	0.10	0.52	0.00	0.04	2.18	1.70	0.01	0.03	0.01	1.89	0.06	0.00	0.30	0.24	8.01	4.98	2.00	0.54
	32	43.47	0.74	11.20	0.00	17.70	0.41	9.74	11.86	1.18	1.25	97.55	6.50	1.50	0.47	0.10	0.50	0.00	0.04	2.17	1.70	0.01	0.01	0.00	1.90	0.07	0.00	0.27	0.24	8.01	4.98	2.00	0.51
	33	43.54	0.77	11.15	0.02	17.82	0.39	9.66	11.90	1.23	1.25	97.73	6.51	1.50	0.47	0.10	0.49	0.00	0.04	2.15	1.73	0.01	0.01	0.00	1.91	0.08	0.00	0.28	0.24	8.01	4.98	2.00	0.52
	34	43.35	0.77	11.08	0.03	17.54	0.39	9.79	11.72	1.17	1.25	97.07	6.51	1.50	0.46	0.10	0.50	0.00	0.04	2.19	1.69	0.01	0.02	0.01	1.89	0.08	0.00	0.26	0.24	8.01	4.97	2.00	0.50
	35	43.55	0.70	11.17	0.02	17.91	0.38	9.87	11.83	1.25	1.21	97.88	6.50	1.51	0.46	0.09	0.51	0.00	0.04	2.19	1.70	0.01	0.03	0.01	1.89	0.06	0.00	0.30	0.23	8.01	4.98	2.00	0.53
	36	43.47	0.75	10.93	0.00	17.44	0.41	9.84	11.77	1.20	1.24	97.04	6.52	1.49	0.45	0.10	0.50	0.00	0.04	2.20	1.68	0.01	0.01	0.00	1.89	0.09	0.00	0.26	0.24	8.01	4.97	2.00	0.50
	37	43.39	0.68	10.96	0.00	17.94	0.38	9.88	11.83	1.19	1.22	97.48	6.50	1.51	0.43	0.09	0.52	0.00	0.04	2.20	1.70	0.01	0.03	0.01	1.90	0.05	0.00	0.29	0.23	8.01	4.98	2.00	0.53
	38	44.01	0.77	10.98	0.00	17.95	0.34	9.92	11.76	1.18	1.25	98.14	6.55	1.46	0.47	0.09	0.49	0.00	0.03	2.19	1.71	0.01	0.03	0.01	1.88	0.07	0.00	0.27	0.24	8.00	4.99	2.00	0.51
	39	43.73	0.77	11.07	0.00	17.76	0.40	9.84	11.83	1.25	1.28	97.92	6.52	1.48	0.46	0.09	0.50	0.00	0.04	2.19	1.70	0.01	0.01	0.00	1.89	0.08	0.00	0.28	0.24	8.00	4.98	2.00	0.53
	40	43.38	0.76	10.81	0.00	17.80	0.39	9.89	11.92	1.19	1.19	97.31	6.51	1.50	0.41	0.10	0.52	0.00	0.04	2.21	1.70	0.01	0.01	0.00	1.92	0.06	0.00	0.29	0.23	8.01	4.97	2.00	0.52
	41	43.68	0.71	10.85	0.02	17.80	0.37	9.93	11.84	1.24	1.22	97.66	6.53	1.48	0.43	0.09	0.50	0.00	0.04	2.21	1.71	0.01	0.02	0.01	1.90	0.07	0.00	0.29	0.23	8.01	4.98	2.00	0.52
	42	43.84	0.77	10.56	0.00	17.79	0.42	9.79	11.74	1.22	1.24	97.37	6.57	1.44	0.42	0.10	0.51	0.00	0.04	2.19	1.72	0.01	0.00	0.00	1.89	0.10	0.00	0.26	0.24	8.01	4.97	2.00	0.50
	43	43.71	0.82	10.51	0.00	17.72	0.43	9.90	11.83	1.26	1.23	97.41	6.55	1.46	0.40	0.10	0.52	0.00	0.04	2.21	1.70	0.01	0.00	0.00	1.90	0.09	0.00	0.28	0.24	8.01	4.97	2.00	0.52
	44	43.85	0.74	11.02	0.00	17.54	0.38	9.89	11.79	1.23	1.25	97.68	6.54	1.46	0.48	0.09	0.48	0.00	0.04	2.20	1.70	0.01	0.01	0.00	1.89	0.09	0.00	0.27	0.24	8.01	4.98	2.00	0.50
	45	43.51	0.79	11.12	0.03	17.71	0.38	9.96	11.64	1.29	1.32	97.75	6.50	1.50	0.45	0.10	0.51	0.00	0.04	2.21	1.67	0.01	0.03	0.01	1.86	0.08	0.00	0.30	0.25	8.01	4.98	2.00	0.55
	46	43.25	0.73	10.41	0.00	17.51	0.39	10.03	11.76	1.20	1.18	96.47	6.53	1.49	0.36	0.10	0.53	0.00	0.04	2.25	1.68	0.01	0.01	0.00	1.90	0.08	0.00	0.28	0.23	8.02	4.96	2.00	0.51
	47	43.16	0.73	10.68	0.03	17.83	0.45	9.96	11.93	1.23	1.25	97.25	6.49	1.53	0.37	0.10	0.55	0.00	0.05	2.23	1.68	0.01	0.01	0.01	1.92	0.05	0.00	0.31	0.24	8.01	4.97	2.00	0.55
	48	43.12	0.79	11.16	0.00	17.98	0.41	9.85	11.68	1.26	1.23	97.48	6.47	1.55	0.43	0.11	0.55	0.00	0.04	2.19	1.67	0.01	0.04	0.02	1.88	0.05	0.00	0.31	0.24	8.01	4.98	2.00	0.55
	49	43.13	0.68	11.08	0.02	17.54	0.42	9.87	11.81	1.22	1.20	96.97	6.48	1.53	0.43	0.10	0.53	0.00	0.04	2.21	1.67	0.01	0.01	0.00	1.90	0.07	0.00	0.29	0.23	8.01	4.97	2.00	0.52
	50	43.27	0.77	11.02	0.00	17.46	0.40	10.08	11.87	1.26	1.21	97.33	6.48	1.53	0.42	0.10	0.52	0.00	0.04	2.24	1.65	0.01	0.02	0.01	1.91	0.06	0.00	0.31	0.23	8.01	4.97	2.00	0.54

doi:10.6342/NTU202202659

Mineral	No.	SiO_2	TiO_2	Al_2O_3	Cr_2O_3	FeO	MnO	MgO	CaO	Na_2O	K_2O	Total	T		C							B					A			$T_{(total)}$	$C_{(total)}$	$B_{(total)}$	$A_{(total)}$
													Si^{4+}	Al^{3+}	Al^{3+}	Ti^{4+}	Fe^{3+}	Cr^{3+}	Mn^{2+}	Mg^{2+}	Fe^{2+}	Mn^{2+}	Fe^{2+}	Mg^{2+}	Ca^{2+}	Na^{+}	Ca^{2+}	Na^{+}	K^{+}				
Amphibolite	51	43.45	0.79	11.02	0.04	17.73	0.42	9.95	11.88	1.11	1.21	97.58	6.50	1.51	0.43	0.10	0.52	0.00	0.04	2.21	1.67	0.01	0.03	0.01	1.90	0.04	0.00	0.28	0.23	8.01	4.98	2.00	0.51
Hb2	52	43.41	0.72	10.71	0.00	17.23	0.39	9.90	11.85	1.19	1.29	96.68	6.53	1.48	0.42	0.09	0.49	0.00	0.04	2.22	1.69	0.01	0.00	0.00	1.91	0.10	0.00	0.25	0.25	8.01	4.96	2.02	0.50
	53	43.39	0.78	10.91	0.00	17.35	0.36	9.86	11.82	1.21	1.30	96.97	6.52	1.49	0.44	0.10	0.48	0.00	0.04	2.21	1.70	0.01	0.00	0.00	1.90	0.09	0.00	0.26	0.25	8.01	4.97	2.00	0.51
	54	43.40	0.72	10.98	0.00	17.61	0.39	9.94	11.58	1.24	1.31	97.17	6.51	1.50	0.44	0.09	0.52	0.00	0.04	2.21	1.66	0.01	0.03	0.01	1.86	0.09	0.00	0.27	0.25	8.01	4.97	2.00	0.52
	55	43.49	0.74	11.05	0.02	17.82	0.41	10.01	11.59	1.30	1.25	97.68	6.50	1.51	0.44	0.10	0.54	0.00	0.04	2.21	1.65	0.01	0.04	0.02	1.86	0.07	0.00	0.30	0.24	8.01	4.98	2.00	0.54
	56	43.59	0.71	10.99	0.00	17.42	0.39	9.95	11.71	1.22	1.09	97.06	6.53	1.48	0.46	0.10	0.50	0.00	0.04	2.22	1.66	0.01	0.02	0.01	1.88	0.08	0.00	0.27	0.21	8.01	4.97	2.00	0.48
	57	43.98	0.73	10.91	0.02	17.56	0.38	9.92	11.78	1.25	1.12	97.66	6.56	1.45	0.47	0.09	0.48	0.00	0.04	2.20	1.70	0.01	0.01	0.00	1.88	0.09	0.00	0.27	0.21	8.01	4.98	2.00	0.49
	58	43.54	0.77	10.65	0.03	17.85	0.41	9.93	11.88	1.15	1.30	97.51	6.52	1.48	0.40	0.10	0.52	0.00	0.04	2.21	1.71	0.01	0.01	0.01	1.91	0.06	0.00	0.27	0.25	8.01	4.98	2.00	0.52
	59	43.42	0.69	10.69	0.00	17.75	0.40	9.98	11.74	1.26	1.28	97.21	6.52	1.49	0.40	0.09	0.53	0.00	0.04	2.23	1.68	0.01	0.01	0.01	1.89	0.08	0.00	0.29	0.25	8.01	4.97	2.00	0.53
	60	43.26	0.77	11.10	0.00	17.89	0.43	9.99	11.85	1.19	1.25	97.72	6.47	1.54	0.42	0.10	0.55	0.00	0.04	2.21	1.66	0.01	0.03	0.01	1.90	0.04	0.00	0.31	0.24	8.01	4.98	2.00	0.55
	61	43.69	0.68	10.99	0.00	17.97	0.38	9.82	11.79	1.11	1.26	97.68	6.53	1.48	0.46	0.09	0.51	0.00	0.04	2.18	1.71	0.01	0.03	0.01	1.89	0.06	0.00	0.26	0.24	8.01	4.98	2.00	0.50
	62	43.69	0.70	10.98	0.02	17.62	0.39	9.89	11.88	1.18	0.95	97.28	6.53	1.48	0.45	0.10	0.50	0.00	0.04	2.20	1.69	0.01	0.02	0.01	1.90	0.06	0.00	0.28	0.18	8.02	4.97	2.00	0.47
	63	43.71	0.79	11.07	0.01	17.58	0.38	9.82	11.91	1.21	0.99	97.48	6.53	1.48	0.47	0.10	0.48	0.00	0.04	2.18	1.70	0.01	0.01	0.00	1.91	0.06	0.00	0.29	0.19	8.01	4.98	2.00	0.48
	64	42.72	0.74	10.93	0.00	17.60	0.37	9.81	11.76	1.18	1.28	96.40	6.47	1.55	0.40	0.10	0.53	0.00	0.04	2.21	1.68	0.01	0.02	0.00	1.91	0.07	0.00	0.28	0.25	8.02	4.96	2.00	0.53
	65	43.21	0.81	10.93	0.00	17.56	0.37	9.78	11.87	1.25	1.33	97.11	6.50	1.51	0.43	0.10	0.49	0.00	0.04	2.19	1.72	0.01	0.00	0.00	1.91	0.08	0.00	0.28	0.26	8.01	4.97	2.01	0.54
	66	42.93	0.81	11.16	0.00	17.86	0.40	9.75	11.71	1.19	1.29	97.10	6.46	1.55	0.43	0.11	0.54	0.00	0.04	2.18	1.68	0.01	0.03	0.01	1.89	0.06	0.00	0.29	0.25	8.01	4.97	2.00	0.54
	67	43.30	0.71	11.04	0.00	18.00	0.39	9.81	11.69	1.24	1.23	97.42	6.49	1.52	0.43	0.10	0.53	0.00	0.04	2.18	1.69	0.01	0.03	0.01	1.88	0.07	0.00	0.30	0.24	8.01	4.98	2.00	0.53
	68	43.63	0.78	10.72	0.00	17.75	0.39	9.83	11.50	1.28	1.25	97.13	6.55	1.46	0.43	0.10	0.52	0.00	0.04	2.19	1.69	0.01	0.02	0.01	1.85	0.11	0.00	0.27	0.24	8.01	4.97	2.00	0.51
	69	44.14	0.71	10.56	0.02	17.81	0.38	9.92	11.60	1.28	1.19	97.60	6.59	1.42	0.44	0.09	0.50	0.00	0.04	2.20	1.71	0.01	0.01	0.01	1.86	0.11	0.00	0.26	0.23	8.01	4.98	2.00	0.49
	70	43.76	0.72	10.65	0.00	17.47	0.42	10.15	11.77	1.25	1.17	97.36	6.54	1.47	0.41	0.10	0.52	0.00	0.04	2.25	1.65	0.01	0.01	0.01	1.89	0.08	0.00	0.28	0.23	8.01	4.97	2.00	0.51
	71	43.42	0.66	11.12	0.03	17.87	0.37	9.90	11.88	1.28	1.28	97.79	6.49	1.52	0.44	0.08	0.51	0.00	0.04	2.20	1.71	0.01	0.02	0.01	1.90	0.06	0.00	0.31	0.25	8.01	4.98	2.00	0.55
	72	43.55	0.72	11.07	0.03	17.54	0.37	9.68	11.85	1.27	1.33	97.40	6.52	1.48	0.48	0.09	0.47	0.00	0.04	2.16	1.74	0.01	0.00	0.00	1.90	0.11	0.00	0.26	0.25	8.00	4.97	2.02	0.52
	73	43.71	0.75	11.10	0.01	17.57	0.38	9.81	11.86	1.34	1.29	97.82	6.52	1.48	0.47	0.09	0.48	0.00	0.04	2.18	1.72	0.01	0.00	0.00	1.90	0.10	0.00	0.29	0.25	8.00	4.98	2.01	0.53
	74	43.64	0.69	10.87	0.00	17.66	0.34	9.93	11.55	1.25	1.26	97.18	6.54	1.47	0.45	0.09	0.50	0.00	0.03	2.21	1.69	0.01	0.02	0.01	1.86	0.10	0.00	0.27	0.24	8.01	4.97	2.00	0.51
	75	43.70	0.70	10.97	0.02	17.87	0.37	9.99	11.55	1.23	1.30	97.69	6.53	1.48	0.45	0.09	0.52	0.00	0.04	2.21	1.67	0.01	0.04	0.02	1.85	0.08	0.00	0.28	0.25	8.01	4.98	2.00	0.53
	76	43.75	0.75	11.01	0.00	17.44	0.41	9.74	11.89	1.26	1.11	97.36	6.54	1.47	0.47	0.10	0.48	0.00	0.04	2.17	1.71	0.01	0.00	0.00	1.91	0.09	0.00	0.27	0.21	8.01	4.97	2.01	0.48
	77	43.56	0.78	10.96	0.03	17.72	0.41	9.80	11.76	1.28	1.11	97.41	6.52	1.49	0.44	0.10	0.51	0.00	0.04	2.18	1.69	0.01	0.02	0.01	1.89	0.08	0.00	0.29	0.21	8.01	4.98	2.00	0.51
	78	43.49	0.78	11.02	0.00	17.82	0.37	9.91	11.82	1.27	1.11	97.58	6.50	1.51	0.43	0.10	0.51	0.00	0.04	2.20	1.69	0.01	0.03	0.01	1.90	0.06	0.00	0.31	0.21	8.01	4.98	2.00	0.52
	79	43.54	0.78	11.04	0.00	17.77	0.39	10.00	11.85	1.29	1.11	97.78	6.50	1.51	0.43	0.10	0.52	0.00	0.04	2.21	1.67	0.01	0.03	0.01	1.90	0.05	0.00	0.32	0.21	8.01	4.98	2.00	0.53
	80	43.23	0.78	10.87	0.00	17.86	0.41	9.82	11.59	1.24	1.10	96.89	6.50	1.51	0.41	0.11	0.54	0.00	0.04	2.19	1.67	0.01	0.03	0.01	1.87	0.07	0.00	0.29	0.21	8.02	4.97	2.00	0.51
	81	43.25	0.76	10.91	0.00	17.65	0.35	9.94	11.74	1.29	1.12	97.01	6.50	1.52	0.42	0.10	0.51	0.00	0.04	2.22	1.68	0.01	0.02	0.01	1.89	0.07	0.00	0.31	0.22	8.01	4.97	2.00	0.52
	82	43.28	0.81	11.01	0.00	17.62	0.38	9.47	11.83	1.33	1.16	96.89	6.51	1.50	0.46	0.11	0.48	0.00	0.04	2.13	1.75	0.01	0.00	0.00	1.91	0.11	0.00	0.28	0.22	8.01	4.96	2.02	0.50
	83	43.26	0.79	10.97	0.00	17.79	0.39	9.48	11.82	1.26	1.09	96.83	6.51	1.50	0.45	0.11	0.49	0.00	0.04	2.13	1.75	0.01	0.00	0.00	1.91	0.09	0.00	0.28	0.21	8.01	4.96	2.01	0.49
	84	43.59	0.78	11.12	0.00	17.74	0.39	9.88	11.41	1.20	1.11	97.22	6.53	1.49	0.47	0.11	0.53	0.00	0.04	2.18	1.64	0.01	0.05	0.02	1.83	0.08	0.00	0.27	0.21	8.01	4.97	1.99	0.49
	85	43.87	0.75	11.13	0.00	17.76	0.41	10.06	11.51	1.25	1.08	97.82	6.53	1.48	0.47	0.10	0.53	0.00	0.04	2.21	1.63	0.01	0.05	0.02	1.84	0.07	0.00	0.29	0.21	8.01	4.98	1.99	0.50
	86	43.31	0.68	10.98	0.02	17.81	0.38	9.88	11.82	1.22	1.07	97.16	6.50	1.52	0.42	0.10	0.52	0.00	0.04	2.20	1.69	0.01	0.02	0.01	1.90	0.05	0.00	0.30	0.21	8.02	4.97	2.00	0.51
	87	43.62	0.77	11.01	0.00	17.59	0.42	9.94	11.81	1.27	1.05	97.48	6.52	1.50	0.44	0.10	0.52	0.00	0.04	2.21	1.66	0.01	0.02	0.01	1.89	0.07	0.00	0.30	0.20	8.01	4.98	2.00	0.50
	88	43.96	0.66	10.95	0.01	17.58	0.42	9.78	11.67	1.24	1.04	97.31	6.57	1.45	0.48	0.09	0.50	0.00	0.04	2.17	1.69	0.01	0.01	0.00	1.87	0.10	0.00	0.26	0.20	8.01	4.98	1.99	0.46
	89	43.79	0.69	10.90	0.00	17.63	0.40	9.85	11.65	1.22	1.06	97.19	6.55	1.46	0.46	0.09	0.51	0.00	0.04	2.19	1.68	0.01	0.02	0.01	1.87	0.09	0.00	0.27	0.20	8.01	4.97	2.00	0.47
	90	43.97	0.69	10.67	0.00	17.73	0.40	10.04	12.01	1.20	1.00	97.72	6.55	1.46	0.42	0.09	0.50	0.00	0.04	2.23	1.70	0.01	0.01	0.00	1.92	0.05	0.00	0.29	0.19	8.01	4.98	2.00	0.49

doi:10.6342/NTU202202659

Mineral	No.	SiO_2	TiO_2	Al_2O_3	Cr_2O_3	FeO	MnO	MgO	CaO	Na_2O	K_2O	Total	T		C							B					A			$T_{(total)}$	$C_{(total)}$	$B_{(total)}$	$A_{(total)}$
													Si^{4+}	Al^{3+}	Al^{3+}	Ti^{4+}	Fe^{3+}	Cr^{3+}	Mn^{2+}	Mg^{2+}	Fe^{2+}	Mn^{2+}	Fe^{2+}	Mg^{2+}	Ca^{2+}	Na^{+}	Ca^{2+}	Na^{+}	K^{+}				
Amphibolite	91	43.61	0.79	10.79	0.00	17.77	0.40	9.89	11.98	1.15	1.17	97.55	6.53	1.48	0.42	0.10	0.50	0.00	0.04	2.20	1.71	0.01	0.01	0.00	1.92	0.05	0.00	0.28	0.22	8.01	4.98	2.00	0.50
Hb3	92	43.37	0.79	10.95	0.00	17.54	0.38	9.87	11.79	1.21	1.14	97.03	6.51	1.50	0.44	0.11	0.50	0.00	0.04	2.20	1.68	0.01	0.02	0.00	1.90	0.07	0.00	0.28	0.22	8.01	4.97	2.00	0.50
	93	43.20	0.71	11.16	0.01	17.77	0.37	9.77	11.74	1.16	1.08	96.97	6.49	1.53	0.45	0.10	0.52	0.00	0.04	2.18	1.68	0.01	0.03	0.01	1.89	0.06	0.00	0.28	0.21	8.02	4.97	2.00	0.49
	94	41.85	0.74	11.10	0.00	17.85	0.37	9.80	11.87	1.20	1.13	95.92	6.38	1.65	0.35	0.12	0.57	0.00	0.04	2.22	1.67	0.01	0.03	0.01	1.93	0.02	0.01	0.34	0.22	8.03	4.96	2.01	0.57
	95	42.95	0.71	11.13	0.00	17.73	0.39	9.81	11.83	1.22	1.13	96.91	6.47	1.55	0.42	0.10	0.53	0.00	0.04	2.20	1.68	0.01	0.02	0.01	1.91	0.05	0.00	0.30	0.22	8.02	4.97	2.00	0.52
	96	43.70	0.79	11.24	0.00	17.73	0.38	9.90	11.94	1.24	1.12	98.04	6.51	1.50	0.47	0.10	0.49	0.00	0.04	2.19	1.70	0.01	0.02	0.01	1.91	0.06	0.00	0.30	0.21	8.01	4.99	2.00	0.52
	97	43.64	0.77	11.11	0.00	17.88	0.41	9.90	11.75	1.25	1.07	97.78	6.51	1.50	0.45	0.10	0.53	0.00	0.04	2.19	1.67	0.01	0.03	0.01	1.88	0.06	0.00	0.30	0.21	8.01	4.98	2.00	0.51
	98	43.52	0.80	10.93	0.02	17.99	0.40	9.39	11.57	1.22	1.12	96.95	6.54	1.47	0.47	0.11	0.50	0.00	0.04	2.10	1.75	0.01	0.01	0.00	1.87	0.10	0.00	0.25	0.22	8.01	4.97	2.00	0.47
	99	43.20	0.85	11.09	0.01	17.97	0.38	9.47	11.88	1.24	1.16	97.25	6.49	1.52	0.45	0.11	0.50	0.00	0.04	2.12	1.76	0.01	0.01	0.00	1.91	0.07	0.00	0.29	0.22	8.01	4.97	2.00	0.51
	100	43.55	0.71	10.99	0.00	17.80	0.37	9.96	10.98	1.27	1.08	96.70	6.54	1.48	0.47	0.10	0.55	0.00	0.03	2.19	1.61	0.01	0.07	0.04	1.77	0.10	0.00	0.27	0.21	8.02	4.96	1.99	0.48
	101	43.59	0.75	11.13	0.00	17.67	0.39	9.80	10.97	1.22	1.11	96.63	6.55	1.47	0.50	0.11	0.54	0.00	0.04	2.16	1.61	0.01	0.06	0.03	1.77	0.11	0.00	0.24	0.22	8.02	4.97	1.99	0.46
	102	43.79	0.74	11.17	0.00	17.98	0.38	9.95	11.61	1.29	1.16	98.05	6.52	1.49	0.47	0.10	0.52	0.00	0.04	2.19	1.67	0.01	0.04	0.02	1.85	0.07	0.00	0.30	0.22	8.01	4.98	2.00	0.53
	103	43.45	0.78	11.16	0.01	17.74	0.38	10.00	11.72	1.22	1.11	97.56	6.49	1.52	0.45	0.10	0.52	0.00	0.04	2.21	1.65	0.01	0.04	0.02	1.88	0.05	0.00	0.30	0.21	8.01	4.98	2.00	0.52
	104	43.35	0.78	11.15	0.00	17.73	0.40	9.80	11.75	1.30	1.09	97.33	6.49	1.52	0.45	0.11	0.52	0.00	0.04	2.18	1.68	0.01	0.02	0.01	1.89	0.07	0.00	0.30	0.21	8.01	4.97	2.00	0.52
	105	42.65	0.73	11.33	0.00	17.94	0.36	9.75	11.61	1.21	1.16	96.74	6.44	1.58	0.43	0.11	0.55	0.00	0.03	2.18	1.67	0.01	0.05	0.02	1.88	0.05	0.00	0.31	0.23	8.02	4.97	2.00	0.53
	106	43.42	0.77	11.26	0.00	17.90	0.36	9.83	11.57	1.17	1.07	97.34	6.50	1.51	0.47	0.11	0.52	0.00	0.03	2.17	1.67	0.01	0.05	0.02	1.86	0.05	0.00	0.29	0.21	8.02	4.98	1.99	0.49
	107	43.76	0.88	11.10	0.01	17.61	0.41	9.80	11.60	1.17	1.08	97.41	6.54	1.47	0.48	0.11	0.50	0.00	0.04	2.17	1.67	0.01	0.03	0.01	1.86	0.08	0.00	0.26	0.21	8.01	4.98	1.99	0.47
	108	43.62	0.79	10.95	0.00	17.25	0.39	9.69	11.94	1.22	1.13	96.99	6.54	1.47	0.47	0.10	0.46	0.00	0.04	2.17	1.72	0.01	0.00	0.00	1.92	0.10	0.00	0.25	0.22	8.01	4.96	2.03	0.47
	109	43.87	0.76	10.93	0.00	17.37	0.39	9.68	11.86	1.19	1.16	97.22	6.57	1.44	0.49	0.09	0.46	0.00	0.04	2.16	1.73	0.01	0.00	0.00	1.90	0.11	0.00	0.24	0.22	8.01	4.97	2.02	0.46
Tonalitic gneiss	255	41.93	0.87	11.34	0.00	19.04	0.34	8.83	11.74	1.14	1.45	96.69	6.39	1.62	0.42	0.12	0.55	0.00	0.04	2.01	1.84	0.01	0.04	0.00	1.91	0.05	0.01	0.29	0.28	8.01	4.97	2.01	0.58
Hb4	256	41.77	0.81	11.25	0.00	18.82	0.41	8.82	11.78	1.24	1.35	96.24	6.39	1.63	0.40	0.12	0.57	0.00	0.04	2.01	1.82	0.01	0.02	0.00	1.92	0.06	0.01	0.30	0.26	8.02	4.95	2.02	0.57
	257	41.74	0.85	11.53	0.00	18.37	0.39	8.88	11.59	1.32	1.43	96.09	6.38	1.63	0.44	0.12	0.54	0.00	0.04	2.02	1.79	0.01	0.02	0.00	1.89	0.09	0.00	0.30	0.28	8.02	4.96	2.01	0.58
	258	41.61	0.83	11.68	0.00	18.34	0.38	8.78	11.60	1.25	1.40	95.86	6.37	1.65	0.46	0.12	0.54	0.00	0.04	2.01	1.79	0.01	0.02	0.00	1.90	0.09	0.01	0.28	0.27	8.02	4.96	2.01	0.56
	259	41.83	0.78	11.98	0.01	18.80	0.39	8.81	11.51	1.23	1.49	96.83	6.36	1.65	0.49	0.11	0.56	0.00	0.04	1.99	1.78	0.01	0.05	0.00	1.87	0.07	0.00	0.29	0.29	8.01	4.98	2.00	0.59
	260	42.27	0.85	11.92	0.00	19.06	0.41	8.70	11.68	1.23	1.41	97.52	6.39	1.62	0.50	0.11	0.54	0.00	0.04	1.96	1.82	0.01	0.04	0.00	1.89	0.06	0.00	0.30	0.27	8.01	4.99	2.00	0.57
	261	42.01	0.79	12.01	0.03	17.83	0.37	8.57	11.65	1.27	1.43	95.97	6.41	1.60	0.56	0.10	0.47	0.00	0.04	1.95	1.82	0.01	0.00	0.00	1.90	0.13	0.01	0.24	0.28	8.01	4.95	2.04	0.52
	262	41.60	0.82	11.61	0.02	17.87	0.39	8.54	11.68	1.26	1.44	95.23	6.40	1.62	0.49	0.11	0.50	0.00	0.04	1.96	1.83	0.01	0.00	0.00	1.92	0.13	0.01	0.24	0.28	8.02	4.93	2.06	0.53
	263	41.50	0.80	11.86	0.03	18.52	0.32	8.44	11.69	1.31	1.35	95.81	6.37	1.65	0.49	0.11	0.50	0.00	0.04	1.93	1.87	0.01	0.01	0.00	1.91	0.10	0.01	0.29	0.26	8.02	4.95	2.03	0.56
	264	41.56	0.81	11.85	0.01	18.72	0.39	8.52	11.69	1.34	1.33	96.22	6.36	1.66	0.47	0.12	0.54	0.00	0.04	1.94	1.84	0.01	0.02	0.00	1.91	0.09	0.01	0.31	0.26	8.02	4.96	2.02	0.58
	265	41.58	0.82	12.27	0.00	18.66	0.39	8.70	11.74	1.29	1.42	96.87	6.32	1.69	0.51	0.11	0.54	0.00	0.04	1.97	1.79	0.01	0.03	0.00	1.91	0.06	0.01	0.32	0.28	8.02	4.98	2.01	0.60
	266	41.35	0.81	12.16	0.00	18.58	0.37	8.57	11.55	1.45	1.38	96.22	6.33	1.69	0.50	0.12	0.54	0.00	0.04	1.95	1.81	0.01	0.02	0.00	1.89	0.10	0.01	0.33	0.27	8.02	4.96	2.02	0.61
	267	41.73	0.84	12.21	0.01	18.74	0.36	8.52	11.60	1.28	1.40	96.69	6.35	1.66	0.53	0.11	0.52	0.00	0.04	1.93	1.83	0.01	0.03	0.00	1.89	0.08	0.01	0.30	0.27	8.01	4.97	2.01	0.57
	268	41.40	0.84	12.37	0.02	19.07	0.38	8.55	11.72	1.32	1.46	97.11	6.30	1.71	0.50	0.12	0.55	0.00	0.04	1.94	1.83	0.01	0.05	0.00	1.90	0.05	0.01	0.34	0.28	8.01	4.98	2.01	0.63
	269	41.78	0.82	12.31	0.02	18.87	0.38	8.45	11.53	1.30	1.43	96.89	6.35	1.66	0.55	0.11	0.53	0.00	0.04	1.92	1.83	0.01	0.04	0.00	1.87	0.09	0.00	0.30	0.28	8.01	4.98	2.01	0.58
	270	41.76	0.78	12.24	0.03	18.96	0.35	8.45	11.50	1.31	1.44	96.82	6.36	1.66	0.54	0.11	0.53	0.00	0.04	1.92	1.85	0.01	0.04	0.00	1.87	0.09	0.00	0.30	0.28	8.01	4.98	2.01	0.58
	271	41.45	0.76	12.23	0.00	18.73	0.37	8.44	11.62	1.29	1.38	96.28	6.34	1.68	0.52	0.11	0.54	0.00	0.04	1.92	1.83	0.01	0.03	0.00	1.90	0.08	0.01	0.30	0.27	8.02	4.96	2.02	0.57
	272	41.71	0.77	12.08	0.00	18.91	0.38	8.55	11.66	1.30	1.49	96.84	6.35	1.66	0.51	0.10	0.54	0.00	0.04	1.94	1.84	0.01	0.03	0.00	1.90	0.08	0.01	0.30	0.29	8.01	4.97	2.01	0.60
	273	41.78	0.79	12.29	0.00	18.61	0.37	8.48	11.77	1.32	1.46	96.85	6.35	1.66	0.54	0.10	0.51	0.00	0.04	1.92	1.85	0.01	0.01	0.00	1.91	0.09	0.01	0.30	0.28	8.01	4.96	2.02	0.58
	274	41.78	0.79	12.25	0.03	18.72	0.37	8.68	11.77	1.31	1.40	97.09	6.34	1.67	0.52	0.11	0.53	0.00	0.04	1.96	1.82	0.01	0.03	0.00	1.91	0.07	0.01	0.32	0.27	8.01	4.98	2.01	0.60
	275	41.89	0.76	12.20	0.00	18.50	0.39	8.58	11.65	1.26	1.45	96.67	6.37	1.64	0.54	0.10	0.52	0.00	0.04	1.95	1.81	0.01	0.02	0.00	1.89	0.10	0.00	0.28	0.28	8.01	4.97	2.01	0.56
	276	41.85	0.85	12.21	0.00	18.90	0.41	8.60	11.64	1.27	1.47	97.19	6.35	1.66	0.52	0.11	0.54	0.00	0.04	1.94	1.81	0.01	0.04	0.00	1.89	0.07	0.00	0.30	0.28	8.01	4.98	2.01	0.59
	277	41.47	0.80	12.00	0.03	18.68	0.39	8.73	11.65	1.21	1.39	96.35	6.34	1.68	0.48	0.12	0.56	0.00	0.04	1.99	1.79	0.01	0.04	0.00	1.90	0.06	0.01	0.30	0.27	8.02	4.97	2.01	0.58
	278	42.02	0.82	11.73	0.00	18.95	0.41	8.91	11.75	1.21	1.34	97.13	6.37	1.64	0.45	0.11	0.57	0.00	0.04	2.01	1.79	0.01	0.04	0.00	1.90	0.04	0.00	0.31	0.26	8.02	4.98	2.00	0.58
	279	40.94	0.83	12.14	0.00	18.96	0.37	8.28	11.66	1.26	1.44	95.87	6.30	1.72	0.49	0.12	0.55	0.00	0.04	1.90	1.86	0.01	0.03	0.00	1.91	0.07	0.01	0.30	0.28	8.02	4.96	2.02	0.60
	280	40.73	0.76	12.32	0.00	18.97	0.36	8.25	11.71	1.26	1.47	95.82	6.28	1.74	0.49	0.11	0.56	0.00	0.04	1.90	1.86	0.01	0.03	0.00	1.92	0.07	0.01	0.31	0.29	8.02	4.96	2.03	0.61

doi:10.6342/NTU202202659

Mineral	No.	SiO_2	TiO_2	Al_2O_3	Cr_2O_3	FeO	MnO	MgO	CaO	Na_2O	K_2O	Total	T		C							B					A			$T_{(total)}$	$C_{(total)}$	$B_{(total)}$	$A_{(total)}$
													Si^{4+}	Al^{3+}	Al^{3+}	Ti^{4+}	Fe^{3+}	Cr^{3+}	Mn^{2+}	Mg^{2+}	Fe^{2+}	Mn^{2+}	Fe^{2+}	Mg^{2+}	Ca^{2+}	Na^{+}	Ca^{2+}	Na^{+}	K^{+}				
Tonalitic gneiss	281	41.84	0.73	12.31	0.00	18.82	0.37	8.71	11.53	1.27	1.46	97.04	6.35	1.67	0.54	0.10	0.55	0.00	0.04	1.97	1.79	0.01	0.05	0.00	1.87	0.07	0.00	0.30	0.28	8.01	4.99	2.00	0.59
Hb4	282	41.85	0.74	12.23	0.00	18.91	0.35	8.72	11.44	1.28	1.39	96.90	6.35	1.66	0.53	0.10	0.55	0.00	0.04	1.97	1.79	0.01	0.06	0.01	1.86	0.07	0.00	0.31	0.27	8.02	4.98	2.00	0.58
	283	41.61	0.77	12.19	0.00	18.85	0.36	8.52	11.80	1.27	1.44	96.80	6.34	1.68	0.51	0.11	0.53	0.00	0.04	1.94	1.85	0.01	0.03	0.00	1.92	0.07	0.01	0.31	0.28	8.01	4.97	2.02	0.59
	284	41.80	0.75	12.34	0.00	18.98	0.33	8.46	11.68	1.32	1.47	97.14	6.35	1.66	0.54	0.10	0.52	0.00	0.04	1.92	1.86	0.01	0.03	0.00	1.90	0.08	0.00	0.31	0.28	8.01	4.97	2.01	0.60
	285	41.05	0.86	12.23	0.00	18.19	0.35	8.65	11.50	1.23	1.46	95.51	6.31	1.71	0.51	0.12	0.54	0.00	0.04	1.98	1.77	0.01	0.03	0.00	1.89	0.08	0.01	0.28	0.29	8.02	4.96	2.01	0.58
	286	42.42	0.75	11.46	0.00	17.73	0.36	9.07	11.47	1.26	1.42	95.94	6.46	1.56	0.50	0.10	0.50	0.00	0.04	2.06	1.76	0.01	0.00	0.00	1.87	0.13	0.00	0.24	0.28	8.01	4.95	2.01	0.52
	287	42.55	0.83	11.29	0.01	18.61	0.35	9.22	11.76	1.13	1.29	97.03	6.44	1.58	0.44	0.11	0.53	0.00	0.04	2.07	1.78	0.01	0.04	0.01	1.90	0.04	0.00	0.29	0.25	8.01	4.97	2.00	0.54
Tonalitic gneiss	288	43.07	0.78	11.03	0.00	18.89	0.34	9.19	11.82	1.18	1.29	97.59	6.48	1.53	0.43	0.10	0.52	0.00	0.03	2.06	1.83	0.01	0.03	0.00	1.90	0.06	0.00	0.29	0.25	8.01	4.98	2.00	0.54
Hb5	289	42.67	0.81	11.21	0.00	18.64	0.40	8.93	11.75	1.24	1.34	96.99	6.46	1.55	0.45	0.11	0.52	0.00	0.04	2.02	1.83	0.01	0.01	0.00	1.90	0.09	0.00	0.28	0.26	8.01	4.96	2.01	0.54
	290	42.33	0.81	11.47	0.00	18.93	0.37	8.82	11.67	1.25	1.40	97.05	6.42	1.59	0.46	0.11	0.54	0.00	0.04	1.99	1.84	0.01	0.03	0.00	1.89	0.08	0.00	0.29	0.27	8.01	4.97	2.01	0.56
	291	42.07	0.83	11.63	0.00	18.58	0.42	8.99	11.78	1.26	1.36	96.92	6.38	1.63	0.45	0.11	0.55	0.00	0.04	2.03	1.78	0.01	0.03	0.00	1.91	0.06	0.00	0.31	0.26	8.01	4.97	2.01	0.58
	292	41.76	0.79	11.77	0.00	18.72	0.37	8.97	11.78	1.15	1.45	96.76	6.36	1.66	0.45	0.11	0.56	0.00	0.04	2.04	1.79	0.01	0.04	0.00	1.91	0.04	0.01	0.30	0.28	8.02	4.98	2.00	0.59
	293	41.70	0.79	11.90	0.03	18.50	0.35	8.63	11.65	1.22	1.50	96.27	6.37	1.64	0.50	0.11	0.51	0.00	0.04	1.97	1.83	0.01	0.02	0.00	1.90	0.09	0.01	0.27	0.29	8.01	4.96	2.02	0.57
	294	41.67	0.82	12.17	0.00	18.47	0.35	8.59	11.64	1.25	1.51	96.45	6.36	1.66	0.53	0.11	0.51	0.00	0.04	1.95	1.82	0.01	0.02	0.00	1.90	0.09	0.01	0.28	0.29	8.01	4.96	2.02	0.58
	295	41.63	0.79	12.40	0.00	18.88	0.38	8.53	11.66	1.36	1.61	97.23	6.32	1.68	0.53	0.10	0.54	0.00	0.04	1.93	1.83	0.01	0.03	0.00	1.89	0.09	0.01	0.31	0.31	8.01	4.98	2.02	0.63
	296	41.78	0.86	12.38	0.00	19.09	0.38	8.50	11.59	1.31	1.51	97.40	6.33	1.67	0.54	0.11	0.54	0.00	0.04	1.92	1.83	0.01	0.05	0.00	1.88	0.07	0.00	0.31	0.29	8.01	4.99	2.01	0.61
	297	41.54	0.84	12.37	0.00	19.04	0.36	8.54	11.62	1.27	1.48	97.04	6.32	1.69	0.52	0.11	0.55	0.00	0.04	1.94	1.83	0.01	0.05	0.00	1.89	0.06	0.01	0.31	0.29	8.01	4.98	2.01	0.61
	298	42.12	0.85	12.38	0.00	19.26	0.42	8.65	11.74	1.32	1.48	98.21	6.34	1.67	0.53	0.11	0.55	0.00	0.04	1.94	1.82	0.01	0.05	0.00	1.89	0.05	0.00	0.33	0.28	8.01	5.00	2.00	0.62
	299	41.15	0.73	12.39	0.00	18.83	0.37	8.62	11.45	1.25	1.54	96.33	6.30	1.72	0.51	0.11	0.57	0.00	0.04	1.97	1.78	0.01	0.06	0.00	1.87	0.07	0.01	0.30	0.30	8.02	4.98	2.00	0.61
	300	41.87	0.78	12.41	0.01	18.98	0.37	8.59	11.57	1.36	1.50	97.44	6.34	1.67	0.54	0.10	0.54	0.00	0.04	1.94	1.82	0.01	0.04	0.00	1.87	0.08	0.00	0.32	0.29	8.01	4.99	2.00	0.61
	301	41.86	0.77	12.02	0.03	18.83	0.38	8.70	11.76	1.31	1.43	97.08	6.36	1.66	0.49	0.10	0.54	0.00	0.04	1.97	1.83	0.01	0.03	0.00	1.91	0.07	0.01	0.31	0.28	8.01	4.98	2.01	0.60
	302	41.44	0.78	12.23	0.03	18.92	0.39	8.77	11.72	1.27	1.43	96.96	6.31	1.71	0.48	0.11	0.57	0.00	0.04	1.99	1.79	0.01	0.05	0.00	1.90	0.04	0.01	0.33	0.28	8.02	4.98	2.00	0.62
	303	41.14	0.82	12.35	0.01	18.44	0.43	8.64	11.60	1.25	1.47	96.14	6.30	1.72	0.51	0.12	0.56	0.00	0.05	1.97	1.76	0.01	0.04	0.00	1.90	0.07	0.01	0.30	0.29	8.02	4.97	2.01	0.60
	304	41.18	0.74	12.28	0.00	18.54	0.38	8.51	11.75	1.27	1.50	96.14	6.31	1.71	0.51	0.11	0.54	0.00	0.04	1.94	1.82	0.01	0.02	0.00	1.92	0.08	0.01	0.30	0.29	8.02	4.96	2.02	0.60
	305	41.50	0.79	12.18	0.00	18.92	0.42	8.67	11.65	1.23	1.36	96.72	6.32	1.70	0.49	0.12	0.58	0.00	0.04	1.97	1.79	0.01	0.05	0.00	1.90	0.05	0.01	0.32	0.27	8.02	4.98	2.00	0.59
	306	41.24	0.85	11.97	0.00	19.10	0.37	8.65	11.76	1.22	1.45	96.60	6.31	1.71	0.45	0.12	0.57	0.00	0.04	1.97	1.82	0.01	0.05	0.00	1.92	0.04	0.01	0.33	0.28	8.02	4.97	2.01	0.62
	307	42.91	0.81	11.26	0.00	18.20	0.36	9.13	11.74	1.08	1.27	96.76	6.49	1.52	0.48	0.11	0.49	0.00	0.04	2.06	1.79	0.01	0.02	0.00	1.90	0.08	0.00	0.24	0.25	8.01	4.97	2.00	0.49
Tonalitic gneiss	362	41.97	0.80	11.58	0.00	19.46	0.40	8.52	11.58	1.29	1.45	97.04	6.39	1.62	0.45	0.11	0.57	0.00	0.04	1.93	1.87	0.01	0.04	0.00	1.88	0.08	0.00	0.30	0.28	8.01	4.97	2.01	0.59
Hb6	363	41.69	0.87	11.67	0.01	19.18	0.36	8.68	11.61	1.26	1.36	96.68	6.36	1.66	0.44	0.12	0.56	0.00	0.04	1.97	1.84	0.01	0.05	0.00	1.89	0.05	0.01	0.32	0.26	8.02	4.97	2.00	0.59
	364	42.23	0.81	11.73	0.00	19.27	0.38	8.63	11.66	1.21	1.37	97.29	6.40	1.61	0.48	0.11	0.55	0.00	0.04	1.95	1.85	0.01	0.04	0.00	1.89	0.06	0.00	0.29	0.27	8.01	4.98	2.00	0.56
	365	42.65	0.86	11.68	0.04	19.09	0.38	8.68	11.61	1.13	1.49	97.61	6.44	1.57	0.51	0.11	0.52	0.00	0.04	1.95	1.85	0.01	0.04	0.00	1.87	0.07	0.00	0.26	0.29	8.00	4.99	2.00	0.55
	366	41.72	0.85	11.63	0.00	19.21	0.36	8.60	11.68	1.26	1.41	96.71	6.37	1.65	0.44	0.12	0.55	0.00	0.04	1.96	1.86	0.01	0.04	0.00	1.90	0.06	0.01	0.31	0.27	8.02	4.97	2.01	0.59
	367	42.56	0.74	11.23	0.01	18.83	0.34	8.76	11.80	1.11	1.33	96.71	6.46	1.55	0.46	0.10	0.51	0.00	0.04	1.98	1.87	0.01	0.01	0.00	1.92	0.08	0.00	0.25	0.26	8.01	4.96	2.01	0.51
	368	42.54	0.81	11.43	0.00	18.33	0.34	8.89	11.68	1.13	1.31	96.45	6.46	1.55	0.49	0.11	0.49	0.00	0.04	2.01	1.82	0.01	0.02	0.00	1.90	0.09	0.00	0.24	0.25	8.01	4.96	2.01	0.50
	369	42.37	0.84	11.77	0.02	18.43	0.35	8.54	11.65	1.11	1.42	96.49	6.44	1.57	0.54	0.11	0.48	0.00	0.04	1.94	1.86	0.01	0.01	0.00	1.89	0.10	0.00	0.22	0.27	8.01	4.96	2.01	0.50
	370	42.06	0.83	11.70	0.01	18.73	0.39	8.57	11.61	1.28	1.38	96.56	6.40	1.61	0.49	0.11	0.53	0.00	0.04	1.95	1.84	0.01	0.02	0.00	1.89	0.10	0.00	0.28	0.27	8.01	4.96	2.01	0.55
	371	41.13	0.83	11.68	0.00	18.47	0.35	8.63	11.73	1.29	1.47	95.57	6.33	1.68	0.44	0.12	0.54	0.00	0.04	1.98	1.83	0.01	0.01	0.00	1.93	0.08	0.01	0.30	0.29	8.02	4.94	2.03	0.60
	372	42.03	0.84	11.81	0.00	18.46	0.39	8.58	11.67	1.28	1.44	96.50	6.40	1.61	0.51	0.11	0.51	0.00	0.04	1.95	1.84	0.01	0.01	0.00	1.90	0.11	0.00	0.27	0.28	8.01	4.96	2.02	0.55
	373	41.71	0.86	11.74	0.00	19.17	0.36	8.64	11.62	1.29	1.44	96.82	6.36	1.66	0.45	0.12	0.56	0.00	0.04	1.96	1.84	0.01	0.04	0.00	1.89	0.06	0.01	0.32	0.28	8.01	4.97	2.01	0.60
	374	42.10	0.83	11.73	0.00	19.21	0.42	8.55	11.63	1.27	1.52	97.25	6.39	1.62	0.48	0.11	0.55	0.00	0.04	1.94	1.85	0.01	0.03	0.00	1.89	0.08	0.00	0.29	0.29	8.01	4.97	2.01	0.59
	375	42.06	0.80	11.81	0.00	18.95	0.34	8.55	11.49	1.31	1.42	96.72	6.40	1.61	0.51	0.11	0.52	0.00	0.04	1.94	1.86	0.01	0.03	0.00	1.87	0.10	0.00	0.29	0.28	8.01	4.97	2.01	0.57
	376	41.67	0.86	11.71	0.00	19.05	0.37	8.48	11.34	1.36	1.38	96.20	6.38	1.64	0.47	0.12	0.56	0.00	0.04	1.93	1.84	0.01	0.04	0.00	1.86	0.10	0.00	0.30	0.27	8.02	4.96	2.01	0.57
	377	41.79	0.83	11.74	0.02	18.98	0.33	8.05	11.46	1.26	1.41	95.87	6.41	1.60	0.52	0.11	0.50	0.00	0.04	1.84	1.93	0.01	0.01	0.00	1.88	0.13	0.00	0.24	0.28	8.01	4.94	2.03	0.52
	378	41.61	0.84	11.69	0.00	19.06	0.36	8.02	11.43	1.29	1.44	95.74	6.40	1.61	0.50	0.12	0.52	0.00	0.04	1.84	1.92	0.01	0.01	0.00	1.88	0.13	0.01	0.25	0.28	8.01	4.94	2.03	0.54
	379	41.58	0.82	11.79	0.00	19.20	0.33	8.63	11.70	1.26	1.48	96.79	6.35	1.67	0.45	0.11	0.55	0.00	0.04	1.96	1.86	0.01	0.04	0.00	1.91	0.05	0.01	0.32	0.29	8.01	4.97	2.01	0.61
	380	39.36	0.80	11.63	0.01	18.98	0.36	8.77	11.60	1.35	1.42	94.27	6.18	1.86	0.30	0.14	0.66	0.00	0.04	2.05	1.77	0.01	0.06	0.00	1.93	0.02	0.02	0.40	0.28	8.04	4.95	2.03	0.70

doi:10.6342/NTU202202659

Mineral	No.	SiO_2	TiO_2	Al_2O_3	Cr_2O_3	FeO	MnO	MgO	CaO	Na_2O	K_2O	Total	T		C							B					A			$T_{(total)}$	$C_{(total)}$	$B_{(total)}$	$A_{(total)}$
													Si^{4+}	Al^{3+}	Al^{3+}	Ti^{4+}	Fe^{3+}	Cr^{3+}	Mn^{2+}	Mg^{2+}	Fe^{2+}	Mn^{2+}	Fe^{2+}	Mg^{2+}	Ca^{2+}	Na^{+}	Ca^{2+}	Na^{+}	K^{+}				
Tonalitic gneiss	381	41.38	0.86	11.43	0.00	19.08	0.34	8.73	11.57	1.30	1.43	96.11	6.35	1.67	0.40	0.12	0.57	0.00	0.04	2.00	1.83	0.01	0.04	0.00	1.90	0.06	0.01	0.32	0.28	8.02	4.96	2.01	0.61
Hb6	382	40.92	0.85	11.70	0.00	19.09	0.35	8.60	11.67	1.28	1.49	95.93	6.30	1.72	0.41	0.12	0.58	0.00	0.04	1.98	1.84	0.01	0.04	0.00	1.92	0.05	0.01	0.33	0.29	8.02	4.96	2.02	0.63
	383	42.02	0.85	11.82	0.00	18.89	0.35	8.68	11.63	1.31	1.41	96.97	6.38	1.63	0.49	0.11	0.53	0.00	0.04	1.97	1.84	0.01	0.03	0.00	1.89	0.08	0.00	0.31	0.27	8.01	4.97	2.01	0.58
	384	42.13	0.86	11.88	0.00	19.23	0.40	8.69	11.63	1.26	1.44	97.52	6.38	1.63	0.48	0.11	0.56	0.00	0.04	1.96	1.83	0.01	0.05	0.00	1.88	0.06	0.00	0.31	0.28	8.01	4.99	2.00	0.59
	385	42.01	0.82	11.65	0.01	19.10	0.38	8.56	11.59	1.35	1.39	96.84	6.39	1.62	0.47	0.11	0.54	0.00	0.04	1.94	1.86	0.01	0.03	0.00	1.89	0.09	0.00	0.31	0.27	8.01	4.97	2.01	0.58
	386	41.99	0.82	11.65	0.00	18.89	0.37	8.77	11.66	1.35	1.35	96.85	6.38	1.63	0.46	0.11	0.54	0.00	0.04	1.99	1.83	0.01	0.03	0.00	1.90	0.08	0.00	0.32	0.26	8.01	4.97	2.01	0.59
	387	40.62	0.81	11.81	0.01	19.01	0.34	8.67	11.68	1.31	1.38	95.66	6.27	1.75	0.40	0.13	0.59	0.00	0.04	2.00	1.81	0.01	0.05	0.00	1.92	0.04	0.01	0.35	0.27	8.03	4.96	2.02	0.64
	388	35.33	0.83	11.79	0.00	19.21	0.38	8.74	11.45	1.32	1.31	90.36	5.86	2.22	0.08	0.20	0.87	0.00	0.04	2.11	1.63	0.02	0.16	0.05	1.98	0.00	0.05	0.42	0.28	8.08	4.93	2.21	0.75
	389	41.92	0.81	11.28	0.01	18.76	0.39	8.66	11.52	1.31	1.40	96.05	6.42	1.60	0.43	0.11	0.55	0.00	0.04	1.98	1.84	0.01	0.02	0.00	1.88	0.11	0.00	0.28	0.27	8.02	4.95	2.02	0.56
	390	42.06	0.79	10.98	0.00	18.85	0.40	8.69	11.59	1.26	1.38	96.00	6.44	1.58	0.40	0.11	0.55	0.00	0.04	1.98	1.85	0.01	0.01	0.00	1.90	0.10	0.00	0.27	0.27	8.02	4.94	2.02	0.54
	391	42.49	0.83	11.58	0.01	18.83	0.41	8.74	11.66	1.18	1.42	97.15	6.43	1.58	0.49	0.11	0.53	0.00	0.04	1.97	1.83	0.01	0.03	0.00	1.89	0.08	0.00	0.26	0.27	8.01	4.97	2.01	0.54
	392	42.33	0.87	11.64	0.01	18.91	0.35	8.81	11.62	1.27	1.46	97.27	6.41	1.60	0.48	0.11	0.52	0.00	0.04	1.99	1.84	0.01	0.03	0.00	1.88	0.08	0.00	0.29	0.28	8.01	4.98	2.00	0.58
	393	42.41	0.85	11.59	0.00	18.87	0.32	8.80	11.65	1.33	1.26	97.07	6.42	1.59	0.48	0.11	0.51	0.00	0.03	1.99	1.85	0.01	0.03	0.00	1.89	0.08	0.00	0.31	0.24	8.01	4.97	2.01	0.56
	394	41.82	0.87	11.45	0.00	18.98	0.37	8.75	11.64	1.28	1.27	96.45	6.38	1.64	0.43	0.12	0.56	0.00	0.04	1.99	1.83	0.01	0.04	0.00	1.90	0.06	0.00	0.32	0.25	8.02	4.96	2.01	0.57
	395	42.21	0.89	11.45	0.02	18.62	0.35	8.80	11.70	1.23	1.35	96.61	6.42	1.59	0.46	0.12	0.51	0.00	0.04	2.00	1.84	0.01	0.02	0.00	1.90	0.08	0.00	0.28	0.26	8.01	4.96	2.01	0.55
	396	42.34	0.88	11.49	0.01	19.05	0.39	8.73	11.66	1.23	1.37	97.15	6.42	1.59	0.46	0.12	0.54	0.00	0.04	1.97	1.84	0.01	0.03	0.00	1.89	0.07	0.00	0.29	0.27	8.01	4.98	2.00	0.56
Tonalitic gneiss	397	42.44	0.86	10.97	0.00	18.98	0.38	8.89	11.63	1.26	1.38	96.79	6.45	1.56	0.41	0.11	0.54	0.00	0.04	2.01	1.84	0.01	0.02	0.00	1.89	0.08	0.00	0.29	0.27	8.01	4.96	2.01	0.56
Hb7	398	42.58	0.85	11.22	0.00	18.96	0.33	8.78	11.63	1.25	1.38	96.99	6.46	1.55	0.46	0.11	0.51	0.00	0.04	1.98	1.87	0.01	0.02	0.00	1.89	0.09	0.00	0.28	0.27	8.01	4.96	2.01	0.55
	399	42.32	0.93	11.40	0.01	18.87	0.37	8.72	11.58	1.29	1.33	96.82	6.43	1.58	0.46	0.12	0.53	0.00	0.04	1.98	1.84	0.01	0.03	0.00	1.88	0.09	0.00	0.29	0.26	8.01	4.97	2.01	0.55
	400	42.43	0.90	11.40	0.01	18.83	0.41	8.67	11.59	1.31	1.35	96.89	6.44	1.57	0.47	0.12	0.53	0.00	0.04	1.96	1.84	0.01	0.02	0.00	1.88	0.10	0.00	0.28	0.26	8.01	4.96	2.01	0.55
	401	41.86	0.84	11.63	0.03	18.47	0.34	8.62	11.35	1.29	1.43	95.86	6.41	1.61	0.49	0.11	0.52	0.00	0.04	1.97	1.82	0.01	0.02	0.00	1.86	0.12	0.00	0.26	0.28	8.01	4.96	2.01	0.54
	402	41.94	0.83	11.60	0.00	18.54	0.38	8.68	11.36	1.33	1.48	96.14	6.41	1.61	0.48	0.11	0.54	0.00	0.04	1.98	1.81	0.01	0.02	0.00	1.86	0.12	0.00	0.27	0.29	8.01	4.96	2.01	0.56
	403	42.10	0.80	11.62	0.00	19.03	0.37	8.64	11.61	1.25	1.44	96.88	6.40	1.61	0.47	0.11	0.54	0.00	0.04	1.96	1.85	0.01	0.03	0.00	1.89	0.08	0.00	0.29	0.28	8.01	4.97	2.01	0.57
	404	42.10	0.89	10.22	0.01	19.32	0.38	8.75	11.57	1.23	1.43	95.89	6.47	1.55	0.30	0.12	0.57	0.00	0.04	2.00	1.89	0.01	0.02	0.00	1.90	0.09	0.00	0.27	0.28	8.01	4.94	2.02	0.56
	405	42.27	0.83	11.39	0.00	19.28	0.37	8.91	11.68	1.34	1.40	97.47	6.40	1.61	0.42	0.11	0.56	0.00	0.04	2.01	1.84	0.01	0.04	0.00	1.89	0.06	0.00	0.33	0.27	8.01	4.98	2.00	0.61
	406	42.19	0.85	11.21	0.01	19.11	0.35	8.87	11.71	1.19	1.33	96.83	6.42	1.60	0.41	0.12	0.55	0.00	0.04	2.01	1.85	0.01	0.04	0.00	1.90	0.05	0.00	0.30	0.26	8.01	4.97	2.00	0.56
	407	42.29	0.86	11.37	0.00	19.11	0.39	8.72	11.73	1.27	1.34	97.07	6.42	1.59	0.44	0.11	0.54	0.00	0.04	1.97	1.86	0.01	0.03	0.00	1.90	0.07	0.00	0.30	0.26	8.01	4.97	2.01	0.57
	408	42.31	0.86	11.45	0.02	19.39	0.37	8.70	11.66	1.26	1.30	97.30	6.41	1.60	0.45	0.12	0.55	0.00	0.04	1.96	1.86	0.01	0.04	0.00	1.89	0.06	0.00	0.31	0.25	8.01	4.98	2.00	0.57
	409	42.33	0.73	10.93	0.02	19.35	0.41	8.90	11.64	1.28	1.30	96.88	6.44	1.58	0.38	0.10	0.59	0.00	0.04	2.01	1.84	0.01	0.03	0.00	1.89	0.06	0.00	0.31	0.25	8.02	4.97	2.00	0.57
	410	42.97	0.76	10.74	0.02	19.23	0.43	8.93	11.71	1.21	1.24	97.24	6.50	1.52	0.40	0.10	0.56	0.00	0.04	2.01	1.85	0.01	0.02	0.00	1.90	0.07	0.00	0.28	0.24	8.01	4.97	2.00	0.52

doi:10.6342/NTU202202659

Mineral	No.	SiO_2	TiO_2	Al_2O_3	Cr_2O_3	FeO	MnO	MgO	CaO	Na_2O	K_2O	Total	Si^{4+}	Ti^{4+}	Al^{3+}	Fe^{2+}	Mn^{2+}	Mg^{2+}	Ca^{2+}	Na^{+}	K^{+}	$Al_{(M)}$	$Al_{(T)}$	$I_{(total)}$	$M_{(total)}$	$T_{(total)}$	X_{Mg}	Ti-in-Bt thermometer (°C)
Biotite	541	36.78	2.69	15.23	0.00	20.71	0.28	10.66	0.00	0.06	9.56	95.97	5.61	0.31	2.74	2.64	0.04	2.43	0.00	0.02	1.86	0.35	2.39	1.88	5.77	8.00	0.48	662
	514	36.42	3.00	15.21	0.00	21.04	0.26	10.16	0.02	0.10	9.41	95.60	5.59	0.35	2.75	2.70	0.03	2.32	0.00	0.03	1.84	0.34	2.41	1.87	5.75	8.00	0.46	677
	531	36.48	2.71	15.10	0.00	20.73	0.25	10.57	0.03	0.10	9.63	95.58	5.60	0.31	2.73	2.66	0.03	2.42	0.00	0.03	1.89	0.33	2.40	1.92	5.76	8.00	0.48	664
	495	35.82	2.60	15.13	0.01	21.32	0.29	10.64	0.02	0.11	9.46	95.40	5.53	0.30	2.75	2.75	0.04	2.45	0.00	0.03	1.86	0.29	2.47	1.90	5.83	8.00	0.47	657
	554	36.48	2.61	14.95	0.00	20.94	0.24	10.62	0.01	0.09	9.40	95.33	5.61	0.30	2.71	2.70	0.03	2.44	0.00	0.03	1.85	0.33	2.39	1.87	5.79	8.00	0.47	658
	518	36.24	2.58	15.06	0.00	21.25	0.24	10.32	0.00	0.10	9.52	95.31	5.59	0.30	2.74	2.74	0.03	2.37	0.00	0.03	1.88	0.33	2.41	1.91	5.78	8.00	0.46	654
	539	36.69	2.76	14.79	0.00	20.49	0.22	10.65	0.00	0.07	9.55	95.23	5.64	0.32	2.68	2.64	0.03	2.44	0.00	0.02	1.87	0.32	2.36	1.89	5.75	8.00	0.48	668
	501	36.59	2.94	15.08	0.05	21.01	0.22	9.80	0.02	0.05	9.45	95.20	5.64	0.34	2.74	2.71	0.03	2.25	0.00	0.02	1.86	0.38	2.36	1.87	5.70	8.00	0.45	673
	513	36.43	2.92	15.35	0.00	20.49	0.21	10.18	0.03	0.13	9.45	95.18	5.60	0.34	2.78	2.63	0.03	2.33	0.01	0.04	1.85	0.38	2.40	1.90	5.72	8.00	0.47	674
	536	36.64	2.74	15.30	0.01	20.19	0.21	10.41	0.03	0.09	9.58	95.18	5.63	0.32	2.77	2.59	0.03	2.38	0.00	0.03	1.88	0.40	2.37	1.91	5.72	8.00	0.48	666
	553	36.35	2.57	14.92	0.00	21.38	0.26	10.37	0.00	0.08	9.25	95.18	5.61	0.30	2.72	2.76	0.03	2.39	0.00	0.02	1.82	0.33	2.39	1.85	5.81	8.00	0.46	654
	521	36.51	2.56	15.11	0.02	20.97	0.26	10.21	0.11	0.09	9.34	95.16	5.63	0.30	2.74	2.70	0.03	2.35	0.02	0.03	1.84	0.37	2.37	1.88	5.75	8.00	0.46	653
	512	36.51	2.89	15.10	0.01	20.81	0.24	10.04	0.02	0.07	9.45	95.13	5.63	0.33	2.74	2.68	0.03	2.31	0.00	0.02	1.86	0.37	2.37	1.88	5.72	8.00	0.46	672
	538	36.66	2.86	14.68	0.04	20.40	0.24	10.59	0.01	0.06	9.59	95.13	5.65	0.33	2.66	2.63	0.03	2.43	0.00	0.02	1.88	0.31	2.35	1.90	5.73	8.00	0.48	673
	515	35.95	2.95	15.19	0.02	20.78	0.23	10.08	0.02	0.08	9.80	95.09	5.56	0.34	2.77	2.69	0.03	2.33	0.00	0.02	1.93	0.33	2.44	1.96	5.72	8.00	0.46	676
	519	36.52	2.49	14.86	0.00	20.73	0.26	10.62	0.02	0.06	9.54	95.08	5.63	0.29	2.70	2.67	0.03	2.44	0.00	0.02	1.88	0.34	2.37	1.90	5.78	8.00	0.48	650
	492	36.04	2.14	15.20	0.00	20.81	0.28	10.89	0.01	0.10	9.60	95.06	5.57	0.25	2.77	2.69	0.04	2.51	0.00	0.03	1.89	0.34	2.43	1.92	5.83	8.00	0.48	626
	530	36.41	2.50	15.26	0.00	20.63	0.24	10.64	0.10	0.07	9.20	95.05	5.60	0.29	2.77	2.66	0.03	2.44	0.02	0.02	1.81	0.37	2.40	1.84	5.79	8.00	0.48	652
	502	36.64	2.71	15.13	0.00	20.23	0.24	10.60	0.00	0.11	9.40	95.03	5.63	0.31	2.74	2.60	0.03	2.43	0.00	0.03	1.84	0.37	2.37	1.87	5.75	8.00	0.48	665
	504	36.23	2.86	15.03	0.02	20.61	0.22	10.30	0.00	0.10	9.65	95.02	5.60	0.33	2.74	2.66	0.03	2.37	0.00	0.03	1.90	0.34	2.40	1.93	5.73	8.00	0.47	672
	532	36.37	2.49	15.10	0.02	20.50	0.28	10.61	0.06	0.10	9.47	95.01	5.61	0.29	2.75	2.64	0.04	2.44	0.01	0.03	1.86	0.36	2.39	1.91	5.77	8.00	0.48	651
	529	36.51	2.56	15.06	0.00	20.65	0.25	10.20	0.03	0.09	9.65	95.00	5.64	0.30	2.74	2.67	0.03	2.35	0.00	0.03	1.90	0.38	2.36	1.93	5.73	8.00	0.47	654
	497	36.20	2.45	15.25	0.02	20.68	0.20	10.72	0.02	0.07	9.38	94.98	5.59	0.28	2.77	2.67	0.03	2.47	0.00	0.02	1.85	0.36	2.41	1.87	5.80	8.00	0.48	649
	547	36.24	2.57	14.70	0.00	21.10	0.23	10.60	0.00	0.09	9.43	94.97	5.61	0.30	2.68	2.73	0.03	2.45	0.00	0.03	1.86	0.29	2.39	1.89	5.80	8.00	0.47	656
	503	36.30	2.83	14.94	0.00	20.51	0.28	10.39	0.00	0.09	9.63	94.95	5.61	0.33	2.72	2.65	0.04	2.39	0.00	0.03	1.90	0.33	2.39	1.92	5.74	8.00	0.47	671
	219	36.37	2.78	14.87	0.00	20.51	0.25	10.58	0.00	0.04	9.54	94.93	5.62	0.32	2.71	2.65	0.03	2.44	0.00	0.01	1.88	0.32	2.38	1.89	5.76	8.00	0.48	669
	516	36.15	2.92	14.92	0.00	20.84	0.24	10.20	0.01	0.07	9.57	94.92	5.60	0.34	2.72	2.70	0.03	2.35	0.00	0.02	1.89	0.32	2.40	1.91	5.74	8.00	0.47	675
	533	36.22	2.66	14.92	0.01	20.59	0.25	10.54	0.00	0.09	9.62	94.90	5.60	0.31	2.72	2.66	0.03	2.43	0.00	0.03	1.90	0.33	2.40	1.93	5.76	8.00	0.48	662
	499	36.01	2.74	15.14	0.00	20.79	0.24	10.32	0.00	0.07	9.58	94.88	5.58	0.32	2.76	2.69	0.03	2.38	0.00	0.02	1.89	0.34	2.42	1.91	5.77	8.00	0.47	665
	493	36.14	2.71	15.16	0.00	20.52	0.21	10.54	0.02	0.11	9.44	94.85	5.59	0.32	2.76	2.65	0.03	2.43	0.00	0.03	1.86	0.35	2.41	1.90	5.77	8.00	0.48	665
	557	36.40	2.44	14.95	0.01	20.89	0.24	10.32	0.02	0.04	9.54	94.85	5.64	0.28	2.73	2.70	0.03	2.38	0.00	0.01	1.88	0.36	2.36	1.90	5.76	8.00	0.47	646
	555	36.45	2.65	14.95	0.01	20.49	0.27	10.65	0.03	0.07	9.30	94.84	5.62	0.31	2.72	2.64	0.03	2.45	0.00	0.02	1.83	0.34	2.38	1.85	5.78	8.00	0.48	662
	542	36.21	2.21	15.11	0.00	20.83	0.22	10.72	0.00	0.10	9.44	94.82	5.60	0.26	2.76	2.70	0.03	2.47	0.00	0.03	1.86	0.36	2.40	1.89	5.81	8.00	0.48	631
	552	36.32	2.57	14.96	0.00	20.72	0.22	10.47	0.00	0.04	9.48	94.78	5.62	0.30	2.73	2.68	0.03	2.41	0.00	0.01	1.87	0.35	2.38	1.88	5.77	8.00	0.47	656
	523	35.96	2.39	15.04	0.01	21.17	0.25	10.56	0.06	0.08	9.26	94.78	5.58	0.28	2.75	2.75	0.03	2.44	0.01	0.02	1.83	0.33	2.42	1.87	5.83	8.00	0.47	644
	498	36.08	2.69	14.93	0.01	20.56	0.24	10.63	0.01	0.06	9.57	94.78	5.59	0.31	2.73	2.66	0.03	2.45	0.00	0.02	1.89	0.31	2.41	1.91	5.78	8.00	0.48	664
	522	36.18	2.61	15.02	0.00	20.71	0.25	10.31	0.00	0.09	9.60	94.76	5.61	0.30	2.74	2.68	0.03	2.38	0.00	0.03	1.90	0.35	2.39	1.92	5.75	8.00	0.47	658
	206	36.58	2.83	14.67	0.00	20.40	0.22	10.41	0.00	0.06	9.58	94.74	5.66	0.33	2.67	2.64	0.03	2.40	0.00	0.02	1.89	0.33	2.34	1.91	5.72	8.00	0.48	671

doi:10.6342/NTU202202659

Mineral	No.	SiO_2	TiO_2	Al_2O_3	Cr_2O_3	FeO	MnO	MgO	CaO	Na_2O	K_2O	Total	Si^{4+}	Ti^{4+}	Al^{3+}	Fe^{2+}	Mn^{2+}	Mg^{2+}	Ca^{2+}	Na^{+}	K^{+}	$Al_{(M)}$	$Al_{(T)}$	$I_{(total)}$	$M_{(total)}$	$T_{(total)}$	X_{Mg}	Ti-in-Bt thermometer (°C)
	543	36.28	2.22	15.20	0.00	20.55	0.22	10.70	0.02	0.05	9.50	94.74	5.61	0.26	2.77	2.66	0.03	2.47	0.00	0.01	1.87	0.38	2.39	1.89	5.80	8.00	0.48	633
	548	36.09	2.51	14.73	0.00	21.14	0.22	10.61	0.07	0.09	9.28	94.74	5.60	0.29	2.69	2.74	0.03	2.45	0.01	0.03	1.84	0.30	2.40	1.88	5.81	8.00	0.47	652
	551	35.17	2.73	14.81	0.01	24.07	0.18	8.52	0.42	0.06	8.78	94.73	5.54	0.32	2.75	3.17	0.02	2.00	0.07	0.02	1.76	0.29	2.46	1.85	5.80	8.00	0.39	655
	222	36.54	2.90	15.06	0.00	20.11	0.25	10.26	0.02	0.05	9.53	94.71	5.64	0.34	2.74	2.60	0.03	2.36	0.00	0.02	1.88	0.38	2.36	1.89	5.70	8.00	0.48	675
	544	36.12	2.65	15.08	0.02	20.65	0.20	10.38	0.01	0.10	9.49	94.70	5.60	0.31	2.75	2.68	0.03	2.40	0.00	0.03	1.87	0.35	2.40	1.91	5.76	8.00	0.47	661
	510	36.22	2.70	15.20	0.00	20.49	0.25	10.13	0.01	0.05	9.64	94.68	5.61	0.31	2.78	2.65	0.03	2.34	0.00	0.01	1.91	0.39	2.39	1.92	5.73	8.00	0.47	663
	488	36.28	2.91	14.75	0.01	20.36	0.24	10.45	0.00	0.07	9.62	94.66	5.62	0.34	2.69	2.64	0.03	2.41	0.00	0.02	1.90	0.31	2.38	1.92	5.73	8.00	0.48	676
	506	36.32	2.74	15.19	0.00	20.22	0.24	10.34	0.01	0.07	9.53	94.66	5.62	0.32	2.77	2.61	0.03	2.38	0.00	0.02	1.88	0.38	2.38	1.90	5.73	8.00	0.48	666
	545	35.95	2.38	14.72	0.01	21.15	0.26	10.55	0.05	0.05	9.49	94.61	5.60	0.28	2.70	2.75	0.03	2.45	0.01	0.02	1.89	0.30	2.40	1.91	5.81	8.00	0.47	644
	205	36.39	2.74	14.70	0.00	20.54	0.21	10.42	0.00	0.10	9.51	94.60	5.64	0.32	2.68	2.66	0.03	2.41	0.00	0.03	1.88	0.33	2.36	1.91	5.74	8.00	0.47	667
	549	36.22	2.64	14.80	0.02	20.39	0.20	10.54	0.00	0.07	9.70	94.58	5.62	0.31	2.71	2.65	0.03	2.44	0.00	0.02	1.92	0.33	2.38	1.94	5.74	8.00	0.48	662
	528	35.96	2.69	14.85	0.00	21.07	0.21	9.98	0.01	0.08	9.73	94.57	5.60	0.32	2.73	2.75	0.03	2.32	0.00	0.02	1.93	0.33	2.40	1.96	5.74	8.00	0.46	661
	540	35.92	2.63	14.98	0.01	20.66	0.21	10.58	0.04	0.09	9.44	94.55	5.58	0.31	2.74	2.68	0.03	2.45	0.01	0.03	1.87	0.32	2.42	1.90	5.79	8.00	0.48	660
	524	35.71	1.83	15.55	0.01	21.26	0.22	10.96	0.12	0.06	8.82	94.55	5.54	0.21	2.84	2.76	0.03	2.53	0.02	0.02	1.75	0.38	2.46	1.78	5.92	8.00	0.48	597
	509	35.91	2.88	14.79	0.00	20.77	0.26	10.32	0.02	0.09	9.48	94.52	5.59	0.34	2.71	2.70	0.03	2.39	0.00	0.03	1.88	0.30	2.41	1.91	5.76	8.00	0.47	674
	491	36.25	2.66	14.75	0.00	20.40	0.22	10.57	0.00	0.10	9.55	94.50	5.62	0.31	2.70	2.65	0.03	2.45	0.00	0.03	1.89	0.32	2.38	1.92	5.76	8.00	0.48	663
	226	36.27	2.42	14.98	0.00	20.46	0.25	10.33	0.02	0.10	9.60	94.42	5.63	0.28	2.74	2.66	0.03	2.39	0.00	0.03	1.90	0.38	2.37	1.93	5.74	8.00	0.47	646
	500	36.25	2.80	15.01	0.03	20.77	0.23	9.78	0.03	0.10	9.40	94.38	5.63	0.33	2.75	2.70	0.03	2.27	0.00	0.03	1.86	0.38	2.37	1.90	5.71	8.00	0.46	667
	517	35.72	2.44	15.01	0.00	21.13	0.23	10.27	0.02	0.08	9.38	94.27	5.58	0.29	2.76	2.76	0.03	2.39	0.00	0.02	1.87	0.34	2.42	1.90	5.81	8.00	0.46	647
	534	35.31	2.57	15.36	0.00	20.55	0.25	10.51	0.00	0.09	9.63	94.25	5.51	0.30	2.83	2.68	0.03	2.45	0.00	0.03	1.92	0.34	2.49	1.94	5.80	8.00	0.48	657
	204	36.24	2.85	14.86	0.00	20.49	0.24	10.28	0.02	0.07	9.15	94.21	5.63	0.33	2.72	2.66	0.03	2.38	0.00	0.02	1.81	0.35	2.37	1.84	5.76	8.00	0.47	673
	486	35.67	2.82	14.87	0.00	20.59	0.26	10.37	0.00	0.10	9.50	94.17	5.57	0.33	2.74	2.69	0.03	2.41	0.00	0.03	1.89	0.30	2.43	1.92	5.77	8.00	0.47	672
	494	35.53	2.70	14.84	0.00	20.88	0.24	10.42	0.06	0.11	9.39	94.17	5.55	0.32	2.73	2.73	0.03	2.43	0.01	0.03	1.87	0.29	2.45	1.91	5.80	8.00	0.47	665
	527	36.54	2.54	14.50	0.00	20.62	0.24	10.34	0.03	0.05	9.30	94.16	5.69	0.30	2.66	2.68	0.03	2.40	0.00	0.01	1.84	0.34	2.31	1.86	5.75	8.00	0.47	654
	535	35.34	2.72	15.29	0.00	20.48	0.22	10.63	0.04	0.07	9.25	94.04	5.52	0.32	2.81	2.67	0.03	2.47	0.01	0.02	1.84	0.33	2.48	1.87	5.82	8.00	0.48	667
	556	36.39	2.67	14.68	0.00	20.25	0.22	10.52	0.00	0.08	9.23	94.03	5.66	0.31	2.69	2.63	0.03	2.44	0.00	0.02	1.83	0.35	2.34	1.85	5.76	8.00	0.48	664
	225	36.18	2.58	14.71	0.01	20.06	0.23	10.45	0.00	0.10	9.68	94.01	5.64	0.30	2.70	2.62	0.03	2.43	0.00	0.03	1.93	0.35	2.36	1.96	5.72	8.00	0.48	659
	505	35.77	2.54	14.93	0.05	20.59	0.24	10.41	0.02	0.04	9.37	93.97	5.59	0.30	2.75	2.69	0.03	2.42	0.00	0.01	1.87	0.34	2.41	1.88	5.78	8.00	0.47	656
	218	35.96	2.89	14.62	0.00	20.84	0.22	10.29	0.03	0.09	9.02	93.97	5.61	0.34	2.69	2.72	0.03	2.40	0.00	0.03	1.80	0.30	2.39	1.83	5.79	8.00	0.47	675
	496	35.79	2.34	15.42	0.00	20.46	0.25	10.57	0.04	0.09	8.91	93.86	5.57	0.27	2.83	2.67	0.03	2.45	0.01	0.03	1.77	0.40	2.43	1.80	5.83	8.00	0.48	642
	490	35.76	2.66	14.76	0.00	20.28	0.25	10.43	0.04	0.08	9.48	93.75	5.60	0.31	2.72	2.66	0.03	2.44	0.01	0.03	1.89	0.32	2.40	1.93	5.76	8.00	0.48	664
	203	36.09	2.82	14.88	0.00	20.24	0.25	10.24	0.02	0.06	9.05	93.66	5.63	0.33	2.74	2.64	0.03	2.38	0.00	0.02	1.80	0.37	2.37	1.82	5.76	8.00	0.47	672
	525	36.48	2.30	13.95	0.00	20.58	0.25	10.48	0.06	0.01	9.45	93.56	5.72	0.27	2.58	2.70	0.03	2.45	0.01	0.00	1.89	0.30	2.28	1.91	5.76	8.00	0.48	640
	520	36.10	2.28	14.85	0.00	20.18	0.24	10.51	0.04	0.09	9.21	93.51	5.65	0.27	2.74	2.64	0.03	2.45	0.01	0.03	1.84	0.38	2.35	1.87	5.78	8.00	0.48	639
	487	34.33	2.97	14.88	0.01	20.88	0.20	10.39	0.00	0.11	9.63	93.40	5.44	0.35	2.78	2.77	0.03	2.45	0.00	0.03	1.95	0.22	2.56	1.98	5.82	8.00	0.47	681
	507	35.10	2.30	15.04	0.03	20.74	0.23	10.36	0.00	0.08	9.34	93.22	5.54	0.27	2.80	2.74	0.03	2.44	0.00	0.02	1.88	0.34	2.46	1.91	5.82	8.00	0.47	640
	526	36.27	2.62	14.21	0.00	20.10	0.21	10.29	0.00	0.06	9.44	93.19	5.70	0.31	2.63	2.64	0.03	2.41	0.00	0.02	1.89	0.33	2.30	1.91	5.72	8.00	0.48	662
	550	35.59	2.49	14.72	0.02	20.13	0.24	10.45	0.01	0.08	9.35	93.08	5.61	0.30	2.73	2.65	0.03	2.45	0.00	0.03	1.88	0.34	2.39	1.91	5.77	8.00	0.48	655
	508	35.08	2.29	15.14	0.00	20.65	0.23	10.39	0.06	0.09	8.88	92.82	5.55	0.27	2.82	2.73	0.03	2.45	0.01	0.03	1.79	0.37	2.45	1.83	5.85	8.00	0.47	640
	546	34.82	2.39	13.85	0.00	21.03	0.28	10.52	0.03	0.09	9.29	92.29	5.58	0.29	2.62	2.82	0.04	2.51	0.01	0.03	1.90	0.20	2.42	1.93	5.85	8.00	0.47	649

doi:10.6342/NTU202202659